2012

Ag on Si(111) from basic science to application

Alex Belianinov
Iowa State University

Ag on Si-(111) surfaces, from basic science to application

by

Aleksey Andreevich Belianinov

A dissertation submitted to the graduate faculty

in partial fulfillment of requirements for the degree of

DOCTOR OF PHILOSOPHY

Major: Analytical Chemistry

Program of Study Committee:

Patricia A. Thiel, Major Professor

Jim Evans

Michael Tringides

Robert S. Houk

Emily Smith

Sriram Sundrararajan

Iowa State University

Ames, Iowa

2012

I dedicate this work to my Mother & Father:

“ Терпи, казак, атаман будешь.”

TABLE OF CONTENTS

LIST OF ABBREVIATIONS

2DAG	Two dimensional adatom gas
AES	Auger electron spectroscopy
ARPES	Angle resolved photoelectron spectroscopy
CMTA	Constant momentum transfer averaging
DAS	Dimer adatom stacking
FHUC	Faulted half unit cell
HCT	Honeycomb chain trimer
HT	High temperature
IET	Inequivalent triangle
IR	Infrared
LEED	Low energy electron diffraction
LEEM	Low energy electron microscopy
LT	Low temperature
MEIS	Medium energy ion spectroscopy
MBE	Molecular beam epitaxy
ML	Monolayer
NEXAFS	Near edge X-ray absorption fine structure
PEM	Photoelectron Microscopy
PES	Photoelectron spectroscopy
RT	Room temperature
SH	Second harmonic
SK	Stranski-Kastranov growth mode

SPE	Solid phase epitaxy
STM	Scanning tunneling microscopy
STS	Scanning tunneling spectroscopy
TEM	Transmission electron microscopy
TED	Transmission electron diffraction
TPD	Temperature programmed desorption
UHUC	Unfaulted half unit cell
UHV	Ultra high vacuum
VT-STM	Variable temperature Scanning tunneling microscopy
XPS	X-ray photoelectron spectroscopy

CHAPTER I

GENERAL INTRODUCTION

The 7x7 reconstruction of Si(111) has been extensively studied over the period of the last 40 years. The history of proposed models on this surface has been comprehensively reviewed by Haneman[1, 2] and Takayanagi[3]. Key experimental contributions to the discovery of the final model were performed by Harrison[4] in 1976 in presenting the concept of adatoms in the outermost layer, then CMTA LEED[5] and ISS[6] studies that revealed non cubic stacking at the edge. Binning[7], in 1983, presented the first 7x7 image in real space. This led Himpsel[8], McRae [9]and Benett[10] to independently propose 7x7 models that feature division of the unit cell into two triangles with different stacking modes. In 1985 Takayanagi[3] was able to put together a model that involved dimers, stacking faults and adatoms proposed in earlier, incomplete models. This model is known as DAS today and has remained a golden standard in elucidating the process of formation and the resulting geometry of the Si(111)-7x7.

Studies of noble metals on the Si(111) surfaces ushered a new technological era in the area of microprocessors, component miniaturization and printed circuit boards. Originally, much work was devoted to Ag[11-15] and Au[16-20] on Si. Understanding the basics of band structure, nucleation, growth modes and temperature relationships of Ag and Au on Si(111) proved instrumental in interpreting results of Cu on Si – the duo ruling the high-throughput semiconductor industry today.

In our work we revisit Ag and Au adsorbates on Si(111)-7x7, as well as experiment with a ternary system of Pentacene, Ag and Si(111). Of particular interest to us is the Si(111)-($\sqrt{3}$x$\sqrt{3}$)R30^o –Ag (Ag-Si-$\sqrt{3}$ hereafter). This surface forms after deposition of 1 ML of Ag on Si(111)-7x7 and a 1.5 - 2 minute 500-800 K anneal. Starting from a Si(111)-7x7 surface, the areal density of Si changes upon conversion to the Ag-Si-$\sqrt{3}$, i.e. the Si surface reconstructs. The consequent mass transfer leads the Ag-Si-$\sqrt{3}$ to form "islands" and "holes," above and below the original (7x7) level, respectively.[21-27] The structure of Ag-Si-$\sqrt{3}$ is best described by HCT and IET models[28-32]. These two models are closely related, in fact, perhaps the easiest way to distinguish the two is acknowledge that HCT is the fully symmetrical version of IET. At low temperature it is easier to distinguish the IET structure as atoms oscillate at time scales compatible with STM time resolution, although Zhang[33] et al., report the coexistence of both phases at RT. In our experiments we observe only the HCT structure.

Ag on Ag-Si-$\sqrt{3}$ has been a subject of many studies. Below RT, there are reports that new phases, ($\sqrt{21}$x$\sqrt{21}$)R10.9^o and (6x6), coexist with the Ag-Si-$\sqrt{3}$ at Ag coverage as low as 0.1-0.2 ML.[34-36] A model for the $\sqrt{21}$ has been proposed on the basis of density functional theory (DFT).[37] There is evidence for a two-dimensional gas of Ag adatoms at low Ag coverage even at 50 K, which implies a high mobility of Ag adatoms on the Ag-Si-$\sqrt{3}$.[38-40] Our own[41] LT study in the 50 – 250 K regime elucidate much of the surface processes such as diffusion, island nucleation and island morphologies.

At temperatures at or above RT, LeLay[42] reported that a $\sqrt{3}$ LEED pattern from the substrate lingers until Ag coverage is well above 3 ML. Later, Gasparov and Riehl-Chudoba replicated this result, and using STM and XPS, they concluded that the $\sqrt{3}$ LEED pattern remains

because Ag exists as metallic islands, separated by flat, clean Ag-Si-√3 terraces.[43] Venables et al. observed that Ag atoms migrate over distances of up to 50 µm at 770 K.[44-46] These are extremely long distances for adatom diffusion. Note that the 50 µm value is also model-independent, being based upon the width of the Ag-Si-√3 border that develops around Ag-rich regions after Ag deposition in a localized area on Si(111)-7x7.[44-46]

Venables et al. also studied island densities as a function of deposition temperature on the Ag-Si-√3,[44-46] as we have in our, previous work. Oshima et al.,[47] studied 6 ML Ag islands deposited on the Ag-Si-√3 at RT using TEM. They report seeing two types of Ag islands, "striped" islands and Ag(1-34) islands. The group refers to striped islands as those growing parallel to the Si(110) direction and having alternating dark and light spots. Ag(1-34) islands are the rough Ag patches we also find in our studies. Authors report seeing reflection spots for the Ag(-1-1-1) in Ag(1-34) structures. In our STM work we see areas of rough Ag islands that reconstruct into flat, faceted Ag(111) films. We believe these films become more prevalent as the annealing temperature increases. These notions are confirmed by Oshima's[48] 2002 TED study.

A second-harmonic (SH) generation study was done by Deng et al[49]., on low 0.02 ML coverage of Ag on the Ag-Si-√3 at RT and at 630 K. For both RT and 630 K even a relatively small amount of additional Ag resulted in a decrease of the SH intensity by half. This result is attributed to by an increase of the 2DAG density and nucleation following a supersaturation density. Overall the growth mode for the Ag on the Ag-Si-√3 can be described as Volmer-Weber.

Patterning of the Ag-Si-√3 surface has been shown by Riehl-Chudoba et al.[50]. This group has

been able to successfully make various size pits on the surface by applying a positive voltage (with respect to the surface), thus extracting material from the surface, and redepositing some of it on the STM tip, leaving a precisely damaged site behind. Varying the distance between the probe and the surface, along with varying voltage, Riehl-Chudoba et al. have been able to quantitatively make pits ranging from 0 – 50 Å wide and 0 – 6 Å deep. Based on the data provided in their article, the height and depth increase linearly until applied voltage reaches 3.4 - 3.6 V. At that point the depth and width are fairly constant around the equilibrium values of 6 Å and 50 Å respectively. The underlying theoretical principle of material removal using an STM tip, has qualitatively been described by Tsong with a model based on field evaporation potential[51]. More recent work by Tseng expands on the concept and compares probe patterning to a miniaturized electron beam lithography[52], the principles of which are understood fairly well[53].

First reported studies of Au on the Si(111) surface were those of Bishop[16] et al., who performed an AES and LEED study. The authors reported a sharp (√3x√3)-R30° LEED pattern after annealing at 740℃ as well as a 1x1 pattern after heating to 1000℃. Due to incomplete understanding of the Si(111) surface at the time, Bishop's[16] work did not receive much attention. The topic was examined by Le Lay[17, 54] in 1977 and then again in 1983 but interest in Au on Si became intense after Takayanagi's[3] Si(111)-7x7 DAS structural solution in 1985. With a solid understanding of the underlying Si(111) – 7 x7, Au on Si(111) became of great interest as a model metal-semiconductor system.

Perhaps one of the reasons for the interest in Au on Si is the large number of surface phases and reconstructions this system has to offer in various coverage and temperature regimes. In

the RT regime on the Si(111) – 7 x 7, no ordered structures are observed at the submonolayer range[19]. Gold initially nucleates on the FHUC[55] of the 7 x 7 and then transitions into 3D islands after the first (1 x 1) layer is complete. Overall, at RT, the growth mode is described as SK on the Si(111) – 7 x 7[19, 56]. Unlike Ag on Si, Au on Si will form a silicide eutectic at 636 K, although Kim[57] and Khramotsova[58] et al., report evidence of silicides at much lower temperature. The silicide formation at the Au-Si interface has been reported even at RT at coverage as low as 3-4 ML of Au deposited on the 7 x 7[59].

At higher temperatures, the Au/Si(111) phases are numerous and complex. The main surface reconstructions are listed as follows: **a)** (5 x 2) forming at coverage of 0.2ML – 1 ML at 300 – 800℃, **b)** (√3x√3)-R30° forming at 0.5ML and higher at 300 – 750℃, **c)** (6 x 6) initiating at 1 ML at 250℃ and stable up to 800℃ and (1 x 1) which is a high temperature 800℃ and higher, phase at all coverages[60-64]. Much effort has been expended to understand these structures and their interactions with one another. As shown in work by Plass[60], the surface phases of Au on Si often coexist as one phase transitions to another. Over time particular attention was given to the (5 x 2)[65-76] and the (√3x√3)-R30° [18, 20, 58, 61, 63, 65, 77-84] surface reconstructions. There is much similarity in the referenced work on the structure of these phases, but no single standard for either (5 x 2) or the (√3x√3)-R30° structure has been established.

Binary studies of Ag + Au on Si(111), and in some cases Cu, have been reported[20, 61, 65, 80, 83, 85-89], but are far less numerous than the volume amassed in individual studies of these noble metals on Si(111). The very first study by Nogami[78] et al., explored submonolayer coverage of Au on the Ag-Si(111)-(√3x√3)-R30° reported existence of a (√21 x √21) overlayer,

initially observed with Ag on the Ag-Si(111)-(√3x√3)-R30°. Gunther[85] et al. followed suit with a diffraction study that shed light on RT growth of Au on the Ag-Si-√3 and perhaps more importantly, this paper started a discussion on Au silicides evident in their system. Yuhara[86] et al. continued to study mixed noble metals on Si(111) by introducing Cu to the Au and Ag overstrucures. Another study by Tong[20] et al. in 2000, focused on conductivity of the Ag-Si(111)-(√3x√3)-R30° with noble metal adatoms. Their work proved to be instrumental in correlating 2DAG with low coverage (√21 x √21) noble metal overlayer and the resulting enhancement in surface conductivity. In 2001 Yuhara[82] et al. put forth another bimetal Ag Au study, this time Ag serving as an adsorbate on the Au-Si(111)-(√3x√3)-R30°. Many reconstructions thought to occur only for the pure Au-Si(111) were observed. The last pertinent study of Au and Ag on Si(111) was released in 2007, by Fukaya[83] et al. with the primary focus on the controversial (√21 x √21) overlayer analysis.

As discussed above a lot of effort has been poured into noble metal interactions with Si(111) surface over the last four decades. While many aspects of theses surfaces are now well understood, we found that the majority of work in Ag and Au overlayers to be somewhat fragmented. In this thesis I systematically explore effects of Ag deposition on the Ag-Si-√3 at different temperatures, film thicknesses and deposition fluxes. The generated insight of the Ag system on the Si(111) is then applied to generate novel methods of nanostructuring and nanowire growth. I then extend our expertise to the Au system on the Ag-Si(111) to gain insight into Au-Si eutectic silicide formation. Finally we explore behavior and growth modes of an organic molecule on the Ag-Si interface.

Thesis Organization

This thesis opens with a List of Abbreviations useful in navigating through some technical jargon and abbreviations contained in the chapters. The chapters are comprised of two published papers, one submitted manuscript and three manuscripts in preparation. The first paper, "Islands and holes as measures of mass balance in growth of the (√3x√3)R30° phase of Ag on Si(111)" is published in Physical Review B, 82 (2010) 245413. The second paper "Nucleation and growth of Ag islands on the (√3x√3)R30° phase of Ag on Si(111)" is published in Journal of Physics: Condensed Matter, 23 (2011) 265002. Manuscript titled "Creating Ag superstructures on the Si(111)-(√3x√3)R30°-Ag by means of self-assembly" has been submitted to the Journal of Vacuum Science and Technology B on February 25th, 2012. The remaining three manuscripts are being readied for submission. The title of the first manuscript is "Pentacene on Ag-Si(111)." Title of the second manuscript is "Gold on Ag-Si(111)-(√3x√3)R30°." The last manuscript is titled "Thick Ag films on Ag-Si(111)-(√3x√3)R30°." Following the chapters are List of Figures and List of Tables. List of Figures contains all the figures prepared for the manuscripts and the publications along with their captions. List of Tables is a compilation of the experimental schedule, notes and relevant information regarding the raw collected data. Thesis closes with Appendix A which contains specs such as technical drawings, assembly directions and general tips concerning UHV chambers, maintenance, involved scientific hardware and computer hardware & software useful for Dr. P. A. Thiel and Thiel group members.

Bibliography

1. D. Haneman, Advances in Physics **31** (3), 165-194 (1982).
2. D. Haneman, Reports on Progress in Physics **50** (8), 1045 (1987).
3. K. Takayanagi, Y. Tanishiro, S. Takahashi and M. Takahashi, Surface Science **164** (2–3), 367-392 (1985).
4. H. Walter A, Surface Science **55** (1), 1-19 (1976).
5. H. Huang, S. Y. Tong, W. E. Packard and M. B. Webb, Physics Letters A **130** (3), 166-170 (1988).
6. R. J. Culbertson, L. C. Feldman and P. J. Silverman, Physical Review Letters **45** (25), 2043-2046 (1980).
7. G. Binnig, H. Rohrer, C. Gerber and E. Weibel, Physical Review Letters **50** (2), 120-123 (1983).
8. F. J. Himpsel, Physical Review B **27** (12), 7782-7785 (1983).
9. E. G. McRae, Physical Review B **28** (4), 2305-2307 (1983).
10. P. A. Bennett, L. C. Feldman, Y. Kuk, E. G. McRae and J. E. Rowe, Physical Review B **28** (6), 3656-3659 (1983).
11. F. Wehking, H. Beckermann and R. Niedermayer, Thin Solid Films **36** (2), 265-268 (1976).
12. Y. Gotoh and S. Ino, Japanese Journal of Applied Physics **17** (12), 2097-2109 (1978).
13. V. Barone, G. Delre, G. Lelay and R. Kern, Surface Science **99** (1), 223-232 (1980).
14. Y. Gotoh and E. Yanokura, Journal of Crystal Growth **87** (4), 408-414 (1988).

15. K. Markert, P. Pervan, W. Heichler and K. Wandelt, Surface Science **211** (1-3), 611-619 (1989).

16. H. E. Bishop and J. C. Rivière, Journal of Physics D: Applied Physics **2** (12), 1635 (1969).

17. L. L. G, Surface Science **132** (1–3), 169-204 (1983).

18. J. Nogami, A. A. Baski and C. F. Quate, Physical Review Letters **65** (17), 2211-2211 (1990).

19. A. Endo and S. Ino, Japanese Journal of Applied Physics Part 1-Regular Papers Short Notes & Review Papers **32** (10), 4718-4725 (1993).

20. X. Tong, C. S. Jiang, K. Horikoshi and S. Hasegawa, Surface Science **449** (1-3), 125-134 (2000).

21. A. Shibata, Y. Kimura and K. Takayanagi, Surf. Sci. **303**, 161-170 (1994).

22. A. Shibata, H. Kimura and K. Takayanagi, J. Vac. Sci. Technol. **B 12** (3), 2026-2030 (1994).

23. A. Shibata and K. Takayanagi, Jpn. J. App. Phys. **32**, 1385-1388 (1993).

24. A. Shibata, Y. Kimura and K. Takayanagi, Surf. Sci. **275**, L697-L701 (1992).

25. K. J. Wan, X. F. Lin and J. Nogami, Phys. Rev. B **47**, 13700-13712 (1993).

26. D. W. McComb, D. J. Moffatt, P. A. Hackett, B. R. Williams and B. F. Mason, Phys. Rev. B **49**, 17139-17148 (1994).

27. A. Belianinov, B. Ünal, N. Lu, M. Ji, K.-M. Ho, C.-Z. Wang, M. Tringides and P. A. Thiel, Phys. Rev. B **82**, 245413 (2010).

28. Y. G. Ding, C. T. Chan and K. M. Ho, Phys. Rev. Lett. **67** (11), 1454-1457 (1991).

29. N. Sato, T. Nagao and S. Hasegawa, Surf. Sci. **442** (1), 65-73 (1999).

30. H. Aizawa, M. Tsukada, N. Sato and S. Hasegawa, Surf. Sci. **429**, L509-L514 (1999).

31. H. M. Zhang, J. B. Gustafsson and L. S. O. Johansson, Phys. Rev. B **74**, 201304(R) (2006).

32. I. Matsuda, H. Morkawa, C. Liu, S. Ohuchi, S. Hasegawa, T. Okuda, T. Kinoshita, C. Ottaviani, A. Cricenti, M. D'angelo, P. Soukiassian and G. Le Lay, Phys. Rev. B **68**, 085407 (2003).

33. H. M. Zhang, J. B. Gustafsson and L. S. O. Johansson, Journal of Physics: Conference Series **61** (1), 1336 (2007).

34. Z. H. Zhang, S. Hasegawa and S. Ino, Phys. Rev. B **52**, 10760-10763 (1995).

35. X. Tong, S. Hasegawa and S. Ino, Phys. Rev. B **55**, 1310 (1997).

36. X. Tong, S. Ohuchi, N. Sato, T. Tanikawa, T. Nagao, I. Matsuda, Y. Aoyagi and S. Hasegawa, Phys. Rev. B **64**, 205316 (2001).

37. H. Jeong, H. W. Yeom and S. Jeong, Phys. Rev. B **77**, 235425 (2008).

38. M. Ueno, I. Matsuda, C. Liu and S. Hasegawa, Jpn. J. App. Phys. **42**, 4894-4897 (2003).

39. Y. Nakajima, S. Takeda, T. Nagao and S. Hasegawa, Phys. Rev. B **56**, 6782-6787 (1997).

40. N. Sato, T. Nagao and S. Hasegawa, Phys. Rev. B **60**, 16083-16087 (1999).

41. A. Belianinov, B. Uenal, K. M. Ho, C. Z. Wang, J. W. Evans, M. C. Tringides and P. A. Thiel, Journal of Physics-Condensed Matter **23** (26) (2011).

42. G. Le Lay, G. Quentel, J. P. Faurie and A. Masson, Thin Sol. Films **35**, 273-287 (1976).

43. V. A. Gasparov and M. Riehl-Chudoba, Surf. Sci. **601**, 5403-5411 (2007).

44. F. L. Metcalfe and J. A. Venables, Surf. Sci. **369**, 99-107 (1996).

45. G. Raynerd, T. N. Doust and J. A. Venables, Surf. Sci. **261** (1-3), 251-266 (1992).

46. J. A. Venables, F. L. Metcalfe and S. Sugawara, Surf. Sci. **371**, 420-430 (1997).

47. Y. Oshima, H. Nakade, S. Shigeki, H. Hirayama and K. Takayanagi, Surface Science **493** (1-3), 366-372 (2001).

48. Y. Oshima, H. Nakade, S. Shigeki, H. Hirayama and K. Takayanagi, Surface Science **498** (3), 307-313 (2002).

49. D. M. Deng, M. Numata and T. Suzuki, Journal of the Physical Society of Japan **73** (12), 3384-3388 (2004).

50. M. Riehl-Chudoba, W. Richter and V. A. Gasparov, Journal of Applied Physics **83** (5), 2500-2503 (1998).

51. T. T. Tsong, Phys. Rev. B **44**, 13703 (1991).

52. A. A. Tseng, A. Notargiacomo and T. P. Chen, Journal of Vacuum Science & Technology B: Microelectronics and Nanometer Structures **23** (3), 877-894 (2005).

53. A. A. Tseng, C. Kuan, C. D. Chen and K. J. Ma, Electronics Packaging Manufacturing, IEEE Transactions on **26** (2), 141-149 (2003).

54. M. M. G. Le Lay, R. Kern, in *Surface Science* (1977), Vol. 65, pp. 271.

55. Y. Zhou, Q.-H. Wu, C. Zhou, H. Zhang, H. Zhan and J. Kang, Surface Science **602** (2), 638-643 (2008).

56. J. H. Kim, G. Yang, S. Yang and A. H. Weiss, Surface Science **475** (1-3), 37-46 (2001).

57. B. J. Kim, J. Tersoff, C. Y. Wen, M. C. Reuter, E. A. Stach and F. M. Ross, Physical Review Letters **103** (15), 155701 (2009).

58. E. A. Khramtsova, H. Sakai, K. Hayashi and A. Ichimiya, Surface Science **433**, 405-409 (1999).

59. J. J. Yeh, J. Hwang, K. Bertness, D. J. Friedman, R. Cao and I. Lindau, Physical Review Letters **70** (24), 3768-3771 (1993).

60. R. Plass and L. D. Marks, Surface Science **380** (2-3), 497-506 (1997).

61. A. Ichimiya, H. Nomura, Y. Ito and H. Iwashige, Journal of Crystal Growth **150** (1-4), 1169-1174 (1995).

62. S. Takahashi, Y. Tanishiro and K. Takayanagi, Surface Science **242** (1–3), 73-80 (1991).

63. J. Yuhara, M. Inoue and K. Morita, Journal of Vacuum Science & Technology A: Vacuum, Surfaces, and Films **10** (6), 3486-3492 (1992).

64. A. A. S. V. G. Lifshits, A. V. Zotov, (1994).

65. A. Endo and S. Ino, Surface Science **346** (1-3), 40-48 (1996).

66. T. Hasegawa, S. Hosoki and K. Yagi, Surface Science **355** (1-3), L295-L299 (1996).

67. R. Losio, K. N. Altmann and F. J. Himpsel, Physical Review Letters **85** (4), 808-811 (2000).

68. S. C. Erwin, Physical Review Letters **91** (20) (2003).

69. S. C. Erwin, Physical Review Letters **91** (20), 206101 (2003).

70. M. H. Kang and J. Y. Lee, Surface Science **531** (1), 1-7 (2003).

71. A. Kirakosian, J. N. Crain, J. L. Lin, J. L. McChesney, D. Y. Petrovykh, F. J. Himpsel and R. Bennewitz, Surface Science **532**, 928-933 (2003).

72. S. Riikonen and D. Sanchez-Portal, Physical Review B **71** (23) (2005).

73. H. S. Yoon, J. E. Lee, S. J. Park, I. W. Lyo and M. H. Kang, Physical Review B **72** (15) (2005).

74. Y. Iwasawa, W. Voegeli, T. Shirasawa, K. Sekiguchi, T. Nojima, R. Yoshida, T. Takahashi, M. Matsumoto, T. Okano, K. Akimoto, H. Kawata and H. Sugiyama, Applied Surface Science **254** (23), 7803-7806 (2008).

75. F. Zheng, I. Barke, X. Liu and F. J. Himpsel, Nanotechnology **19** (44) (2008).

76. S. C. Erwin, I. Barke and F. J. Himpsel, Physical Review B **80** (15) (2009).

77. Y. G. Ding, C. T. Chan and K. M. Ho, Surface Science **275** (3), L691-L696 (1992).

78. J. Nogami, K. J. Wan and X. F. Lin, Surface Science **306** (1-2), 81-86 (1994).

79. R. Plass and L. D. Marks, Surface Science **357** (1-3), 42-46 (1996).

80. J. Yuhara, D. Ishikawa and K. Morita, Applied Surface Science **117**, 94-98 (1997).

81. T. Nagao, S. Hasegawa, K. Tsuchie, S. Ino, C. Voges, G. Klos, H. Pfnür and M. Henzler, Physical Review B **57** (16), 10100-10109 (1998).

82. J. Yuhara, K. Soda and K. Morita, Surface Science **482**, 32-38 (2001).

83. Y. Fukaya, A. Kawasuso and A. Ichimiya, Surface Science **601** (22), 5187-5191 (2007).

84. J. Y. Lee and M. H. Kang, Journal of the Korean Physical Society **53** (6), 3671-3674 (2008).

85. S. Gunther, A. Kolmakov, J. Kovac, L. Casalis, L. Gregoratti, M. Marsi and M. Kiskinova, Surface Science **377** (1-3), 145-149 (1997).

86. J. Yuhara and K. Morita, Applied Surface Science **123**, 56-60 (1998).

87. K. Pedersen, T. B. Kristensen, T. G. Pedersen, T. Jensen, P. Morgen, Z. S. Li and S. V. Hoffmann, Surface Science **523** (1-2), 21-29 (2003).

88. S. Iaiche, N. Benouattas, A. Bouabellou, L. Osmani and L. Salik, Microelectronic Engineering **81** (2-4), 349-352 (2005).

89. Y. Liu, M. Li and Y. Suo, Surface Science **600** (24), 5117-5122 (2006).

CHAPTER II

ISLANDS AND HOLES AS A MEASURE OF MASS BALANCE IN GROWTH OF THE ($\sqrt{3}$x$\sqrt{3}$)R30^o PHASE OF Ag ON Si(111)

A paper published in the journal of *Physical Review B*

Alex Belianinov,[1,2] Barış Ünal,[5] Ning Lu,[1,4] Min Ji,[1,4] K.-M. Ho,[1,4] C.-Z. Wang,[1,4] M. C. Tringides,[1,4] and P. A. Thiel [1,2,3]

[1]Ames Laboratory, [2]Department of Chemistry, [3]Department of Materials Science and Engineering, and [4]Department of Physics and Astronomy

Iowa State University, Ames Iowa 50011 USA

[5]Present address: Department of Chemical Engineering, Massachusetts Institute of Technology, Cambridge MA 02139 USA

Abstract

It is well-known that conversion of Si(111)-(7x7) into the ($\sqrt{3}$x$\sqrt{3}$)R30^o phase of adsorbed Ag requires a change in the Si density, and causes formation of islands and holes at the surface. By mass balance, the ratio of areas of islands and holes (R_{IH}) should be approximately 1. However, we find that the ratio is significantly higher, depending on

preparation conditions. A possible explanation would be that there are different types of $(\sqrt{3}x\sqrt{3})R30^o$ structures. However, neither scanning tunneling microscopy nor density functional theory (implemented as a genetic algorithm search) supports this explanation. The reason for the unexpectedly high values of R_{IH} is unknown.

Introduction

The $(\sqrt{3}x\sqrt{3})R30^o$ surface phase of Ag on Si(111)—called $\sqrt{3}$ herein—is an important structure that has been studied intensely,[1] since it was first reported in 1967.[2] It is established that conversion of the (7x7) to the $\sqrt{3}$ in the presence of adsorbed Ag is an activated process, occurring in the range of about 500 - 900 K. It is also known that the areal density of Si is not preserved when the (7x7) converts to the $\sqrt{3}$. This change in Si density, in the presence of limited diffusion on large terraces, causes the $\sqrt{3}$ to partition locally into regions above the (7x7), i.e. "islands", and regions below the (7x7), i.e. "holes."[3-7] These features are illustrated schematically in Fig. 1A, and by experimental data in Fig. 1B. A similar partitioning occurs during the development of the $\sqrt{3}$ structure of Au on Si(111).[7, 8]

Because of Si mass balance, the areal ratio of islands to holes (R_{IH}) can be, and has been,[5-7] used to deduce the density of Si in the $\sqrt{3}$ phase. (See Appendix.) Using scanning tunneling microscopy (STM), both Shibata et al.[5, 7] and Wan et al.[6] measured $R_{IH} \approx 1$ and deduced the Si surface density to be 1 atom per (1x1) unit cell area, i.e. 1 monolayer (ML). This means that one full layer of Si is missing in the $\sqrt{3}$ relative to the unreconstructed Si surface.

These results helped to shape and support the current model for the √3. This model is known as the Inequivalent Triangle (IET) model,[9, 10] and can be viewed as an asymmetrical variation of the Honeycomb Chain Trimer (HCT) model.[11] Accordingly, some groups report that structures with IET symmetry transform reversibly to apparent HCT symmetry around 300 K, due to thermal fluctuations in the IET structure.[12-14] However, Zhang et al. report that both structures can co-exist statically even at room temperature.[15, 16] In the present work, we observe only the apparent HCT structure.

We pose two questions: Does the measured value of R_{IH} depend on the conditions under which the √3 is prepared? If so, since R_{IH} is determined by the Si coverage in the √3 phase, is it possible that there is more than one type of √3 phase with different Si and Ag coverages? We employ both STM and density functional theory (DFT) to find the answers.

Experimental and computational details

The experimental ultrahigh vacuum system, including the variable-temperature STM and Ag evaporator, are described elsewhere.[17] The Si sample is p-type with resistivity of 0.02 Ωcm. Ag flux is typically 0.1-0.2 ML/min. Ag is deposited or annealed at elevated temperature, then cooled to room temperature for STM imaging in constant-current mode. Ag coverage is determined as follows. We assume that local Ag coverage in the islands and holes is 1 ML when $R_{IH} = 1$. Then the total Ag coverage is calculated as the combined area of islands and holes, divided by the total surface area when $R_{IH} = 1$. Silver coverage is assumed constant throughout an individual experiment (no loss of Ag due to evaporation or subsurface

migration). R_{IH} is extracted from STM data by setting a height cutoff and summing the area (number of pixels) above or below this cutoff.[18] Images are examined carefully to make sure that cutoffs are physically reasonable.

In the computations, we implement a variable-number genetic algorithm (GA) search in which both the number of Ag and Si atoms are variable. The structures in each generation are relaxed using DFT. The calculations are carried out within the local density approximation of DFT[19, 20] using projector-augmented-wave potentials,[21] as implemented in the Vienna ab initio Simulation Package.[22] The kinetic energy cutoff is set to 250 eV and the 4x4 Monkhorst-Pack grid is used for the surface Brillouin zone. The system is modeled as a periodically repeating slab consisting of: two fixed Si bilayers, the bottom one hydrogen passivated; a reconstructed Ag/Si layer on the top; and a vacuum gap of ~0.8 nm. All the models are based on a $(\sqrt{3} \times \sqrt{3})R30^{o}$ surface unit cell, using a Si bulk lattice constant of 0.540 nm. The two Si bilayers are fixed at the bulk crystalline positions, and the Si-H distance is fixed at 0.151 nm. The remaining Ag and Si atoms are relaxed until the residual force is smaller than 0.25 eV/nm.

The formation energy, E_f [per (1x1) unit cell] is calculated from $E_f = (1/3)(E_{tot} - E_{sub}) - N_{Si}*\mu_{Si} - N_{Ag}*\mu_{Ag}$, where E_{tot} is the total energy, E_{sub} is the energy of the sub-surface region (two Si bilayers and one layer of hydrogen). The μ_{Si} and μ_{Ag} are chemical potentials of Si and Ag bulk phases, respectively, while $N_{Si,\sqrt{3}}$ and $N_{Ag,\sqrt{3}}$ are the number of Si and Ag atoms in the surface layer per (1x1) unit cell (identical to coverages in ML) on top of the fixed substrate. See also the Appendix and Fig. 1.

Experimental Results and Interpretation

In our STM experiments, residual (7x7) always coexists with islands and holes because the Ag coverage is deliberately adjusted to be in the submonolayer range, i.e. insufficient for complete conversion. The two parameters that we vary systematically are (i) the temperature at which Ag is deposited, T_{dep}; and (ii) the time, t_{ann}, of annealing after deposition ends. Focusing first on the deposition temperature, Fig. 2 is a series of STM images after deposition of 0.4 to 0.6 ML Ag at varying temperatures, followed by annealing for 1-2 minutes. The fractional area of 7x7 that remains unconverted ranges from 0.6 to 0.4 in these experiments. We count the elevated regions as islands, regardless of the structure (or lack thereof) on top of the island. The dark areas—holes—are so small that they are barely evident in Fig. 2A, but they become larger as T_{dep} increases.

Inspection of the islands and holes indicates that under some conditions, especially for $R_{IH} > 3$ and/or $T_{dep} < 600$ K, the island tops contain substantial disordered regions. Other authors have identified the disordered phase as Ag which is a precursor to the $\sqrt{3}$.[3, 4] Its variation during the transformation to $\sqrt{3}$ will be discussed elsewhere.[23]

The ratio R_{IH} varies both with T_{dep} and t_{ann}. Fig. 3 shows the variation with T_{dep}. R_{IH} is as high as 6 after Ag deposition at 500 K. It falls to $R_{IH} \approx 1$ at $T_{dep} = 800$ K. For annealing, Fig. 4A shows that R_{IH} falls from an initial value of 2.7, and approaches 1 at long t_{ann}, following deposition at 600 K. From both the deposition and annealing experiments, we conclude that $T_{dep} < 800$ K can easily lead to $R_{IH} > 1$, but $R_{IH} \approx 1$ is the limiting value.

Is the decrease in R_{IH}—e.g. in Fig. 3 and 4A—attributable to decreasing area (A) of the islands, increasing area of the holes, or both? Figure 5 shows the changes in absolute areas during annealing at 600 K, where the initial value of R_{IH} is 2.7 (cf. Fig. 4A). During annealing, A_{hole} increases by a factor of 4, and this is compensated by a decrease in the area of the 7x7. The variation in A_{island} is much less than the other two variables. Therefore, the decrease in R_{IH} is predominantly due to an increase in the denominator, A_{hole}, with a concomitant decrease in the (7x7) area. In other words, the holes expand and consume the 7x7. A reservoir of Ag must exist that feeds the holes during annealing, and correspondingly, a sink must exist to consume the displaced Si.

Shibata et al. have reported that Ag nucleates into islands that serve as precursors to the √3. From data taken with *in situ* STM, and working at temperatures of ~440-525 K, they concluded that these Ag islands can convert to √3, but only if they are above a critical size of two 7x7 unit cells (about 12 nm^2). We therefore consider the possibility that small islands are Ag-rich, and that they can provide the Ag needed for expansion of the holes. Indeed, we see small islands in the STM images, and they disappear during annealing. However, their disappearance is only partially correlated with the change in R_{IH}. Figure 4B shows the number density of islands in two size ranges during annealing. Most islands in the range below 50 nm^2 disappear very quickly, long before the value of R stabilizes. We conclude that the small islands may contribute some of the Ag needed, especially early in the process, but certainly not all.

When surfaces are prepared by deposition of Ag at 600 K, a good √3 structure exists both on island tops and in holes throughout the range $3 \geq R_{IH} \geq 1$. This statement is based upon STM

inspection of many islands and holes. The existence of √3 throughout the range $3 \geq R_{IH} \geq 1$, and not just at $R_{IH} \approx 1$ as predicted by the IET model, naturally leads one to question whether there might be different types of √3 structures—perhaps including metastable phase(s) with high Ag:Si ratios. However, high-resolution images of the √3, measured on both islands and holes for different values of R_{IH}, do not support this hypothesis. Some of the STM images are shown in Fig. 6. For comparable tunneling conditions, there is no apparent difference in the structure. Thus, these data support only a single type of √3.

A further characterization of the √3 is the vertical separation between islands, holes, and (7x7) regions for different T_{dep}. (Note that only 2 of the 3 separations are independent.) Because the separations measured with STM can depend upon electronic as well as topographic variations, we measure separations at different tunneling bias. Results are shown in Fig. 7, derived from pixel height histograms. Data are only shown for surfaces where $3 \geq R_{IH} \geq 1$. The vertical separation between islands and holes, averaged over bias voltages between $\pm$2 V and over the 3 experiments where $3 \geq R_{IH} \geq 1$, is 0.293 $\pm$ 0.026 nm. This compares well with 0.314 nm, which is the bulk separation between equivalent Si(111) planes and which is expected based upon Fig. 1A. From this, it appears that the heights are primarily topographic. The measured island-to-(7x7) separation (not shown), taken as an average over the same range of bias voltage (V_T) and the same 3 experiments, is 0.148 $\pm$ 0.048 nm. This is half the former value—as it should be if the structure on the island tops is the same as in the holes. We conclude that, within experimental error, the average heights of islands and holes does not depend significantly on preparation conditions or R_{IH}-value, under

conditions where a good √3 exists on both features. This lack of variation is again consistent with a single type of √3 structure.

Computational Results

Figure 8 shows results of the GA search for different types of √3 structures. In order to show the variation in both Si and Ag coverage, we use a 2-digit notation for the x-axis. The 1st digit is the number of Si atoms and the 2nd digit is the number of Ag atoms. In the bottom x-axis labels, these numbers are normalized to the (1x1) unit cell area, and in the top axis they are normalized to the √3 unit cell area. The point with the lowest E_f has x = (1,1) per (1x1). This is the IET structure. The energy of the (7x7) is shown by the dashed horizontal line. [The surface energy of (2x1) Si(111) is calculated with DFT, and the (7x7) Si(111) is taken to be 0.33 eV/(1x1) lower than the (2x1) surface.[11]] We conclude that the IET is the only √3 structure that is more stable than the (7x7), and hence is the only viable model for the portions of the surface identified experimentally as √3.

Conclusions

Using STM, we have shown that values of R_{IH} as high as 3 can be obtained under conditions where both islands and holes are covered by the √3 phase. However, the limiting value of R_{IH} is 1. This value is achieved by deposition at 800 K, and it is approached by annealing at lower temperatures. The observation of $R_{IH} > 1$ engenders the question of whether different types of √3 structures exist. However, STM data support only a single type of structure.

Furthermore, a genetic algorithm-based search does not reveal any √3 phase that could be energetically competitive with the IET structure. Therefore, the inequality between areas of √3 islands and √3 holes is an open question that calls for further investigation.

Acknowledgments

This work was performed at the Ames Laboratory under contract number DE-AC02-07CH11358 with the U.S. Department of Energy. The document number assigned to this thesis/dissertation is IS-T 3050.

Appendix

If both islands and holes are covered with perfect √3 phase, the density of Si in the √3 is related to R_{IH} by:[5, 6]

$$N_{Si,\sqrt{3}} = N_{Si,7} - \frac{2A_{island}}{A_{hole} + A_{island}} = N_{Si,7} - \frac{2R_{IH}}{1 + R_{IH}} \qquad (1)$$

Here, A is area of the type of √3 indicated by the subscript [normalized to the (1x1) unit cell area], and N_{Si} is the number of Si atoms in the structure indicated by the subscript [i.e. (√3 or (7x7)], within the area of a (1x1) unit cell. The factor of $2A_{island}$ appears because islands are

higher than holes by a bilayer of Si. See Fig. 1. Since it is known that $N_{Si,7} = 2.08$ (vs. 2.00 for the unreconstructed surface),[24] experimental measurement of R_{IH} yields $N_{Si,\sqrt{3}}$ from Eq. (1). If $N_{Si,\sqrt{3}} = 1.00$ as in the IET model, then ideally $R_{IH} = 53/45 \approx 1.2$ from exact mass balance. In the text, for simplicity, the ideal value of R is given as 1. To relate surface atom densities N to notation used in the main text, note that $N_{Si,\sqrt{3}} = N_{Ag,\sqrt{3}} = 1.00$ is equivalent to 1 ML of Si or Ag, respectively.

Bibliography

1. V.G. Lifshits, A.A. Saranin, and A.V. Zotov, *Surface Phases on Silicon: Preparation, Structures, and Properties* (John Wiley & Sons, Inc., West Sussex, England, 1994).

2. K. Spiegel, Surface Sci. **7**, 125 (1967).

3. A. Shibata, H. Kimura, and K. Takayanagi, J. Vac. Sci. Technol. **B 12**, 2026 (1994).

4. A. Shibata, Y. Kimura, and K. Takayanagi, Surface Sci. **303**, 161 (1994).

5. A. Shibata, Y. Kimura, and K. Takayanagi, Surface Sci. **275**, L697 (1992).

6. K.J. Wan, X.F. Lin, and J. Nogami, Phys. Rev. B **47**, 13700 (1993).

7. A. Shibata and K. Takayanagi, Jpn. J. App. Phys. **32**, 1385 (1993).

8. I. Mochizuki, R. Negishi, and Y. Shigeta, J. Phys: Condens. Matter. **61**, 1056 (2007).

9. H. Aizawa, M. Tsukada, N. Sato, and S. Hasegawa, Surface Sci. **429**, L509 (1999).

10. N. Sato, T. Nagao, and S. Hasegawa, Surface Sci. **442**, 65 (1999).

11. Y.G. Ding, C.T. Chan, and K.M. Ho, Phys. Rev. Lett. **67**, 1454 (1991).

12. N. Yoshimichi, Y. Kondo, J. Nakamura, and S. Watanabe, Phys Rev. Lett. **87**, 156102 (2001).

13. I. Matsuda, H. Morkawa, C. Liu, S. Ohuchi, S. Hasegawa, T. Okuda, T. Kinoshita, C. Ottaviani, A. Cricenti, M. D'angelo, P. Soukiassian, and G. Le Lay, Phys. Rev. B **68**, 005407 (2003).

14. K. Sakamoto, T. Suzuki, K. Mawatan, K. Kobayashi, J. Okabayashi, K. Ono, N. Ueno, and M. Oshima, Phys. Rev. B **73**, 193303 (2006).

15. H.M. Zhang, J.B. Gustafsson, and L.S.O. Johansson, J. Phys: Conf. Series **61**, 133 (2007).

16. H.M. Zhang, J.B. Gustafsson, and L.S.O. Johansson, Phys. Rev. B **74**, 201304(R) (2006).

17. B. Ünal, F. Qin, Y. Han, D.J. Liu, D. Jing, A.R. Layson, C. Jenks, J.W. Evans, and P.A. Thiel, Phys. Rev. B **76**, 195410 (2007).

18. I. Horcas, R. Fernandez, J.M. Gomez-Rodriguez, J. Colchero, J. Gomez-Herrero, and A.M. Baro, Rev. Sci. Instr. **78**, 013705 (2007).

19. W. Kohn and L.J. Sham, Phys. Rev. A **140**, 1133 (1965).

20. P. Hohenberg and W. Kohn, Phys. Rev. B **136**, 864 (1964).

21. G. Kresse and J. Joubert, Phys. Rev. B **59**, 1758 (1999).

22. G. Kresse and J. Hafner, Phys. Rev. B **47**, 558 (1993).

23. A. Belianinov, B. Ünal, N. Lu, K.-M. Ho, C.-Z. Wang, M.C. Tringides, and P.A. Thiel, in preparation (2010).

24. K. Oura, V.G. Lifshits, A.A. Saranin, A.V. Zotov, and M. Katayama, *Surface Science. An Introduction.* (Springer, Berlin, 2003).

CHAPTER III

NUCLEATION AND GROWTH OF Ag ISLANDS ON THE (√3x√3)R30° PHASE OF Ag ON Si(111)

A paper published in the *Journal of Physics: Condensed Matter*

A Belianinov[1,2], B Ünal[1,3,†,] K.-M. Ho[1,4], C.-Z. Wang[1,4], J W Evans [1,5]

M C Tringides[1,4] and P A Thiel [1,2,3]

[1]Ames Laboratory, [2]Department of Chemistry, [3]Department of Materials Science and Engineering, [4]Department of Physics and Astronomy, and [5]Department of Mathematics

Iowa State University, Ames Iowa 50011 USA

Abstract

We use scanning tunneling microscopy to measure densities and characteristics of Ag islands that form on the (√3x√3)R30°-Ag phase on Si(111), as a function of deposition temperature. Nucleation theory predicts that the logarithm of island density varies linearly with inverse deposition temperature. The data show two linear regimes. At 50-125 K, islands are relatively small, and island density decreases only slightly with increasing temperature. At 180-250 K, islands are larger and polycrystalline, and island density decreases strongly with increasing temperature. At 300 K, Ag atoms can travel for distances on the order of 1 μm. Assuming that Ag diffusion occurs via thermally-activated motion of single atoms

† Present address: Department of Chemical Engineering, Massachusetts Institute of Technology, Cambridge MA 02139 USA

between adjacent sites, the data can be explained as follows. At 50-125 K, the island density does not follow conventional Arrhenius scaling due to limited mobility and a consequent breakdown of the steady-state condition for the adatom density. At ~115-125 K, a transition to conventional Arrhenius scaling with critical nucleus size (*i)* of 1 begins, and at 180-250 K, $i > 1$ prevails. The transition points indicate a diffusion barrier of 0.20-0.23 eV and a pairwise Ag-Ag bond strength of 0.14 eV. These energy values lead to an estimate of $i \approx 3$-4 in the regime 180-250 K, where island density varies strongly with temperature.

Introduction

Metallized semiconductor surfaces are scientifically and technologically important, because they yield insight into ohmic contacts in electronic devices and because they serve as models for understanding the relationship between electronic properties and atomic structure. Ag on Si(111) is particularly well-studied, partly because Ag does not form bulk silicides and thus the system is relatively tractable. Here, we report a study of the characteristics of silver when it is deposited on top of a particular Ag-Si surface phase on Si(111). The surface phase has a $(\sqrt{3}x\sqrt{3})R30^{o}$ unit cell—denoted √3 hereafter.

The √3 phase has been thoroughly investigated.[1-7] It forms at temperatures in the range 500 – 800 K, and contains 1.0 monolayer (ML) of Ag. Starting from a Si(111)-7x7 surface, the areal density of Si changes upon conversion to the √3, i.e. the Si surface reconstructs. The consequent mass transfer leads the √3 to form "islands" and "holes," above and below the original (7x7) level, respectively.[1, 2, 4-8] Two models are widely cited for the √3, known as the

Inequivalent Triangle model and the Honeycomb Chain Trimer model.[9-13] These are closely related. Both contain Ag-atom triangles, and Si-atom triangles, that are potential high-symmetry adsorption sites.

There have been previous experimental investigations of surface structures that form when Ag is added to the √3. (The amount of Ag added to the √3, in units of ML, will be called here θ^{+}_{Ag}.) The reported results are very sensitive to adsorption temperature. At room temperature (RT), LeLay et al. reported that the low-energy electron diffraction (LEED) pattern from the substrate √3 remains until θ^{+}_{Ag} is well above 3 ML.[14] Later, Gasparov and Riehl-Chudoba replicated this result, and using STM and XPS, they concluded that the √3 LEED pattern remains because Ag exists as metallic islands, separated by flat, clean √3 terraces.[15] Below RT, there are reports that new phases, (√21x√21)R10.9° and (6x6), coexist with the √3 if θ^{+}_{Ag} is as low as 0.1-0.2 ML,[16-18] and a model for the √21 has been proposed on the basis of density functional theory (DFT).[19] There is also evidence for a two-dimensional gas of Ag adatoms at lower θ^{+}_{Ag}, even at 50 K, which implies a high mobility of Ag adatoms on the √3.[20-22] At the other extreme of temperature, ~600-800 K, Venables' group carried out extensive investigations of the Ag islands that form on the √3.[23-25] They concluded that Ag can diffuse over distances on the order of 50 μm at 770 K.

DFT calculations have also been carried out. Aizawa and Tsukada showed that individual Ag atoms preferentially adsorb in the Ag triangles, not the Si triangles, of the √3.[26] Later, Jeong and Jeong (JJ) confirmed this result, but went further and showed that a Ag atom on a Ag-atom triangle site can actually immerse itself in the √3 structure, i.e. it becomes essentially coplanar with Ag in the √3.[27] JJ also studied Ag diffusion across the √3, showing that an

exchange mechanism has a far lower activation barrier than direct hopping–1.78 vs. 0.22 eV, respectively.[28] Exchange involves replacement of a Ag atom within the √3, at a point where two of the Ag-atom triangles share a vertex.[28]

Here, we systematically investigate the Ag islands that form as a result of deposition on the √3, in the temperature range 50-300 K and at $\theta^{+}_{Ag} \approx 0.3$. This type of study has not been undertaken previously. We observe discrete Ag islands at all temperatures. Their number density and size vary with increasing temperature in a way that is qualitatively consistent with an increasing rate of diffusion. There are two regimes where the logarithm of the island density varies linearly with reciprocal temperature. At 50-125 K, islands are relatively small, and island density decreases slightly, with increasing temperature. At 180-250 K, islands are larger and polycrystalline, and island density decreases strongly with increasing temperature. Possible explanations are discussed, and comparisons are made with the prior results.

Experimental Details

Experiments were performed in an Omicron VT-STM described elsewhere.[29] Chamber base pressure did not exceed 1.0×10^{-10} mbar throughout the experiments, including Ag evaporation. The Si sample was p-type with resistivity of 0.02 Ohm*cm.

To form the √3, 1.0 to 1.2 ML of Ag was deposited at room temperature, and the sample was subsequently annealed at 750-800 K for 1.5 minutes. The sample was then cooled to the desired temperature, where Ag was deposited a second time, followed by STM imaging. The second deposition added 0.2-0.4 ML to the prepared √3 surface. Ag flux was calibrated by depositing Ag on the Si(111)-7x7 surface and measuring the fractional area covered by the

wetting layer, which has a known coverage of 0.5 ML.[30] The Ag flux ranged from 0.0038 to 0.0067 ML/s, but in most experiments it was 0.0050 ML/s.

Island densities were derived from STM images using WsXM software.[31] For counting island densities, images were processed in identical manner with flattening and planing techniques. The image area analyzed for the 50-140 K temperature regime was 0.21-0.26 μm^2, for the 140-173 K regime it was 0.27-1.25 μm^2, and for the 180-250 K regime it was 0.625-10 μm^2. A minimum height and a minimum area requirement was applied in order to exclude artificial features due to noise. Both the height and area cut-offs were adjusted within reasonable limits to judge their effect on island densities. The error bar in the island density for each deposition temperature represents a convolution of the (relatively small) uncertainty due to variation in the height cutoffs, and the variation in island density over multiple images, within a single experiment.

Results and Interpretation

STM data

Figure 1 shows STM images at $\theta^{+}_{Ag} \approx 0.3$ ML. Ag islands nucleate on terraces when Ag is deposited at and below 250 K. For all temperatures, similar islands are observed also at lower $\theta^{+}_{Ag} \approx 0.10$-0.15 ML. From 50 K through 180 K, small islands are evident. Their size increases, and density decreases, slightly in this temperature range. This trend is evident in Fig. 1(A-C). These small islands are almost always less than 1 nm high, and less than 10 nm in diameter, after deposition of 0.3 ML. At 140 K, a few larger islands appear. As temperature increases these larger islands become more numerous until, above 180 K, they

are the only type present. See Fig. 1(D-F). As temperature increases, these larger islands become increasingly rough, with internal striations or geometric shapes that suggest a polycrystalline structure. Examples, together with line profiles, are shown in Fig. 2. Analysis of the ratio of height to baseline width suggests that these larger islands have grown much faster laterally, than vertically. For instance, at 250 K, these islands are 50-120 nm wide, but their maximum height is only about 4 nm.

If the deposition temperature increases to 300 K, there are no Ag islands of the types just described, over distances that span at least 2 μm. Instead, it appears that deposited Ag selectively accumulates in regions of the surface where many Si steps are close together. This is shown in Fig. 3, where 1.7 ML of Ag has been deposited atop the √3 at 300 K. Panel A is an untreated image of a smooth region of the surface. The √3 island-hole texture is evident, plus the remnants of steps that bounded the original Si(111) terraces. In spite of the large amount of Ag deposited onto the √3, no islands of the type evident in Fig. 1(G), at 250 K, appear in these smooth regions. Panel B is an image in derivative mode that encompasses both a smooth region (the left half) and a step-bunch region (the right half). In the step bunch region, Ag forms islands that are up to 10 nm high.

This result shows that, at 300 K, Ag is extremely mobile on the √3 phase. Over a distance of a micron, a diffusing Ag atom encounters many √3 island-hole boundaries, including those that are vestiges of the original Si steps. However, it is able to diffuse freely over such features. It becomes trapped preferentially at Si step bunches.

Also, the √3 domain boundaries within islands or holes seem to capture some Ag. Ag capture gives them a very bright appearance in the STM images. This can be seen in Figure 4, which

compares the appearance of √3 domain boundaries before (A) and after (B) deposition of a very high coverage, over 5 ML of Ag. However, even at such a high coverage, it is clear that the domain boundaries do not serve as nucleation centers for Ag islands.

The result is much different if the Si surface is prepared such that it contains a mixture of √3 and residual (7x7), as in Fig. 5. In this case, Ag deposited at 300 K nucleates and forms many small islands. This implies that Ag atoms diffusing on the √3 become much less mobile when they encounter the (7x7) areas. These data highlight the relatively rapid Ag diffusion on the √3 areas.

In summary, a qualitative inspection of the data shows that both the island density, and the island size, change with deposition temperature between 50 and 300 K. The density decreases with T, and the island size increases. At 250 K, islands are very large and rare, and at 300 K they show a strong tendency to nucleate only at step bunches. Therefore, Ag must diffuse freely across many √3 island-hole boundaries. Some Ag is also captured preferentially at √3 domain boundaries, although these regions do not nucleate large islands.

Analysis of island densities

A classical approach to nucleation kinetics considers the following basic processes: atoms are deposited (irreversibly, in our case) at a rate given by the flux, F; atoms move between stable sites at a rate determined by the diffusion barrier, E_d, by the diffusion pre-exponential factor, ν_d, and by the surface temperature, T; and diffusing atoms can be consumed either by randomly meeting other atoms to form new islands (island nucleation) or by attaching to edges of existing stable islands (island growth). The latter two processes– nucleation and

growth–compete for adatoms, although growth typically dominates. Nucleation is assumed to be homogeneous (i.e. not defect-mediated), and is characterized by i , the critical size. This is defined such that a cluster with i +1 atoms is (on average) stable enough to survive and grow, but clusters with i or fewer atoms typically dissolve.

Rate-equation analysis has been applied to this model.[32-36] Typically, the adatom density is assumed to be at a quasi-steady-state (i.e. a steady-state exists between the incoming atom flux and the rate of surface adatom incorporation into islands). With this assumption, the result is that ln (N_{isl}) varies linearly with the inverse surface temperature, T^{-1}, and the slope of the line equals an Arrhenius energy, E, divided by Boltzmann's constant, k_B. This holds true for homogeneous nucleation over a range of submonolayer coverages. E is a function of three variables:

$$E = \left(\frac{i}{i+2}\right)\left(E_d + \frac{E_i}{i}\right) \qquad (1)$$

Here E_i is the binding energy of the critical nucleus. If i = 1, then E_i = 0 and E takes its minimum value of $E = E_d/3$. The critical size can increase as a function of surface temperature, and this is signaled by an increase in the slope of ln (N_{isl}) vs. T^{-1}.[37]

Figure 6 shows our data in this form for the temperature range 50 to 250 K, and at an additional Ag coverage of 0.3 ML. The data can be broken down into regions. From 50 K through 125 K, the data can be fit reasonably well with a straight line. Its slope corresponds to E = 0.0027 $\pm$ 0.0002 eV. This is followed by a transition to a different regime with steeper slope and lower island densities. That steeper regime occurs from 180 through 250 K, where

a linear fit gives a value for E of 0.20 $\pm$ 0.04 eV. The transition between these two regimes occurs at the same temperatures (140-175 K) as the transition from small Ag clusters to large, polycrystalline Ag clusters.

In terms of nucleation theory, the simplest assumption would be that i = 1 at 50-125 K, since this is relatively low temperature. Then one finds E_d =3E = 0.0081 $\pm$ 0.0007 eV. The viability of this result can be tested, because the dependence of N_{isl} on the ratio between the rate of atom movement between adjacent sites, $\nu_d e^{-Ed/kT}$, and F, has been established and tabulated from Monte Carlo simulation,[38] and even when an exact value is not available, interpolation or extrapolation is possible. [In order to use the published values, one must adopt a value of the adsorption site density. Here we use 6.3 nm^{-2}, which corresponds to 2 sites per $\sqrt{3}$ unit cell, but for our purposes the exact value is unimportant so long as it is the correct order of magnitude.] Using E_d = 0.0081 eV, and a typical value of ν_d = 5 x 10^{12} s^{-1}, one finds that N_{isl} predicted from simulation is a little more than 3 orders of magnitude lower than the measured value at, say, 65 K. Alternatively, in order to match the predicted and measured values of N_{isl}, a value of $\nu_d \approx 10^3$ s^{-1} would be needed. Since values of ν_d on metal surfaces are almost always in the range 10^{11}-10^{13} s^{-1},[39] a value of $\nu_d \approx 10^3$ s^{-1} would be unreasonable.

We can apply a similar analysis to the180-250 K regime, for which E = 0.20 eV (from the slope). Using i =1, E_d = 3E = 0.60 $\pm$ 0.12 eV, and ν_d = 5 x 10^{12} s^{-1}, one finds that N_{isl} predicted from simulation is 3.6 orders of magnitude *higher* than the measured value at, say, 210 K. Taking a different perspective, in order to match the predicted and measured values of N_{isl}, a value of $\nu_d \approx 10^{20}$ s^{-1} would be needed. Again, this is a nonphysical value. Thus, in

each temperature regime where ln (N_{isl}) vs. T^{-1} is linear over a reasonably wide range, 50-125 K and 180-250 K, there is a discrepancy of several orders of magnitude assuming $i = 1$.

Such huge discrepancies indicate the need for an alternative interpretation of the above regimes. Either a modification of the above assumptions is needed, or significantly different physics is at play, e.g., a different diffusion mechanism than single-atom displacement between adjacent sites. In the remainder of this section we will retain the picture of single-atom displacement, and discuss alternative mechanisms in Section 4.

In the temperature regime 50-125 K, it may be that Ag adatom diffusion is so slow that the steady-state approximation for adatom density is not valid, and also that other processes (specifically, the transient mobility discussed in Section 4) become relatively important. As a result, there would be deviations from the simple Arrhenius behavior for N_{isl}, the actual density being lower than predicted by this form. There can be other complications from very slow diffusion as well, such as post-deposition nucleation of islands.[40, 41] However, the basic conclusion is that ln(N_{isl}) vs T^{-1} can appear to have linear Arrhenius behavior but with a slope lower than $3E_d$. Evidence for this type of behavior has been reported for Ag/Ag(100)[42] and Cu/Cu(100)[37, 43] at deposition temperatures below 170 and 220 K, respectively (although the temperature at which this phenomenon takes place depends also on F).

Within this picture, the system begins a transition to standard Arrhenius behavior for $i = 1$ when T increases to about 115-125 K. Comparing the measured island density at 115 K (125 K) with tabulated data yields E_d = 0.20 eV (0.23 eV) for $i = 1$ and $\nu_d = 5 \times 10^{12}$ s^{-1}. The slope of the line that would be predicted for the $i = 1$ regime is indicated by the dashed line in Fig.

6. The value E_d = 0.20-0.23 eV falls between the two extrema for Ag atom diffusion on low-index Ag surfaces, i.e. E_d = 0.05-0.10 eV on Ag(111), and E_d = 0.40-0.45 eV on Ag(100).[39]

More information can be gained by assessing the upper temperature limit of the presumed i =1 range, about 150 K. At this transition temperature, T^*, the Ag-Ag bond of the dimer breaks on the time-scale of aggregation, causing an increase in the critical size. If we call the Ag-Ag dimer bond energy E_b, then the transition temperature is related to E_b and other parameters by a quantity called the natural crossover variable, Y:[44]

$$Y(T) = \left(\frac{\nu}{F}\right) \exp\left[-\left(E_d + \frac{3}{2}E_b\right) \Big/ k_B T^*\right] \qquad (2)$$

It has been shown that $Y < 1$ if i =1, and $Y >> 1$ if i >1.[44] At T^*, $Y(T^*) \approx 10$. Using values of E_d = 0.21 eV (from the above analysis) and T^* =150 K, setting $Y(T^*)$ = 10 in Eq. (2) and solving for E_b yields 0.14 eV. This is not an unreasonable value, given that E_b takes a robust value of 0.2 eV on Ag surfaces. Values lower than 0.2 eV would be expected in a heteroepitaxial system such as this, since the nearest-neighbor Ag-Ag bond separation is probably less favorable than in Ag homoepitaxy.

The next regime, 180-250 K, must then correspond to i >1. We can use Eq. (1) to estimate the value of i from the slope. In this regime, E_d would be the same as at i = 1, 0.21 eV. E_i is related to E_b by $E_i = b_i E_b$, where b_i is the number of Ag-Ag bonds in the critical cluster. This relationship assumes that Ag-Ag bonds are pairwise additive. The geometry of the cluster

relates i and b_i, but for this system the relationship is unknown. However, in the 180-250 K regime, the slope of ln (N_{isl}) vs. T^{-1} can be fit with i = 3-4 and b_i = 2-3. This fit is represented by the left-most solid line in Fig. 6.

Finally, the data at 300 K in Fig. 3 can be compared with the island density data at 180-250 K in Fig. 6. If the straight line fit to the 180-250 K data is extrapolated to 300 K, the predicted island density at 300 K is 4 x 10^{-6} nm^{-2}, or 4 μm^{-2}. This means that, on average, a 4 μm^2 area like that shown in Fig. 3(A) should contain about 16 islands. At 300 K, we observe no islands at submonolayer coverage, meaning that the straight line toward the left edge (180-250 K regime) in Fig. 6 should probably be slightly steeper, implying a larger critical size.

In summary, if we assume that Ag diffusion occurs via thermally-activated, single-atom movement on this surface, then the data in Fig. 6 can be explained as follows. At 50-125 K, the island density does not follow conventional Arrhenius scaling due to limited mobility and a consequent breakdown of the steady-state condition for the adatom density. From ~115-125 K, conventional behavior for i = 1 is realized, and at 180-250 K, i > 1 prevails. Based on the assumption that i = 1 for 115-125 K, one calculates E_d = 0.20-0.23 eV. Using 150 K as the temperature for the transition to i > 1, one finds $E_b \approx 0.14$ eV. These energy values lead to an estimate of $i \approx$ 3-4 in the regime of 180-250 K, where island density varies strongly with temperature.

Discussion

Nature of the substrate

As noted in Section 1, there are reports that √21 and (6x6) phases partially replace the √3 at low temperature, if $\theta^{+}_{Ag} \geq 0.1$.[16-18] Figure 2 of Ref.[17] is a surface phase diagram, in which Ag islands only exist in a very restricted region of θ^{+}_{Ag} –T space below 300 K. The majority of phase-space is dominated instead by √21 + √3, plus some (6x6), where the √21 and (6x6) serve to incorporate the extra Ag atoms. In our work, there is clear evidence for Ag island formation, rather than √21 or (6x6), over a wide range of temperatures and at $\theta^{+}_{Ag} \approx 0.1$-0.3. (Islands also form at higher coverages than those discussed in this paper). The reason for the discrepancy between the previous work and our own is not clear at this time. It may be due to a competition between incorporating extra Ag into Ag islands, or into √21, with the outcome depending sensitively upon the conditions of preparation and deposition. However, general conditions (such as flux and √3 preparation) used in our work are similar to those employed by others.[16-18]

Comparison with DFT calculations

Previously, JJ have calculated a diffusion barrier of 0.22 eV for a single Ag atom on the √3.[28] This agrees with the present experimental result, 0.20-0.23 eV.

As noted in the Introduction, the easiest diffusion mechanism found by JJ is exchange.[28] Such a mechanism is also well-known for metals on metal surfaces.[39] None of the arguments or assumptions made in analyzing the data in Section 3 depend upon whether the diffusion mechanism is exchange or simple hopping. In particular, for metals, note that the frequency

factor, ν_d, falls in the same range for exchange as for simple hopping.[39] In other words, our results are independent of, but compatible with, the exchange mechanism of diffusion.

It is more problematic to deduce the nature of the critical cluster from the DFT work. JJ have calculated cluster energies for situations where 2, 3, and 4 Ag atoms are immersed in the √3, in close proximity. They find that the energy of the immersed group is a highly non-linear function of the number of immersed Ag atoms, presumably because of strain in the √3. In fact, they report that a set of 3 immersed atoms is much more stable than a set of 4, indicating that a 3-atom set would not grow. Therefore, it is not clear that a small set of Ag atoms immersed in the √3 actually serves to nucleate metallic Ag. Further DFT work could clarify the nature of the critical steps in nucleation of metallic Ag islands on the √3.

Diffusion mechanism

It is useful to consider other possible diffusion mechanisms, beyond thermally-activated motion between adjacent stable sites.

One is non-thermal diffusion (a.k.a. ballistic diffusion, or transient mobility), which occurs for Ti/GaAs(110)[45] and which may occur also for Ag/Si(100).[46] In this mechanism, the kinetic energy of the impinging atom is not immediately dissipated upon adsorption (as it is for metals on metals[47]), but rather it is converted into translational kinetic energy which allows the atom to move across the semiconductor surface. If this occurs in the present system, we expect its effect to be most pronounced at low temperature. It may contribute to the long plateau region between 50 and 125 K.

Another possibility is thermally-activated diffusion of small clusters such as dimers, instead of or in addition to motion of single atoms. Cluster diffusion is faster than single-atom hopping for metals on some metal and oxide surfaces.[40, 48-50] Cluster diffusion could change the energies derived from island densities in Section 3.[48] However, cluster diffusion is a collective, interactive version of hopping. From the DFT results of JJ, the diffusion barrier for exchange is lower by about an order of magnitude than the barrier for single atom hopping. Given this large energy difference, it is not likely that any variation of hopping could compete with single-atom exchange, and so we rule out the possibility of cluster diffusion.

Effect of √3 step edges

Classically, step edges can exert two types of effects on surface diffusion. For a moving particle that meets a downward-step, the well-known Ehrlich-Schwoebel (ES) barrier [39]–if present–can impede step-crossing. For a moving particle that meets an upward-step, or for one that meets a downward-step edge with no ES barrier, there is often a high probability of trapping on the lower terrace, leading to step growth or step decoration. In other words, steps can potentially be barriers and/or traps. It is reasonable to ask whether either of these phenomena could affect our data analysis, especially given the rather high density of steps between √3 regions.

Inspection of the data of Fig. 1 reveals that the Ag island separation is far below the size of the √3 regions, all the way up to 170 K, i.e., not just in the low temperature regime (which extends only up to 125 K) but also through the transition to the high temperature regime of steep Arrhenius slope. Because the island separation is far below the √3 “terrace” size, any

modification of transport across √3 step edges will have no significant effect on island density behavior up to 170 K.

Above 170 K, the separation between islands becomes larger than the average √3 terrace size. In this regime, if there were a significant ES barrier, then there should be a range of temperatures where one finds one island in each √3 region (i.e., the Ag island density would be higher than in the case of no ES barrier). Furthermore, above some higher transition temperature where transport across √3 steps becomes facile, the Ag island density should drop suddenly. There is no evidence for this behavior in the present experimental data, in the regime above 170 K.

As for preferential trapping at step edges, there is occasional–although not consistent–evidence for this at 170-180 K. In some STM images, the largest islands of Ag are most commonly found at √3 steps. Above 180 K, diffusion across steps must dominate, since then the Ag islands are often separated by several √3 steps. We conclude that trapping at step edges can occur, but it is not a major effect. Presumably this small effect is compounded at step bunches, which accounts for the Ag trapping in those regions at 300 K.

Comparison with high-temperature data

Regardless of the model, one of the most striking results from the present work is the fact that Ag atoms can migrate over distances of at least 1 μm at 300 K (cf. Fig. 3). Venables et al. earlier observed that Ag atoms migrate over distances of up to 50 μm at 770 K.[23-25] These are both extremely long distances for adatom diffusion. Note that the 50 μm value is also

model-independent, being based upon the width of the √3 border that develops around Ag-rich regions after Ag deposition in a localized area on Si(111)-7x7.[23-25]

Venables et al. also studied island densities as a function of deposition temperature on the √3,[23-25] as we do in the present work. They used scanning electron microscopy and focused on a high-temperature adsorption regime, ~600-800 K, where the islands are relatively large. Figure 7 provides a comparison of our data at 180-250 K, and theirs at 660-780 K, for comparable values of Ag flux. The solid line is a fit to our 4 data points at 180-250 K, the same as the left-most line in Fig. 6. (The result is unchanged if island densities at 170-173 K are included in the fit.) The solid line passes above the 660-780 K data, by about an order of magnitude. This is not unreasonable, since transition(s) to larger critical size(s) would be expected with increasing temperature. Such transition(s) would cause the curve to bend down between 250 and 660 K. Indeed, Venables et al. noted that their critical size was probably very large.[23]

In our data, Ag islands nucleate preferentially at step bunches at 300 K. This should produce a constant island density at T > 300 K. (The island density would be fixed by the density of pre-existing step bunches, i.e. nucleation would be heterogeneous.) However, the data of Venables et al. in Fig. 7 indicates that island density decreases above 300 K. This can be explained if, above 300 K, trapping at step bunches occurs in only a narrow temperature range. Above this range (and below the onset of the high-temperature data set at about 660 K), Ag atoms can overcome the barrier that confines them to step bunches, resulting in a resumption of homogeneous nucleation.

Venables et al. also derived energetic barriers from their data. Assuming that critical cluster size is very large, they applied the limiting form of Eq. (1):

$$E = E_d + 3E_b \qquad (3)$$

and found that the sum, E, is 0.60 $\pm$ 0.05 eV.[25] For our values of E_d = 0.20-0.23 eV, and E_b = 0.14 eV, the sum in Eq. (3) has a value of 0.62-0.65 eV, which is the same as Venables' result within error. Furthermore, they placed a lower limit on E_d of 0.25 eV, which is only slightly higher than our estimate of 0.20-0.23 eV. In short, there is a good level of consistency in the energetic parameters derived from these two sources of data. And with respect to the diffusion barrier, E_d, both results agree with the DFT result of 0.22 eV.

Conclusions

We use scanning tunneling microscopy to measure densities and characteristics of Ag islands that form on the ($\sqrt{3}$x$\sqrt{3}$)R30^o-Ag phase on Si(111). There are two clear regimes. At 50-125 K, islands are relatively small, and island density decreases only slightly with increasing temperature. At 180-250 K, islands are larger and polycrystalline, and island density decreases strongly with increasing temperature. Assuming that Ag diffusion occurs via thermally-activated movement of single-atoms between adacent stable sites, the data can be explained as follows. At 50-125 K, the island density does not follow conventional Arrhenius scaling due to limited mobility and a consequent breakdown of the steady-state condition for

the adatom density. Transient mobility may also play a significant role in this regime. At ~115-125 K, a transition to $i = 1$ begins, and at 180-250 K, $i > 1$ prevails. These transition points indicate a diffusion barrier of 0.20-0.23 eV and a Ag-Ag bond strength of 0.14 eV. The diffusion barrier is the same as that derived from DFT.[28] These energy values lead to an estimate of $i \approx 3$-4 in the regime of 180-250 K. Extrapolation of the data to higher temperature yields reasonable agreement with island densities measured by Venables et al. using scanning electron microscopy.[23] Energetic parameters are also consistent.

Acknowledgments

This work was performed at the Ames Laboratory under contract number DE-AC02-07CH11358 with the U.S. Department of Energy. The document number assigned to this thesis/dissertation is IS-T 3050.

Bibliography

[1] A. Shibata, Y. Kimura, K. Takayanagi, *Surf. Sci.*, **275** (1992) L697.

[2] A. Shibata, K. Takayanagi, *Jpn. J. App. Phys.*, **32** (1993) 1385.

[3] V.G. Lifshits, A.A. Saranin, A.V. Zotov, Surface Phases on Silicon: Preparation, Structures, and Properties, John Wiley & Sons, Inc., West Sussex, England, 1994.

[4] A. Shibata, Y. Kimura, K. Takayanagi, *Surf. Sci.*, **303** (1994) 161.

[5] A. Shibata, H. Kimura, K. Takayanagi, *J. Vac. Sci. Technol.*, **B 12** (1994) 2026.

[6] K.J. Wan, X.F. Lin, J. Nogami, *Phys. Rev. B*, **47** (1993) 13700.

[7] D.W. McComb, D.J. Moffatt, P.A. Hackett, B.R. Williams, B.F. Mason, *Phys. Rev. B*, **49** (1994) 17139.

[8] A. Belianinov, B. Ünal, N. Lu, M. Ji, K.-M. Ho, C.-Z. Wang, M. Tringides, P.A. Thiel, *Phys. Rev. B*, **82** (2010) 245413.

[9] Y.G. Ding, C.T. Chan, K.M. Ho, *Phys. Rev. Lett.*, **67** (1991) 1454.

[10] N. Sato, T. Nagao, S. Hasegawa, *Surf. Sci.*, **442** (1999) 65.

[11] H. Aizawa, M. Tsukada, N. Sato, S. Hasegawa, *Surf. Sci*., **429** (1999) L509.

[12] H.M. Zhang, J.B. Gustafsson, L.S.O. Johansson, *Phys. Rev. B*, **74** (2006) 201304(R).

[13] I. Matsuda, H. Morkawa, C. Liu, S. Ohuchi, S. Hasegawa, T. Okuda, T. Kinoshita, C. Ottaviani, A. Cricenti, M. D'angelo, P. Soukiassian, G. Le Lay, *Phys. Rev. B*, **68** (2003) 085407.

[14] G. Le Lay, G. Quentel, J.P. Faurie, A. Masson, *Thin Sol. Films*, **35** (1976) 273.

[15] V.A. Gasparov, M. Riehl-Chudoba, *Surf. Sci*., **601** (2007) 5403.

[16] Z.H. Zhang, S. Hasegawa, S. Ino, *Phys. Rev. B*, **52** (1995) 10760.

[17] X. Tong, S. Hasegawa, S. Ino, *Phys. Rev. B*, **55** (1997) 1310.

[18] X. Tong, S. Ohuchi, N. Sato, T. Tanikawa, T. Nagao, I. Matsuda, Y. Aoyagi, S. Hasegawa, *Phys. Rev. B*, **64** (2001) 205316.

[19] H. Jeong, H.W. Yeom, S. Jeong, *Phys. Rev. B*, **77** (2008) 235425.

[20] M. Ueno, I. Matsuda, C. Liu, S. Hasegawa, *Jpn. J. App. Phys.*, **42** (2003) 4894.

[21] Y. Nakajima, S. Takeda, T. Nagao, S. Hasegawa, *Phys. Rev. B*, **56** (1997) 6782.

[22] N. Sato, T. Nagao, S. Hasegawa, *Phys. Rev. B*, **60** (1999) 16083.

[23] G. Raynerd, T.N. Doust, J.A. Venables, *Surf. Sci.*, **261** (1992) 251.

[24] F.L. Metcalfe, J.A. Venables, *Surf. Sci.*, **369** (1996) 99.

[25] J.A. Venables, F.L. Metcalfe, S. Sugawara, *Surf. Sci.*, **371** (1997) 420.

[26] H. Aizawa, M. Tsukada, *Phys. Rev. B*, **59** (1999) 10923.

[27] S. Jeong, H. Jeong, *Phys. Rev. B*, **76** (2007) 085423.

[28] S. Jeong, H. Jeong, *Phys. Rev. B*, **81** (2010) 195429.

[29] B. Unal, F. Qin, Y. Han, D.J. Liu, D. Jing, A.R. Layson, C. Jenks, J.W. Evans, P.A. Thiel, *Phys. Rev. B*, **76** (2007) 195410.

[30] L. Gavioli, K.R. Kimberlin, M.C. Tringides, J.F. Wendelken, Z. Zhang, *Phys. Rev. Lett.*, **82** (1999) 129.

[31] I. Horcas, R. Fernandez, J.M. Gomez-Rodriguez, J. Colchero, J. Gomez-Herrero, A.M. Baro, *Rev. Sci. Instr.*, **78** (2007) 013705.

[32] G. Zinsmeister, *Thin Sol. Films*, **7** (1971) 51.

[33] R. Kern, G.L. Lay, J.J. Metois, "Basic mechanisms in the early stages of epitaxy," in: E. Kaldis (Ed.) Current Topics in Materials Science, North-Holland, Amsterdam, 1979, 135.

[34] S. Stoyanov, D. Kashchiev, "Thin film nucleation and growth theories: A confrontation with experiment," in: E. Kaldis (Ed.) Current Topics in Materials Science, North Holland, Amsterdam, 1981, 71.

[35] J.A. Venables, G.D.T. Spiller, M. Hanbucken, *Rep. Prog. Phys.*, **47** (1984) 399.

[36] J.A. Venables, *Phil. Mag.*, **27** (1973) 697.

[37] J.W. Evans, P.A. Thiel, M.C. Bartelt, *Surf. Sci. Reports*, **61** (2006) 1.

[38] M.C. Bartelt, J.B. Hannon, A.K. Schmid, C.R. Stoldt, J.W. Evans, *Colloids and Surfaces A: Physicochemical and Engineering Aspects*, **165** (2000) 373.

[39] G. Antczak, G. Ehrlich, Surface Diffusion. Metals, Metal Atoms, and Clusters, Cambridge University Press, Cambridge, UK, 2010.

[40] H. Brune, G. Steven Bales, J. Jacobsen, C. Boragno, K. Kern, *Phys. Rev. B*, **60** (1999) 5991.

[41] B. Müller, L. Nedelmann, B. Fischer, H. Brune, K. Kern, *Phys. Rev. B*, **54** (1996) 17858.

[42] S. Frank, H. Wedler, R.J. Behm, J. Rottler, P. Maass, K.J. Caspersen, C.R. Stoldt, P.A. Thiel, J.W. Evans, *Phys. Rev. B*, **66** (2002) 155435.

[43] H. Durr, J.F. Wendelken, J.-K. Zuo, *Surf. Sci.*, **328** (1995) L527.

[44] M.C. Bartelt, J.W. Evans, L.S. Perkins, *Surf. Sci.*, **344** (1995) L1193.

[45] Y.-N. Yang, B.M. Trafas, Y.-S. Luo, R.L. Siefert, J.H. Weaver, *Phys. Rev. B*, **44** (1991) 5720.

[46] A. Samsavar, T. Miller, T.-C. Chiang, *Phys. Rev. B*, **38** (1988) 9889.

[47] J.W. Evans, D.E. Sanders, P.A. Thiel, A.E. DePristo, *Phys. Rev. B*, **41** (1990) 5410.

[48] S. Liu, L. Bonig, H. Metiu, *Phys. Rev. B*, **52** (1995) 2907.

[49] L. Xu, G. Henkelman, C.T. Campbell, H. Jónsson, *Surf. Sci.*, **600** (2006) 1351.

[50] L. Xu, G. Henkelman, C.T. Campbell, H. Jónsson, *Phys. Rev. Lett.*, **95** (2005) 146103.

CHAPTER IV

CREATING Ag SUPERSTRUCTURES ON THE Si-(111)-(√3x√3)R30°-Ag BY MEANS OF SELF ASSEMBLY

A paper submitted to *Journal of Vacuum Science and Technology B*

Alex Belianinov[1,2], Barış Ünal[1,3,4] M. C. Tringides[1,4] and Pat Thiel[1,2,3]

[1] Ames Laboratory, [2] Department of Chemistry, [3] Department of Material Science and Engineering, [4]Department of Physics, Iowa State Univeristy, Ames Iowa 50011 USA,

[5]Present address: Department of Chemical Engineering, Massachusetts Institute of Technology, Cambridge MA 02139 USA

Abstract

Using scanning tunneling microscopy we were able to pattern a Si-(111)-(√3x√3)R30°-Ag surface. After making a variety of surface structures – different sized pits arranged in geometric pattern; we deposit additional Ag at room temperature. Due to high silver mobility on the Si √3 surface, the terraces remain clean, no additional Ag islands nucleate. However, we observe effective material capture at the STM patterned sites. We are able to create Ag wires and dots 3-4 nm in size using only an STM and a metal evaporation source. Herein we describe methods that allow creation of many different types of Ag superstructures, on the Si-(111)-(√3x√3)R30°-Ag surface, by STM patterning followed by a silver deposition.

Introduction

Since miniaturized transistors made their debut in the early 1950's, scientists across different fields have been working on making smaller, faster and lower energy consumption devices[1]. Today, in the age of consumer microelectronics, rising demand for portability has acted as additional pressure to miniaturize circuits. Widely used semiconducting materials such as silicon, germanium and more recently GaAs, have been an object of lithographic studies for many decades.[2,3, 4,5] Patterning the surface with a probe is an appealing technique, as design can be transferred on the surface directly without intermediate, chemical steps. While the current, industrial, methods of wet etching and optical lithography are getting better, there is, and always has been, an interest to make circuits smaller, cleaner and cheaper. In this paper we describe a new way of patterning a certain Ag-rich surface phase of Si(111) using a scanning tunneling microscope (STM) tip. The constituents of the patterns are nanometer-scale clusters of Ag.

Ag on Si(111) has been a popular surface system to study the effects of metal-semiconductor interfaces[6]. Initial studies focused on the 7x7 reconstruction of the Si surface[7], but since then the field broadened to encompass a myriad of adsorbates, nanolithography and other aspects of nano technology.

Si √3 has been a surface of interest since the late 1960's with initial experiments performed by Spiegel[8]. Since Spiegel's pioneering LEED study, the geometry of this surface has been studied using a wide variety of surface techniques [9]. However, even with all the information on this system in the literature, there is no consensus on geometric structure and the exact coverage of Ag in the √3. Currently, the most popular models are IET and HCT [10,11,12,] but

even these models are showing weaknesses as more detail oriented studies are coming out[13]. The following facts are most germane to the present investigation. The Si-(111)-($\sqrt{3}$x$\sqrt{3}$)R30^{o}-Ag forms from the Si(111)-(7x7) at temperatures in the range 500 – 800 K, and contains 1.0 monolayer (ML) of Ag. Exactly 1.06 ML of Si is displaced when the Si-(111)-($\sqrt{3}$x$\sqrt{3}$)R30^{o}-Ag forms. This displacement leads to $\sqrt{3}$ holes and $\sqrt{3}$ islands that are above and below the level of the original (7x7), respectively.

We present results of patterning a Si-(111)-($\sqrt{3}$x$\sqrt{3}$)R30^{o}-Ag (Si $\sqrt{3}$ hereafter) surface with STM and depositing Ag to form Ag superstructures at the patterned sites.

Patterning of the Si $\sqrt{3}$ surface has been shown by Riehl-Chudoba et al.[14]. This group has been able, using STM, to successfully make various size pits on the surface by applying a positive voltage (with respect to the surface), thus extracting material from the surface, and redepositing some of it on the STM tip, leaving a precisely damaged site behind. Varying the distance between the probe and the surface, along with varying voltage, Riehl-Chudoba et al. have been able to quantitatively make pits ranging from 0 – 5nm wide and 0 – 6A deep. Based on the data provided in their article, the height and depth increase linearly until applied voltage reaches 3.4-3.6V. At that point the depth and width are fairly constant around the equilibrium values of 6 Åand 50 Å respectively.

The underlying theoretical principle of material removal using an STM tip has qualitatively been described by Tsong with a model based on field evaporation potential[15]. More recent work by Tseng expands on the concept and compares probe patterning to a miniaturized electron beam lithography[16], principles of which are understood fairly well[17].

Our work builds on STM patterning studies done by Riehl-Chudoba and the previously demonstrated propensity for Ag to accumulate at defect sites on the Si $\sqrt{3}$ at room

temperature; we found that Ag can diffuse freely over the island-hole boundaries[18, 19]. In fact, it can diffuse over distances of at least 1 μm, if the surface is completely covered by Si √3. If it is not completely covered by Si √3, regions of the Si(111)-(7x7) selectively trap the Ag. The long diffusion length on the Si √3 was attributed to a moderate diffusion barrier of 0.2 eV, plus a critical size greater than 1 for homogeneous nucleation at this temperature.

Experimental

All experiments were performed in an Omicron VT-STM, previously described elsewhere[20]. Chamber pressure did not exceed 1.0 x 10^{-10} mbar throughout the experiments. Typical Ag flux was 0.0067ML/s, deposited from an Omicron EFM-3 e-beam evaporator. The Ag coverage was calibrated by deposition on the clean Si(111) – 7x7, as the wetting layer has a known Ag coverage of 0.5ML[6]. The Si sample is a p-type with resistivity of 0.02 Ohm*cm. The Si (111)-7x7 surface was prepared using well-known 1200K flashing and stepwise cooling methods. Si √3 surface was prepared by depositing 1ML of Ag on the 7x7 and annealing the sample for 2 minutes at 800K. We used W wire with electrochemically etched tips, biased with respect to the sample, for both – imaging and nanolithography in our STM. Surface modification was done through a programmed sequence developed in a software environment distributed with our Omicron instrument. Nanostructures on the surface are made by voltage pulsing sequences at 4V, for 10msec at room temperature[14]. Lines were drawn using a dense, linear set of 80 individual pulses separated by 1 nm. Larger and deeper features (pits) were made by applying a rastered sequence of 500 x 500 individual pulses within a 10 x 10 nm^2 surface region. The feedback loop was on during all these processes,

with current set at 0.2-0.4 nA.These conditions have shown to create reproducible size pits without removing large quantities of excess material and causing it to recondense into the patterned structure. Subsequent imaging was done at 0.2 to -2V at 0.2 to 2nA. We did not encounter problems with imaging directly after creating pits. However, tip cleanliness and apex stability seem to be of importance as polarity is switched. We have also found that unstable tips with poor tip geometry are unable to make clean, reproducible patterns or are ineffective when imaging the area. We have used a homemade STM tip flasher to ensure the cleanliness of our tips before structuring and imaging to ensure quality structures were created on the surface[21]. Images were processed using WsXM software package[22]. Ag superstructures and other nanostructures were formed by deposition at room in temperature in the STM stage.

Results & Discussion

Figures 1&2 illustrate general material removing capabilities of the STM patterning technique. In Fig.1 panel (A) shows a region of clean Si √3 surface at room temperature, prior to any surface modification sequence. In Fig. 1 (B) pulses were placed in close proximity to each other to create a linear structure. Due to the fact that we create line patterns by means of excavating material spot by spot, we found that there is occasional material redeposition back into structured site. We believe there to be a way to circumvent these issues if lines were created in a single, smooth patterning process.

Fig. 2 panel (A) and (C) show additional variations possible with the technique, an attempt to create a wire-like trench, made out of individual dots; and a large ($10x10nm^2$) pit. We created

the pit using the same conditions as for creating small dots. Pit depth is 1-1.2nm. Fig. 2 panel (B) shows the surface after applying a series of 4V pulses for 10msec at each spot. Typical dot width is 5nm with a depth of 2-3A. This figure also represents the flexibility in our technique, we can place dots in close proximities, along with generating some curves with precision; also we are able to place structures within structures.

Perhaps more interesting is the effect of the deposited silver atop of the patterned Si √3 surface. As Ag is deposited at room temperature on the Si √3 surface, the Ag atoms do not nucleate into islands on terraces, rather they diffuse across great distances (up to few um) [23] to the areas of high step density. There, Ag coagulates in a highly faceted, rough, tall islands leaving the terraces Ag island free [24].

As the deposited material comes across patterned areas, or other surface imperfections, Ag gets captured at damaged sites. This effect can be seen in Fig. 3. As we progress from panel (A) to panel (E), the amount of deposited Ag increases from 0.5 to 3.25ML. While the coverage of Ag is increasing in the linear structures, readers may note the increase is not uniformly distributed. The issue ties back to the structures' preparation methods. We believe since the lines were created dot by dot there is residual material in the linear structure, perhaps in the space between the dots, as a result of Si redeposition from the tip as the bias oscillates. This effect is shown better in Fig. 1(B). While there is no doubt that there are linear patterned structures on the surface, those structures are littered with "blobs" of material at the edges. The final effect - Ag nucleation is not homogeneous throughout the created structure. We believe that adjusting the structuring voltage along with sample – tip distance, will give us finer control over the quality of the structure, minimizing redeposition.

As we progress through the deposition, note that the surrounding terrace stays Ag free

throughout the experiment. This is shown in Fig. 4, panels (B) – (E) in a series of three 3D images show the same region on the surface, where we patterned a ~10x10nm^2 pit. As the coverage of deposited silver increases from 0 to 0.5 and subsequently to 3.25ML, the amount of captured material steadily increases. However the adjacent √3 terrace stays Ag free. We believe this effect to be of paramount importance, since such Ag self-assembly eliminates the need for masking parts of the surface to create an Ag-superstructure in the STM patterned area. The excess Ag simply diffuses away, only covering the patterned area of interest. Given the conditions used 4V bias, 10msec delay at a constant tip-surface tunneling conditions, the created mini pits are uniform size averaging 5 +/-1nm wide and 5.2 +/- 1.7 A deep. The creation of a large pit was achieved by applying the bias without the use of 10msec delays, but rather just letting the tip scan the 10x10nm^2 area at 4V. The result is increased depth of the structure to 1.2nm +/- 30A.

We found the STM nanopatterning process to be quick and robust. There are few limits to what can be patterned on the surface due to high precision of material removal by the tip and piezo control. Building Ag superstructures is a straight forward process as well, since the deposition is carried out at room temperature and the excess silver quickly diffuses away on the √3 terrace.

Conclusion

We were able to create Ag filled lines, dots and pits on top of a Si-(111)-(√3x√3)R30^o-Ag surface. STM was used to create the structures by means of tip lithography on the Si √3-Ag. Due to particular surface dynamics of the Si √3, damaged areas of the surface, act as capture

sites for the highly mobile silver atoms at room temperature. Since the majority of the Ag diffuse over the clean √3 surface without nucleating, there is no need for masking and later etching the surface to achieve similar effects. The Ag superstructures can be called self-assembling since the entire process is diffusion mediated. We believe pursuing this system may allow for quicker and environmentally cleaner methods for manufacturing highly miniaturized Ag circuitry components.

Acknowledgments

This work was performed at the Ames Laboratory under contract number DE-AC02-07CH11358 with the U.S. Department of Energy. The document number assigned to this thesis/dissertation is IS-T 3050.

Bibliography

1. J. Chelikowski, *Introduction: Silicon in all its Forms,"Silicon: evolution and future of a technology*. (Sringer, 2004

2. H. Uchida, D. Huang, F. Grey, ccedil, ois and M. Aono, Physical Review Letters **70** (13), 2040 (1993).

3. A. R. Smith, K.-J. Chao, Q. Niu and C.-K. Shih, Science **273** (5272), 226-228 (1996).

4. M. J. Lercel, G. F. Redinbo, H. G. Craighead, C. W. Sheen and D. L. Allara, Applied Physics Letters **65** (8), 974-976 (1994).

5. K. R. Harikumar, I. R. McNab, J. C. Polanyi, A. Zabet-Khosousi and W. A. Hofer, Proceedings of the National Academy of Sciences **108** (3), 950-955.

6. L. Gavioli, K. R. Kimberlin, M. C. Tringides, J. F. Wendelken and Z. Zhang, Physical Review Letters **82** (1), 129-132 (1999).

7. T. Y. T. S. Takayanagi K and M. Takahashi, Surf. Sci. **164** (2-3), 367 (1985).

8. K. Spiegel, Surf. Sci. **7**, 125 (1967).

9. A. A. S. V. G. Lifshits, A. V. Zotov, *Surface Phases on Silicon Preparation, Structures and Properties*. (John Wiley and Sons, 1994).

10. N. Sato, T. Nagao and S. Hasegawa, Surface Science **442** (1), 65-73 (1999).

11. H. Aizawa, M. Tsukada, N. Sato and S. Hasegawa, Surface Science **429** (1-3), L509-L514 (1999).

12. Y. G. Ding, C. T. Chan and K. M. Ho, Physical Review Letters **67** (11), 1454 (1991).

13. A. Belianinov, Uuml, B. nal, N. Lu, M. Ji, K. M. Ho, C. Z. Wang, M. C. Tringides and P. A. Thiel, Physical Review B **82** (24), 245413.

14. M. Riehl-Chudoba, W. Richter and V. A. Gasparov, Journal of Applied Physics **83** (5), 2500-2503 (1998).

15. T. T. Tsong, Phys. Rev. B **44**, 13703 (1991).

16. A. A. Tseng, A. Notargiacomo and T. P. Chen, Journal of Vacuum Science & Technology B: Microelectronics and Nanometer Structures **23** (3), 877-894 (2005).

17. A. A. Tseng, C. Kuan, C. D. Chen and K. J. Ma, Electronics Packaging Manufacturing, IEEE Transactions on **26** (2), 141-149 (2003).

18. A. Belianinov, B. Ünal, K. M. Ho, C. Z. Wang, J. W. Evans, M. C. Tringides and P. A. Thiel, Journal of Physics: Condensed Matter **23** (26), 265002 (2011).

19. S. Jeong and H. Jeong, Physical Review B **81** (19), 195429 (2010).

20. B. Unal, F. Qin, Y. Han, D.-J. Liu, D. Jing, A. R. Layson, C. J. Jenks, J. W. Evans and P. A. Thiel, Physical Review B **76** (19), 195410 (2007).

21. F. B. A. G. C. a. M. Hopkinson, J. Vac. Sci. Technol. B **28** (2), 371 (2010).

22. I. Horcas, R. Fernandez, J. M. Gomez-Rodriguez, J. Colchero, J. Gomez-Herrero and A. M. Baro, Review of Scientific Instruments **78** (1), 013705-013708 (2007).

23. G. Raynerd, M. Hardiman and J. A. Venables, Physical Review B **44** (24), 13803 (1991).

24. B. Ü. A. Belianinov, K.-M. Ho, C.-Z. Wang, J. W. Evans, M. C. Tringides P. A. Thiel, Submitted (2011).

CHAPTER V

PENTACENE ON THE Ag-Si(111)

Introduction

Pentacene is currently viewed as one of the most capable organic molecules for organo-electronic devices[1]. It is most noted for its relatively high field effect mobility and its ability to form ordered films[2, 3]. Our own research interests are directed towards studying the epitaxial growth of nanostructures that result in monodispersive particle dimensions. Using quantum size effects (QSE) for selecting preferential heights[4] we utilize the Ag-Si(111) surface as a substrate for our pentacene study. A well-known example of the QSE is Pb on Si(111)[5, 6]. In our work we want to combine the favorable characteristics of pentacene films with the selectivity of the island heights in the Ag-Si(111) 2 and 3 layer high islands. We want to test if the special QSE induced preferential selection of the 2 layer high island has any effect on the growth mode of pentacene compared to the 3 layer high islands on the same surface.

Yong et al. report a wealth of information on pentacene behavior on the Si(111) surface[7]. In their work using STM and DFT calculations they have been able to identify three preferred configurations and binding energies for low pentacene coverage on the Si(111) – 7x7 . Similar to the results from the Si(100) – 2x1, pentacene utilizes π orbitals for covalent C-Si bonding, as well as adopting flat lying configurations to maximize bond overlap[8].

On Ag (111) in the RT regime, work started by Eremtchenko[9] et al. and then continued by Dougherty[10] et al. have provided the most complete picture of nucleation and growth for films in the 0 – 1 ML coverage regime. Both teams are in accord that the initial pentacene bilayer, at RT, grows as a disordered first layer. At 50% coverage of the first layer, the second layer starts to grow. Dougherty[10] shows excellently resolved images of pentacene layers progressing from 0.3 to 1 ML in 0.2 ML increments. In the initial nucleation steps little can be distinguished on the surface, but at 0.6 ML ordered rows begin to appear growing perpendicularly to the Ag(111) step, until they cover the entire terrace. As coverage increases to 1 ML, these ordered rows eventually also grow parallel to the surface. It is unclear whether the pentacene can overcome the step barrier and begin nucleating additional layers at terraces below.

For thick pentacene films on Ag(111) at RT, Kafer et al[11]. have reported an excellent XPS, SEM, TPD and NEXAFS study. While the primary focus of their work is the actual structure of the pentacene film, they provide interesting insight into growth mechanisms beyond the initial monolayer. According to Kafer[11], pentacene begins nucleating as 3D polycrystalline islands as soon as the first layer is complete. They further suggest that these islands do not grow as single crystals, but rather contain a number of preferred orientations with respect to the [111] substrate. XRD angular scans of 30 nm thick films show common orientations such as: [022], [121], [122], [1-2-1] and [123]. Kafer's[11] team concludes that "film growth is characterized by a Stranski‐Krastanov mode which leads to the formation of distinct islands beyond a chemisorbed monolayer exhibiting the crystalline bulk phase of pentacene without any evidence for a substrate mediated thin film phase."

At 50 K on Ag(111) there is definite order in the first layer. Shown by Dougherty[10], the growth is still characterized by a bilayer growth, but the 1st bilayer can now be distinguished and described. There are two similar structures. Unit cell dimensions of the two structures are given as a_1 = 0.85 nm b_1 = 1.7 nm $\alpha_1 = 60^\circ$ and a_2 = 1.0 nm b_2 = 1.5nm $\alpha_2 = 71.2^\circ$. Another interesting observation made in the study, is at 50 K, the 2nd layer in the 1st bilayer exhibits molecules tilting out of plane instead of just lying flat – a suggestion similar to Kafer's[11] finding at RT.

On the Ag-Si-√3 at RT Guaiono et al. report two main pentacene orientations at RT. First is a loose packing structure designated as "head to head" where pentacene forms rows of molecules arranged head to head a = 18.4 Å, b= 15.8 Å. Head to head structure is reported at submonolayer coverage, but another group, Jing et al.,[12] do not see this configuration. At 1 ML coverage a structure denoted "brick wall" appears, with unit vectors a = 16.04 Å, b= 6.5 Å. Brick wall is a more tightly packed strucutre with reported surface molecular density of 8.7×10^{13} mol cm^{-2}. As coverage increases Guaiono et al.[13] reports pentacene tilting upwards, not unlike Ag(111) behavior described above.

When the Ag-Si-√3 is cooled down to 120 K Jing et al.[12] report a reconstruction of the "brick wall" structure. The molecular axis and the inter row separation is retained, but the new structure has a larger intermolecular distance 34.6 Å. As a result the molecular density of the 120 K reconstruction is 75% of the "brick wall" structure. The pentacene becomes epitaxial with the underlying √3 and the structure has been described as Ag/Si(111)-(2√3 x 2√3)-Pentacene.

Experimental Details

All experiments were performed in an Omicron VT-STM, previously described elsewhere[14]. Chamber pressure did not exceed 1.0 x 10^{-10} mbar throughout the experiments. Si sample was a p-type with resistivity of 0.02 Ohm*cm. The Si (111)-7x7 surface was prepared using well-known 1200 K flashing and stepwise cooling methods. The Si √3 surface was prepared by depositing 1 ML of Ag on the 7x7 and annealing the sample for 2 minutes at 800 K. Typical Ag flux was 0.0067 ML/s, deposited from an Omicron EFM-3 e-beam evaporator. The Ag coverage was calibrated by deposition on the clean Si(111) – 7x7, from the wetting layer, which has a known Ag coverage of 0.5 ML[15]. The Ag-Si(111) 2 and 3 layer high islands system were prepared by depositing 1.5 ML of Ag on the Si(111) – 7x7 at RT.

Pentacene (Sigma Aldrich) was deposited thermally from a homebuilt molybdenum Knudsen-like cell (See Appendix) at 300℃. The deposition was done in the prep chamber and then the sample was transferred into the main chamber for analysis. The pentacene cell was outgassed at 200℃ for 6 hours prior to deposition.

For low temperature experiments the pentacene-Ag-Si(111) systems were prepared at RT and subsequently cooled down to the desired temperature. We used W electrochemically etched tips for our STM experiments. Data analysis was done using the WsXM software package[16].

Results and Interpretation

Pentacene on the Si-Ag-√3

Figure 1 shows a Si-Ag-√3 surface covered by 2.5ML of pentacene at room temperature. Panels A and C demonstrate the 'closed-packed side by side' configuration reported by Guiano et al[13]. This structured is denoted 'brick wall' on in the text. The distance between the pentacene rows is 6-7 Å and the distance between the approximate centers of two molecules is 11 Å. Previously reported distances by Teng[12] et.al. are 6.7 Å and 13.3 Å respectively. Panel B shows a 20x20nm^2 area that provides a better overview of the pentacene covered surface. Here we can distinguish the closed packed 'brick wall' configuration and also observe the holes left in the pentacene overlayer – due to incomplete coverage. It is important to note here that it has previously been shown that polyacene molecules tend to adsorb parallel to the surface[17]. In Panel D, Si-Ag-√3 clean surface is given as comparison. Structure for the 'brick wall' room temperature pentacene layer, in Wood's notation, can be given by surface cell vectors a_0 and b_0 (relative to the a_s & b_s of the √3 substrate):

$$\begin{pmatrix} a0 \\ b0 \end{pmatrix} = \begin{pmatrix} 3 & -1 \\ 0 & 2 \end{pmatrix} \begin{pmatrix} as \\ bs \end{pmatrix}$$

In Figure 2 a higher coverage, 4ML, of pentacene is on the Si-Ag-√3. Here, in addition to the 'brick wall' structure in Panels C and D, on A and B we can see island nucleation at the steps of the √3 island/hole pairs as well as smaller islands on terraces. The data show that large islands nucleate on the terraces as well, but islands tend to cluster next to areas of high defects. In addition, in panel E we resolve an area with loose packing 'brick wall' structure. More explicitly, there now is a gap between individual pentacene molecules in each row. A more open surface, much like what we see in panel E, has been reported at 120 K by Teng[18]

and deemed as more symmetric, with inter row separation of 6.7 Å, as at 2.5ML, but increased intermolecular distance of 23 $Å^2$. This change decreases the molecular density of pentacene making it 75% of 'closed pack' structure and can be denoted as Si(111)-Ag-(2√3 x 2√3).

Our pentacene results correspond well to the multilayer data presented in the literature[18]. There is no consensus in the field on the first layer growth at RT. While we do not observe the 'head to tail' configuration reported by Guaino[19], we do see the 'brick wall' structure, a lookalike ¾ ML loose 'brick wall' reported by Jing, albeit at room temperature as well as a similar result of island nucleation past the 3rd layer reported by Teng[1,2,4]. Based on this information we can suggest that at RT on Si-Ag-√3 Pentacene grows via SK growth mode. Initial three layers grow in the layer by layer mode, with the initial wetting layer possibly having a higher degree of disorder, followed by second and third layers with orientations discussed above and further growth in 3D island growth.

Pentacene on the Ag-Si(111)

In these experiments we focused on coverage in the 0 – 1 ML range, in low temperature and RT regimes. What we wanted to focus on is any observable differences in the nucleation and growth of pentacene on 2 and 3 layer high Ag islands. We deposit pentacene atop Ag-Si(111) surface at room temperature and then cool down to the desired temperature in the STM. Figure 3 shows small surface region ~6x6 nm^2 of the pentacene molecules sitting on the small Ag islands in the Ag-Si wetting layer at 100 K. The pentacene molecules coagulate together, but without any clear order in assembly. At 50 K Dougherty[10] et al. report an

ordered first pentacene layer on the Ag(111) surface after cooling it[10]. They describe the structure as "flat lying molecules arranged in oblique unit cells that are typical for pentacene on single-crystal metal surfaces." There is no evidence of similar growth at 100 K. In the RT regime the same group and an earlier study done by Eremtchenko[9] et al. are in consensus that on Ag(111) first layer growth is disordered.

Figure 4 shows 0.5ML of pentacene on the 2-layer high island at 70 K, note that there still is no any long range order in the first layer structure. The longest molecular assembly is seen on the left hand side of the Panel B, where one could distinguish a small sample of molecules stacking side by side. Dougherty[10] et al. describe two possible candidates for this surface (on Ag(111)) and denote them as *Structure 1* and *Structure 2*. Unit cell dimensions of the two structures are given as a_1 = 0.85 nm b_1 = 1.7 nm $\alpha_1 = 60^\circ$ and a_2 = 1.0 nm b_2 = 1.5nm $\alpha_2 = 71.2^\circ$. The long axis in *Structure 1* coincides with [1-10] direction of the Ag surface, in *Structure 2* the long axis makes an angle of ~10˚ with the [1-10].

On the 3-layer high Ag islands, seen in Figure 5, we observe a similar result. At 70 K and 0.5ML pentacene, there isn't a clearly obvious, well-ordered first layer. The molecules are largely disordered and appear to be lying in different configurations on the surface. Similar results have been reported by Pedio[20] et al. in their NEXAFS on Ag(111) surfaces. They report molecules tilting with respect to the surface by 10 +/-5˚ at 1ML Pentacene coverage. It is interesting to add that for submonolayer coverage the tilt angles of up to 25 +/-5˚ are reported. This result may appear somewhat contradictory with the STM work reported earlier, but a diffraction technique would survey a larger area and Dougherty's[10] work was done at 50K.

Figure 6 Panel A is 100x100nm^2 differentiated images of 2 and 3 layer Ag islands with 0.75ML of pentacene at 100 K. These images allow side by side comparison of different growth modes pentacene attains; contrasting Ag 2 and 3 layer high islands in the same image. Again, no long range order can be observed in either case. Panel B offers a 21x21nm2 view of the pentacene on the 3 (left) and 2 (right) layered islands. A notable detail in the figure is the shape of the pentacene and how it corresponds to the shape and size of the Ag island. In Panels A, it is clear that the pentacene overlayer takes the shape of the island; furthermore, pentacene layer ends abruptly up to 14 nm away from the perceived edge of the silver island. This can be attributed to the Elhrich-Schwoebel barrier at the edge blocking any diffusion of the pentacene molecules. Eremtchenko[9] and Dougherty's[10] work support that notion on the basis of very high pentacene mobility at RT [5,6]. They commonly refer to the Pentacene-Ag(111) system at RT as mobile "2D gas." It is therefore reasonable to assume that as the temperature is lowered to 100 K the mobility of the pentacene decreases and step barriers act much more prohibitively to diffusion. This however does not fully explain the reason for pentacene's strict adherence to the Ag island shape while varying the distances between the edge of the pentacene layer with respect to the edge of the silver island.

An example of LT (100 K) pentacene growth beyond a single monolayer is shown in Figure 7. Panel A is a 100x100 nm^2 image of a large, multilayer pentacene island. This structure reaches 2.2 nm in height at its maximum, with respect to the pentacene on the Ag wetting layer, and is best approximated as a circle with a radius of 100 nm. Panels B, C and D are small area magnifications of the island surface. From these images it is evident that multilayer pentacene grows as ordered layers. In Panels C and D rows of pentacene are

distinguishable, Panel B features rows and some molecular orientation in the rows. In our experiments this island was the only example of high coverage growth. All of the other pentacene islands we encountered were much smaller without any clearly resolvable structure in the top layer. Unfortunately, since this is the only example of ordered growth, we do not have much high quality data that may show what kind of the top structure without leaving any doubts. All we can say from our data is that at higher coverage the pentacene starts forming ordered rows of pentacene that grow side by side.

Figure 8, Panel A shows a system with two Ag islands that are fused over a Si step. The island on the left hand side is 11 Å high, the island on the right is 8 Å high as seen in Panel B and C respectively. The heights of the islands are measured with respect to the Ag wetting layer with pentacene. The height of the island on the left is denoted as X in Panel D, on the right, 2 layer island height is denoted as Y, the height of the Si(111) step, 3.1 Å, is denoted as K; finally the height of the pentacene ridge (Shown in Figure 9, Panels C) is labeled Z. Assuming the bulk Ag lattice constant of 2.89 Å, the island on the left (X) corresponds to 3 layers while the one on the right (Y) is closer to 2 layers. $Y + K - X = Z$ That is to say that the difference, of sum of height of the island on the right ($X = 8$) and Si step ($K= 3.1$), and the island on the left ($X = 11$) should equal the height of the pentacene ridge ($Z = 1$). Figure 9 shows areas of the 2 and 3 layer high overstructures. Panel A is zoomed in top layer of the 2 layer high island on the right hand side (Fig. 8 Panel A and B). Figure 9 Panel B is a close up region of the pentacene layer interface between the 2 and 3 islands. We can see from the Figures that the coverage on the 2 layer tall island appears to be fuller, with molecules assembling into rows, but not exhibiting a high degree of long range order as seen in Figure

7. At the same time, the left hand side, the top of the 3 layer island appears to have a lower pentacene coverage. The ridge separating the two areas is a notable feature, the maximum height if this feature is 1 Å and it appears to run exactly over the area where a Si step would be. This system provides an interesting insight into the Ag-Si(111) 2 and 3 layer QSE system. Based on our limited data, there appears to be a subtle difference in the nucleation process depending whether it occurs on the 2 or the 3 layer island. The presence of the separating ridge is telling in this case, one would expect a smooth transition between the tops of the two islands with the pentacene either flowing smoothly, or forming an edge, similar to the morphology seen in Figure 6. Instead, the intermediate area of the two islands serves as a pad for pentacene molecule congregation transitioning into 3D growth, or preferential orientation where pentacene molecules do not lay flat on the surface, but rather stand up out of the plane.

Conclusions

For thin pentacene layers on the Si-Ag-√3 our findings align closely with the previous work on this system. The initial nucleating layer of pentacene at RT is most likely largely disordered, increasing in order as the coverage increases. The next two layers grow ordered "brick wall' layers with the lattice structure loosely following the packing of the Si-Ag-√3 underneath. At low temperatures the 2^{nd} and 3^{rd} layers open up to Si(111)-Ag-(2√3 x 2√3) lattice that is 75% of coverage of the RT lattice. Following the nucleation of the 2^{nd} and 3^{rd} layer, transition to 3D island growth is observed. Islands have a slightly higher preference on nucleating at defects and step barriers. Nucleation is also observed on the terrace, but island

tend to cluster around defects. Overall, SK growth mechanism can be assigned to this surface system.

On the Ag-Si(111) system with 2 and 3 layer high Ag islands, no pentacene can be observed nucleating at RT. At low temperature initial, disordered wetting layer forms at temperatures over 70 K. Pentacene nucleates at the centers of the Ag islands and extends outward until confronted with a step edge barrier. At that stage, at 100 K any additional pentacene will start stacking in 3D growth. Past the initial wetting layer, we have observed an ordered layer growth forming long range pentacene chains. The additional layers start to nucleate as large 3D islands with low aspect ratio. Order in the pentacene layers can be observed in the 3D islands at 100 K.

More pertinently, there is no observable difference in the initial LT modes of the pentacene growth on 2 and 3 layer high Ag islands. Pentacene molecules can be found lying in a variety of configurations, in and out of the surface plane, but no long range order is observed at either 70 or 100 K in both 2 and 3 layer tall islands. However, in a mixed system, where 2 and 3 layer islands connect over a Si step, there appear to be subtle differences with pentacene preferentially nucleating at the 2 layer island. Even at 0.75ML the pentacene molecules form a 3D barrier at the interface of the 2 and 3 layer island following the flow of the Si step. This may imply different pentacene mobilities on the two Ag island surfaces.

Acknowledgements

This work was performed at the Ames Laboratory under contract number DE-AC02-07CH11358 with the U.S. Department of Energy. The document number assigned to this thesis/dissertation is IS-T 3050.

Bibliography

1. R. Ruiz, D. Choudhary, B. Nickel, T. Toccoli, K.-C. Chang, A. C. Mayer, P. Clancy, J. M. Blakely, R. L. Headrick, S. Iannotta and G. G. Malliaras, Chemistry of Materials **16** (23), 4497-4508 (2004).
2. T. W. Kelley, L. D. Boardman, T. D. Dunbar, D. V. Muyres, M. J. Pellerite and T. P. Smith, The Journal of Physical Chemistry B **107** (24), 5877-5881 (2003).
3. J. G. Laquindanum, H. E. Katz, A. J. Lovinger and A. Dodabalapur, Chemistry of Materials **8** (11), 2542-2544 (1996).
4. B. Ünal, A. Belianinov, P. A. Thiel and M. C. Tringides, Physical Review B **81** (8), 085411 (2010).
5. M. Hupalo, V. Yeh, L. Berbil-Bautista, S. Kremmer, E. Abram and M. C. Tringides, Physical Review B **64** (15), 155307 (2001).
6. W. B. Su, S. H. Chang, W. B. Jian, C. S. Chang, L. J. Chen and T. T. Tsong, Physical Review Letters **86** (22), 5116-5119 (2001).
7. K. S. Yong, Y. P. Zhang, S. W. Yang, P. Wu and G. Q. Xu, The Journal of Physical Chemistry C **111** (11), 4285-4293 (2007).

8. G. Hughes, J. Roche, D. Carty, T. Cafolla and K. E. Smith, Sante Fe, New Mexico, 2002 (unpublished).

9. M. Eremtchenko, R. Temirov, D. Bauer, J. A. Schaefer and F. S. Tautz, Physical Review B **72** (11), 115430 (2005).

10. D. B. Dougherty, W. Jin, W. G. Cullen, J. E. Reutt-Robey and S. W. Robey, The Journal of Physical Chemistry C **112** (51), 20334-20339 (2008).

11. D. Käfer and G. Witte, Chemical Physics Letters **442** (4-6), 376-383 (2007).

12. T. Jing and et al., Journal of Physics: Condensed Matter **19** (35), 356005 (2007).

13. P. Guaino, D. Carty, G. Hughes, P. Moriarty and A. A. Cafolla, Applied Surface Science **212-213**, 537-541 (2003).

14. B. Unal, F. Qin, Y. Han, D.-J. Liu, D. Jing, A. R. Layson, C. J. Jenks, J. W. Evans and P. A. Thiel, Physical Review B **76** (19), 195410 (2007).

15. L. Gavioli, K. R. Kimberlin, M. C. Tringides, J. F. Wendelken and Z. Zhang, Physical Review Letters **82** (1), 129-132 (1999).

16. I. Horcas, R. Fernandez, J. M. Gomez-Rodriguez, J. Colchero, J. Gomez-Herrero and A. M. Baro, Review of Scientific Instruments **78** (1), 013705-013708 (2007).

17. M. Böhringer, W.-D. Schneider and R. Berndt, Surface Science **408** (1–3), 72-85 (1998).

18. J. Teng, K. Wu, J. Guo and E. Wang, Surface Science **602** (22), 3510-3514 (2008).

19. G. Ph and et al., Journal of Physics: Condensed Matter **15** (38), S2693 (2003).

20. M. Pedio, B. Doyle, N. Mahne, A. Giglia, F. Borgatti, S. Nannarone, S. K. M. Henze, R. Temirov, F. S. Tautz, L. Casalis, R. Hudej, M. F. Danisman and B. Nickel, Applied Surface Science **254** (1), 103-107 (2007).

CHAPTER VI

GOLD ON Si(111)

Introduction

Gold surfaces are often used as substrates in studies of organic structures on surfaces, since they are stable in various biochemical environments and allow attachment of biomolecules through thiol groups. Thus a large number of studies of the interactions between molecules and Au surfaces have been performed[1]. Typically, surfaces of bulk Au crystals or thin films on mica are used. However, formation of well-ordered thin Au films on Si would be a step in the direction of direct integration of biosensors on wafers containing Si electronics[2]. Au on Si has been studied for over forty years. Despite the efforts of many research groups worldwide, there are still unanswered questions when it comes to this system. In this chapter we elucidate some of the remaining queries as well as pose new questions in this area. First reported studies of Au on the Si(111) surface were those of Bishop[3] et al., who performed an AES and LEED study. The authors reported a sharp ($\sqrt{3}x\sqrt{3}$)-R30° LEED pattern after annealing at 740℃ as well as a 1x1 pattern after heating to 1000℃. Due to incomplete understanding of the Si(111) surface at the time, Bishop's[3] work did not receive much attention. The topic was examined by Le Lay[4, 5] in 1977 and then again in 1983 but interest in Au on Si became intense after Takayanagi's[6] famous Si(111)-7x7 DAS structural solution in 1985. With a solid understanding of the underlying Si(111) – 7 x7, Au on Si(111) became of great interest as a model metal-semiconductor system.

Perhaps one of the reasons for the interest in Au on Si is the large number of surface phases and reconstructions this system has to offer in various coverage and temperature regimes. In the RT regime on the Si(111) – 7 x 7, no ordered structures are observed at the submonolayer range[7]. Gold initially nucleates on the FHUC[8] of the 7 x 7 and then transitions into 3D islands after the first (1 x 1) layer is complete. Overall, at RT, the growth mode is described as SK on the Si(111) – 7 x 7[7, 9]. Unlike Ag on Si, Au on Si will form a silicide eutectic at 636 K, although Kim[10] and Khramotsova[11] et al., report evidence of silicides at much lower temperature. The silicide formation at the Au-Si interface has been reported even at RT at coverage as low as 3-4 ML of Au deposited on the 7 x 7[12].

At higher temperatures, the Au/Si(111) phases are numerous and complex. The main surface reconstructions are listed as follows: (5 x 2) forming at coverage of 0.2ML – 1 ML at 300 – 800℃, (√3x√3)-R30° forming at 0.5ML and higher at 300 – 750℃, (6 x 6) initiating at 1 ML at 250℃ and stable up to 800℃ and (1 x 1) which is a high temperature 800℃ and higher, phase at all coverages[13-17]. Much time and effort has been expended to understand these structures and their interactions with one another. As shown in Plass'[13] work, the surface phases of Au on Si often coexist as one phase transitions to another. Over time particular attention was given to the (5 x 2)[18-29] and the (√3x√3)-R30° [11, 14, 16, 18, 30-39] surface reconstructions. There is much similarity in the referenced work on the structure of these phases, but no single standard for either (5 x 2) or the (√3x√3)-R30° structure has been established.

Binary studies of Ag + Au on Si(111), and in some cases Cu have been reported[14, 18, 34, 36, 38, 40-44], but are far less numerous than the volume amassed in individual studies of these noble

metals on Si(111). The very first study was done by Nogami[32] et al., and it served to explore submonolayer coverage of Au on the Ag-Si(111)-(√3x√3)-R30° and to report existence of a (√21 x √21) overlayer, initially observed with Ag on the Ag-Si(111)-(√3x√3)-R30°. Gunther[40] et al. followed suit with an excellent diffraction study that shed light on RT growth of Au on the Ag-Si-√3 and perhaps more importantly, started a discussion on Au silicides evident in their system. Yuhara[41] et al. continued to study mixed noble metals on Si(111) by introducing Cu to the Au and Ag overstrucures. Another study focused on conductivity of the Ag-Si(111)-(√3x√3)-R30° with noble metal adatoms was done by Tong[36] et al. in 2000. Their work proved to be instrumental in correlating 2DAG with low coverage (√21 x √21) noble metal overlayer and the resulting enhancement in surface conductivity. In 2001 Yuhara[37] et al. put forth another bimetal Ag Au study, this time Ag serving as an adsorbate on the Au-Si(111)-(√3x√3)-R30°. Many reconstructions thought to occur only for the pure Au-Si(111) were observed. The last pertinent study of Au and Ag on Si(111) was released in 2007, by Fukaya[38] et al. with the primary focus on the controversial (√21 x √21) overlayer analysis.

Experimental Details

All experiments were performed in an Omicron VT-STM, previously described elsewhere[45]. Chamber pressure did not exceed 1.0 x 10^{-10} mbar throughout the experiments. Si sample is a p-type doped with 3x10^{18} Boron atoms per cm^3 and a resistivity of 0.02 Ohm*cm. Si (111)-7x7 surface was prepared using well-known 1200K flashing and stepwise cooling methods. Au and Ag were deposited from a Mantis QUAD EV-S evaporator. Typical Ag flux was 0.0067ML/s, calibrated from Ag deposition on the clean Si(111) – 7x7, under the assumption

that the wetting layer has a Ag coverage of 0.5ML[46]. Typical Au flux was 0.0055ML/s, calibrated as for Ag, although unlike silver the wetting layer of Au completes at 1 ML[11]. The Si √3 surface was prepared by depositing 1ML of Ag on the 7x7 and annealing the sample for 2 minutes at 800K. We used W wire with electrochemically etched tips in STM. Images were processed using the WsXM software package[47].

Results and Interpretation

Au on the Si(111)-(7x7)

Initially, some studies of the Au alone on the Si(111)-(7x7) were performed as a benchmark check. Figure 1, Panel A is the clean Si(111)-(7x7), Panels B-D shows a Si(111)-7x7 surface after three consecutive rounds of RT Au deposition. In Panel B, 0.3 ML of Au is deposited, followed by another 0.3 ML and a final deposition bringing up the total coverage to 1 ML. Like Ag, Au is known to initially nucleate on the faulted half unit cells of the Si-7x7[8]. As additional gold is deposited, the unfaulted sites of the 7x7 will become covered as well. 1 ML of Au on the Si(111) corresponds to the 7.8 x 10^{14}atoms/cm^2, the atomic density of the Si(111)[11]. However, unlike Ag, Au will complete the first layer to a coverage of 1.0 ML before growing as 3D islands[7]. Ag, on the other hand, completes the wetting layer at 0.5 ML coverage and grows 3D islands with additional material[46]. Both Ag and Au at RT on Si(111)-7x7 grow in SK growth mode.

After annealing 1 ML of Au at 800K for 1.5min on the Si(111)-7x7, in Figure 2, we see a coexistence of Au/Si(√3x√3)-R30° (Panel A) along with the Au-Si(111) – (5 x 2) structure (Panel B -D). The coexistence of both phases has been reported by Plass[13] et al. in their comprehensive study of submonolayer phases of Au on Si(111)(Figure 5, Panel A), as well as

earlier pioneering studies of this system[4, 5, 15, 16]. Both, the Au/Si(√3x√3)-R30° and the Au-Si(111) – (5 x 2) surfaces have been studied extensively in the past[14, 18, 19, 48]. More recent studies[39] of the Au/Si(√3x√3)-R30° conclude that while the proposed honeycomb-chained-trimer model[31] is compatible with the simulated STM images, the calculated surface band structure shows discrepancy with the latest ARPES study done by Zhnag[49] et al. The model for the Au-Si(111) – 5x2 surface has recently been revisited by Erwin[29] et al. Erwin reports excellent agreement with ARPES and STM studies using a refined model, and they assert that the Au coverage is 0.6 ML in the Au-Si(111) – 5x2, as opposed to 0.4 ML as their[22] group had reported earlier in 2003.

Au on the Ag-Si(111)-(√3x√3)-R30°

Figure 3 shows 1 ML of Au on the Ag/Si(√3x√3)-R30°. Panel A is a 1x1 μm^2 area showing Au nucleating on the Ag-Si-√3. Panels B and C illustrate shapes and preferential nucleation areas of the Au islands. Larger islands appear highly faceted and positioned at the island/hole steps. There is evidence of Au on the grain boundary areas on Panels B and C, shown by arrows. Preferred nucleation at grain boundaries and at island-hole boundaries indicates significant surface mobility of Au. This notion is confirmed by Tong[36] et al., their study of noble thin films on the Ag-Si-√3 suggest that at coverage of ~0.1 ML noble metals exist as 2DAG before turning into √21 x √21 superstructures.

Gunther[40] et al. was the first to study Au on the Ag/Si(√3x√3)-R30° system beyond submonolayer coverage with PEM and LEED. They show that at RT Au has a profound effect on the Ag-Si bonding. According to Gunther, Ag 3d, Au 4f and Si 2p core level spectra show that at Au coverage of > 0.7 ML, Au readily substitutes for Ag in Ag-Si bond. We

confirm this result with Figure 4. Panels A - C feature a circular surface feature that is 100 nm wide and 10 nm tall. The structure is rooted ~3 nm below the surface (Panel D), surrounded by etched steps. See a schematic side view of a typical mount in Figure 8. Panels E-H in Figure 4, provide additional insight to what the mound structure look like on the surface. Mass displacement calculation of a mound similar to the one shown in Figure 4, Panel C show that the amount of material atop the surface is 27% larger than the volume of the surrounding hole. We calculated the volume of the empty hole (110nm wide at 1nm deep) the mound is sitting in at $9.5x10^3nm^3$. Through image flooding, we calculated the empty, subsurface volume of the hole to be $1.3x10^3nm^3$(the volume below the dotted red line in Figure 8 not taken up by the mound). The size of the mound on top of the surface is $4.7x10^3nm^3$. This brings the total volume of the mound to (4.5 + (9.5-1.3)) to $13x10^3nm^3$, or 30% larger than the volume of the hole it resides in. This analysis suggests the mound to be rich in material besides Si.

Pitting by Au on the Si(111) has previously been reported by Jing[50] et al. in their IR microscopy study. It is important to add that Au and Si are miscible and will form a silicide at 360℃ as seen in the Au-Si phase diagram in Figure 5 Panel B. Jing's observations of the gold silicide at RT, along with our, similar observations of the silicide on the Ag-Si-√3 at RT can be explained by results from Kim[10] et al.. It is however, important to add that Jing used a bonder to treat the Au-Si at 400°C. According to Kim's work, at nanoscale sized Au and Si domains, there is a downward shift as large as 240°C shift in the transition lowering the silicide formation. This work is further supported by Matthews[51] and Silva[52] et al., in their work on Si deposited on Au(111) surfaces at elevated at RT. Rota[53] et al., report Au islands preferentially nucleating at step edges of Si(111) – 7x7 at temperatures ranging 340-430℃. In

our work with Au on Ag-Si-√3 at 200℃ we see a result similar to Rota's[53] work coupled with original studies done by Gunther[40]. This result is shown in Figure 6, Panel B. The image shows that Au attacks step bunching areas of the Ag-Si-√3 that are Si rich. In the process, the Ag-Si bond is disrupted by silicide formation and the Ag-√3 network is destroyed. Figure 6 Panel A shows large 3D Au islands nucleating on the island/hole steps of the Ag-√3, similar to high temperature Au behavior on the Si(111) – 7x7[53, 54]. Annealing 1.25 ML of Au on the Ag-Si-√3 at 300˚C gives similar results, shown in Figure 7. Panel A is the surface prior to annealing. The Au islands are the dominating feature on the surface with larger islands sitting on the island/hole interfaces. The presence of the silicide is also evident. Post anneal, Panels B-D, the number of islands is drastically decreased by two orders of magnitude, the number of silicide forming holes is increased. The islands are much taller, wider and clearly show Au(111) hexagonal faceting.

There are remaining questions about the nature of the Au-Si structure itself. One study of Au on Si(111) - 7x7 at RT, addressing the nature of the silicide, has been done by Hoshino[55] et al. using MEIS combined with PES. According to their findings, the Au-silicide layer starts forming at 0.31 ML of Au at RT. For coverage above 5.2 ML of Au the surface is a stable Au_3Si_2 with a lateral density of 1.5×10^{15} molecules/cm^2 in the top plane and an underlying metallic Au layer which contains Si atoms probably trapped in the boundaries of fine Au clusters. With increasing Au coverage from 5.2 to 12.8 ML, the thickness of the Au_3Si_2 layer does not change, while thickness of the underlying Au layer increases and the concentration of Si in the Au layer decreases linearly. Total amount of Si atoms contained in the Au_3Si_2 and underlying Au layers coincides with the number of Si atoms constituting the 7 × 7 reconstruction.

Au on Si(111) – 7 x 7 silicides at higher temperature 800 < T < 930 K have been studied by Ferralis[56] et al. using LEEM. Although this does not relate directly to the experiments we have performed, it provides insight into the behavior of this surface at the temperatures higher than we studied. These authors assert that at temperature above 636 K the composition of the eutectic melt of Au-Si readjusts following the eutectic liquidus shown in Figure 5 Panel B. At equilibrium, 636 K, the Au-rich eutectic has a composition of $Au_{81}Si_{19}$ The solubility of gold in Si is negligible and the AuSi drop does not wet the Si surface[57]. In the dewetting equilibrium, an isolated liquid AuSi drop coexists with a thin adsorbed Au film, uniformly spread over the Si substrate. This film consists of a crystalline monolayer of gold silicide (i.e., a reconstruction of the Si surface in which Au atoms form three chemical bonds with √3 x √3 structure), upon which a second layer of mobile gold atoms can assemble at high temperature with varying degrees of order[30, 35].

Conclusions

Our data for Au alone one the Si(111)-(7x7) are consistent with the results of many previous studies of Au on Si(111). At RT in the submonolayer range, Au starts out preferentially nucleating on the FHUC of the Si(111) - 7 x 7. As 1 ML of Au is approached, a 1x1 Au surface forms. Annealing 1 ML Au at 800 K results in Au – Si(111) – 5 x 2 in which there are topological features of the Au - Si(√3x√3)-R30°. RT deposition of 1 ML of Au atop the Ag - Si(√3x√3)-R30° results in small faceted islands preferentially nucleating at the steps of the √3 island/hole interface. At the same time Au starts displacing Ag atoms and breaking

Ag-Si bonds. As soon as the top layer of the Ag-Si-√3 is penetrated, the Au continues to consume Si underneath getting to depths of 2-3 nm. The most likely candidate for the silicide is Au_3Si_2. Ag and the silicide form mounds around the area where Au penetrates into the Si. The role and the level of intermixing of the Ag in the silicide remains an open question. Annealing 1 ML of Au atop the Ag - Si(√3x√3)-R30° at 500 > T > 600 K for 1.5 mins results in a surface where Au islands are highly faceted, 3D structures reaching 200 nm footprint in diameter and 20 – 30 nm in height. The frequency of the Au etched holes is also strongly increased. The holes are always found on either island/hole steps of the Ag-Si-√3, or at the Si rich step bunching sites. The mounds are usually 2-3 nm in depth and up to 100 nm wide. They are usually surrounded by material in various configurations and the amount of material is consistently 30-40% extra than the sub surface volume of the hole.

Acknowledgements

This work was performed at the Ames Laboratory under contract number DE-AC02-07CH11358 with the U.S. Department of Energy. The document number assigned to this thesis/dissertation is IS-T 3050.

Bibliography

1. S. Frank, Progress in Surface Science **65** (5–8), 151-257 (2000).

2. H. B. Akkerman, P. W. M. Blom, D. M. de Leeuw and B. de Boer, Nature **441** (7089), 69-72 (2006).

3. H. E. Bishop and J. C. Rivière, Journal of Physics D: Applied Physics **2** (12), 1635 (1969).

4. M. M. G. Le Lay, R. Kern, in *Surface Science* (1977), Vol. 65, pp. 271.

5. L. L. G, Surface Science **132** (1–3), 169-204 (1983).

6. K. Takayanagi, Y. Tanishiro, S. Takahashi and M. Takahashi, Surface Science **164** (2–3), 367-392 (1985).

7. A. Endo and S. Ino, Japanese Journal of Applied Physics Part 1-Regular Papers Short Notes & Review Papers **32** (10), 4718-4725 (1993).

8. Y. Zhou, Q.-H. Wu, C. Zhou, H. Zhang, H. Zhan and J. Kang, Surface Science **602** (2), 638-643 (2008).

9. J. H. Kim, G. Yang, S. Yang and A. H. Weiss, Surface Science **475** (1-3), 37-46 (2001).

10. B. J. Kim, J. Tersoff, C. Y. Wen, M. C. Reuter, E. A. Stach and F. M. Ross, Physical Review Letters **103** (15), 155701 (2009).

11. E. A. Khramtsova, H. Sakai, K. Hayashi and A. Ichimiya, Surface Science **433**, 405-409 (1999).

12. J. J. Yeh, J. Hwang, K. Bertness, D. J. Friedman, R. Cao and I. Lindau, Physical Review Letters **70** (24), 3768-3771 (1993).

13. R. Plass and L. D. Marks, Surface Science **380** (2-3), 497-506 (1997).

14. A. Ichimiya, H. Nomura, Y. Ito and H. Iwashige, Journal of Crystal Growth **150** (1-4), 1169-1174 (1995).

15. S. Takahashi, Y. Tanishiro and K. Takayanagi, Surface Science **242** (1–3), 73-80 (1991).

16. J. Yuhara, M. Inoue and K. Morita, Journal of Vacuum Science & Technology A: Vacuum, Surfaces, and Films **10** (6), 3486-3492 (1992).

17. A. A. S. V. G. Lifshits, A. V. Zotov, (1994).

18. A. Endo and S. Ino, Surface Science **346** (1-3), 40-48 (1996).

19. T. Hasegawa, S. Hosoki and K. Yagi, Surface Science **355** (1-3), L295-L299 (1996).

20. R. Losio, K. N. Altmann and F. J. Himpsel, Physical Review Letters **85** (4), 808-811 (2000).

21. S. C. Erwin, Physical Review Letters **91** (20) (2003).

22. S. C. Erwin, Physical Review Letters **91** (20), 206101 (2003).

23. M. H. Kang and J. Y. Lee, Surface Science **531** (1), 1-7 (2003).

24. A. Kirakosian, J. N. Crain, J. L. Lin, J. L. McChesney, D. Y. Petrovykh, F. J. Himpsel and R. Bennewitz, Surface Science **532**, 928-933 (2003).

25. S. Riikonen and D. Sanchez-Portal, Physical Review B **71** (23) (2005).

26. H. S. Yoon, J. E. Lee, S. J. Park, I. W. Lyo and M. H. Kang, Physical Review B **72** (15) (2005).

27. Y. Iwasawa, W. Voegeli, T. Shirasawa, K. Sekiguchi, T. Nojima, R. Yoshida, T. Takahashi, M. Matsumoto, T. Okano, K. Akimoto, H. Kawata and H. Sugiyama, Applied Surface Science **254** (23), 7803-7806 (2008).

28. F. Zheng, I. Barke, X. Liu and F. J. Himpsel, Nanotechnology **19** (44) (2008).

29. S. C. Erwin, I. Barke and F. J. Himpsel, Physical Review B **80** (15) (2009).

30. J. Nogami, A. A. Baski and C. F. Quate, Physical Review Letters **65** (17), 2211-2211 (1990).

31. Y. G. Ding, C. T. Chan and K. M. Ho, Surface Science **275** (3), L691-L696 (1992).

32. J. Nogami, K. J. Wan and X. F. Lin, Surface Science **306** (1-2), 81-86 (1994).

33. R. Plass and L. D. Marks, Surface Science **357** (1-3), 42-46 (1996).

34. J. Yuhara, D. Ishikawa and K. Morita, Applied Surface Science **117**, 94-98 (1997).

35. T. Nagao, S. Hasegawa, K. Tsuchie, S. Ino, C. Voges, G. Klos, H. Pfnür and M. Henzler, Physical Review B **57** (16), 10100-10109 (1998).

36. X. Tong, C. S. Jiang, K. Horikoshi and S. Hasegawa, Surface Science **449** (1-3), 125-134 (2000).

37. J. Yuhara, K. Soda and K. Morita, Surface Science **482**, 32-38 (2001).

38. Y. Fukaya, A. Kawasuso and A. Ichimiya, Surface Science **601** (22), 5187-5191 (2007).

39. J. Y. Lee and M. H. Kang, Journal of the Korean Physical Society **53** (6), 3671-3674 (2008).

40. S. Gunther, A. Kolmakov, J. Kovac, L. Casalis, L. Gregoratti, M. Marsi and M. Kiskinova, Surface Science **377** (1-3), 145-149 (1997).

41. J. Yuhara and K. Morita, Applied Surface Science **123**, 56-60 (1998).

42. K. Pedersen, T. B. Kristensen, T. G. Pedersen, T. Jensen, P. Morgen, Z. S. Li and S. V. Hoffmann, Surface Science **523** (1-2), 21-29 (2003).

43. S. Iaiche, N. Benouattas, A. Bouabellou, L. Osmani and L. Salik, Microelectronic Engineering **81** (2-4), 349-352 (2005).

44. Y. Liu, M. Li and Y. Suo, Surface Science **600** (24), 5117-5122 (2006).

45. B. Unal, F. Qin, Y. Han, D.-J. Liu, D. Jing, A. R. Layson, C. J. Jenks, J. W. Evans and P. A. Thiel, Physical Review B **76** (19), 195410 (2007).

46. L. Gavioli, K. R. Kimberlin, M. C. Tringides, J. F. Wendelken and Z. Zhang, Physical Review Letters **82** (1), 129-132 (1999).

47. I. Horcas, R. Fernandez, J. M. Gomez-Rodriguez, J. Colchero, J. Gomez-Herrero and A. M. Baro, Review of Scientific Instruments **78** (1), 013705-013708 (2007).

48. K. Fuchigami and A. Ichimiya, Surface Science **357** (1-3), 937-942 (1996).

49. H. M. Zhang, T. Balasubramanian and R. I. G. Uhrberg, Physical Review B **66** (16), 165402 (2002).

50. E. Jing, B. Xiong and Y. Wang, Materials Letters **64** (7), 827-829 (2010).

51. T. S. Matthews, C. Sawyer, D. F. Ogletree, Z. Liliental-Weber, D. C. Chrzan and J. Wu, Physical Review Letters **108** (9), 096102 (2012).

52. A. Silva, K. Pedersen, L. Diekhoner, P. Morgen and Z. Li, 2007 (unpublished).

53. A. Rota, A. Martinez-Gil, G. Agnus, E. Moyen, T. Maroutian, B. Bartenlian, R. Megy, M. Hanbucken and P. Beauvillain, Surface Science **600** (6), 1207-1212 (2006).

54. S. Klages, M. Schock, C. Surgers and H. Von Lohneysen, Journal of Low Temperature Physics **137** (3-4), 509-522 (2004).

55. Y. Hoshino, Y. Kitsudo, M. Iwami and Y. Kido, Surface Science **602** (12), 2089-2095 (2008).

56. N. Ferralis, F. El Gabaly, A. K. Schmid, R. Maboudian and C. Carraro, Physical Review Letters **103** (25) (2009).

57. N. Ferralis, R. Maboudian and C. Carraro, Journal of the American Chemical Society **130** (8), 2681-2685 (2008).

CHAPTER VII

THICK Ag FILMS ON Ag-Si(111)-(√3 x √3)R30°

Introduction

The Ag-Si(111)-(√3 x √3)R30° surface has been an object of many investigations, first one starting in 1980's.[1-73] This surface forms after 1 ML of Ag is deposited on the Si(111)-7x7 in temperature range 500 – 800 K. Starting from a Si(111)-7x7 surface, the areal density of Si changes upon conversion to the √3, i.e. the Si surface reconstructs. The consequent mass transfer leads the √3 to form "islands" and "holes," above and below the original (7x7) level, respectively.[2, 3, 5-8, 74] Two widely accepted models for this system are HCT and IET[75-79]. Two models are closely related, Zhang[67] et al., report the coexistence of both phases at RT. There have been some previous studies of Ag deposition atop the Ag-Si-√3 at temperature above or at RT[80, 81 13, 82-84]. LeLay[80] reported that LEED pattern from the substrate √3 remains until Ag coverage is well above 3 ML. Later, Gasparov and Riehl-Chudoba replicated this result, and using STM and XPS, they concluded that the √3 LEED pattern remains because Ag exists as metallic islands, separated by flat, clean √3 terraces.[81] Venables' group carried out extensive investigations of the Ag islands that form on the √3.[82-84] They concluded that Ag can diffuse over distances on the order of 50 μm at 770 K. Oshima et al.,[54] studied 6 ML Ag islands deposited on the Ag-Si-√3 at RT using TEM. They report seeing two types of Ag islands, 'striped islands and Ag(1-34) islands. The group refers to striped islands as those growing parallel to the Si(110) direction and having alternating dark and light spots. We believe those to be islands grown at the step bunching sites, as those do have a preference of

growing parallel to the steps in [110] direction. Ag(1-34) islands are the rough Ag patches we also find in our work. Authors report seeing reflection spots for the Ag(-1-1-1) in those structures. In our STM work we see areas of rough Ag islands that reconstruct into flat, faceted Ag(111) films. In our work these films become more prevalent as the annealing temperature increases. These notions are confirmed by Oshima's[56] 2002 TED study.

A Second-harmonic generation study was done by Deng et al[85]., on low 0.02 ML coverage of Ag on the Ag-Si-√3 at RT and at 630 K. For both RT and 630 K even a relatively small amount of additional Ag resulted in a decrease of the SH intensity by half. This result is attributed to by an increase of the 2DAG density and nucleation following a supersaturation density. This result, although hard for us to test in a pure Ag-Si-√3 study, is somewhat confirmed in a study of Ag on 9:1 ratio mixed domain of Si(111)-7x7 and Ag-Si-√3.

On the computational front, Aizawa and Tsukada showed that individual Ag atoms preferentially adsorb in the Ag triangles, not the Si triangles, of the √3.[86] Jeong and Jeong confirmed this result, and also showed that a Ag atom on a Ag-atom triangle site can immerse itself in the √3 structure, i.e. it becomes essentially coplanar with Ag in the √3.[87] Jeong and Jeong also studied Ag diffusion across the √3, showing that an exchange mechanism has a far lower activation barrier than direct hopping–1.78 vs. 0.22 eV, respectively.[88] Exchange involves replacement of a Ag atom within the √3, at a point where two of the Ag-atom triangles share a vertex.[88]

In this study we systematically investigate the behavior of thick Ag films, 10, 20 ML, on the Ag-Si-√3 in the temperature range of 300-850 K. We look at effects of annealing post and during deposition at different anneal times. We investigate island morphology, mobility and

nucleation preference. The results are compared to the behavior of additional thick Ag films annealed on a mixed domain system 9:1 ratio Ag-Si-√3 and Si(111)-7x7.

Experimental

All experiments were performed in an Omicron VT-STM, previously described elsewhere[89]. Chamber pressure did not exceed 1.0 x 10^{-10} mbar throughout the experiments. Si sample is a p-type doped with 3x10^{18} Boron atoms per cm^3 and a resistivity of 0.02 Ohm*cm. Si (111)-7x7 surface was prepared using well-known 1200K flashing and stepwise cooling methods. Ag was deposited from a Mantis QUAD EV-S evaporator. Typical Ag flux was 0.0067ML/s, calibrated from Ag deposition on the clean Si(111) – 7x7, under the assumption that the wetting layer has a Ag coverage of 0.5ML[90]. The Si √3 surface was prepared by depositing 1ML of Ag on the 7x7 and annealing the sample for 2 minutes at 800K. We used W wire with electrochemically etched tips in STM. Images were processed using the WsXM software package[91].

Results and Interpretation

Ag on Ag-Si(111)-(√3 x √3)R30°

Figure 1 Panel A shows a clean Ag-Si(111)-(√3 x √3)R30°. This structure is best described by IET[41, 92], or as an asymmetric version of HCT[93]. There are reports describing a reversible transition of IET to HCT at RT, due to thermal fluctuations.[53, 63, 67, 79] Panel B shows a

differentiated image of a high step density site after 10 ML of Ag has been deposited at RT. Approximating the island footprint to be circular in shape, the average diameter of the Ag islands is ~100 nm. The average height of the islands is 2-3nm, suggesting a very high aspect ratio. Our previous work[72] has shown that at RT there is no Ag nucleation on the Ag-Si(111)-($\sqrt{3}$ x $\sqrt{3}$)R30° terraces, instead Ag preferentially nucleates on the step bunching sites or defects in the Ag-Si-$\sqrt{3}$. Panel C is a close-up image of the steps on the Ag-Si-$\sqrt{3}$ surface. The steps are converted to Ag-Si-$\sqrt{3}$ as well. Panel D is a differentiated image illustrating the details of Ag island morphology at step bunching sites. These islands are growing in the [110] direction parallel to the Ag-Si-$\sqrt{3}$ step edges. These islands have features of both 'striped islands' and 'Ag(1-34) islands as described by Oshima et al.[54]

Figure 2 Panels A-D feature 10 ML of Ag on the Ag-Si-$\sqrt{3}$ surface post a 5 minute 550 K anneal. Panels A, B show the Ag island behavior on scale of 1x1um^2 and 250x250nm^2 respectively. Note islands no longer appear as individual mounds at the step bunches as seen in Figure 1 Panel B. Instead, islands seem to move around the vicinal surface created at the steps, and coagulate around the areas of Ag-Si-$\sqrt{3}$ step sites. Figure 2 Panel B shows islands that are extending even onto parts of the terrace. While the terraces themselves remain free of Ag islands, the increased mobility of the Ag allows for some island nucleation on edges of terraces that are adjacent to areas of high defect density. Panel C features a high resolution image of the Ag island morphology. Both, Panels B and C illustrate high faceting step-like features in the Ag islands themselves. The heights of these steps are 2-6 Å. Ag bulk lattice constant is 2.89 Å, this suggest that the Ag island step heights are mono or bi atomic in

nature. Panel D is a high resolution image featuring the HCT structure of the Ag-Si-√3. No notable difference in the structure is observed, as compared to the clean Ag-Si-√3 at RT.

Figure 3 is a compilation of images showing 10 ML of Ag on Ag-Si-√3 post 5 minute 600 K anneal. Panels A and B feature 1x1um^2 and 500x500nm^2 range behavior of Ag islands at areas of high step density. No notable change is observed at this scale when compared to the 500 K anneal. Compared to the RT images, these islands are more elongated along the direction of the Si steps. Panels C and D show magnified images of a high density step bunching sites in the Ag-Si-√3. Note the subtle differences in the step decoration in Panel D emphasized by a blue square. In the center, the steps that are ~5 nm wide are not fully covered by the Ag-Si-√3. The image suggests that the edge of the step inside the blue square is a Si step that has either didn't finish the √3 growth, or has had some Ag desorb as a result of a 600 K anneal. The later results seems more plausible based on our studies of Ag-Si-√3 island/hole flow[94] as well as ~1nm wide spherical step decorations that are likely to be small Ag clusters.

Figure 4 is 10 ML of Ag on the Ag-Si-√3 post 5 minute 650 K anneal. Panels A, B display very high density step areas, and similar to results for 500 and 550 K anneals. Note the amount of Ag islands in the stepped sites consistently recedes with an increase in anneal temperature, leaving fewer islands behind. The islands themselves change in size and morphology. At RT the islands are larger and more faceted, here the islands are elongated and rectangular. Panels C and D illustrate additional Ag overlayer changes as a result of a 650 K anneal. In Panel C, the left side of the image is dominated by a flat top island, 3 nm in height. In the same panel, on the opposite side we see highly faceted, very smooth, flat

overlayer terraces that are most likely Ag(111). Separating two regions is a circular foot print island that is 50 nm wide and 4 nm tall, most reminiscent of the RT island morphology. In Panel D, we see another flat top island featuring Ag faceting at top layers, as well as disordered Ag phase that stretches across the middle terrace region into the upper and lower step bunching sites.

Increasing anneal temperature to 700 K for 5 minutes, incites further changes into the 10 ML thick Ag overlayer. Figure 5 Panel A is a 1x1um^2 area that is nearly completely covered by highly faceted islands that are flat tops and are 3 nm in height. This island behavior is drastically different from RT and substantially different from the 500-650 K anneals. Perhaps at 700 K the Ag becomes so mobile that the areas of high Ag density form a nearly perfectly ordered overlayer film of constant height to relieve stress. These islands, or more accurately – film slabs, are much larger compared to their RT counterparts; some larger than 200 nm in the foot print diameter. Panel B shows what the interface between these very large, highly faceted Ag slabs looks like. Here Ag is more disordered between the slabs, and also taller by 2 nm. Panels C and D are close-ups of the stepped areas. In panel C, where one can distinguish the island/hole signature of the Ag-Si-√3, there are no islands, unlike in the RT case. In Panel D, there are definitely some islands left behind on the steps, however it is unclear whether those steps are Ag-Si-√3 or just Si. The evidence for the possible dichotomy is that the islands are not uniformly distributed over the steps, rather two of the steps contain the majority of the islands. This implies that Ag-Si-√3 and Si steps coexist, evident in Figure 3 Panel D, and Si presence is enhanced by increase in anneal temperature. Additional insight into this system is given in Figure 9 Panels A-D. The main difference between Figure 5 and

Figure 9 is the annealing process. In Figure 5 we deposit 10 ML of Ag on Ag-Si-√3 and anneal for 5 minutes. In Figure 9, the Ag-Si-√3 is kept at 700 K as 10 ML of Ag are being deposited (~40 minutes at the flux conditions used). While we do not have any direct confirmation of Ag desorbing from the Ag-Si-√3 in Figure 5, Figure 9 Panel A provides ample evidence. Dark spots in the image are hallmarks of desorbed Ag atoms from the HCT trimers. This confirms the notion that in Figure 5 Panel D small islands are most likely Ag on the Si steps. Figure 9 Panel B is a great insight for the Ag morphology at the 700 K anneal. Much like Figure 5 Panel A, both show very large flat Ag islands of high aspect ratio, with some disordered Ag filling in the gaps between the islands. Mainly the difference between Figure 9 Panel B and Figure 5 Panel A is in Figure 5 the Ag seems to lie on a flat part of Ag-Si-√3 underneath, whereas in Figure 9 Panel B the Ag islands span over a highly stepped Ag-Si-√3 underneath.

The idea of Si and Ag-Si-√3 coexisting (even with the presence of all the excess Ag!) and the system being thermally driven towards more exposed Si in the steps, is well supported by Figure 6 Panels C and D. In these images it is clear as we increase anneal temperature to 750 K for 5 minutes, Ag begins to desorb from the Ag-Si-√3 surface. Panels A and B show large scale changes on the surface. As noted previously, little Ag remains in islands on step bunches. Rather, Ag seems to aggregate in vast amounts on certain areas of the sample – presumably close to areas of high defect density. As Ag nucleates on the defects, additional mobile Ag atoms diffuse over distances of up to 50 um[82-84] and attach forming expansive Ag-covered areas that are either flat and faceted islands of high aspect ratio (Figure 5 Panel A), or highly rough, disordered, 3D Ag ‘rough patches.’

As anneal temperature increase to 800 K, at the 2 minute anneal mark, Ag forms Ag-Si-√3 when deposited on the Si(111)-(7x7). The resulting Ag-Si-√3 is a 1:1 ratio of islands and holes[94]. Annealing for longer than 2 minutes results in Ag desorption form the Ag-Si-√3 and marks the beginning of transition to formation of the Si(111)-Ag-(3 x 1)[26, 92, 95-97]. In Figure 7 Panel D, we can see the evidence of the Ag desorbing from the Ag-Si-√3. Panel B shows an island with a footprint diameter of ~200nm, consistent with data for 700 K anneals. Panel A is an area of Ag aggregation that features both, large, highly ordered, faceted islands alongside with smaller, seemingly less ordered Ag clusters that decorate the areas in betwixt.

Taking the anneal temperature a step further to 850 K for 5 minutes, results in a surface with little Ag existing as individual islands on the surface. Figure 8 Panel A-C show the Ag-Si-√3 virtually void of the types of islands we observed at RT. The surface is mostly clean Ag-Si-√3 terraces, with areas, such as Panel D, where Ag is present in large quantities as rough, disordered 3D features.

In summary 10 ML thick Ag films on Ag-Si-√3 grow at RT grow via Volmer-Weber growth mode. Islands nucleate at defect sites of the Ag-Si-√3 as well as vicinal surfaces provided by high step density areas. As the film is annealed past up to 650 K 3D islands move and rearrange at areas of maximum defect density. Past 700K the islands start to coagulate together forming a highly faceted, closing, flat Ag film. This process continues past 800 K, the Ag desorption from the Ag-Si-√3 is evident, although no Ag 3 x 1 formation is observed, presumably due to high concentration of additional, free Ag on the surface.

Ag on Si(111) – (7x7) + Ag-Si(111)-(√3 x √3)R30°

Prior to running a controlled study of 10 ML Ag overlayer on the Ag-Si-√3 annealed in the 550-850 K range, we experimented with higher Ag coverage and shorter anneals in the 300-600 K region on an incompletely converted Ag-Si-√3. Figures 10 – 12 serve to illustrate the results of those experiments.

Figure 10 Panel A shows the clean starting surface. The surface is a Si(111)-(7x7) with 0.9 ML of Ag annealed at 800 K for 2 minutes. The result is a hybrid surface that features the Ag-Si-√3 island/hole morphology alongside the Si(111)-(7x7) sites. 90% of the surface converted to the Ag-Si-√3. Hence the surface can be denoted as 9:1 ratio hybrid of Ag-Si-√3 and Si(111)-(7x7). Since Si(111)-(7x7) acts as a capture site for the diffusing Ag we wanted study the effects of the anneal, explore any interesting morphology that may arise and get more insight in nucleation and island mobility at high temperature. Panel B is a $1x1um^2$ overview of the surface post 20 ML Ag deposition at RT. Note that the terrace still remains largely unadultered by Ag which still exhibits preferential nucleation at stepped sites. However, in Panel B there appears to be some Ag spillover onto the terrace. One would expect the Si(111)-(7x7) sites to be evenly distributed on the Ag-Si-√3, if the Ag islands take hold on the Si(111)-(7x7) and then grow outward we should see the Ag-Si-√3 terraces feature an even distribution of islands as well. Panels C and D are the surface post 350 K 5 second anneal. Panel C shows islands that are infringing upon the terrace without any large defects sites seen in the image. Based on the results presented in the *Ag on Ag-Si(111)-(√3 x √3)R30°* section above, the crux for explanation of Ag islands on the terrace in this system may also be in the Ag mobility. At RT Ag already exists as 2DAG, annealing at 350 K just enhances

the adatom mobility. As the Ag moves over the surface it'll nucleate on the Si(111)-(7x7) as well as step bunches (Panel D) and other defects. Ag on the 7x7 will capture additional Ag adatoms until some maximum is reached and equilibrium in adatom exchange is established. At this point any Ag in 2DAG will have to find more defects or other Ag islands. Captured Ag atoms at nearby 7x7 sites, which have not reached adatom exchange equilibrium, are prime candidates for the 2DAG. This may explain why we see some islands on the terraces, but not as evenly distributed population but instead, clusters close to defects.

Based on the assumptions made in the previous paragraph we should see a continuation or an enhancement of the described behavior as we anneal at higher temperature. This is indeed the effect as seen in Figure 11. Panels E, F are 20 ML of Ag post 5 second 450 K anneal. The behavior of the islands on steps (Panel F) is largely unchanged from what we saw in the previous section. However, Panel E, shows Ag clustering on what once again appears to be a largely defect free area of a terrace. In panels G, H the surface was annealed at 500 K for 5 seconds. In Panel G we see evidence of a closed faceted Ag film (highlighted by a blue rectangle) very similar in nature to what we saw in Figure 5 Panel A, on the pure Ag-Si-$\sqrt{3}$. The film and the adjacent Ag islands sit on a flat surface with parts of a terrace on the right hand site. Since there are many more rough islands than the area the Ag film covers, it is reasonable to assume that the film forms after the formation of the islands. This furthers the of Ag capturing at the Si(111)-(7x7) and island cluster into the terrace. There is a large source of Ag around the rough Ag islands, so converting to a Ag(111) could be more energetically favorable. Panel H shows many faceted islands on the step sites in the lower left corner, as well as islands extending onto the terrace, through the mechanism described above.

Figure 12 Panels I and J are images of the surface post 5 second 550 K anneal. Panel I shows step sites of medium density. In concordance with the results on the pure Ag-Si-√3 surface the island density is reduced post anneal. Panel J, shows another Ag cluster formation that is penetrating on the mixed domain surface. This consistency is further supported by the results post 600 K anneal featured in Panels K, L. Panel K is a closed, flat, highly faceted Ag film that is 3 nm in height. The Ag film is once again is on a flat surface, suggesting it is a product of Ag migration by Si(111)-(7x7) capture and clustering, followed by a conversion to the Ag(111) that is probably thermally activated. Panel L shows a number of high density step sites that have islands growing on the steps as well as the terraces.

Thick Ag films on a mixed Ag-Si-√3 and Si(111)-(7x7), (in ratio of 9:1), annealed at 350 – 600 K for 5 seconds, exhibit analogous morphology to the results of the pure Ag-Si-√3 in the similar temperature range presented above. However we observe island clustering on terraces as well as Ag(111) film formation at 500 K, 200 K lower than in the pure Ag-Si-√3 system. We propose the following explanation for the observed phenomena. As Ag mobility is enhanced by increasing anneal temperature, Ag adatoms are captured by the Si(111) – (7x7) sites that serve as nucleation centers for the rough 3D islands. As those islands reach mass equilibrium, adatoms are forced to find other nucleation sites. The sites that are nearby are the best candidates, resulting in island clustering on the terrace. If the Ag adatom does not get captured by a nearby site, it quickly diffuses on the surface past the size resolution limit of the STM image capture. Since there is always a high concentration of Ag at the 3D islands, conversion to a thick faceted Ag(111) film is enhanced. As the anneal temperature increases

the film forms more readily on the terraces, effectively preferring mostly the terrace, as it now has a 10% enhancement in defect areas.

Conclusions

10 ML thick Ag films on pure Ag-Si-√3 grow at RT grow via Volmer-Weber growth mode. Islands nucleate at defect sites of the Ag-Si-√3 as well as vicinal surfaces provided by high step density areas. As the film is annealed past up to 650 K, highly mobile Ag allows the 3D islands to move and rearrange at areas of maximum defect density. Past 700K the islands start to coagulate together forming a highly faceted, closing, flat Ag film. This process continues past 800 K, the Ag desorption from the Ag-Si-√3 is evident, although no Ag 3 x 1 formation is observed, presumably due to high concentration of additional, free Ag on the surface.

Thick Ag films on a mixed Ag-Si-√3 and Si(111)-(7x7), (in ratio of 9:1), annealed for 5 seconds at 350 – 600 K, exhibit analogous morphology to the results of the pure Ag-Si-√3 system in the similar temperature range. We observe island clustering on terraces as well as Ag(111) film formation at 500 K, 200 K lower than in the pure Ag-Si-√3 system. We propose the following explanation for the observed phenomena. As Ag mobility is enhanced by increasing anneal temperature, Ag adatoms are captured by the Si(111) – (7x7) sites that serve as nucleation centers for the rough 3D islands. As those islands reach mass equilibrium, adatoms are forced to find other nucleation sites. The sites that are nearby are the best candidates, resulting in island clustering on the terrace. If the Ag adatom does not get

captured by a nearby site, it quickly diffuses on the surface past the size resolution limit of the STM image capture. Since there is always a high concentration of Ag at the 3D islands, conversion to a thick faceted Ag(111) film is enhanced. As the anneal temperature increases the film forms more readily on the terraces, effectively preferring mostly the terrace, as it now has a 10% enhancement in defect areas.

Acknowledgments

This work was performed at the Ames Laboratory under contract number DE-AC02-07CH11358 with the U.S. Department of Energy. The document number assigned to this thesis/dissertation is IS-T 3050.

Bibliography

1. V. Barone, G. Delre, G. Lelay and R. Kern, Surface Science **99** (1), 223-232 (1980).
2. A. Shibata, Y. Kimura and K. Takayanagi, Surf. Sci. **275**, L697-L701 (1992).
3. A. Shibata and K. Takayanagi, Jpn. J. App. Phys. **32**, 1385-1388 (1993).
4. V. G. Lifshits, A. A. Saranin and A. V. Zotov, *Surface Phases on Silicon: Preparation, Structures, and Properties*. (John Wiley & Sons, Inc., West Sussex, England, 1994).
5. A. Shibata, Y. Kimura and K. Takayanagi, Surf. Sci. **303**, 161-170 (1994).

6. A. Shibata, H. Kimura and K. Takayanagi, J. Vac. Sci. Technol. **B 12** (3), 2026-2030 (1994).

7. K. J. Wan, X. F. Lin and J. Nogami, Phys. Rev. B **47**, 13700-13712 (1993).

8. D. W. McComb, D. J. Moffatt, P. A. Hackett, B. R. Williams and B. F. Mason, Phys. Rev. B **49**, 17139-17148 (1994).

9. Y. Gotoh, A. Chauvet, M. Manneville and R. Kern, Japanese Journal of Applied Physics **20** (12), L853-L855 (1981).

10. T. Takahashi, S. Nakatani, N. Okamoto, T. Ishikawa and S. Kikuta, Japanese Journal of Applied Physics Part 2-Letters **27** (5), L753-L755 (1988).

11. T. Takahashi, S. Nakatani, N. Okamoto, T. Ishikawa and S. Kikuta, Review of Scientific Instruments **60** (7), 2365-2368 (1989).

12. E. L. Bullock, G. S. Herman, M. Yamada, D. J. Friedman and C. S. Fadley, Physical Review B **41** (3), 1703-1706 (1990).

13. B. Vogt, B. Schmiedeskamp and U. Heinzmann, Physical Review B **42** (14), 9267-9270 (1990).

14. M. Chester and T. Gustafsson, Surface Science **256** (1-2), 135-146 (1991).

15. Y. Tanishiro, K. Takayanagi and K. Yagi, Surface Science **258** (1-3), L687-L690 (1991).

16. S. Y. Tong and H. Huang, Surface Science **243** (1-3), L46-L48 (1991).

17. J. K. Zuo and J. F. Wendelken, Physical Review Letters **66** (17), 2227-2230 (1991).

18. J. K. Zuo and J. F. Wendelken, Applied Surface Science **48-9**, 366-372 (1991).

19. A. Shibata, Y. Kimura and K. Takayanagi, Surface Science **275** (3), L697-L701 (1992).

20. K. J. Wan, X. F. Lin and J. Nogami, Physical Review B **45** (16), 9509-9512 (1992).

21. S. Watanabe, M. Aono and M. Tsukada, Applied Surface Science **60-1**, 437-442 (1992).

22. G. S. Herman, J. C. Woicik, A. B. Andrews and J. L. Erskine, Surface Science **290** (1-2), L643-L648 (1993).

23. A. A. Saranin, E. A. Khramtsova and V. G. Lifshits, Surface Science **296** (2), L21-L26 (1993).

24. S. Watanabe, M. Aono and M. Tsukada, Surface Science **287**, 1036-1040 (1993).

25. H. Huang, H. Over, S. Y. Tong, J. Quinn and F. Jona, Physical Review B **49** (19), 13483-13487 (1994).

26. R. Ishigami, J. Yuhara and K. Morita, Surface Science **321** (1-2), 100-104 (1994).

27. D. W. McComb, D. J. Moffatt, P. A. Hackett, B. R. Williams and B. F. Mason, Physical Review B **49** (24), 17139-17148 (1994).

28. H. Ohnishi, Y. Yamamoto, I. Katayama, Y. Ohba and K. Oura, Japanese Journal of Applied Physics Part 2-Letters **33** (8A), L1106-L1109 (1994).

29. E. J. J. Kirchner, E. J. Baerends, G. Tevelde and E. Vlieg, Surface Science **330** (2), 113-125 (1995).

30. D. W. McComb, R. A. Wolkow, D. J. Moffatt and P. A. Hackett, Surface Science **340** (1-2), L955-L959 (1995).

31. Z. H. Zhang, S. Hasegawa and S. Ino, Physical Review B **52** (15), 10760-10763 (1995).

32. M. Lijadi, H. Iwashige and A. Ichimiya, Surface Science **357** (1-3), 51-54 (1996).

33. Y. Nakajima, G. Uchida, T. Nagao and S. Hasegawa, Physical Review B **54** (19), 14134-14138 (1996).

34. A. Natori, M. Murayama and H. Yasunaga, Surface Science **357** (1-3), 47-50 (1996).

35. K. Oura, H. Ohnishi, Y. Yamamoto, I. Katayama and Y. Ohba, Journal of Vacuum Science & Technology B **14** (2), 988-991 (1996).

36. S. Gunther, A. Kolmakov, J. Kovac, M. Marsi and M. Kiskinova, Physical Review B **56** (8), 5003-5013 (1997).

37. Y. Nakajima, S. Takeda, T. Nagao, S. Hasegawa and X. Tong, Physical Review B **56** (11), 6782-6787 (1997).

38. J. K. Zuo and J. F. Wendelken, Physical Review B **56** (7), 3897-3902 (1997).

39. X. Tong, Y. Sugiura, T. Nagao, T. Takami, S. Takeda, S. Ino and S. Hasegawa, Surface Science **408** (1-3), 146-159 (1998).

40. J. Viernow, M. Henzler, W. L. O'Brien, F. K. Men, F. M. Leibsle, D. Y. Petrovykh, J. L. Lin and F. J. Himpsel, Physical Review B **57** (4), 2321-2326 (1998).

41. H. Aizawa and M. Tsukada, Physical Review B **59** (16), 10923-10927 (1999).

42. T. Minobe, T. Uchihashi, T. Tsukamoto, S. Orisaka, Y. Sugawara and S. Morita, Applied Surface Science **140** (3-4), 298-303 (1999).

43. N. Sato, S. Takeda, T. Nagao and S. Hasegawa, Physical Review B **59** (3), 2035-2039 (1999).

44. Y. Sugawara, T. Minobe, S. Orisaka, T. Uchihashi, T. Tsukamoto and S. Morita, Surface and Interface Analysis **27** (5-6), 456-461 (1999).

45. S. Hasegawa, N. Sato, I. Shiraki, C. L. Petersen, P. Boggild, T. M. Hansen, T. Nagao and F. Grey, Japanese Journal of Applied Physics Part 1-Regular Papers Short Notes & Review Papers **39** (6B), 3815-3822 (2000).

46. S. Morita and Y. Sugawara, in *Microbeam Analysis 2000, Proceedings*, edited by D. B. S. R. Williams (2000), pp. 371-372.

47. N. Sasaki, H. Aizawa and M. Tsukada, Applied Surface Science **157** (4), 367-372 (2000).

48. X. Tong, C. S. Jiang, K. Horikoshi and S. Hasegawa, Surface Science **449** (1-3), 125-134 (2000).

49. K. Kakitani, A. Yoshimori, H. Aizawa and M. Tsukada, Surface Science **493** (1-3), 200-205 (2001).

50. B. Li, C. G. Zeng, H. Q. Wang, B. Wang and J. G. Hou, Chinese Physics Letters **18** (2), 181-183 (2001).

51. Y. Nakamura, Y. Kondo, J. Nakamura and S. Watanabe, Physical Review Letters **87** (15) (2001).

52. Y. Nakamura, Y. Kondo, J. Nakamura and S. Watanabe, Surface Science **493** (1-3), 206-213 (2001).

53. Y. Nakamura, Y. Kondo, J. Nakamura and S. Watanabe, Physical Review Letters **87** (15), 156102 (2001).

54. Y. Oshima, H. Nakade, S. Shigeki, H. Hirayama and K. Takayanagi, Surface Science **493** (1-3), 366-372 (2001).

55. N. Sasaki, S. Watanabe, H. Aizawa and M. Tsukada, Surface Science **493** (1-3), 188-193 (2001).

56. Y. Oshima, H. Nakade, S. Shigeki, H. Hirayama and K. Takayanagi, Surface Science **498** (3), 307-313 (2002).

57. I. Matsuda, H. Morikawa, C. Liu, S. Ohuchi, S. Hasegawa, T. Okuda, T. Kinoshita, C. Ottaviani, A. Cricenti, M. D'Angelo, P. Soukiassian and G. Le Lay, Physical Review B **68** (8) (2003).

58. Y. Nakamura, H. Koga and S. Watanabe, Journal of the Physical Society of Japan **72** (1), 13-16 (2003).

59. L. Chen, H. J. Xiang, B. Li, A. D. Zhao, X. D. Xiao, J. L. Yang, J. G. Hou and Q. S. Zhu, Physical Review B **70** (24) (2004).

60. D. Deng and T. Suzuki, Physical Review B **72** (8) (2005).

61. C. H. Liu, S. Yamazaki, R. Hobara, I. Matsuda and S. Hasegawa, Physical Review B **71** (4) (2005).

62. D. Deng, Y. Karaki and T. Suzuki, Surface Science **600** (15), 3052-3057 (2006).

63. K. Sakamoto, T. Suzuki, K. Mawatari, K. Kobayashi, J. Okabayashi, K. Ono, N. Ueno and M. Oshima, Physical Review B **73** (19), 193303 (2006).

64. Y. Fukaya, A. Kawasuso and A. Ichimiya, Physical Review B **75** (11) (2007).

65. H. Jeong, H. W. Yeom and S. Jeong, Physical Review B **76** (8) (2007).

66. H. Kaji and K. Kakitani, Surface Science **601** (12), 2491-2497 (2007).

67. H. M. Zhang, J. B. Gustafsson and L. S. O. Johansson, Journal of Physics: Conference Series **61** (1), 1336 (2007).

68. H. Jeong, H. W. Yeom and S. Jeong, Physical Review B **77** (23) (2008).

69. S. Minamoto, T. Ishizuka and H. Hirayama, Surface Science **602** (2), 470-474 (2008).

70. J. Teng, J. Guo, K. Wu and E. Wang, Journal of Chemical Physics **129** (3) (2008).

71. S. Jeong and H. Jeong, Physical Review B **81** (19) (2010).

72. A. Belianinov, B. Uenal, K. M. Ho, C. Z. Wang, J. W. Evans, M. C. Tringides and P. A. Thiel, Journal of Physics-Condensed Matter **23** (26) (2011).

73. H. Minoda, H. Yazawa, M. Morita, S. N. Takeda and H. Daimon, Physical Review B **83** (3) (2011).

74. A. Belianinov, B. Ünal, N. Lu, M. Ji, K.-M. Ho, C.-Z. Wang, M. Tringides and P. A. Thiel, Phys. Rev. B **82**, 245413 (2010).

75. Y. G. Ding, C. T. Chan and K. M. Ho, Phys. Rev. Lett. **67** (11), 1454-1457 (1991).

76. N. Sato, T. Nagao and S. Hasegawa, Surf. Sci. **442** (1), 65-73 (1999).

77. H. Aizawa, M. Tsukada, N. Sato and S. Hasegawa, Surf. Sci. **429**, L509-L514 (1999).

78. H. M. Zhang, J. B. Gustafsson and L. S. O. Johansson, Phys. Rev. B **74**, 201304(R) (2006).

79. I. Matsuda, H. Morkawa, C. Liu, S. Ohuchi, S. Hasegawa, T. Okuda, T. Kinoshita, C. Ottaviani, A. Cricenti, M. D'angelo, P. Soukiassian and G. Le Lay, Phys. Rev B **68**, 085407 (2003).

80. G. Le Lay, G. Quentel, J. P. Faurie and A. Masson, Thin Sol. Films **35**, 273-287 (1976).

81. V. A. Gasparov and M. Riehl-Chudoba, Surf. Sci. **601**, 5403-5411 (2007).

82. G. Raynerd, T. N. Doust and J. A. Venables, Surf. Sci. **261** (1-3), 251-266 (1992).

83. F. L. Metcalfe and J. A. Venables, Surf. Sci. **369**, 99-107 (1996).

84. J. A. Venables, F. L. Metcalfe and S. Sugawara, Surf. Sci. **371**, 420-430 (1997).

85. D. M. Deng, M. Numata and T. Suzuki, Journal of the Physical Society of Japan **73** (12), 3384-3388 (2004).

86. H. Aizawa and M. Tsukada, Phys. Rev. B **59** (16), 10923 (1999).

87. S. Jeong and H. Jeong, Phys. Rev. B **76**, 085423 (2007).

88. S. Jeong and H. Jeong, Phys. Rev. B **81**, 195429 (2010).

89. B. Unal, F. Qin, Y. Han, D.-J. Liu, D. Jing, A. R. Layson, C. J. Jenks, J. W. Evans and P. A. Thiel, Physical Review B **76** (19), 195410 (2007).

90. L. Gavioli, K. R. Kimberlin, M. C. Tringides, J. F. Wendelken and Z. Zhang, Physical Review Letters **82** (1), 129-132 (1999).

91. I. Horcas, R. Fernandez, J. M. Gomez-Rodriguez, J. Colchero, J. Gomez-Herrero and A. M. Baro, Review of Scientific Instruments **78** (1), 013705-013708 (2007).

92. T. Sato, T. Sueyoshi, S. Kitamura and M. Iwatsuki, Japanese Journal of Applied Physics Part 1-Regular Papers Short Notes & Review Papers **32** (6B), 2923-2928 (1993).

93. Y. G. Ding, C. T. Chan and K. M. Ho, Surface Science **275** (3), L691-L696 (1992).

94. A. Belianinov, B. Ünal, N. Lu, M. Ji, K. M. Ho, C. Z. Wang, M. C. Tringides and P. A. Thiel, Physical Review B **82** (24), 245413 (2010).

95. A. A. S. V. G. Lifshits, A. V. Zotov, (1994).

96. A. Endo and S. Ino, Surface Science **293** (3), 165-182 (1993).

97. D. Wall, I. Lohmar, K. R. Roos, J. Krug, M. Horn-von Hoegen and F. J. M. Z. Heringdorf, New Journal of Physics **12** (2010).

LIST OF FIGURES

CHAPTER II FIGURES

Figure 4. (A) R_{IH} as a function of t_{ann} at 600 K. At t_{ann} = 0, deposition has just ended. Values are averages over multiple images, and error bars are standard deviations over images within a single run. (B) Densities of islands as a function of t_{ann} at 600 K. The diamonds show all islands, triangles show islands with individual areas < 50 nm^2, and squares show larger islands. Error bars show the standard deviation of the island density in various images. Images are weighted according to their size. When error bars are not visible, they are covered by the individual data point.

Figure 5. Graph illustrating the change in areas of Si(111)-7x7 phase (triangles), √3 islands (diamonds) and √3 holes (circles) with annealing time at 600 K. Values are averages over multiple images, and error bars are standard deviations. Most error bars are obscured by the symbols.

Figure 6. STM images showing the √3 structure in islands and holes, after preparation using different conditions. (A, B) Prepared by deposition at 500 K, followed by 10 minute anneal. V_T = -1.0 V and I_T= 2 nA. (C) Prepared by deposition at 600 K, followed by 2 minute anneal. V_T = -1.0 V and I_T= 0.2 nA.

Figure 7. STM images of islands, showing rims. V_T = -1.0 V and I_T= 0.2 nA. (A) Prepared by deposition at 615 K, annealed 2 minutes. 50 x 50 nm^2. (B) Prepared by deposition at 800 K, annealed 2 minutes. 65 x 65 nm^2.

Figure 8. Genetic algorithm search results, showing E_f for various √3 structures. Each value of the abscissa is labeled with both the Si coverage (first digit) and the Ag coverage (second digit) on the bottom axis, equivalent to N√3, Si and N√3, Ag. For each value of N√3, Si (first

digit), the value of N√3, Ag ranges from 0 to 3. The (7x7) energy is the dashed horizontal line. The top axis is labeled with the number of Si and Ag atoms per √3 unit cell, i.e. each value on the lower axis is multiplied by 3.

Figure 9. Schematic illustration of the growth of a hole around a √3 island.

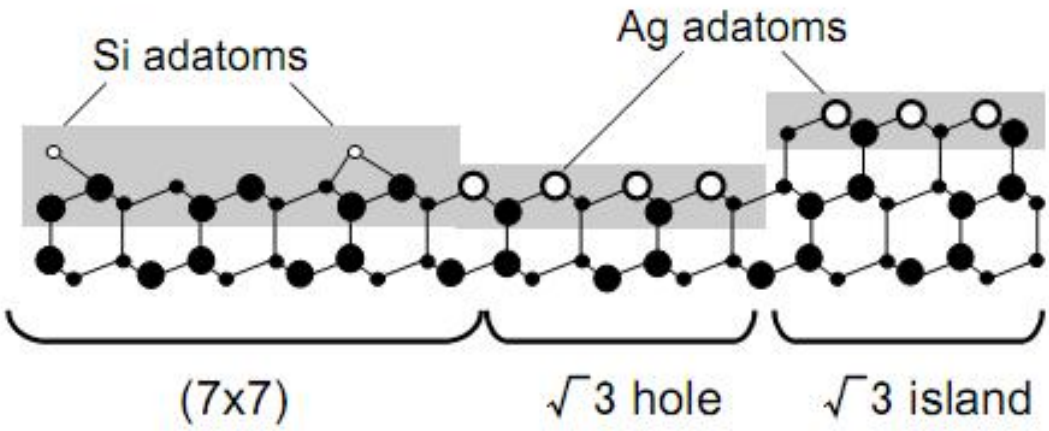

Figure 1A

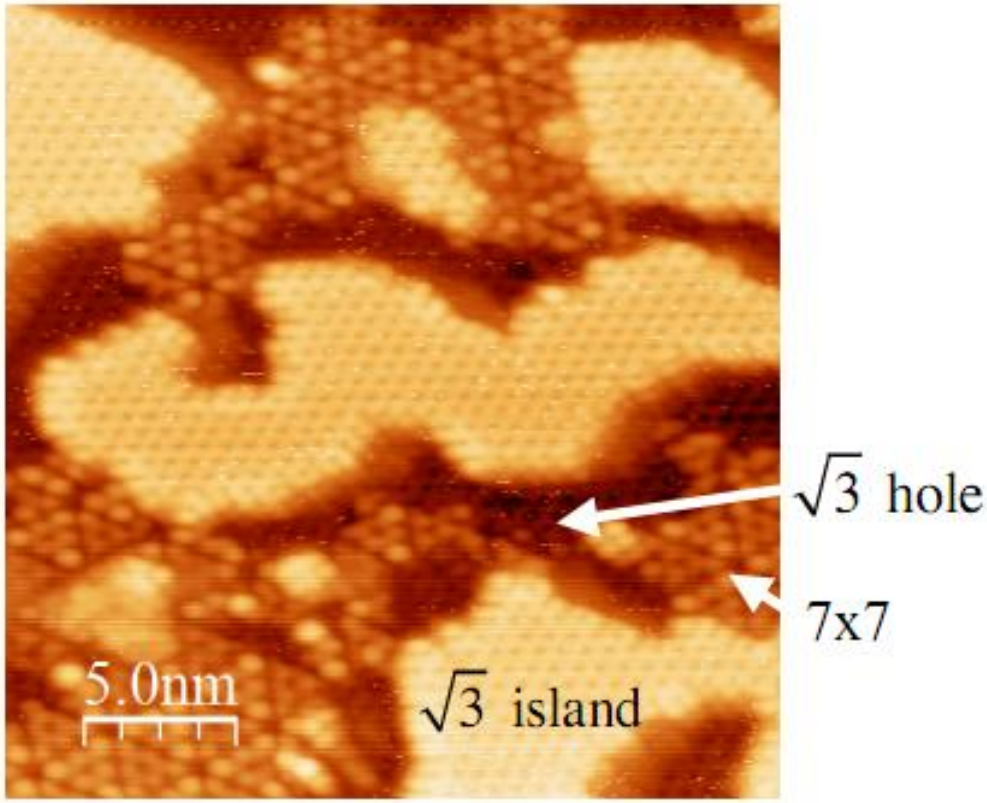

Figure 1B

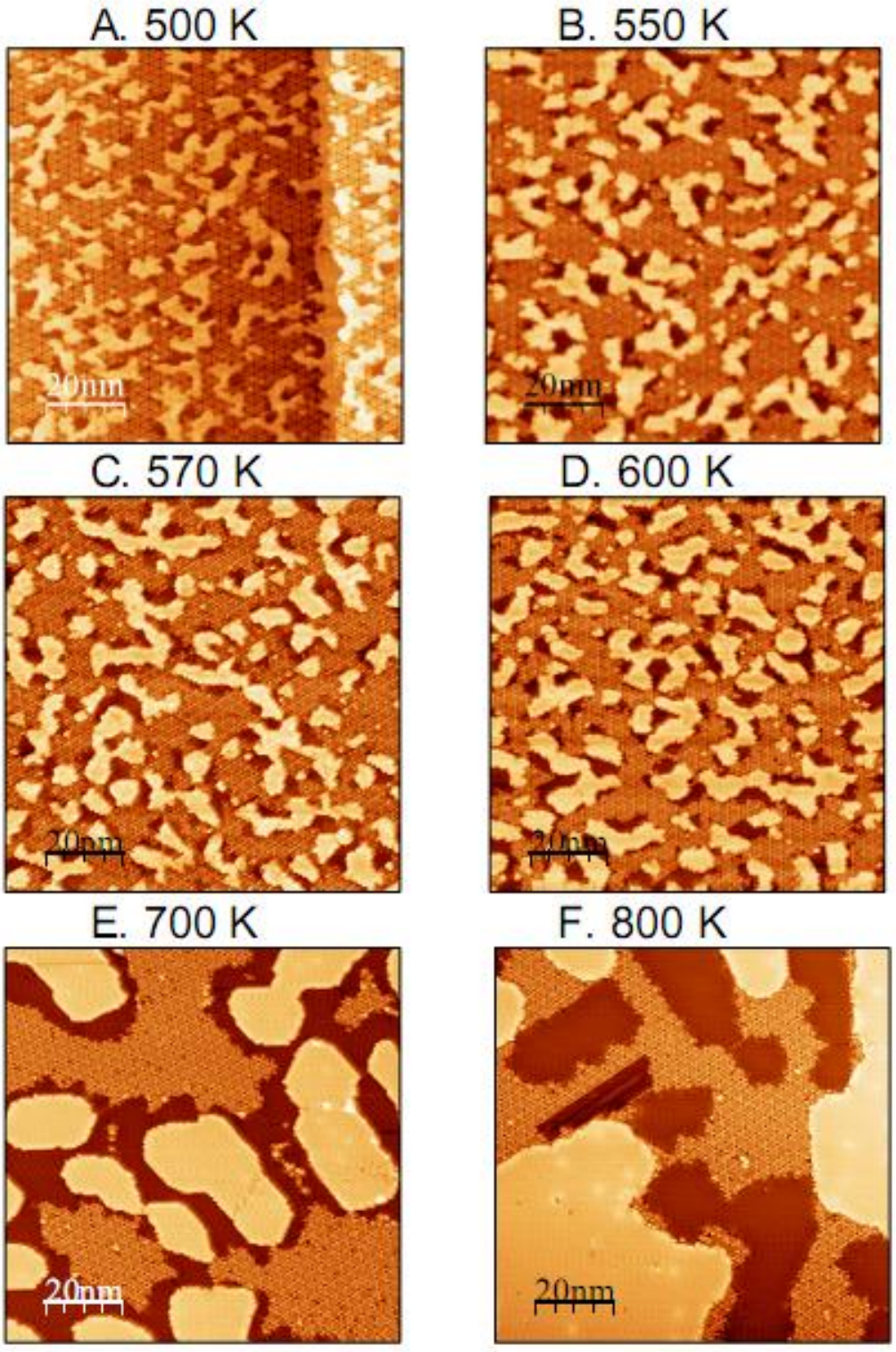

Figure 2

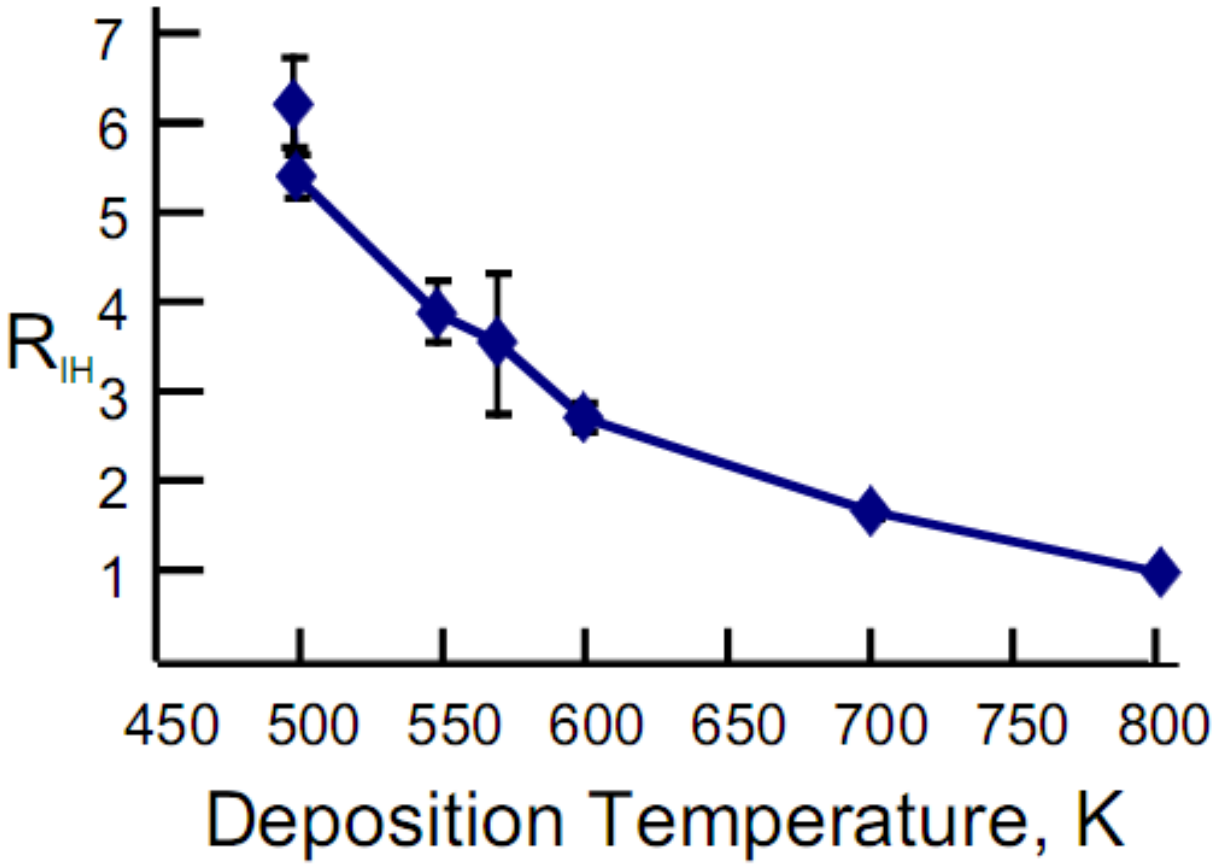

Figure 3

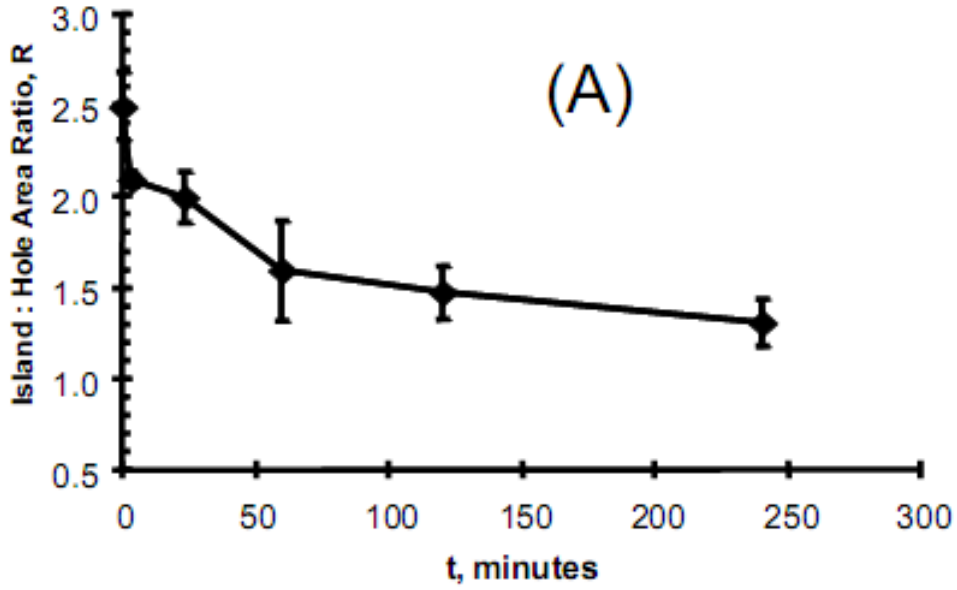

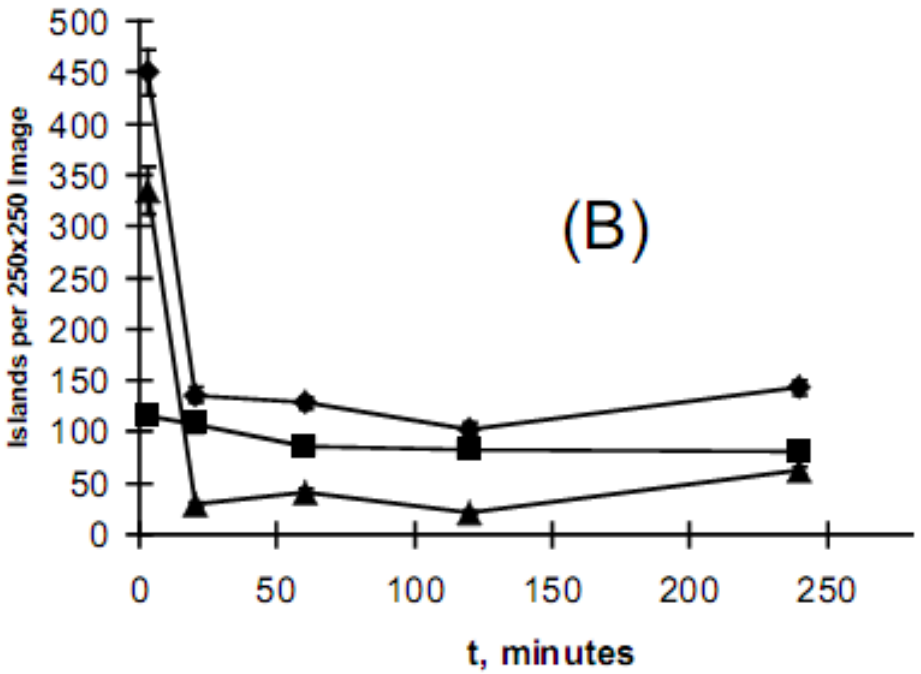

Figure 4

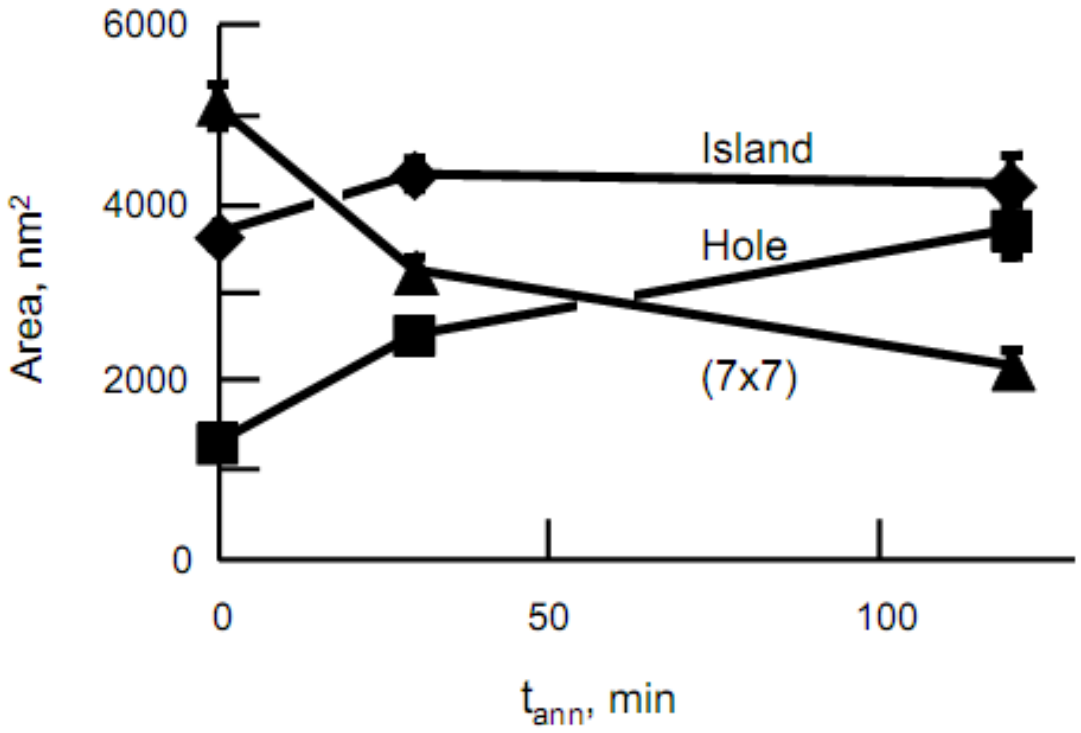

Figure 5

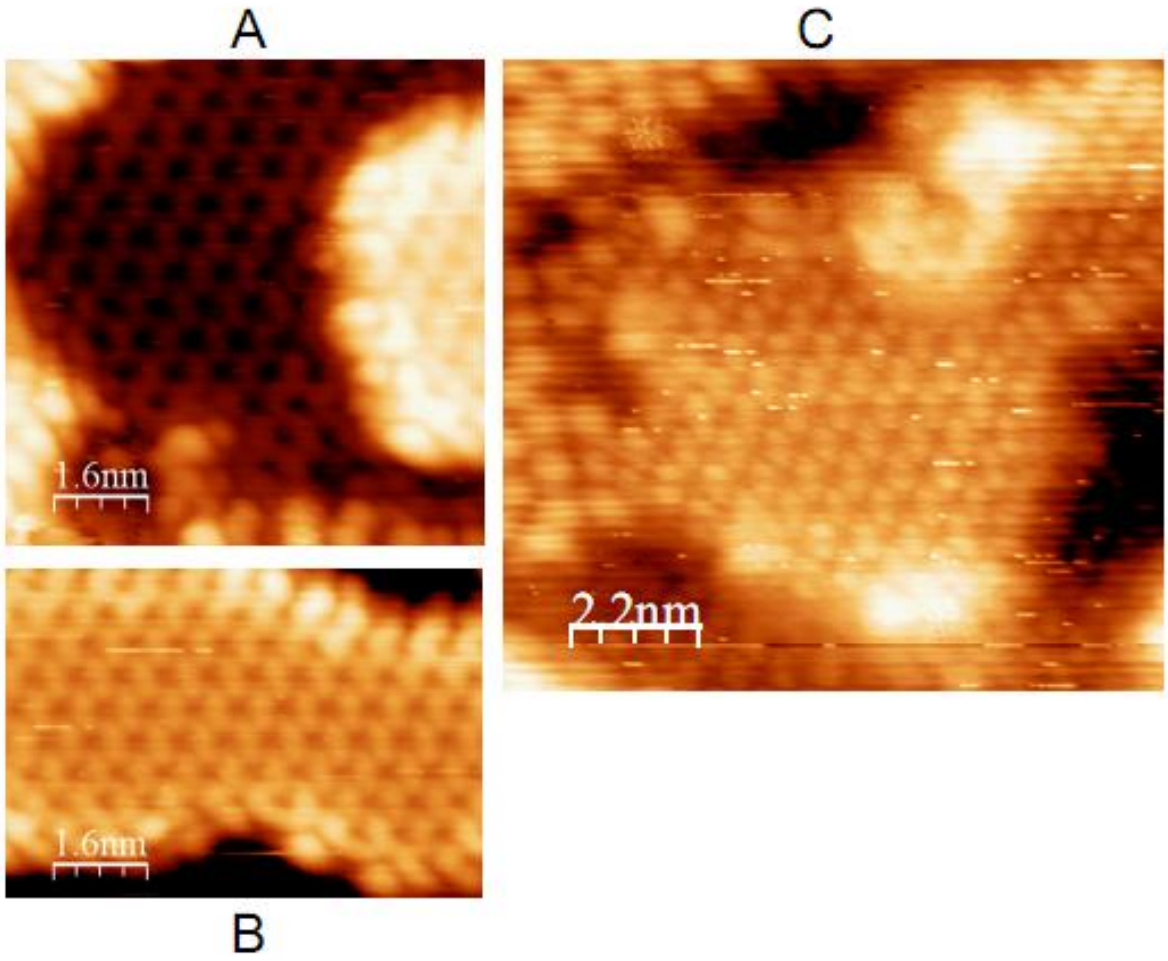

Figure 6

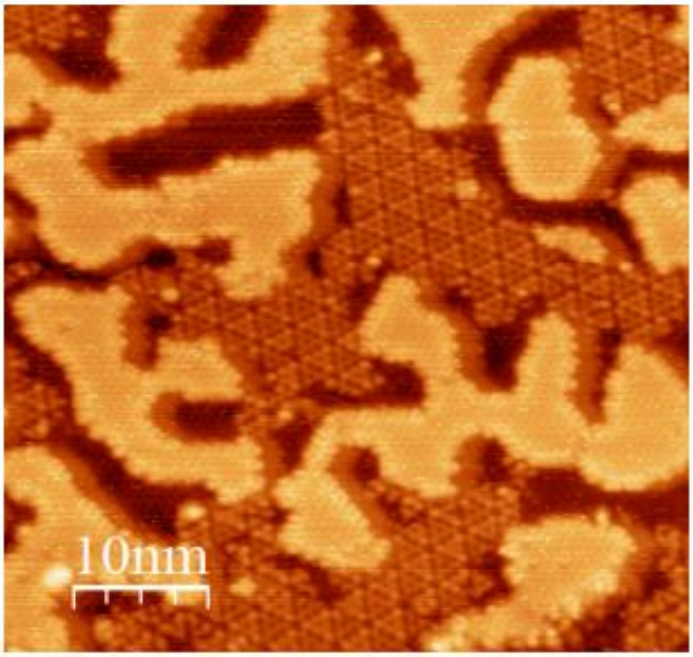

A

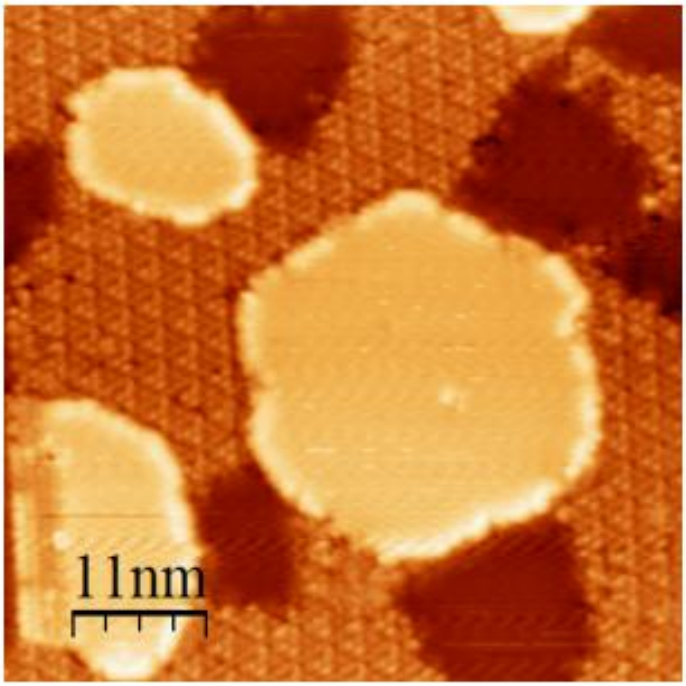

B

Figure 7

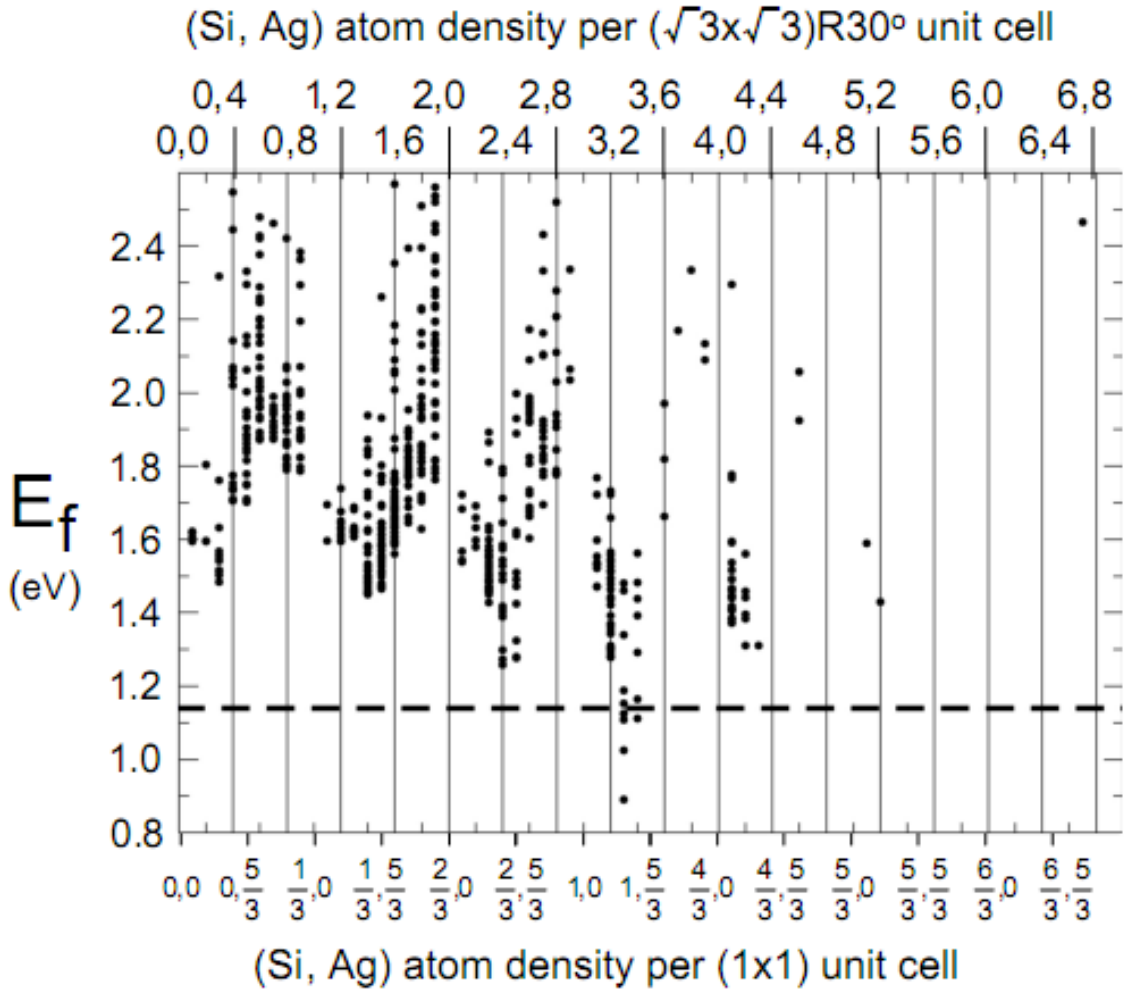

Figure 8

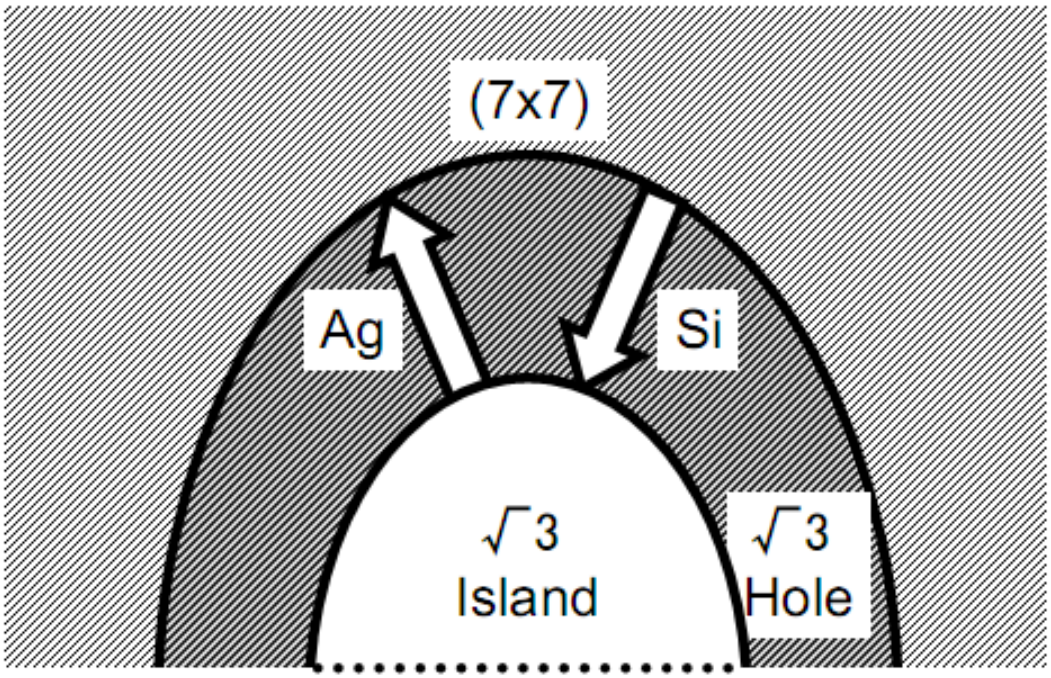

Figure 9

CHAPTER III FIGURES

Figure 1. STM images showing Ag islands at the temperatures indicated. Figures A-C are raw topographic images, while Figures D-F are differentiated images.

Figure 2. High-magnification images of Ag islands. (A) T = 115 K. (B) T = 180 K. (C) T = 250 K. The top (bottom) line in each STM images corresponds to the line profile shown in the top (bottom) part of that panel.

Figure 3. Low-magnification images of the √3 surface, following deposition of 1.7 ML Ag at 300 K. In panel (B), the right-hand side of the image is a region of closely-bunched steps.

Figure 4. STM images showing typical appearance of √3 domain boundaries (A) before, and (B) after deposition of 5 ML of Ag at 300 K. Images sizes are (A) 50 x 50 nm^2. and (B) 100 x 100 nm^2.

Figure 5. STM images showing the result of Ag deposition on Si(111) surfaces that were mixed (7x7) and √3 phase at 300 K. (A) is a semi-3D perspective of the islands, and (b) is a topographic image of a different region. Ag islands are labeled with their height in layers, L. Other regions are labeled as √3 or WL (wetting layer), where the WL is a (7x7) containing 0.5 ML Ag.[30]

Figure 6. Natural logarithm of N_{isl} as a function of T^{-1}. Error bars are calculated as described in Section 2. When error bars are not visible, they are so small that they are obscured by the data symbol. From 50 through 125 K, the data are fit best by the straight line shown, which is of the form $ln\ (N_{isl}) = 31.5T^{-1} - 4.57$, for which $R^2 = 0.95$. (R^2 is the square of the correlation coefficient.) From 180 through 250 K, the best fit is given by $ln\ (N_{isl}) = (2.28 \times 10^3)T^{-1} - 20.1$, for which $R^2 = 0.91$. The dashed line represents a region in which $i = 1$ is presumed, with slope calculated from the value of N_{isl} at 115-125 K (see Section 3.2).

Figure 7. Natural logarithm of N_{isl} as a function of T^{-1}, comparing data acquired in this study (180-250 K) with data acquired by Venables et al.[23] (570-780 K). The high-temperature data are reproduced with permission. The solid line is a fit to the four data points from 180 to 250 K. It is the same as the line drawn through the same data points in Fig. 6. For the high-temperature data, there are two different values of Ag flux: 0.011 ML/s (triangles) and 0.0033 ML/s (diamonds).[23] These bracket the typical value in the low-temperature experiments, 0.0050 ML/s.

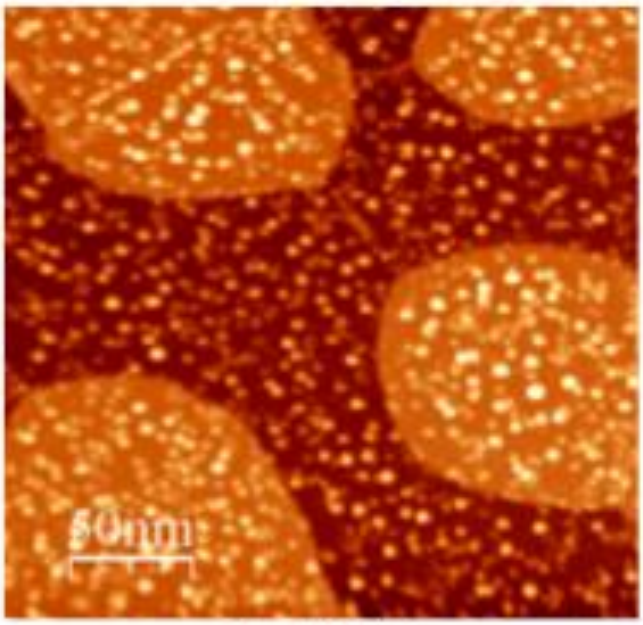

A: 115K

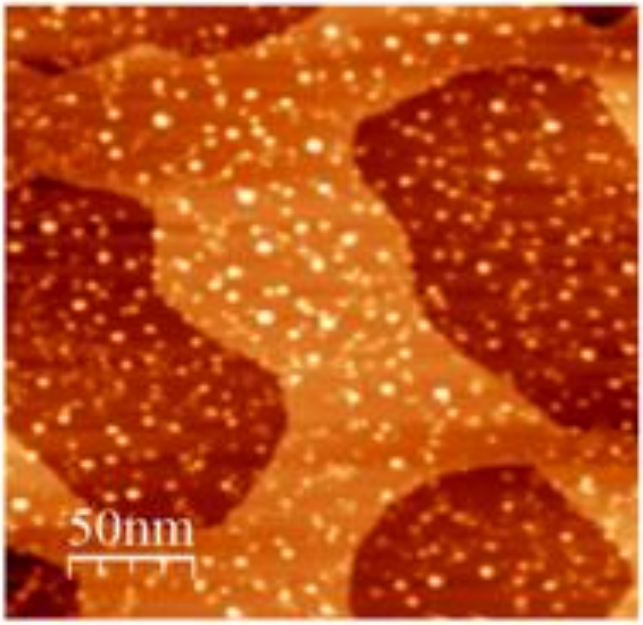

B:150K

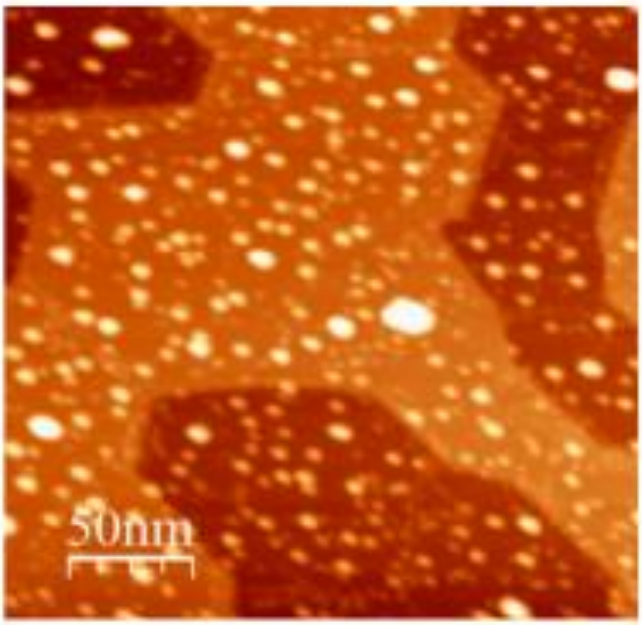

C: 170K

Figure 1 A-C

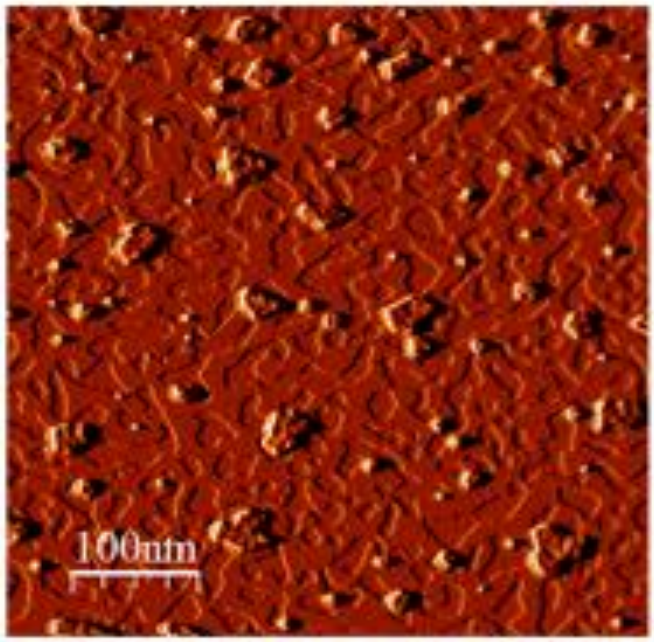

D: 200K

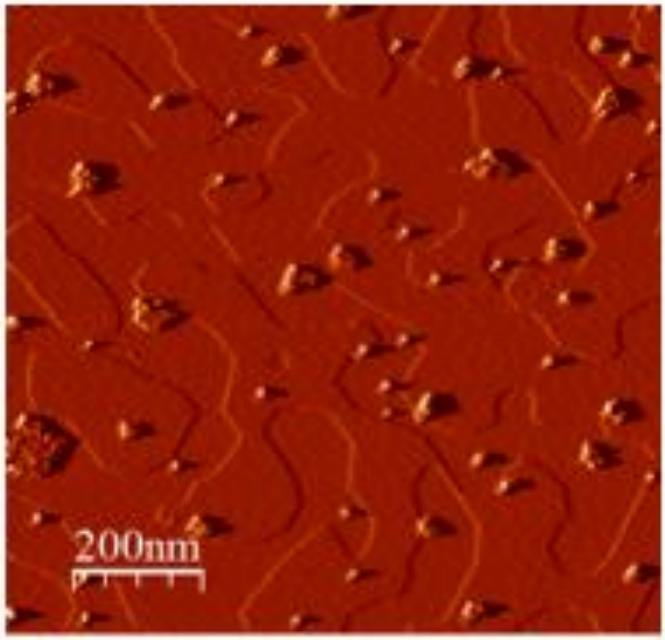

E: 212K

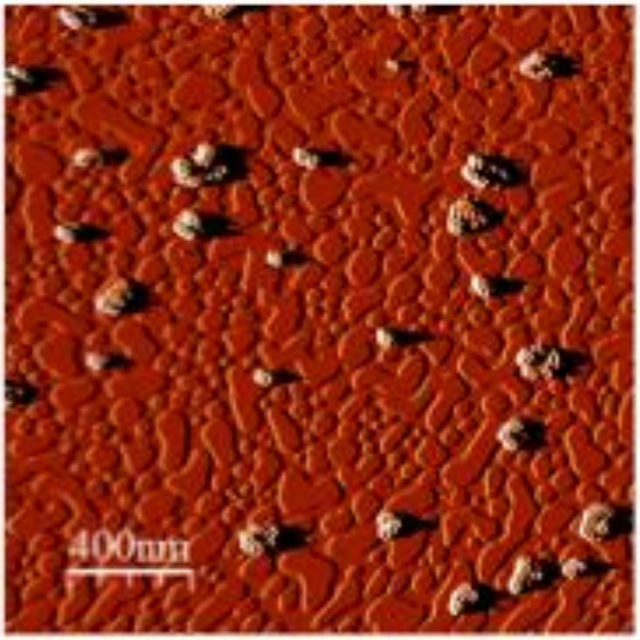

F:250K

Figure 1 D-F

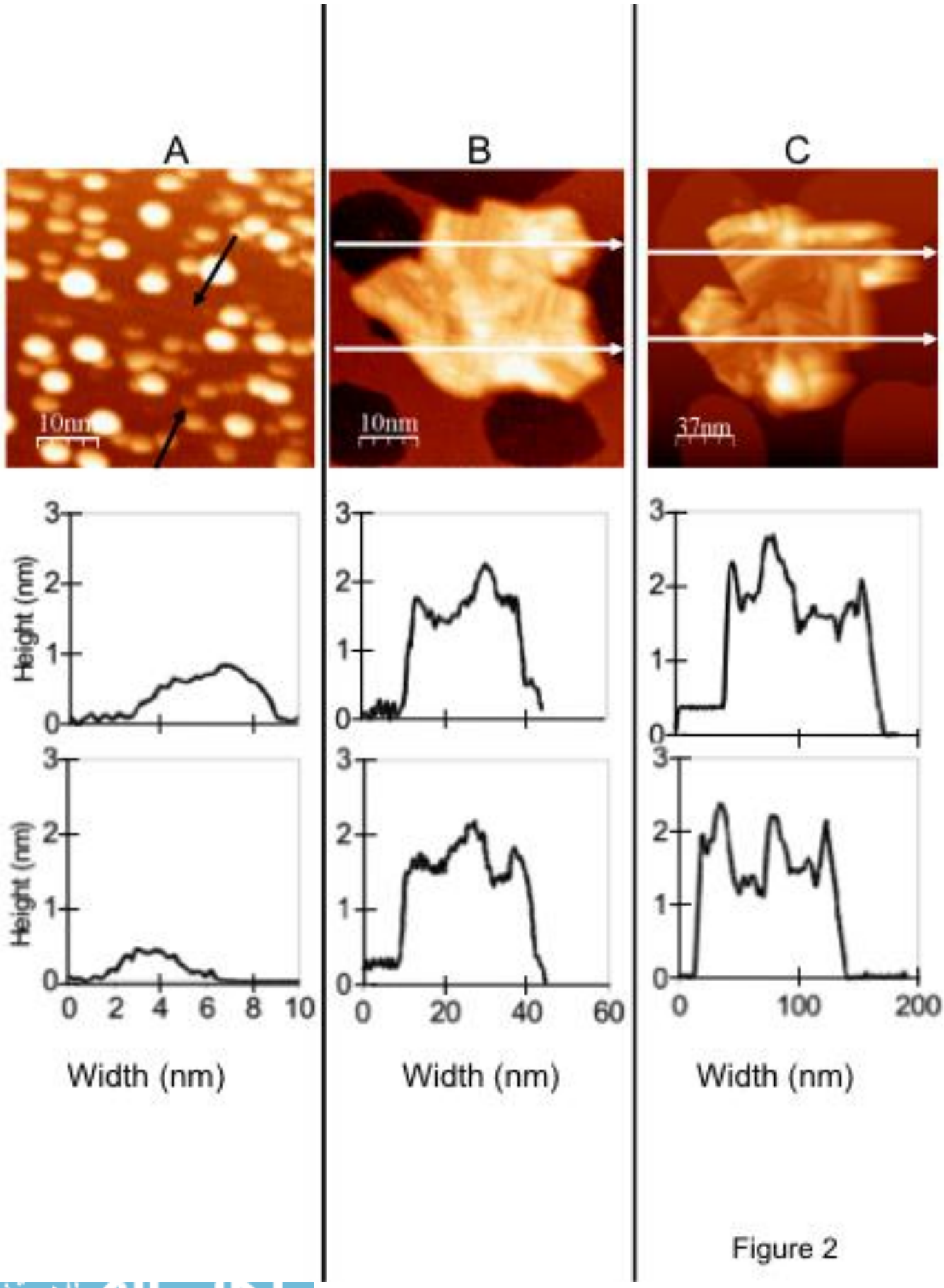

Figure 2

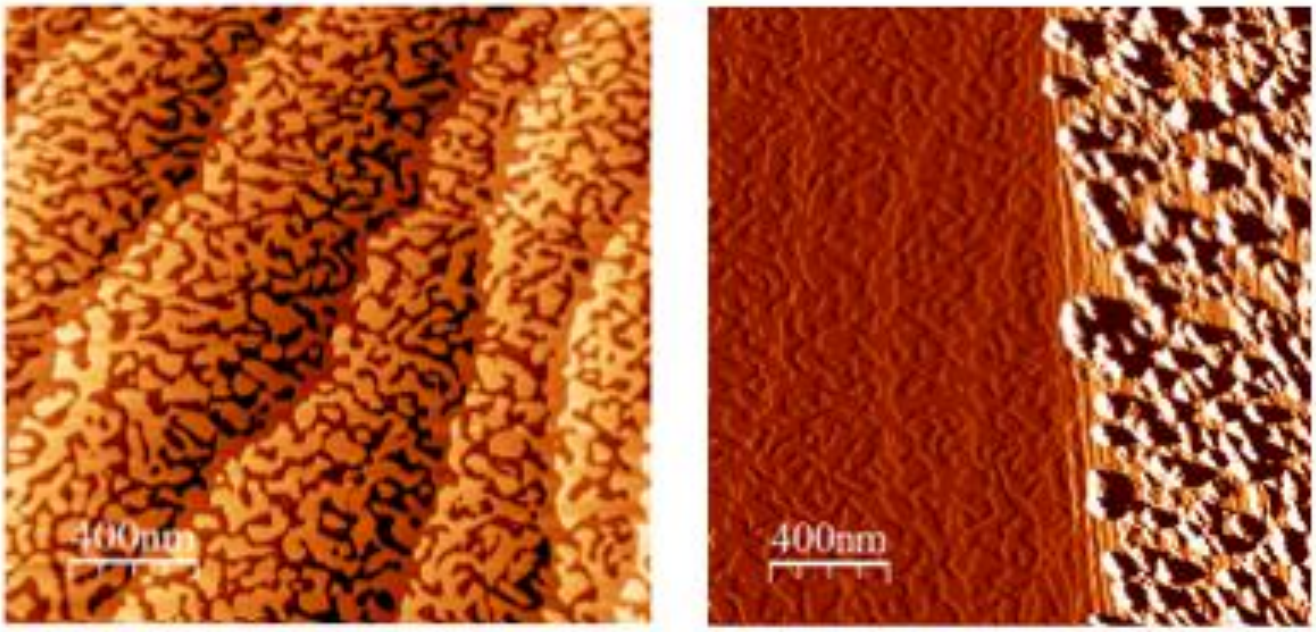

A B

Figure 3

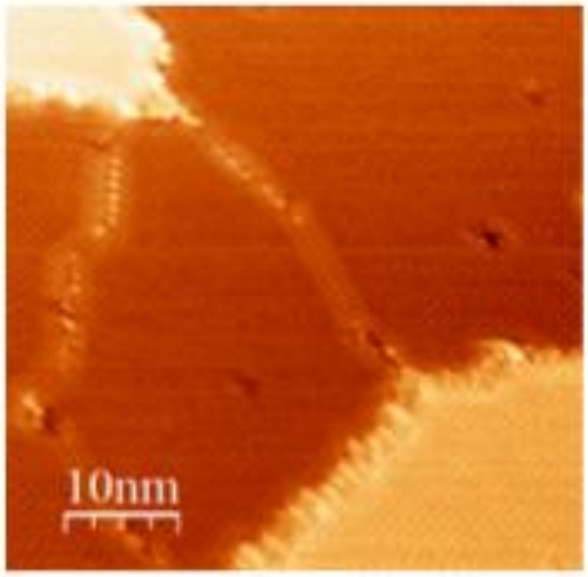

A

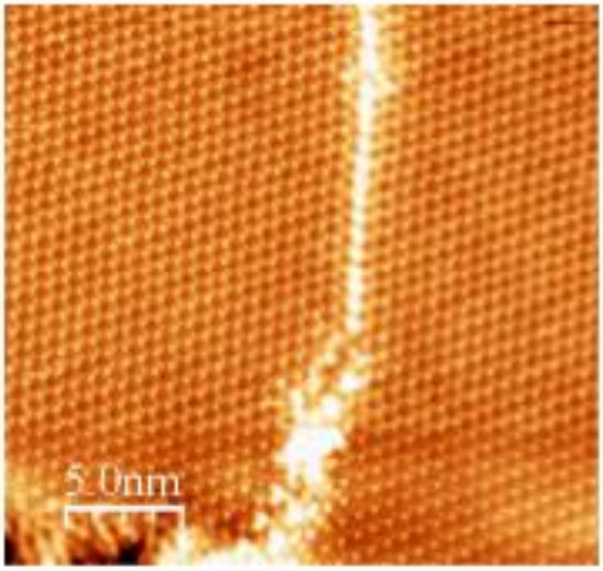

B

Figure 4

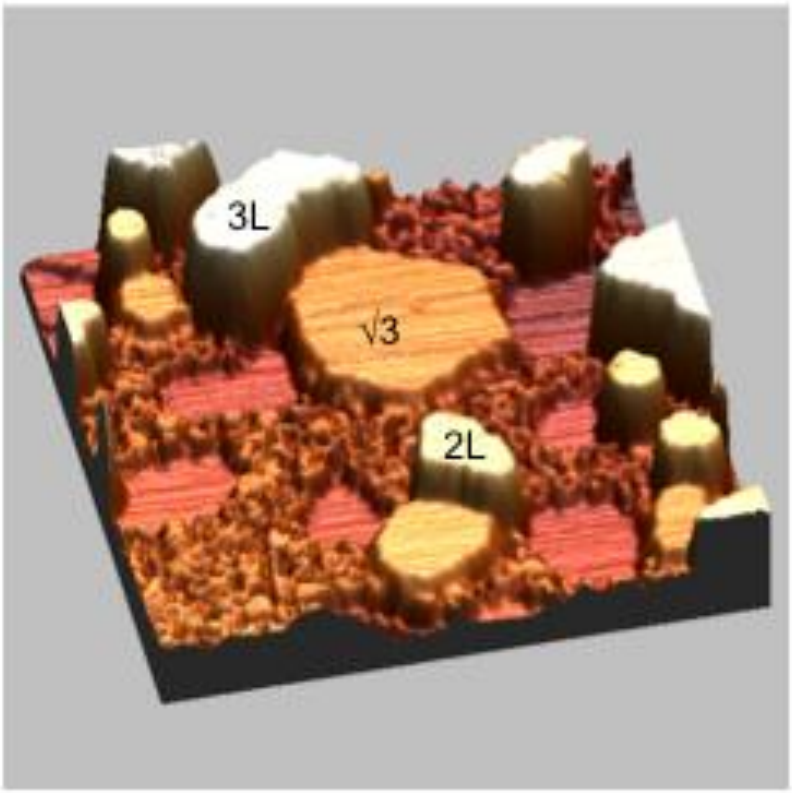

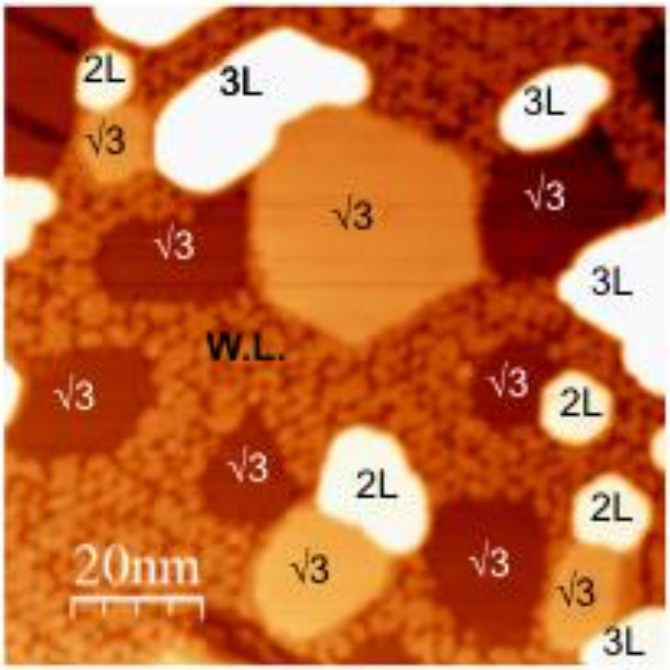

Figure 5

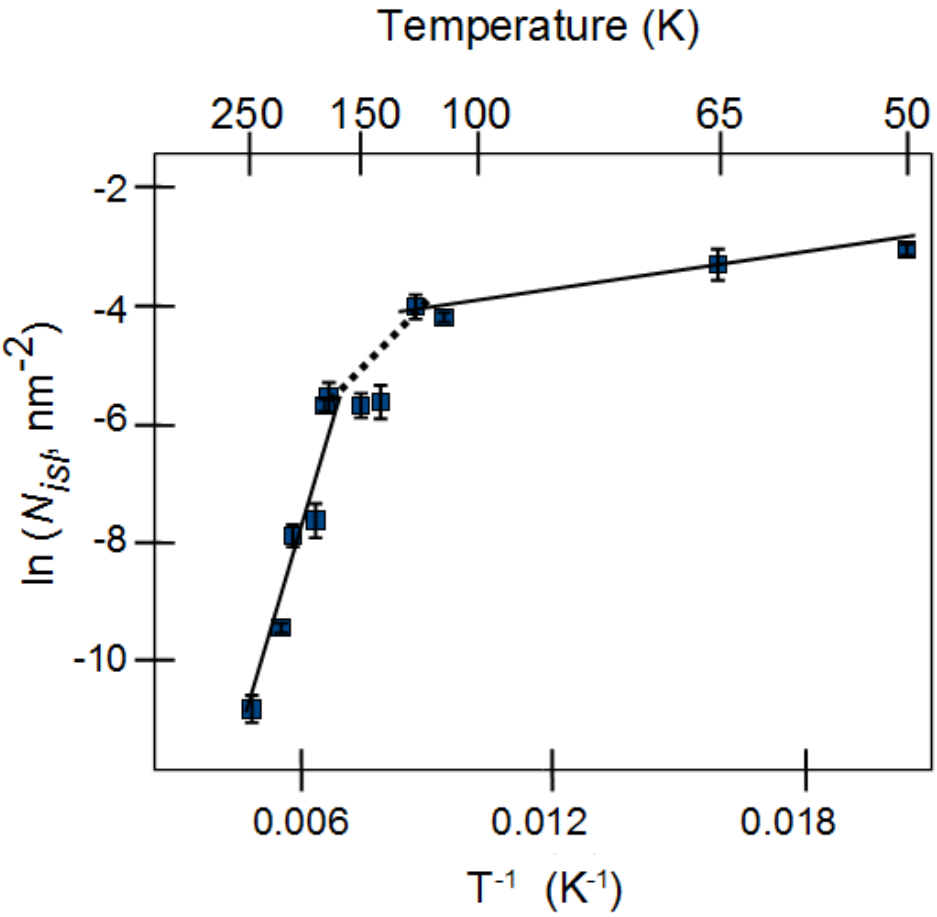

Figure 6

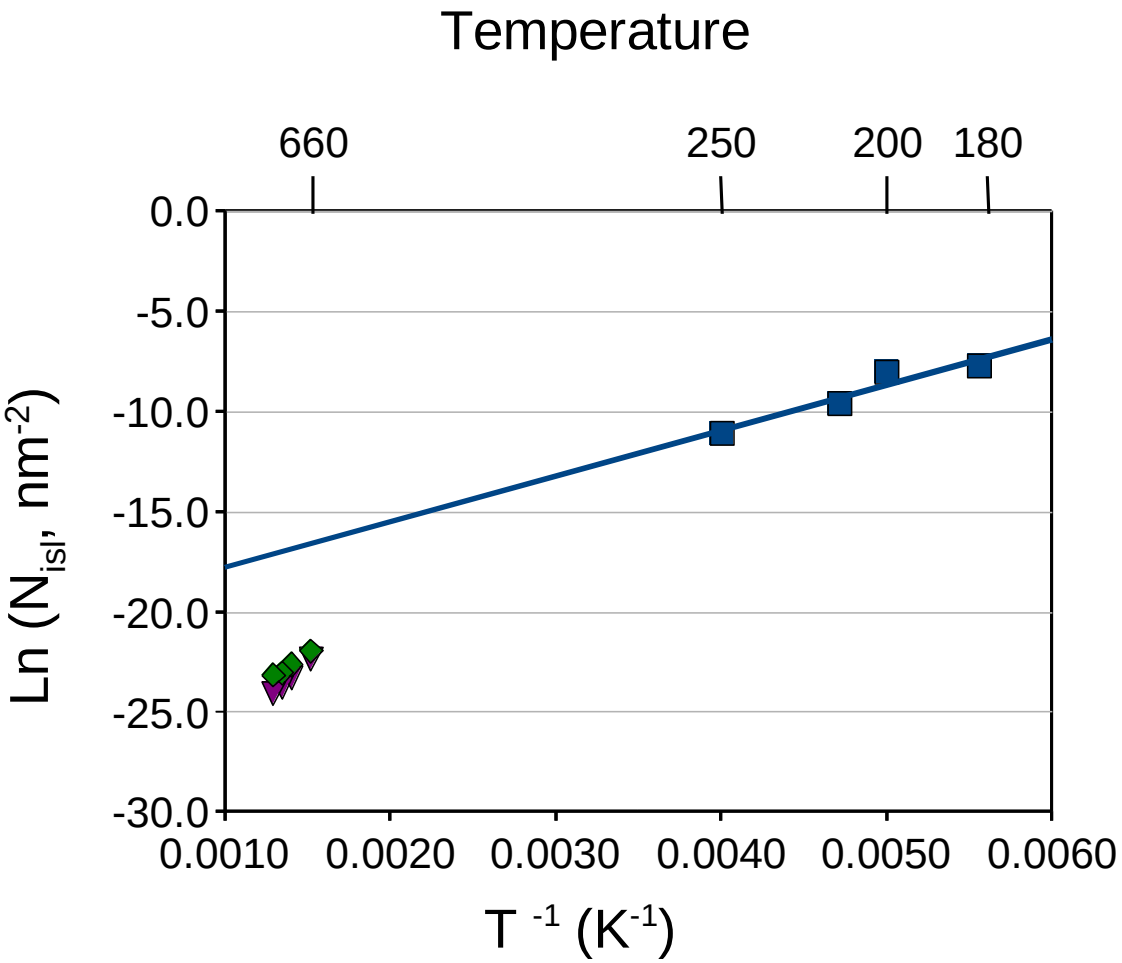

Figure 7

CHAPTER IV FIGURES

F1. Nanopatterned Ag-Si-√3 surface. Topographic images are on the left, Differentiated images are on the right. (A) Line, made of dots 50x50 nm^2 -0.2V, 2nA, (B) Dots, 50x50 nm^2 0.2V, 2nA, (C) - Pit , 50x50 nm^2 -0.2V, 2nA.

Figure 2. Nanopatterned Ag-Si-√3 surface, line profiles are taken on topographic images. (A) Line, made of dots 50x50 nm^2 -0.2V, 2nA, Differentiated, (B) Dots, 50x50 nm^2 0.2V, 2nA, Differentiated, (C) - Pit , 50x50 nm^2 -0.2V, 2nA, Differentiated.

Figure 3. Same nanopatterned region after a series of Ag depositions: (A) 0.5ML of Ag, 50x50 nm^2, -1V, 2nA, Differentiated, 3D; (B) 1ML of Ag, 50x50 nm^2, -1V, 2nA, Differentiated, 3D; (C) 1.5ML of Ag, 50x50 nm^2, -1V, 0.2nA, Differentiated, 3D; (D) 2.0ML of Ag 50x50 nm^2, -1V, 2nA, Differentiated, 3D; (E) 3.25ML of Ag 50x50 nm^2, -1V, 2nA, Differentiated, 3D.

Figure 4. Nanopatterned Ag-Si-√3 surface: (A) Dots, filled with Ag 3.25ML, 50x50 nm^2, -1V, 2nA, Differentiated, 3D; (B) Pit with 0.5ML Ag, 50x50 nm^2, 0.2V, 2nA, Differentiated, 3D; (C) Pit with 1ML Ag, 50x50 nm^2, -1V, 2nA, Differentiated, 3D; (D) Pit with 2ML of Ag, 50x50 nm^2, -1V, 2nA, Differentiated, 3D; (E) Pit with 3.25ML of Ag, 50x50 nm^2, -1V, 2nA, Differentiated, 3D.

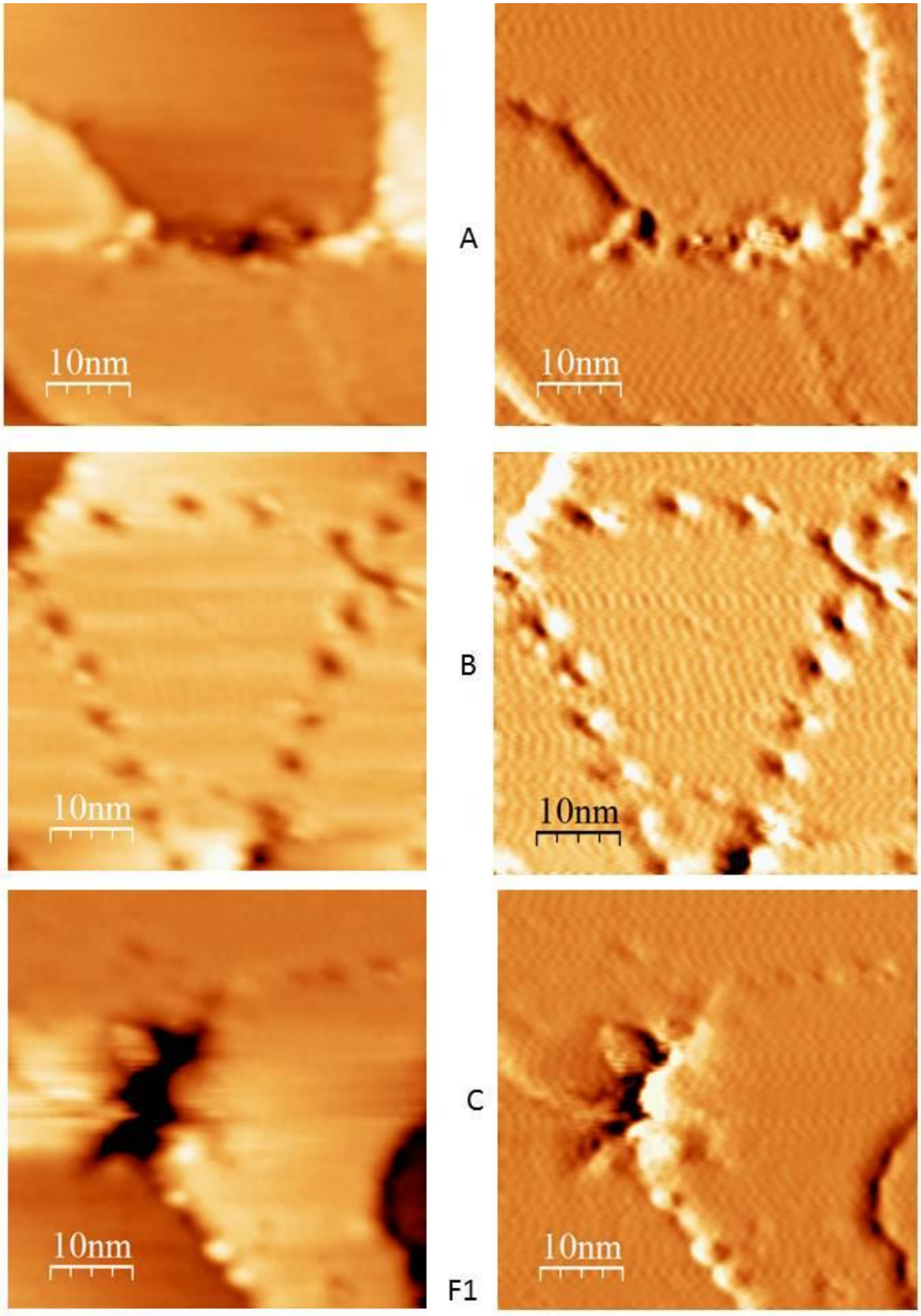

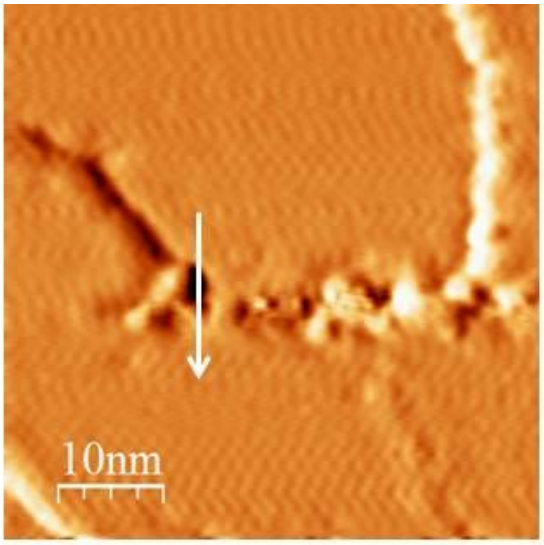

A

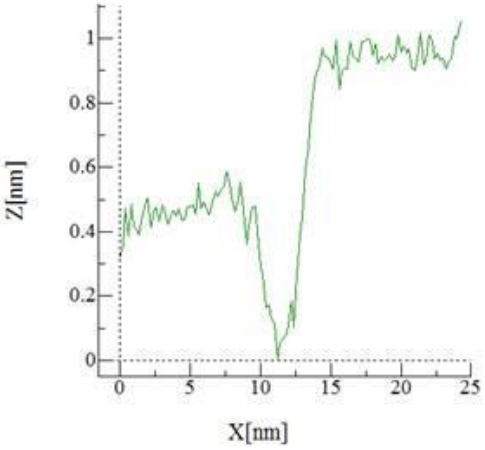

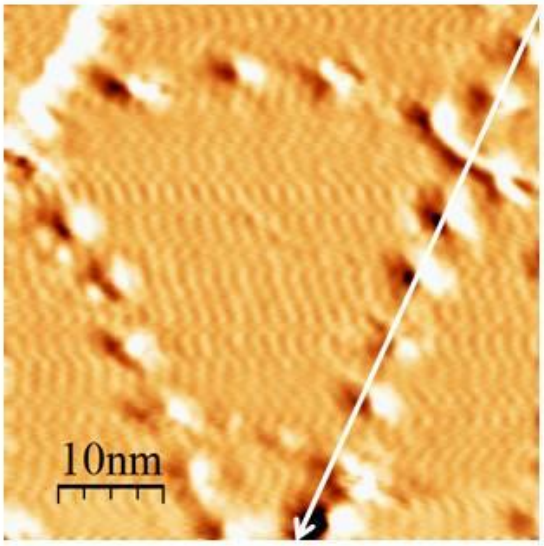

B

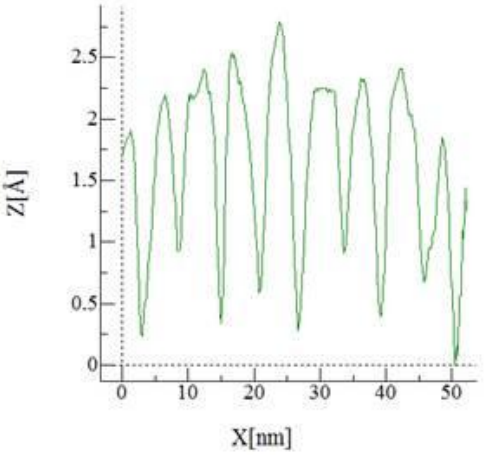

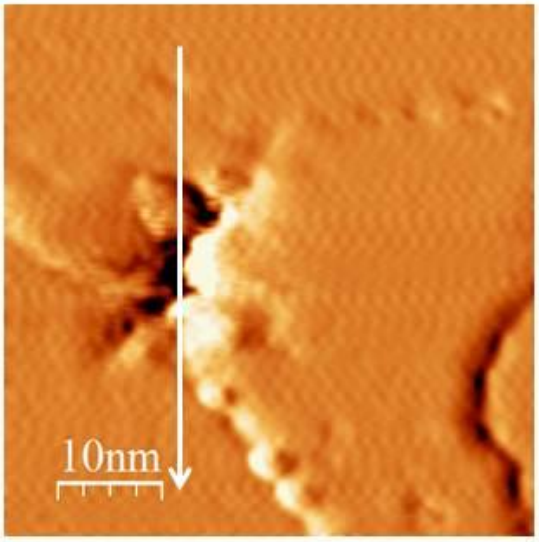

C

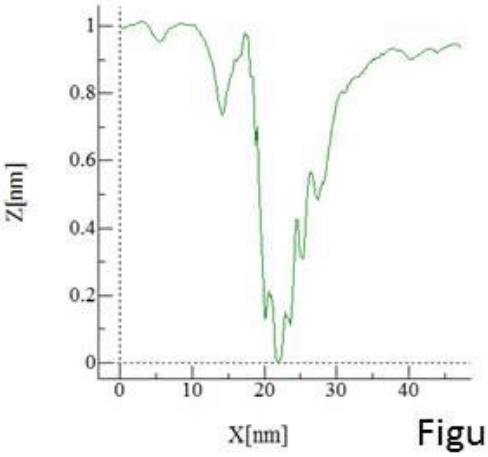

Figure 2

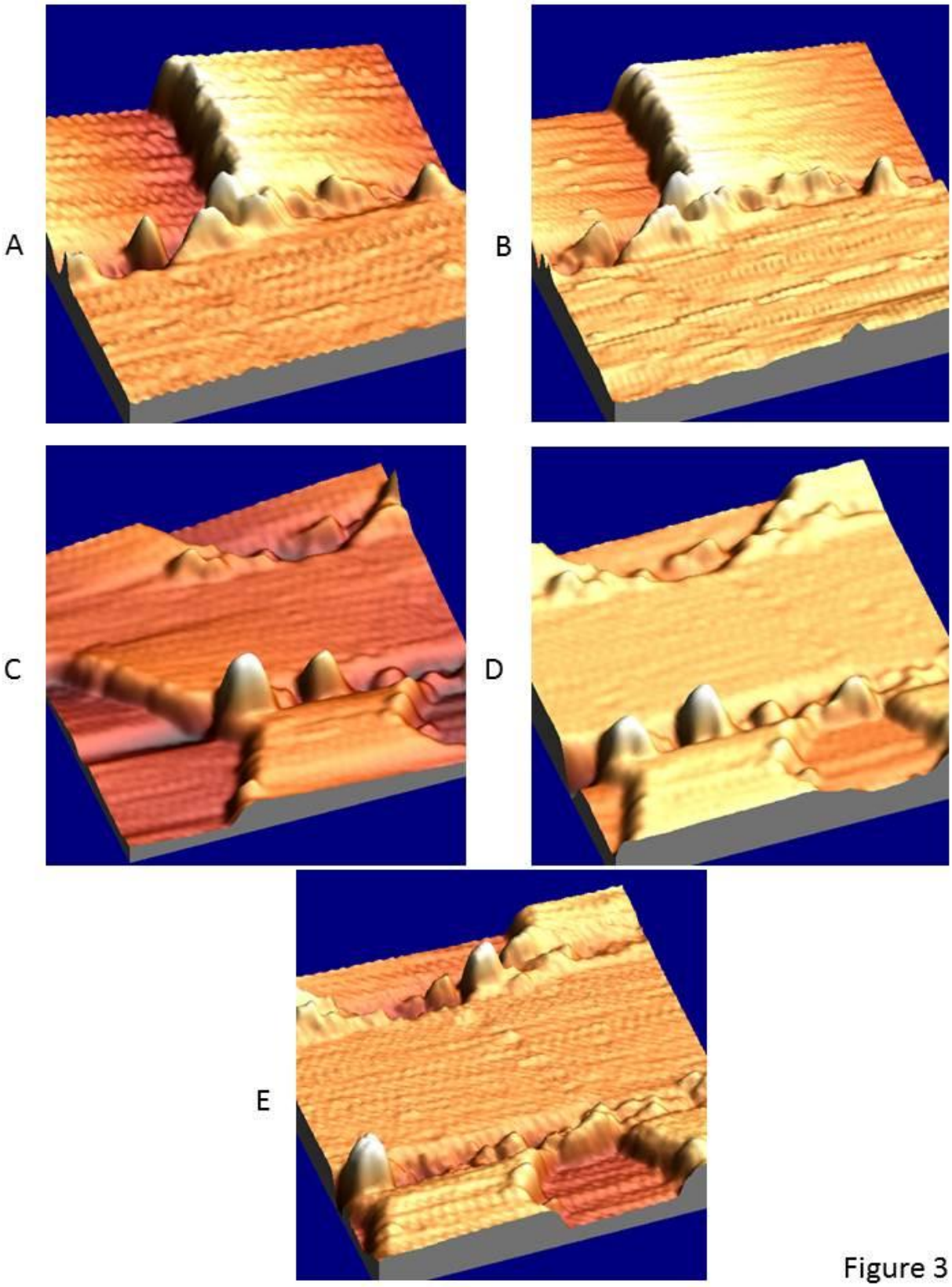

Figure 3

Figure 4

A

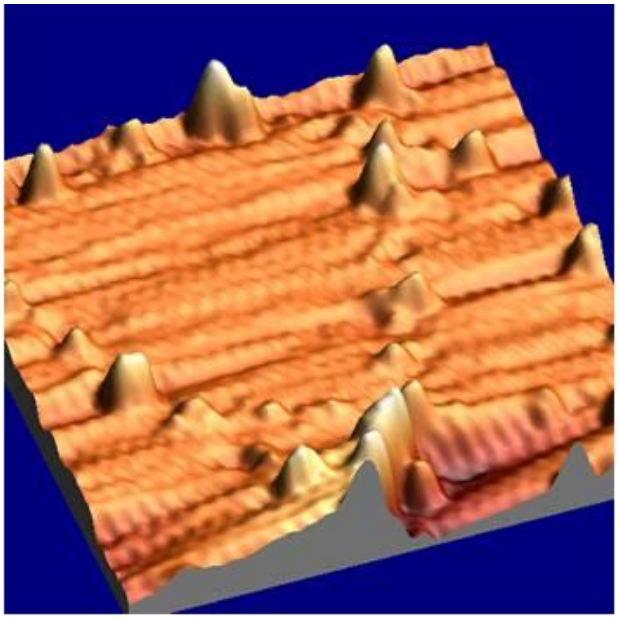

B

C

D

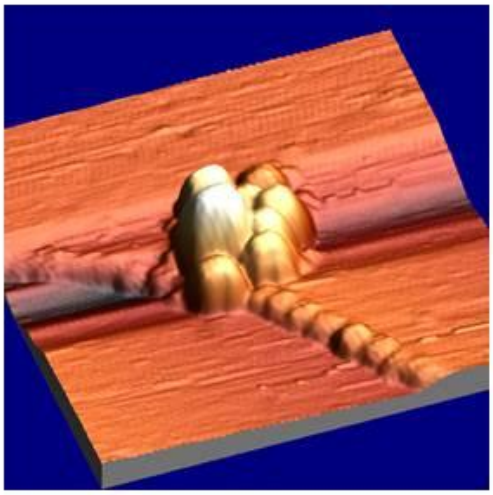

E

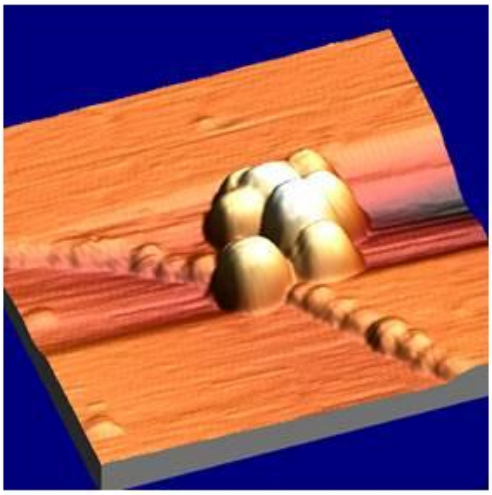

CHAPTER V FIGURES

Figure 1. ~2.5ML of Pentacene of the Si(111)-(√3 x √3)-Ag at R.T. (A) - Close up Pentacene 'Brick wall' 1.2V, 400pA, 7x7nm^2; (B) – Pentacene 'Brick wall' with vacancies in top layer 1.3V, 400pA, 20x20nm^2, (C) – Differentiated image of Pentacene layer 1.2V, 400pA, 12x12nm^2, (D) – Clean Ag-Si-√3, -0.9V, 5nA, 5x5nm^2.

Figure 2. ~4 ML of Pentacene of the Si(111)-(√3 x √3)-Ag at R.T. (A) – Differentiated image of Pentacene islands on the Si -√3 1.3V, 450pA, 1x1um^2; (B) – Pentacene islands on Si -√3 1.2V, 450pA, 250x250nm^2; (C) - 'Brick wall' closeup 1.2V, 450pA, 25x25nm^2; (D) – Pentacene covered terrace 1.2V, 400pA, 50x50nm^2; (E) – Top Pentacene layer resolved 1.3V, 400pA, 10x10nm^2.

Figure 3. 0.75ML of Pentacene nucleation centers on Ag-Si(111) islands at 100K. All images differentiated. (A) – 1.4V, 400pA, 7x7nm^2; (B) – 1.4V, 400pA, 6.5x6.5nm^2; (C) – 1.2V, 400pA, 5.5x5.5nm^2

Figure 4. 0.5ML of Pentacene on 2-layer-Ag-Si(111) islands at 70K. All images differentiated. (A) – Top of island 1.2V, 400pA, 11x11nm^2; (B) – Top of island 1.1V, 430pA, 19x19nm^2; (C) – Top of island 1.1V, 430pA, 11x19nm^2

Figure 5. 0.5ML of Pentacene on 3-layer-Ag-Si(111) islands at 70K. All images differentiated. (A) – Top of island 1.3V, 430pA, 15x12nm^2; (B) – Top of island 1.1V, 430pA, 18x18nm^2; (C) – Top of island 1.1V, 430pA, 25x18nm^2

Figure 6. 0.75ML of Pentacene on 2/3-layer-Ag-Si(111) islands at 100K. All images differentiated. (A) – 1.4V, 400pA, 100x100nm^2; (B) – 3 layer -Left 1.2V, 327pA, 21x21nm^2 ; 2 layer - Right 1.1V, 300pA, 21x21nm^2

Figure 7. 0.75ML of Pentacene on 3-layer-Ag-Si(111) islands at 100K. All images differentiated. (A) – 1.4V, 350pA, 100x100nm^2; (B) – 1.4V, 350pA, 16.5x16.5nm^2; (C) – 1.4V, 350pA, 24x20nm^2; (D) – 1.4V, 350pA, 33x27nm^2

Figure 8. Ag islands on Si(111) grown together over a step. (A) -1.8 V, 253pA, 100x100nm^2; (B) - Line Profile of Left Island; (D) – Line Profile of Right Island; (E) – Side view diagram of the two islands and interaction with the step.

Figure 9. Fused 2/3 layer Ag islands over a Si step – close up of surface. (A) – 2 layer high island top; (B) – 3 layer island on left, 2 layer high island on right; (C) – Line profile over the pentacene overlayer at two island's junction.

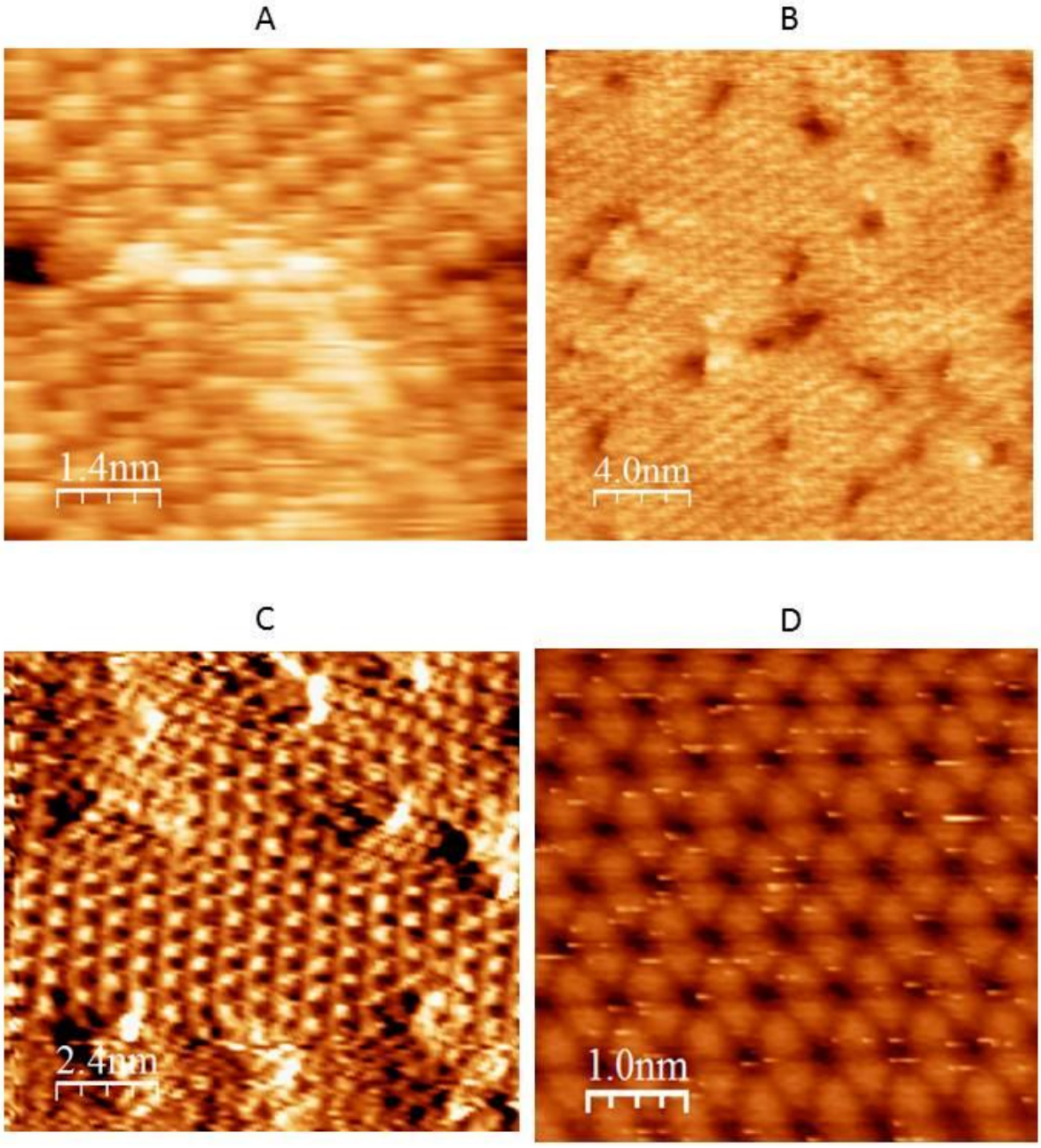

Figure 1

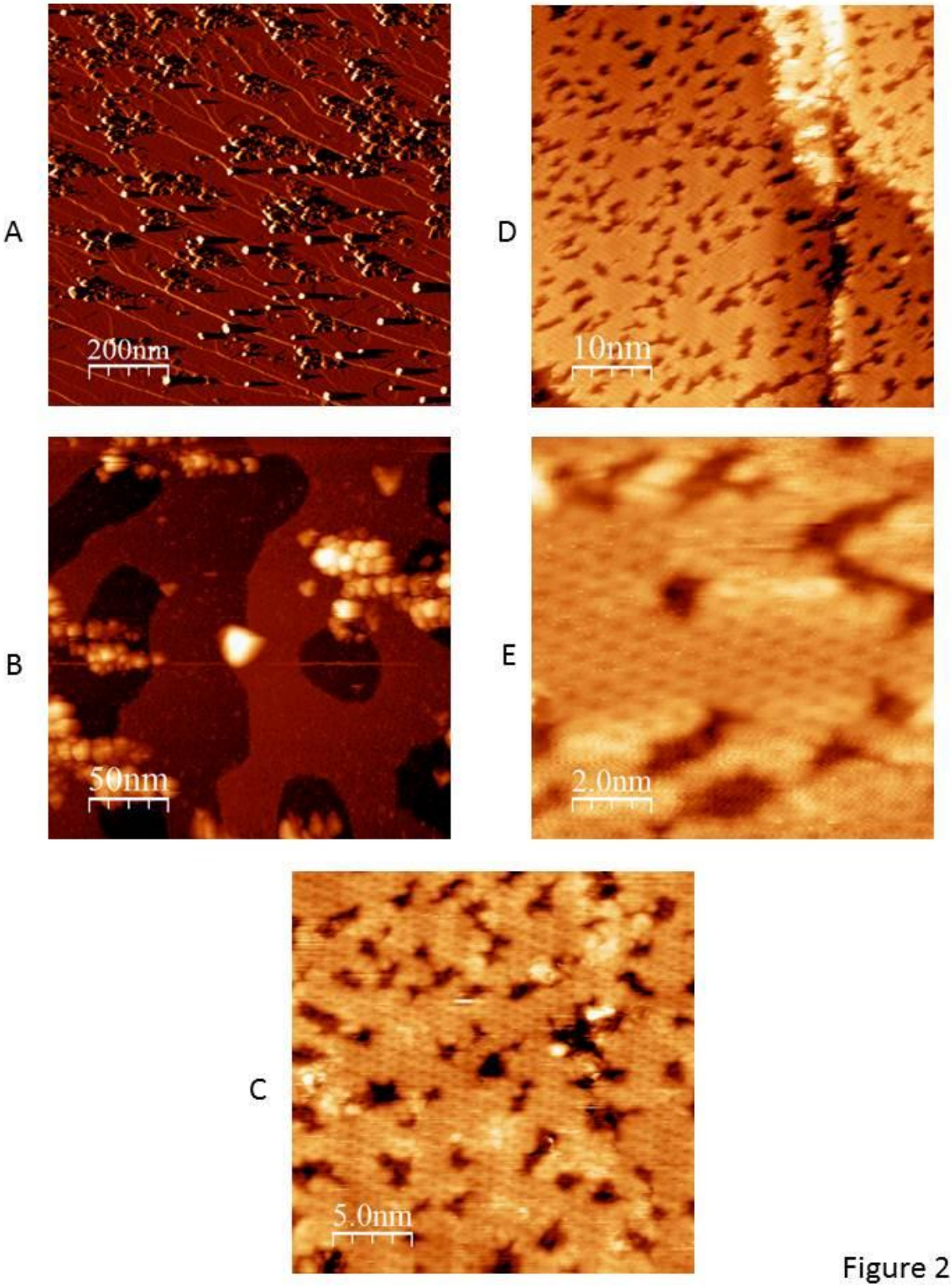

Figure 2

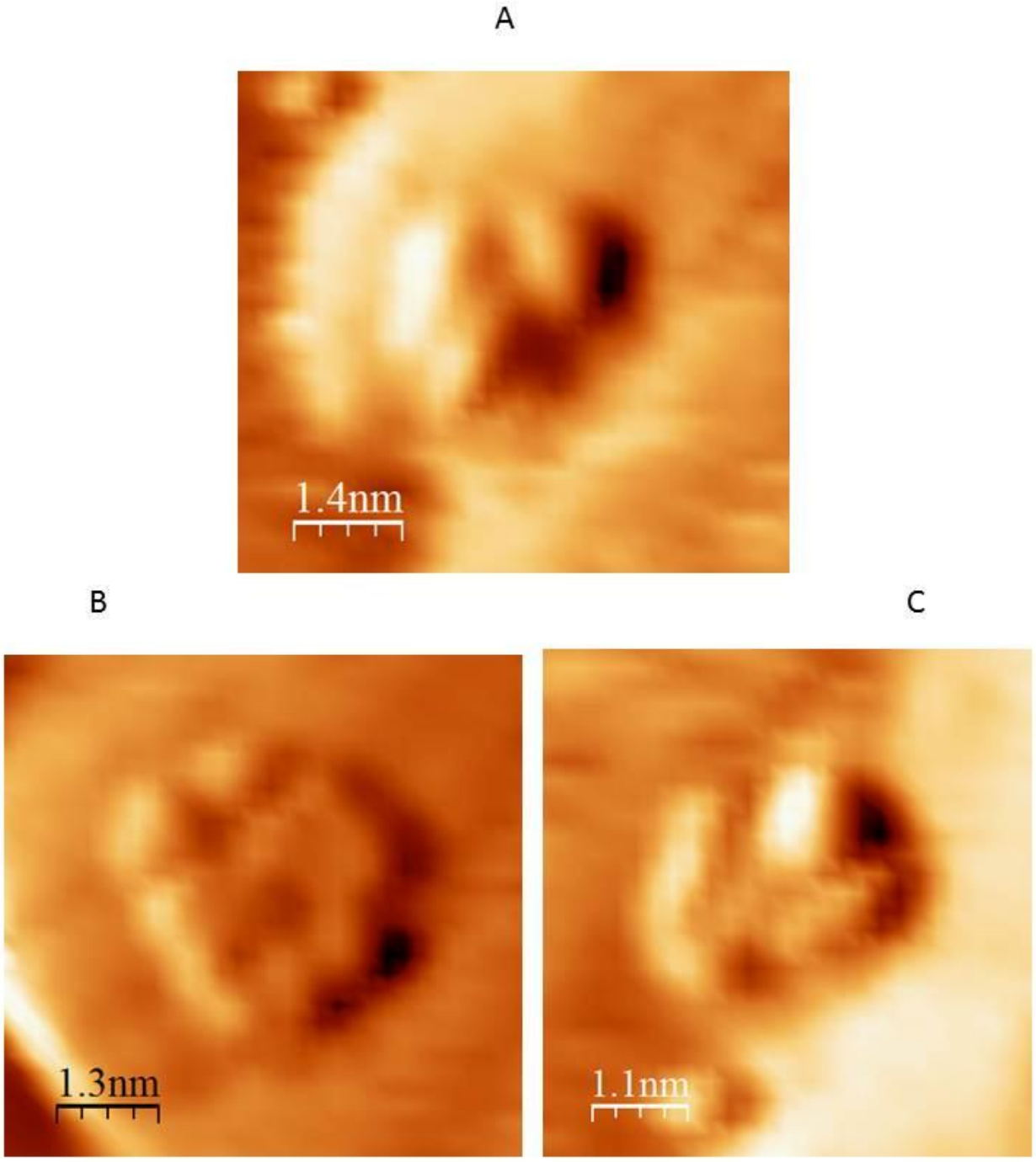

Figure 3

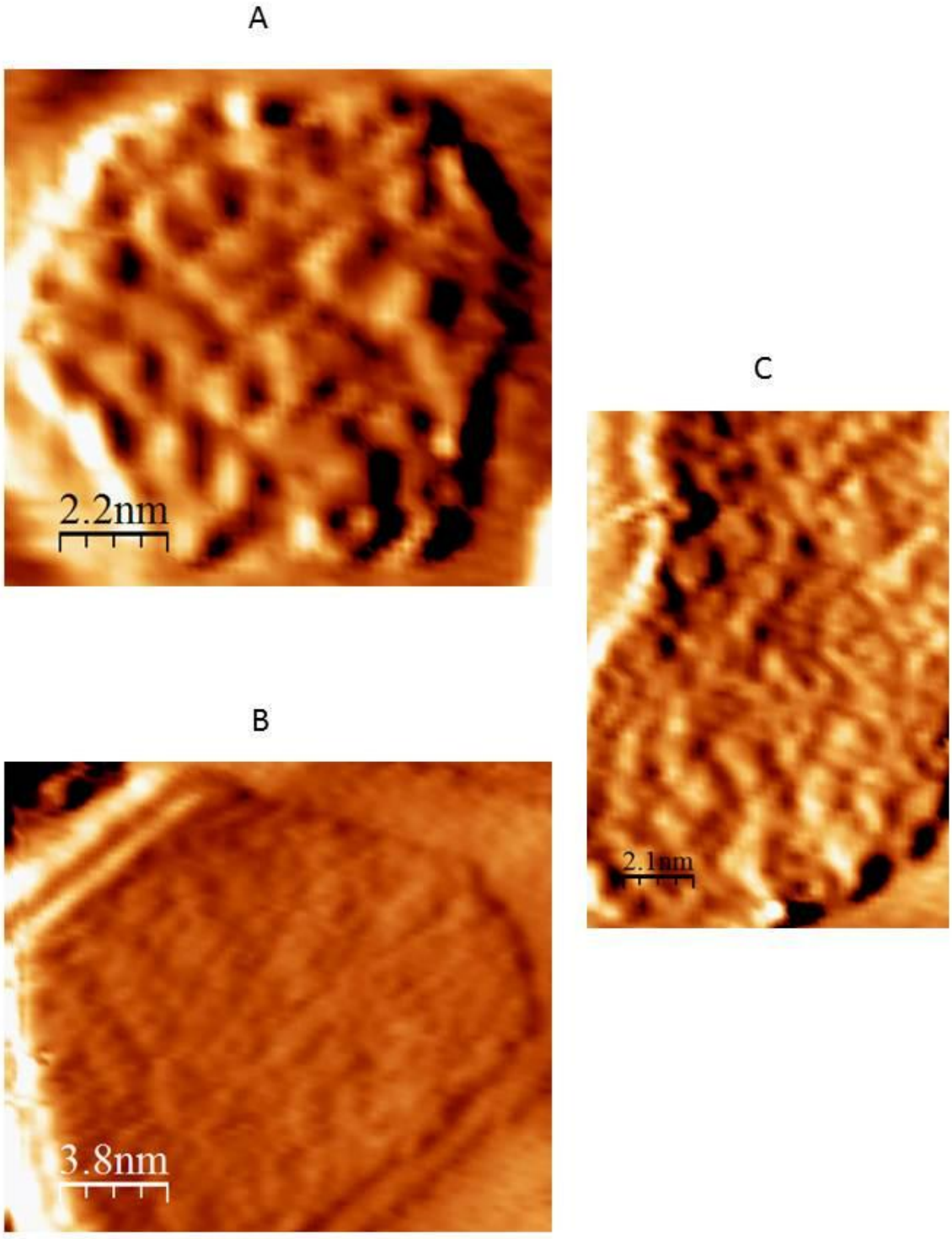

Figure 4

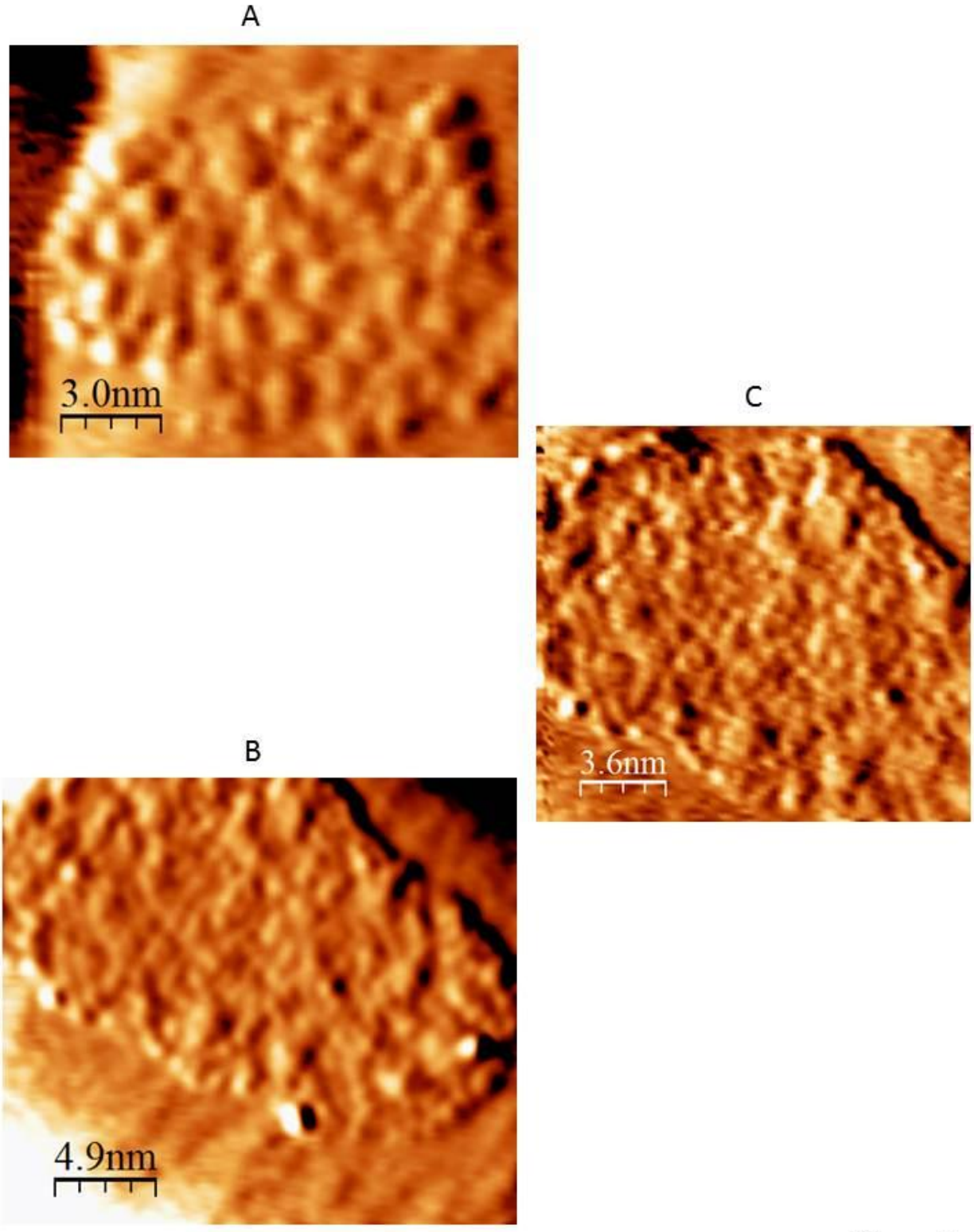

Figure 5

A

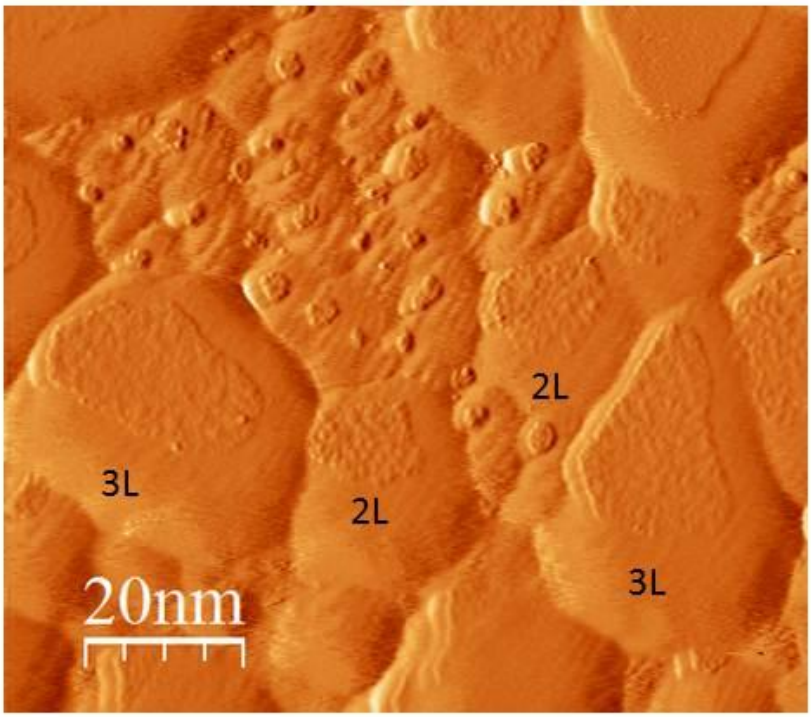

B

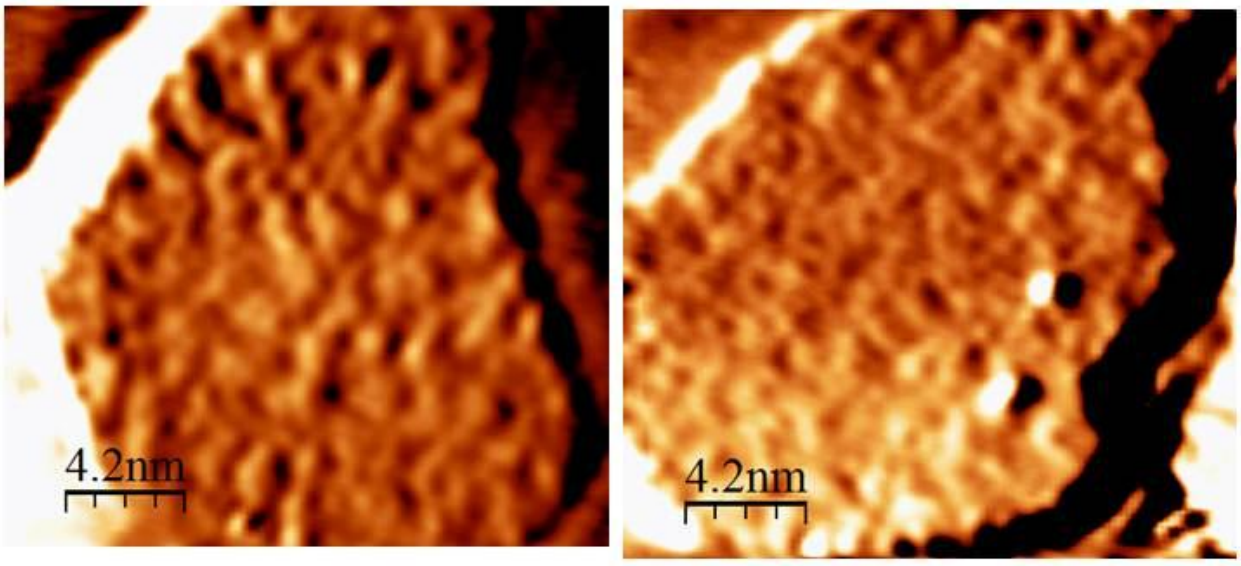

Figure 6

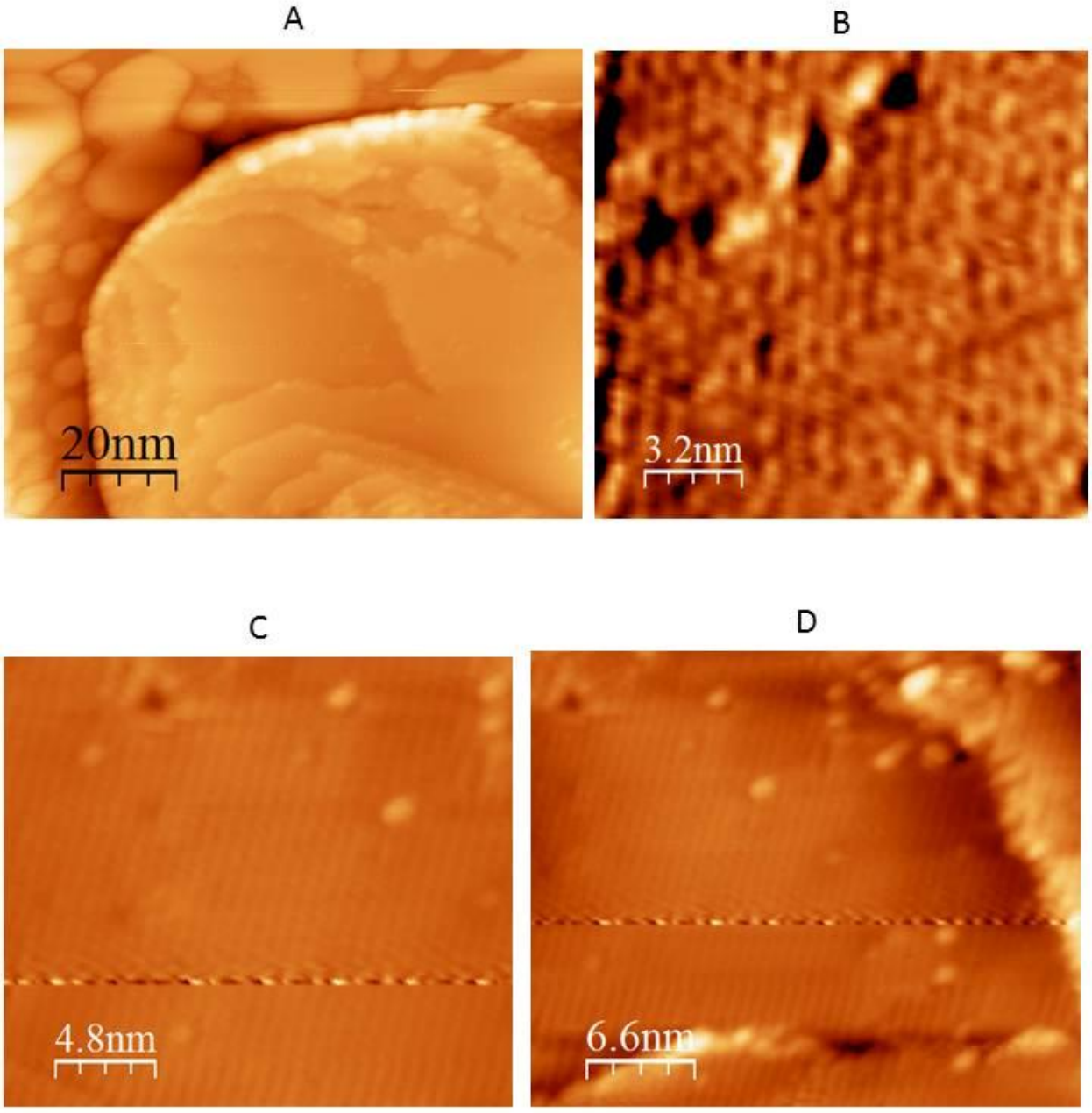

Figure 7

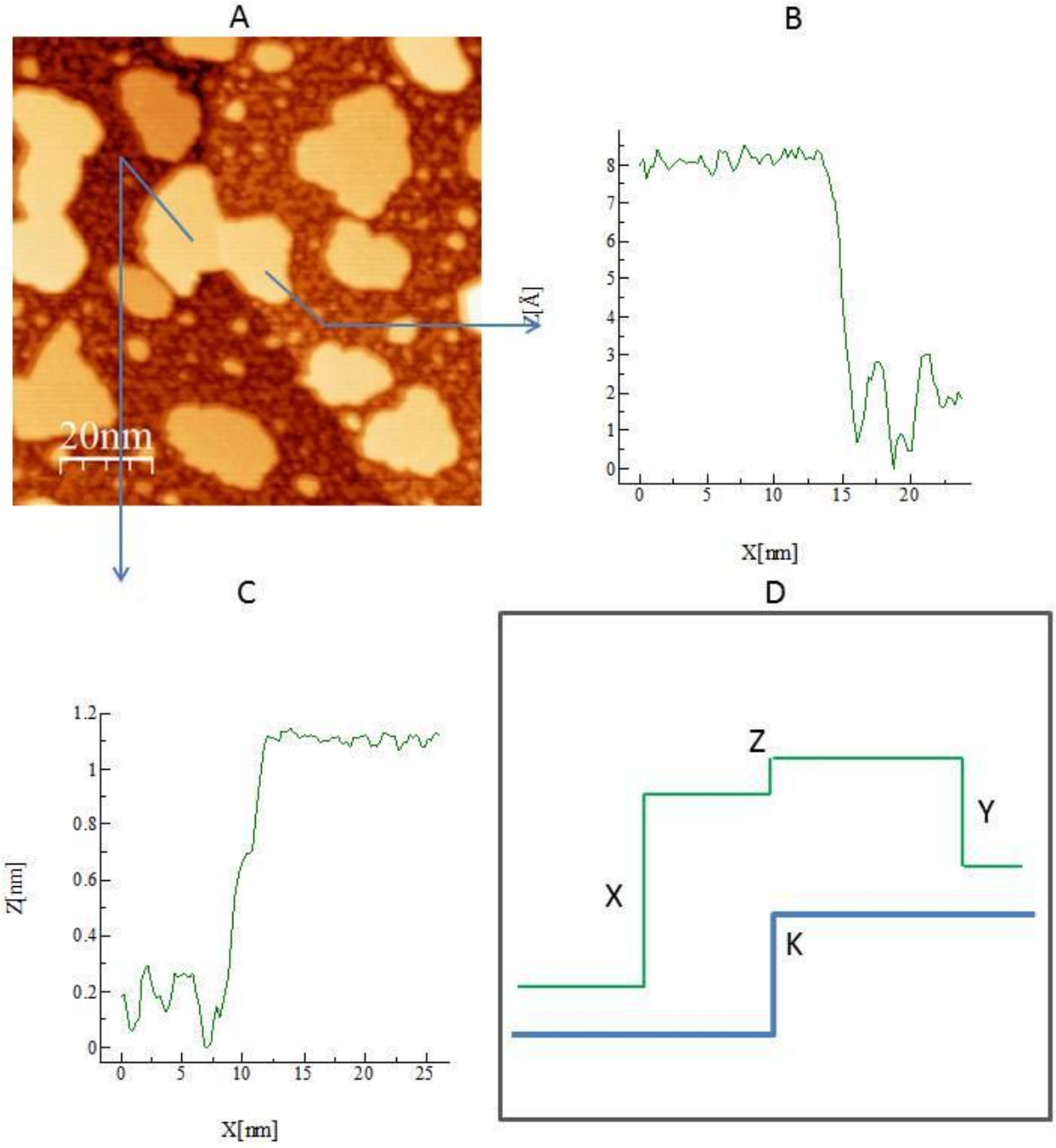

Figure 8

A

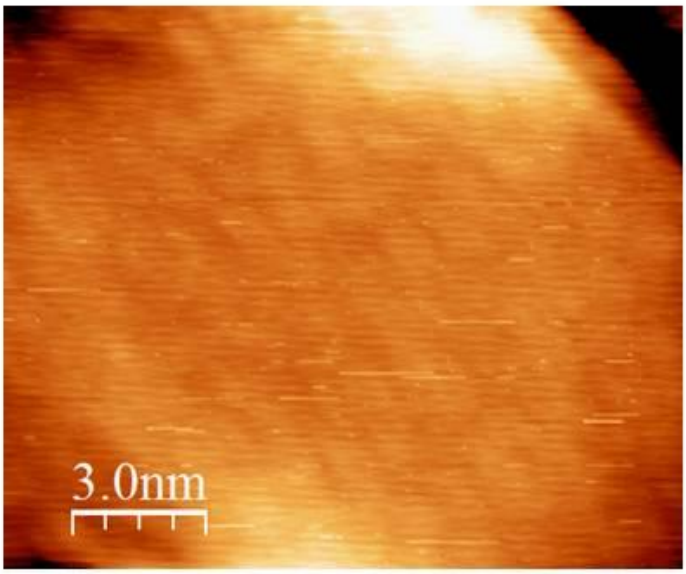

B

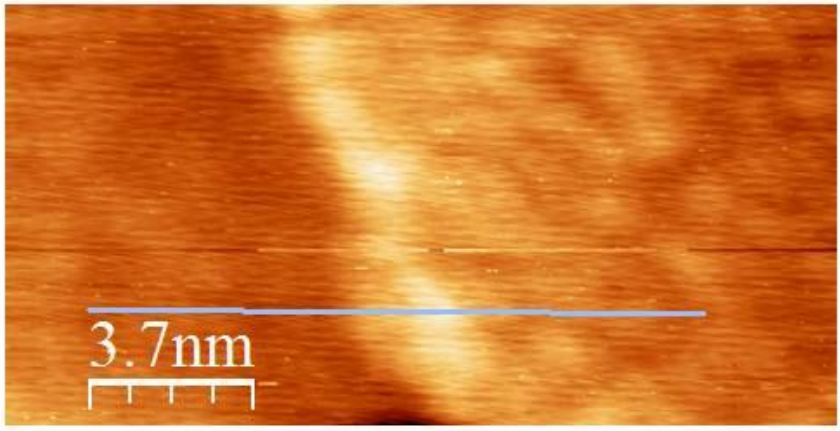

C

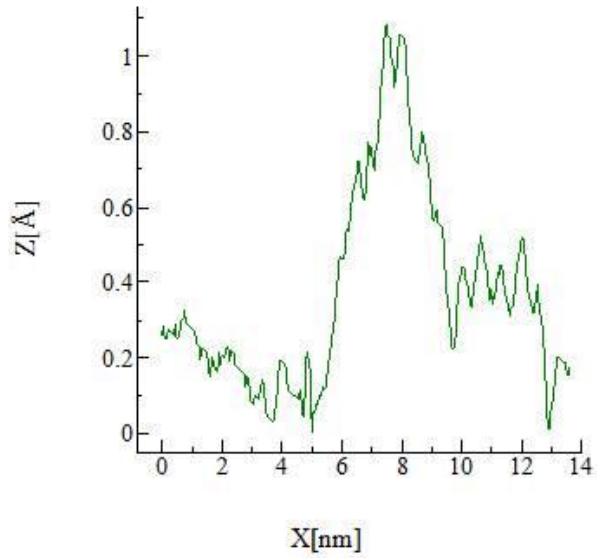

Figure 9

CHAPTER VI FIGURES

Figure 1. Au on Si(111) at RT. (A) –Clean Si(111)-(7x7), 100x100nm^2, 1.0V, 200pA; (B) – 0.3ML of Au, 100x100nm^2, -0.74V, 6.4nA; (C) – 0.6ML of Au, 250x250nm^2, -0.66V, 6.4nA; (D) – 1 ML of Au, 250x250nm^2, -1.1V, 5.1nA.

Figure 2. 1ML of Au on Si(111) post 800K anneal for 1.5 min. (A) –Au - Island Hole, 500x500nm^2, -2.5, 3.7nA; (B) - 100x100nm^2, -2.0V, 6nA; (C) – 50x50nm2, -1.3V, 6nA; (D) – 25x25nm^2, -1.0V, 6nA, the rectangle shows a single (5x2) unit cell.

Figure 3. 1 ML of Au on Si-(111)-($\sqrt{3}$x$\sqrt{3}$)R30-Ag at RT, Au islands formation and growth. (A) – 1x1um^2, -2.0V, 5nA Differentiated; (B) – 100x100nm^2, -1.2V, 5nA, Blue arrows indicate locations of grain boundaries in the Ag-$\sqrt{3}$; (C) - 100x100nm^2, -1.2V, 5nA, Blue arrows indicate locations of grain boundaries in the Ag-$\sqrt{3}$; (D) – 50x50nm^2, -0.95V, 5nA.

Figure 4. 1 ML of Au on Si-(111)-($\sqrt{3}$x$\sqrt{3}$)R30-Ag at RT, Mounds of Au-silicide. (A) – Mound Silicide on terrace, 500x500nm^2, -2.2V, 5nA Differentiated; (B) – 250x250nm^2, -2.0V, 0.5nA, Differentiated; (C) - 140x140nm^2, -2.0V, 5nA, Differentiated; (D) Line profile of the Mound in (C) – topographic image, (E) – 150x150nm^2, -2.0V, 500pA, Differentiated; (F) – 150x150nm^2, -2.0V, 500pA, Differentiated; (G) – 150x150nm^2, -2.0 V, 5nA, Differentiated; (H) – 150x150nm^2, -2.0V, 5nA, Differentiated; (I) – Post 2 min 500K anneal, 100x100nm^2, -2.0V, 7.7nA; (J) – Post 2 min 500K anneal, 100x100nm^2, -2.0V, 7.7nA; (K) – Post 2 min 500K anneal, 100x100nm^2, -1.5V, 7.7nA; (L) - Post 2 min 500K anneal, 1x1um^2, -2.0V, 7.7nA, Differentiated.

Figure 5. Au & Si phase diagrams. A) - Phase Diagram for 1ML of Au on Si (111) for T 100-900 C, from reference [7]; (B) - Au-Si phase diagram from MTDATA from UK National Physical Laboratory.

Figure 6. 1.25 ML of Au on Si-(111)-($\sqrt{3}$x$\sqrt{3}$)R30-Ag post 500K anneal for 2 mins. (A) – Au islands and Silicide formation on terrace 500x500nm^2, -4.0V, 0.7nA, Differentiated; (B) –

Gold Silicide etching the steps 250x250nm^2, -2.0V, 0.7nA; (C) – Silicide Mound 100x100nm^2, -2.0V, 7.7nA; (D) – Line profile of (C).

Figure 7. 1.25ML of Au on the Si-(111)-(√3x√3)R30-Ag. (A) – Au at RT, 450 islands and 3 mounds, high preference for steps, 500x500nm^2, -2.0V, 7.7nA, Differentiated; (B) – Au post 500K anneal, 2 islands and 11 mounds, 500x500nm^2, -2.0V, 600pA Differentiated; (C) – Au post 600K anneal, 1x1um^2, -3.0V, 772pA, Differentiated; (D) - Au post 600K anneal, 1x1um^2, -3.0V, 772pA, Differentiated.

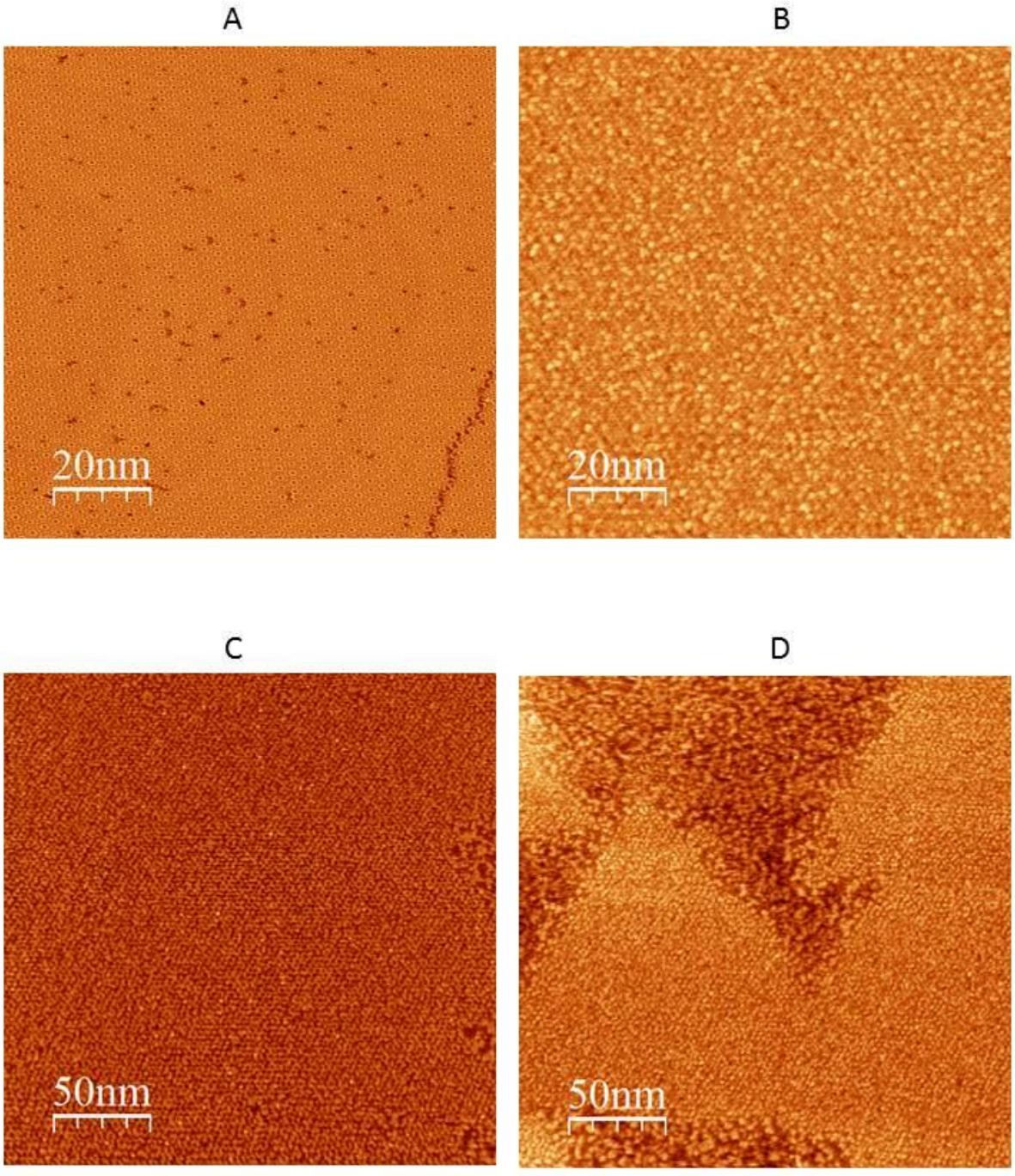

Figure 1

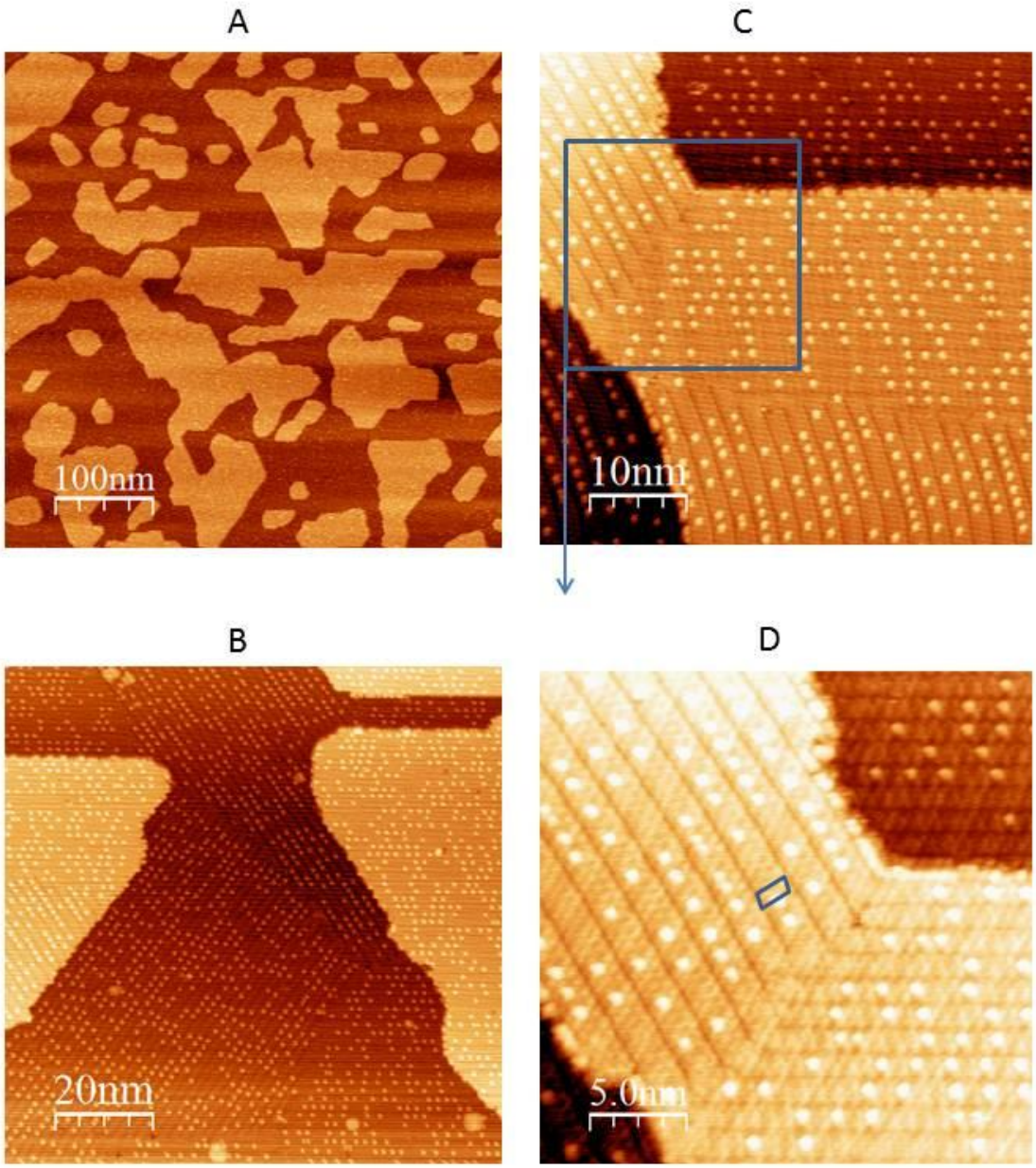

Figure 2

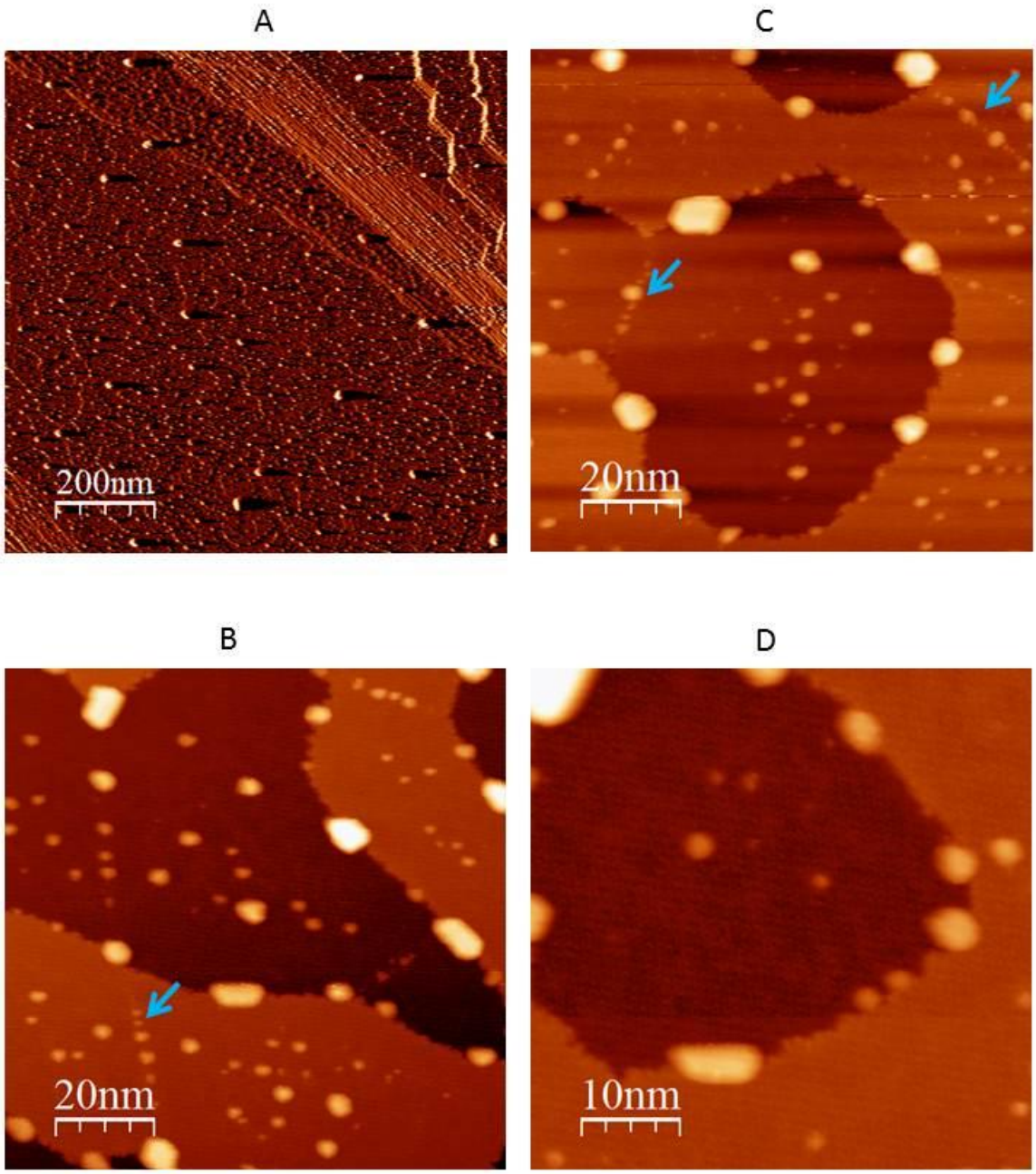

Figure 3

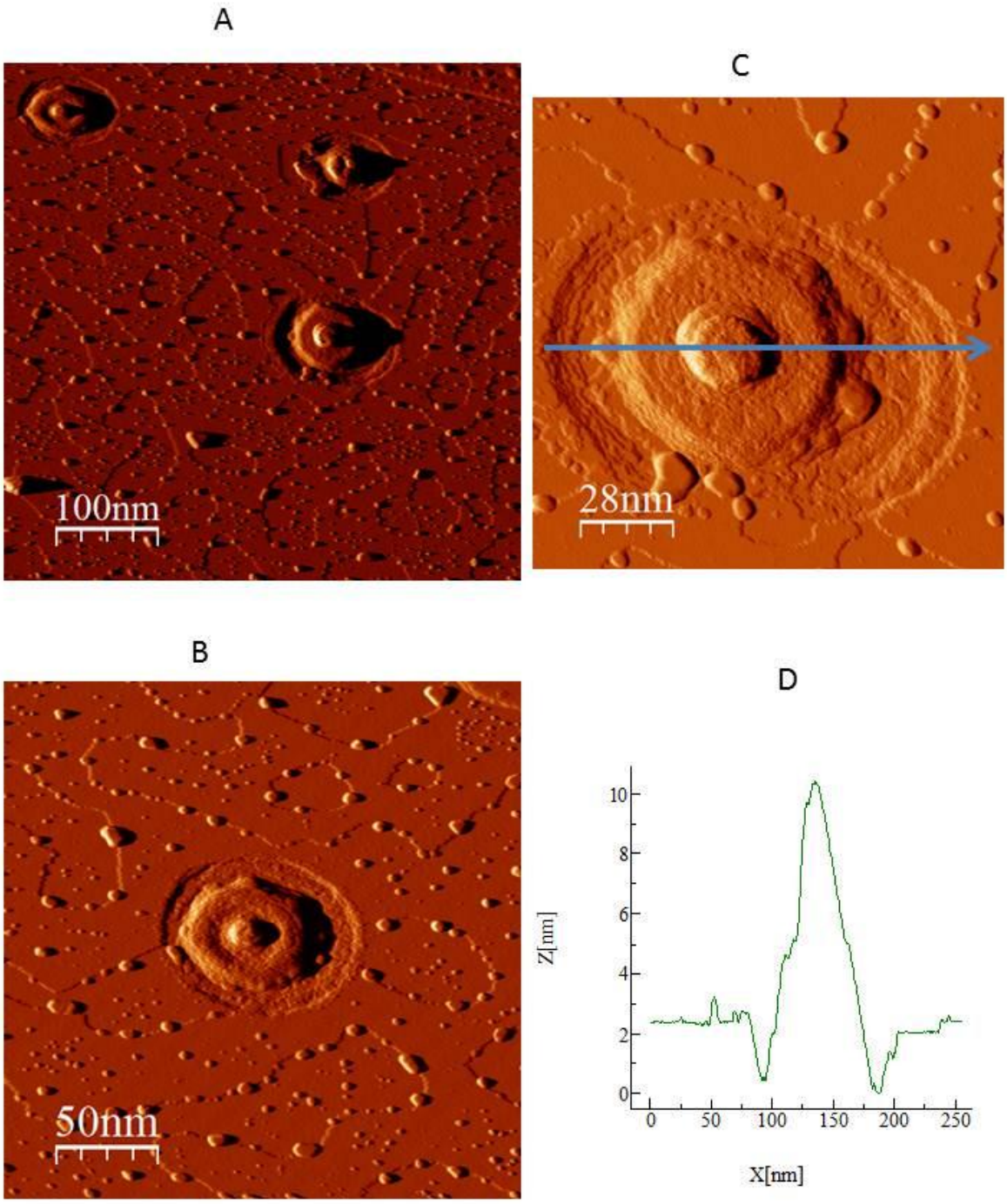

Figure 4

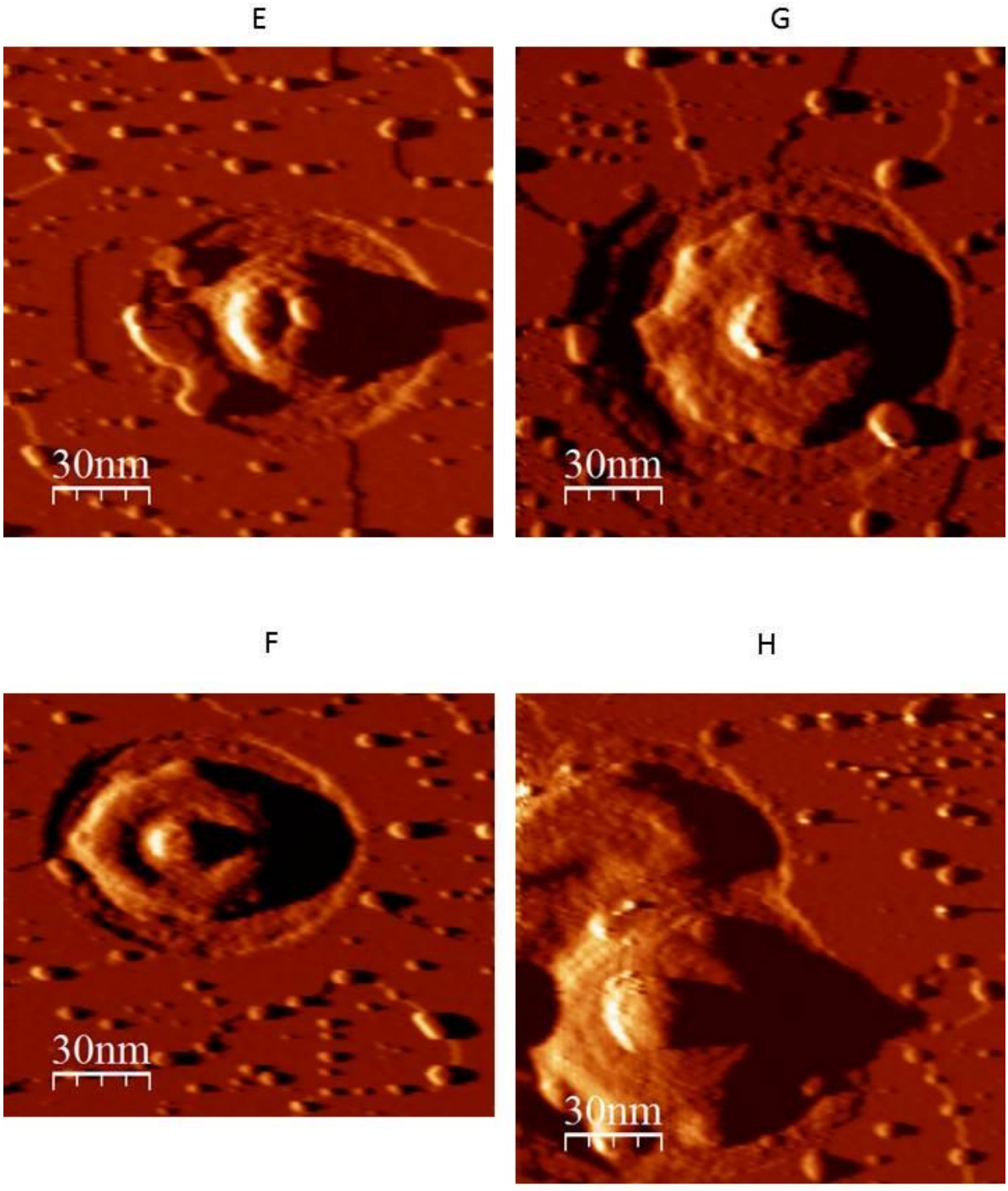

Figure 4

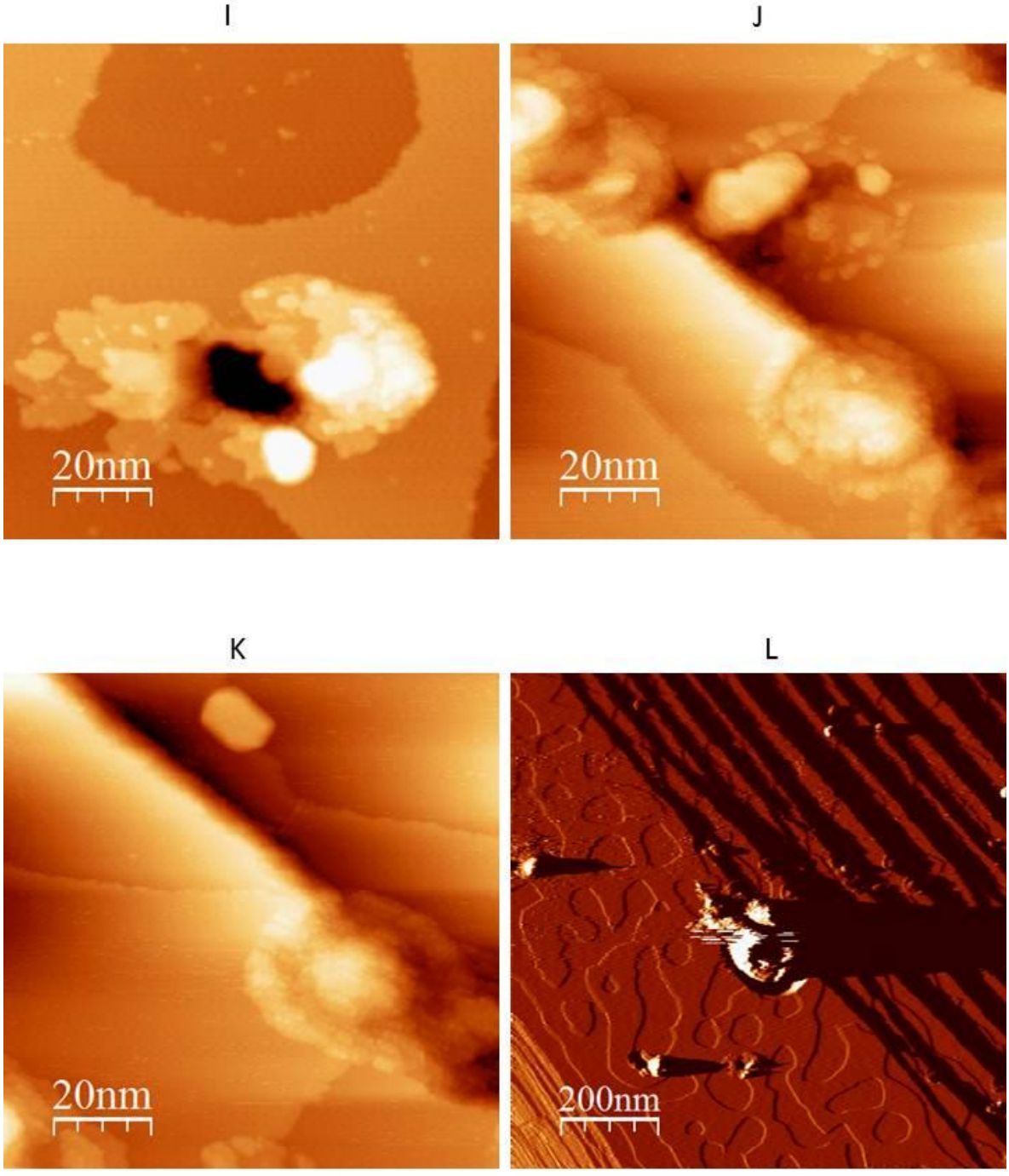

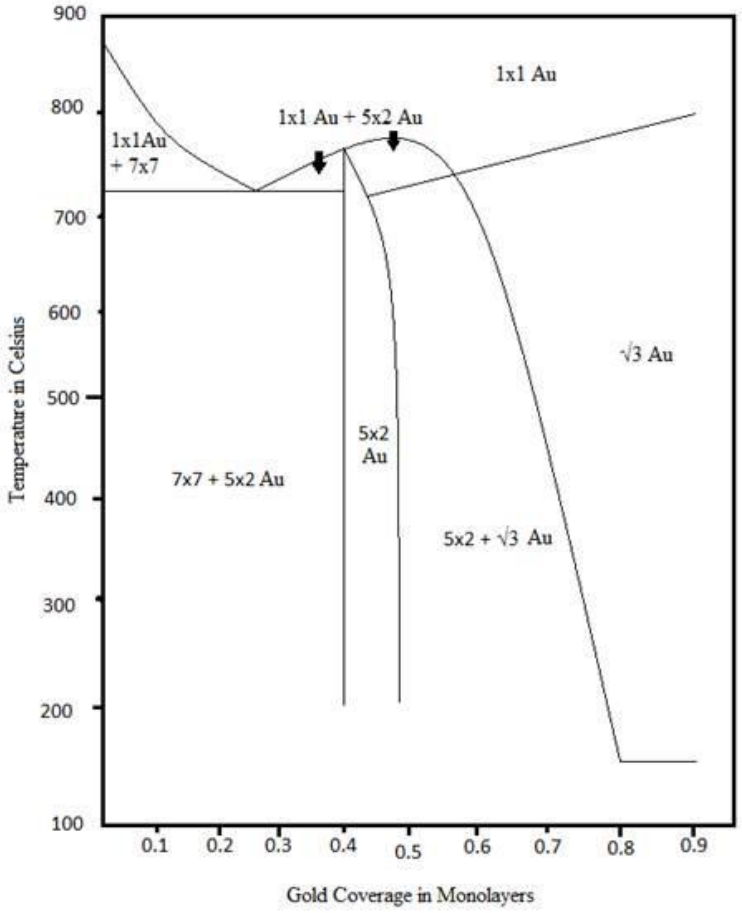

A

B

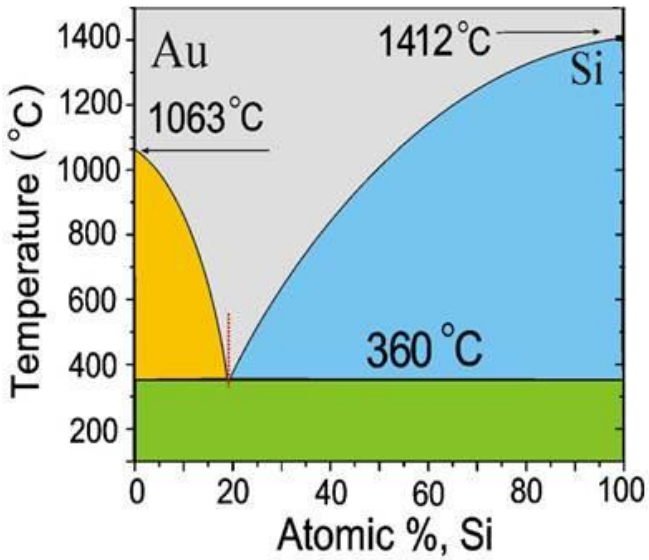

Figure 5

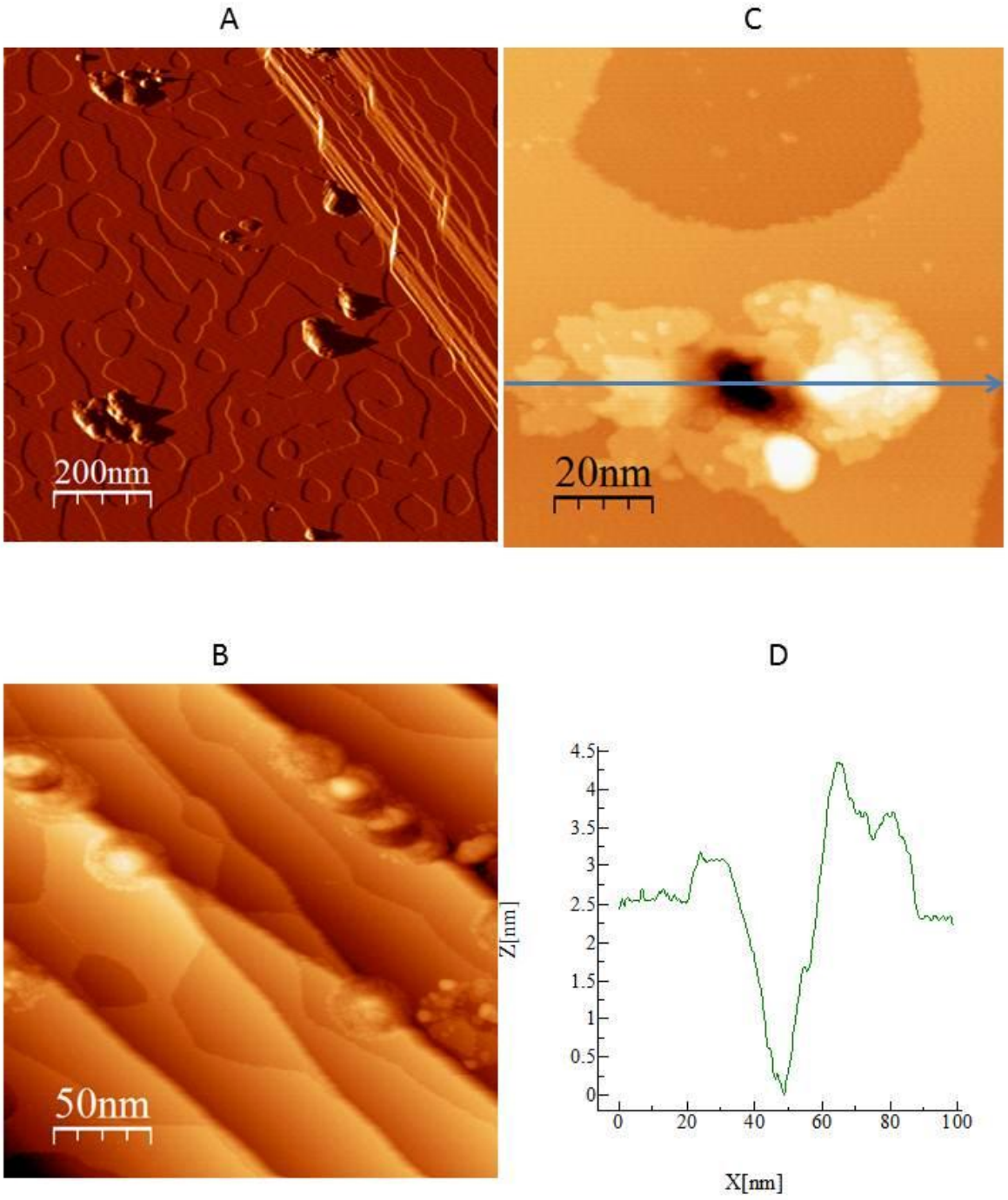

Figure 6

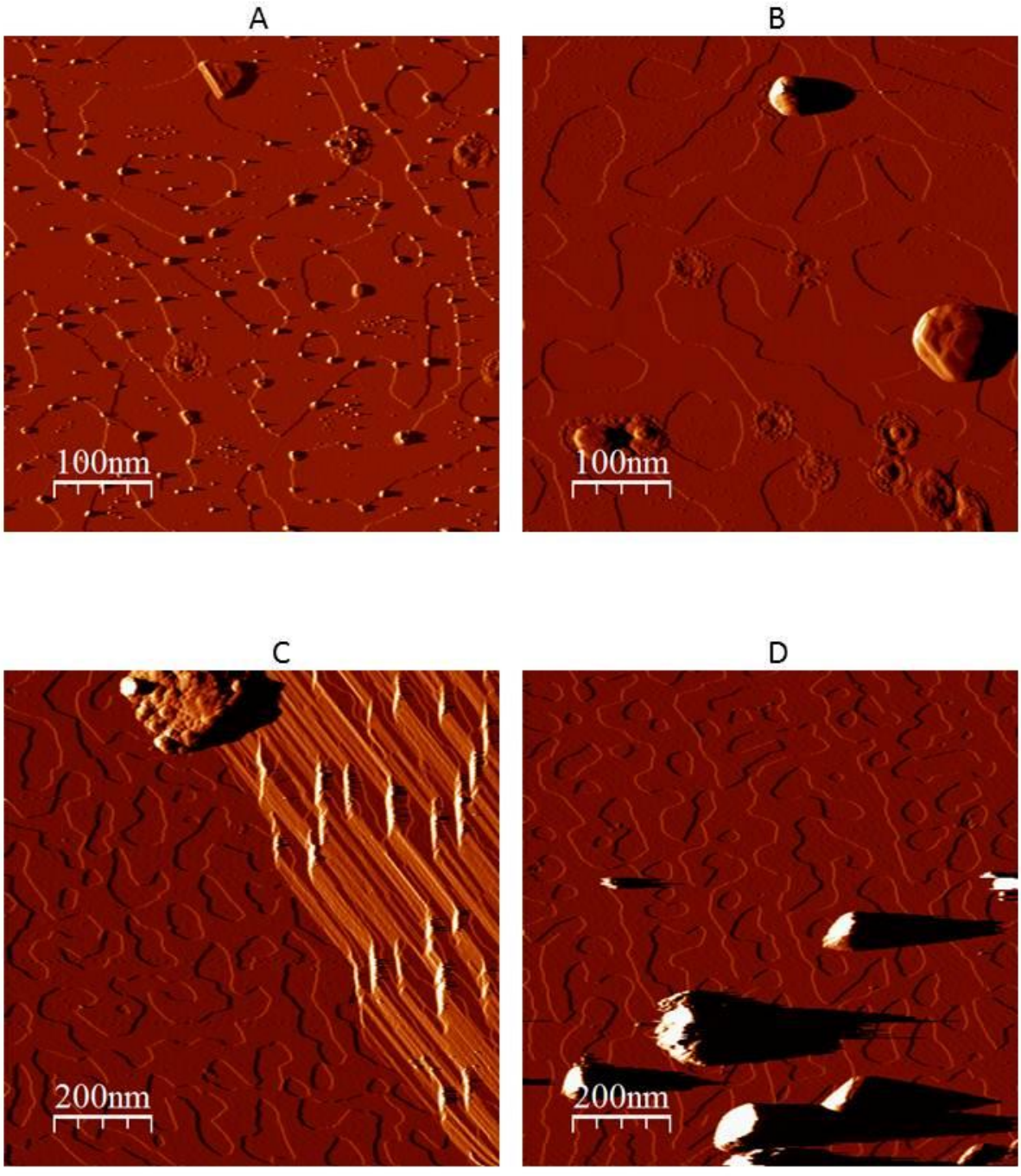

Figure 7

Schematic Representation of the Au-Si silicide mound with spatial dimensions

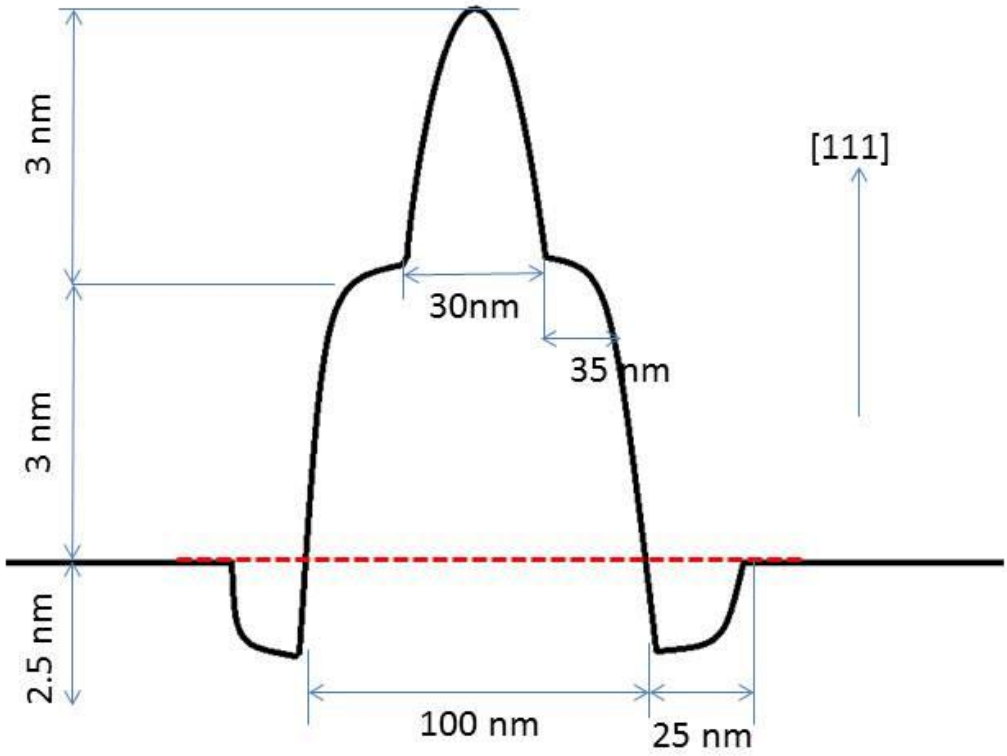

Side View

Figure 8

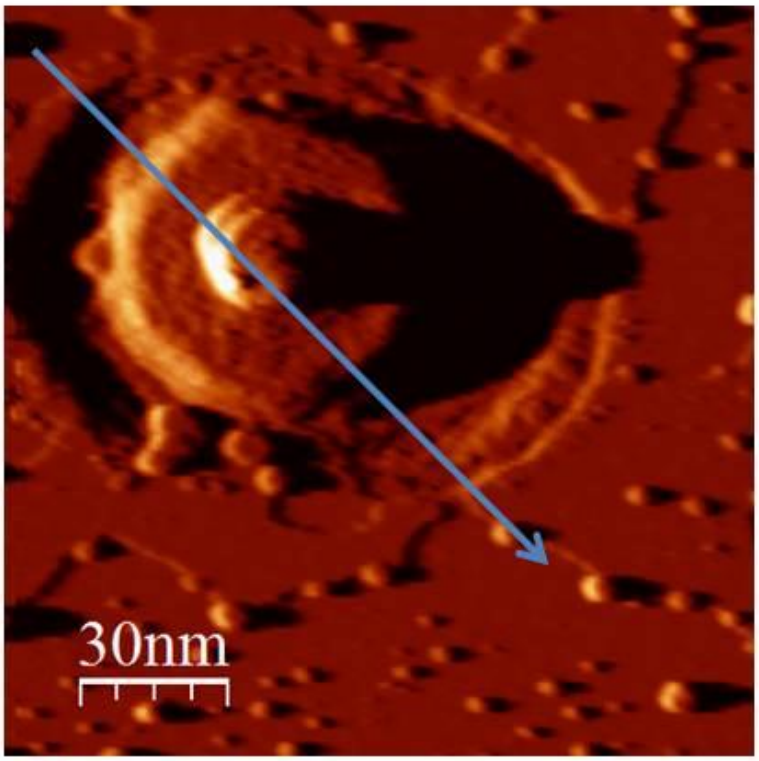

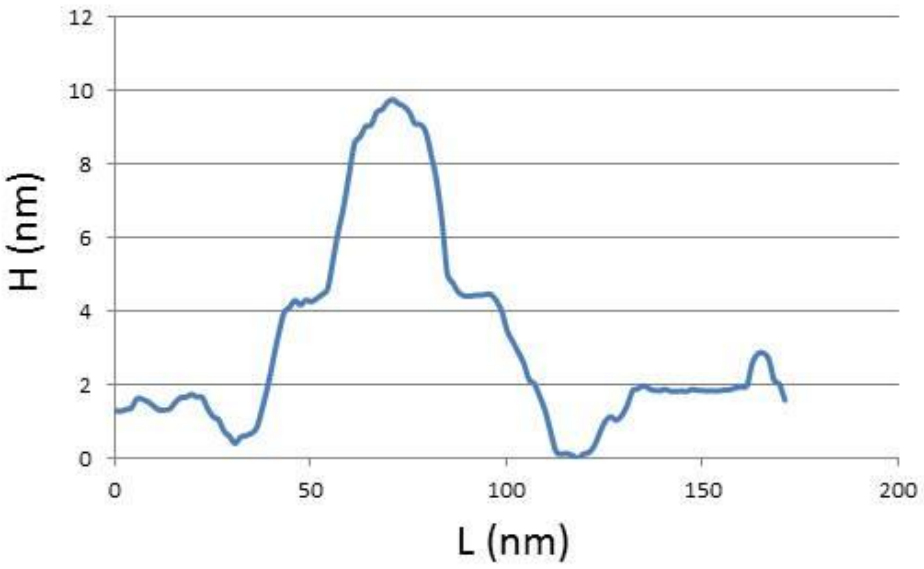

Mote (nm3)	Above Surface (nm3)	Island within hole (nm3)
2781	10098	8303

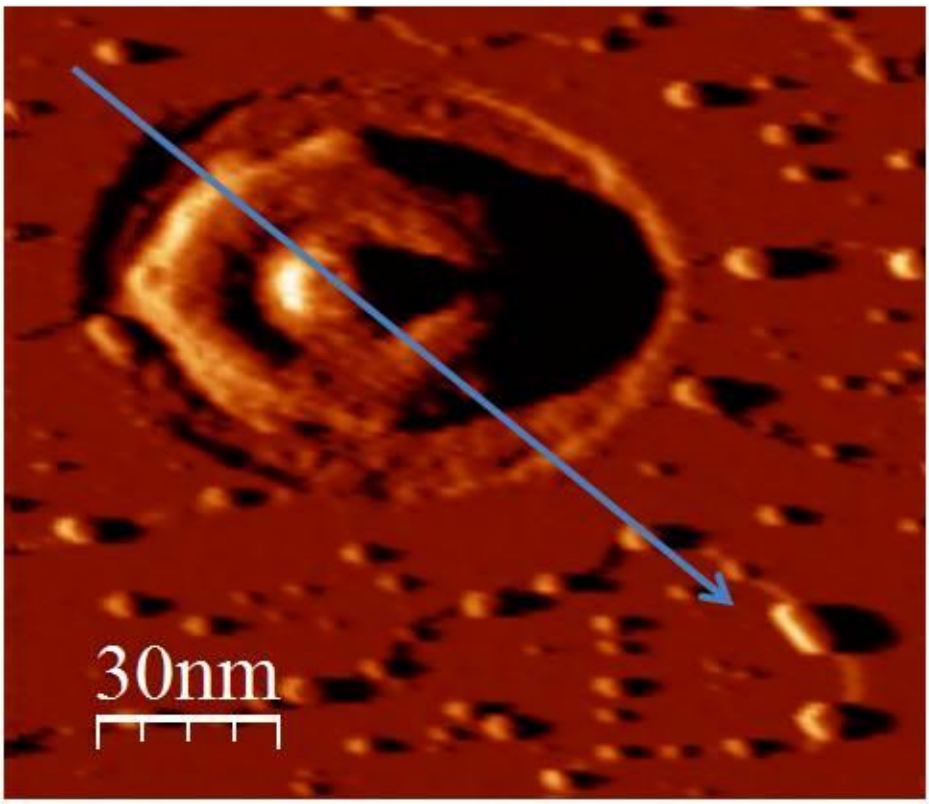

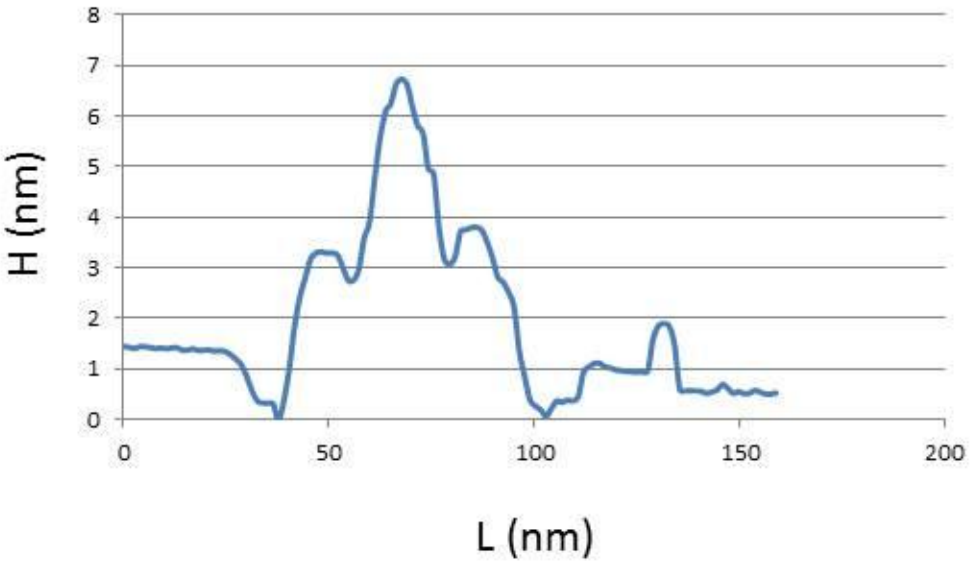

Mote (nm3)	Above Surface (nm3)	Island within hole (nm3)
1293	4316	5157

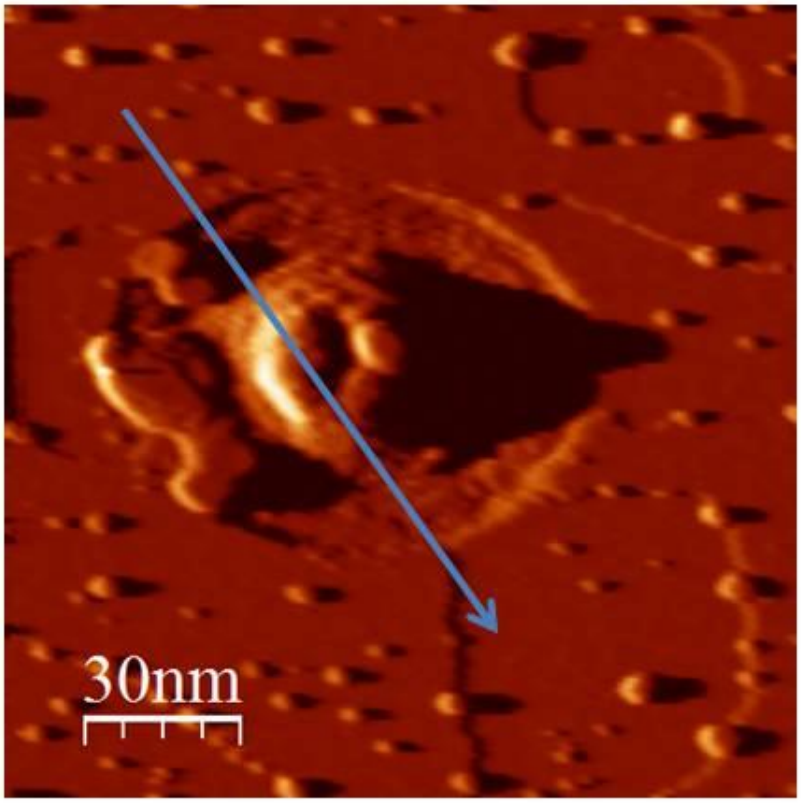

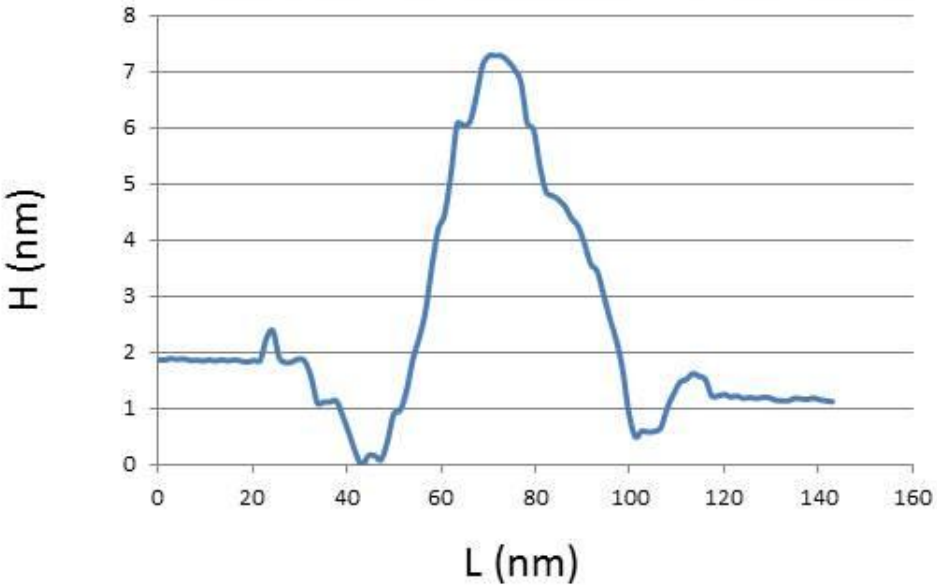

Mote (nm3)	Above Surface (nm3)	Island within hole (nm3)
1921	4769	6492

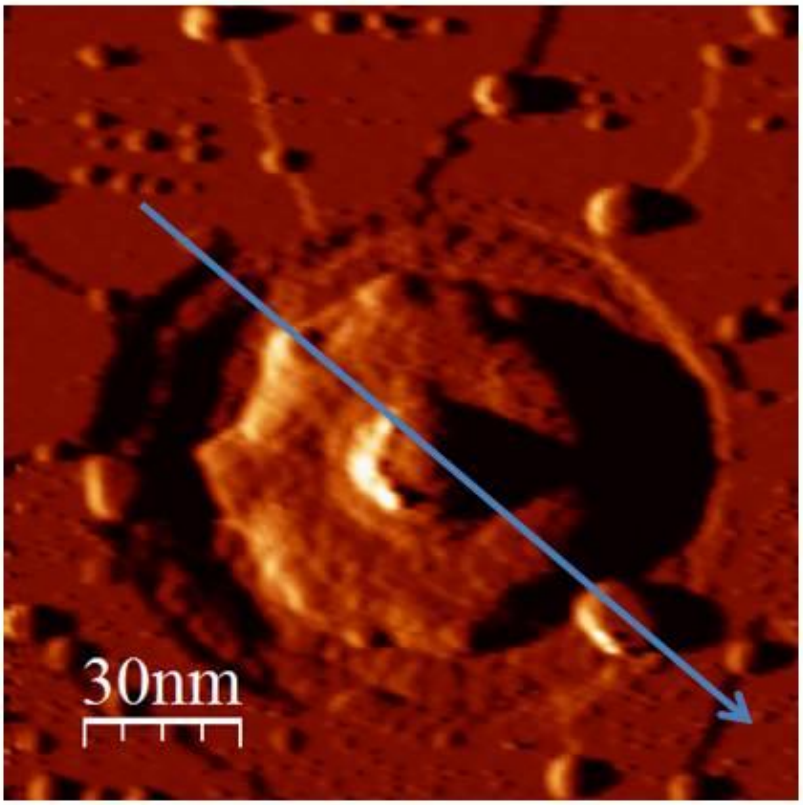

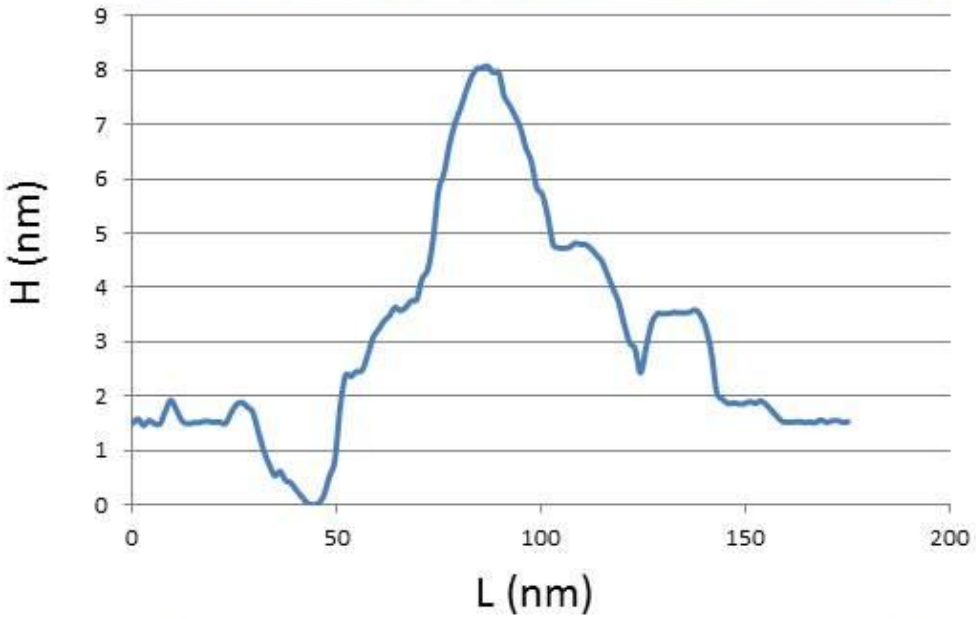

Mote (nm3)	Above Surface (nm3)	Island within hole (nm3)
3290	9121	9125

CHAPTER VII FIGURES

Figure 1. Ag on the Ag-Si(111)-(√3x√3)R30. (A) – Clean Ag-Si(111)-(√3x√3)R30, 50x50nm^2 -0.69V, 8.4nA; (B) – 10 ML of Ag on Ag-Si-√3, -3V, 726pA, 1x1um^2, Differentiated; (C) – 10 ML of Ag on Ag-Si-√3, -0.67V, 726pA, 50x50nm^2; (D) - 10 ML of Ag on Ag-Si-√3, -3V, 726pA, 1x1um^2, Differentiated.

Figure 2. 10 ML of Ag post 5min 550K anneal on the Ag-Si(111)-(√3x√3)R30. (A) – 1x1um^2, -3.0V, 500pA, Differentiated; (B) – 250x250nm^2, -2.0V, 5nA, Differentiated; (C) – 100x100nm^2, -2.0V, 5nA; (D) – 10x10nm^2, -0.21V, 5nA

Figure 3. 10 ML of Ag post 5min 600K anneal on the Ag-Si(111)-(√3x√3)R30. (A) – 1x1um^2, -3.0V, 726pA, Differentiated; (B) – 500x500nm^2, -2.0V, 726pA, Differentiated; (C) – 100x100nm^2, -1.0V, 7.2nA; (D) – 50x50nm^2, -1.5V, 7.2nA, Blue square highlights a different step decoration at this surface compared to the RT Ag-Si-√3.

Figure 4. 10 ML of Ag post 5min 650K anneal on the Ag-Si(111)-(√3x√3)R30. (A) – 1x1um^2, -3.0V, 726pA, Differentiated; (B) – 500x500nm^2, -3.0V, 726pA, Differentiated; (C) – 250x250nm^2, -3.0V, 500nA, Differentiated; (D) – 250x250nm^2, -3.0V, 500nA, Differentiated.

Figure 5. 10 ML of Ag post 5min 700K anneal on the Ag-Si(111)-(√3x√3)R30. (A) – 1x1um^2, -3.0V, 500pA, Differentiated; (B) – 250x250nm2, -3.0V, 500pA, Differentiated; (C) – 100x100nm^2, -2.0V, 5nA; (D) – 50x50nm^2, -2.0V, 5nA

Figure 6. 10 ML of Ag post 5min 750K anneal on the Ag-Si(111)-(√3x√3)R30. (A) – 1x1um^2, -7.0V, 500pA, Differentiated; (B) – 1x1um^2, -3.0V, 500pA, Differentiated; (C) – 50x50nm^2, -2.0V, 5nA; (D) – 18.5x18.5nm^2, -2.0V, 5nA

Figure 7. 10 ML of Ag post 5min 800K anneal on the Ag-Si(111)-(√3x√3)R30. (A) – 1x1um^2, -0.9V, 712pA, Differentiated; (B) – 1x1um^2, -0.9V, 712pA, Differentiated; (C) – 100x100nm^2, -1.5V, 5nA; (D) – 36x36nm^2, -1.5V, 5nA

Figure 8. 10 ML of Ag post 5min 850K anneal on the Ag-Si(111)-(√3x√3)R30. (A) – 1x1um^2, -3.0V, 500pA, Differentiated; (B) – 1x1um^2, -3.0V, 500pA, Differentiated; (C) – 1x1um^2, -3.0V, 500pA, Differentiated; D) – 1x1um^2, -3.0V, 500pA, Differentiated.

Figure 9. 10 ML of Ag deposited at 700K on the Ag-Si(111)-(√3x√3)R30. (A) – 100x100nm^2, -1.1V, 772pA; (B) – 1x1um^2, -8.0V, 656pA, Differentiated; (C) – 1x1um^2, -3.0V, 772pA, Differentiated; (D) – 1x1um^2, -3.0V, 772pA, Differentiated.

Figure 10. 20 ML of Ag deposited at RT on the Ag-Si(111)-(√3x√3)R30 + Si(111)-7x7 and then annealed. (A) – 50x50nm^2, clean surface, 7x7 and √3 coexisting, -0.98V, 5nA; (B) – 20 ML of Ag deposited at RT on the Ag-Si(111)-(√3x√3)R30, 1x1um^2, -4.0V, 500pA, Differentiated; (C) - 20 ML of Ag deposited at RT on the Ag-Si(111)-(√3x√3)R30, annealed at 350K for 5sec, 1x1um^2, -5.0V, 500pA, Differentiated; (D) - 20 ML of Ag deposited at RT on the Ag-Si(111)-(√3x√3)R30, annealed at 350K for 5sec, 1x1um^2, -5.0V, 500pA, Differentiated.

Figure 11. 20 ML of Ag deposited at RT on the Ag-Si(111)-(√3x√3)R30 + Si(111)-7x7 and then annealed. (E) – 20 ML of Ag deposited at RT on the Ag-Si(111)-(√3x√3)R30, annealed at 450K for 5sec, 1x1um^2, -5.0V, 500pA, Differentiated; (F) – 20 ML of Ag deposited at RT on the Ag-Si(111)-(√3x√3)R30, annealed at 450K for 5sec, 1x1um^2, -5.0V, 500pA, Differentiated; (G) – 20 ML of Ag deposited at RT on the Ag-Si(111)-(√3x√3)R30, annealed at 500K for 5sec, 1x1um^2, -5.0V, 500pA, Differentiated; (H) – 20 ML of Ag deposited at RT on the Ag-Si(111)-(√3x√3)R30, annealed at 500K for 5sec, 1x1um^2, -5.0V, 500pA, Differentiated.

Figure 12. 20 ML of Ag deposited at RT on the Ag-Si(111)-(√3x√3)R30 + Si(111)-7x7 and then annealed. (I) - 20 ML of Ag deposited at RT on the Ag-Si(111)-(√3x√3)R30, annealed at 550K for 5sec, 1x1um^2, -5.0V, 500pA, Differentiated; (J) – 20 ML of Ag deposited at RT on the Ag-Si(111)-(√3x√3)R30, annealed at 550K for 5sec, 1x1um^2, -5.0V, 500pA,

Differentiated; (K) – 20 ML of Ag deposited at RT on the Ag-Si(111)-(√3x√3)R30, annealed at 600K for 5sec, 1x1um^2, -5.0V, 500pA, Differentiated; (L) - 20 ML of Ag deposited at RT on the Ag-Si(111)-(√3x√3)R30, annealed at 600K for 5sec, 1x1um^2, -5.0V, 500pA, Differentiated.

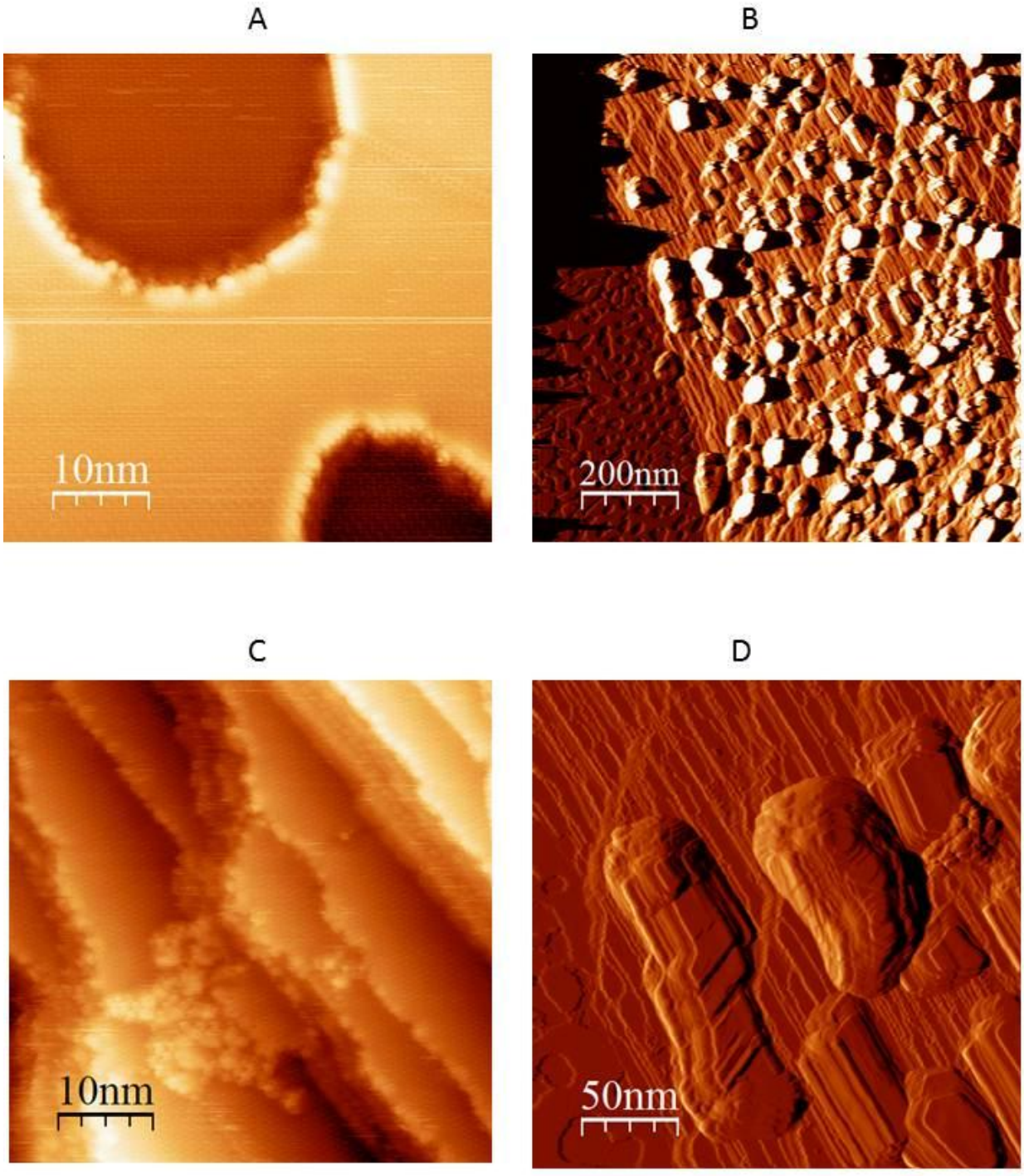

Figure 1

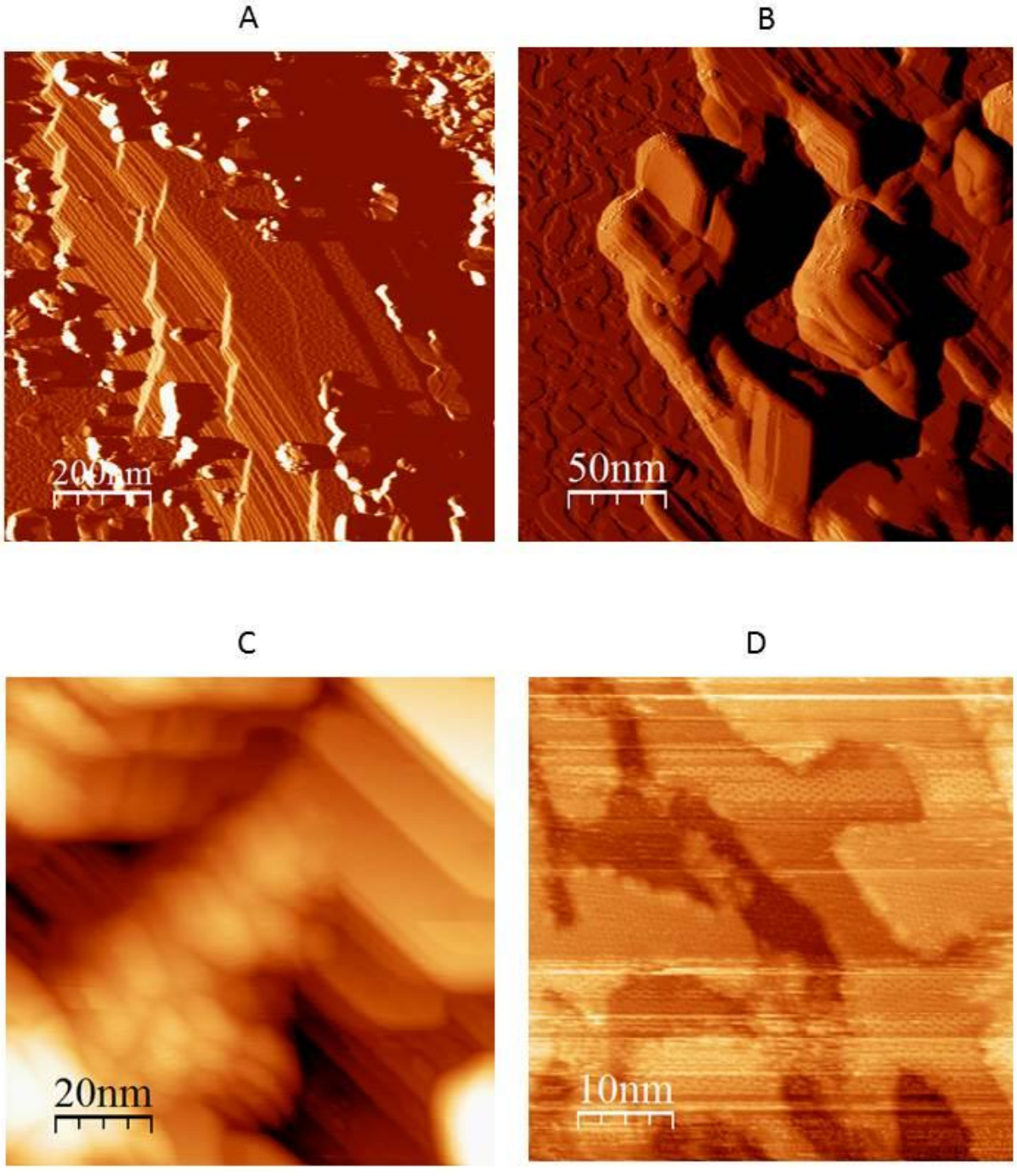

Figure 2

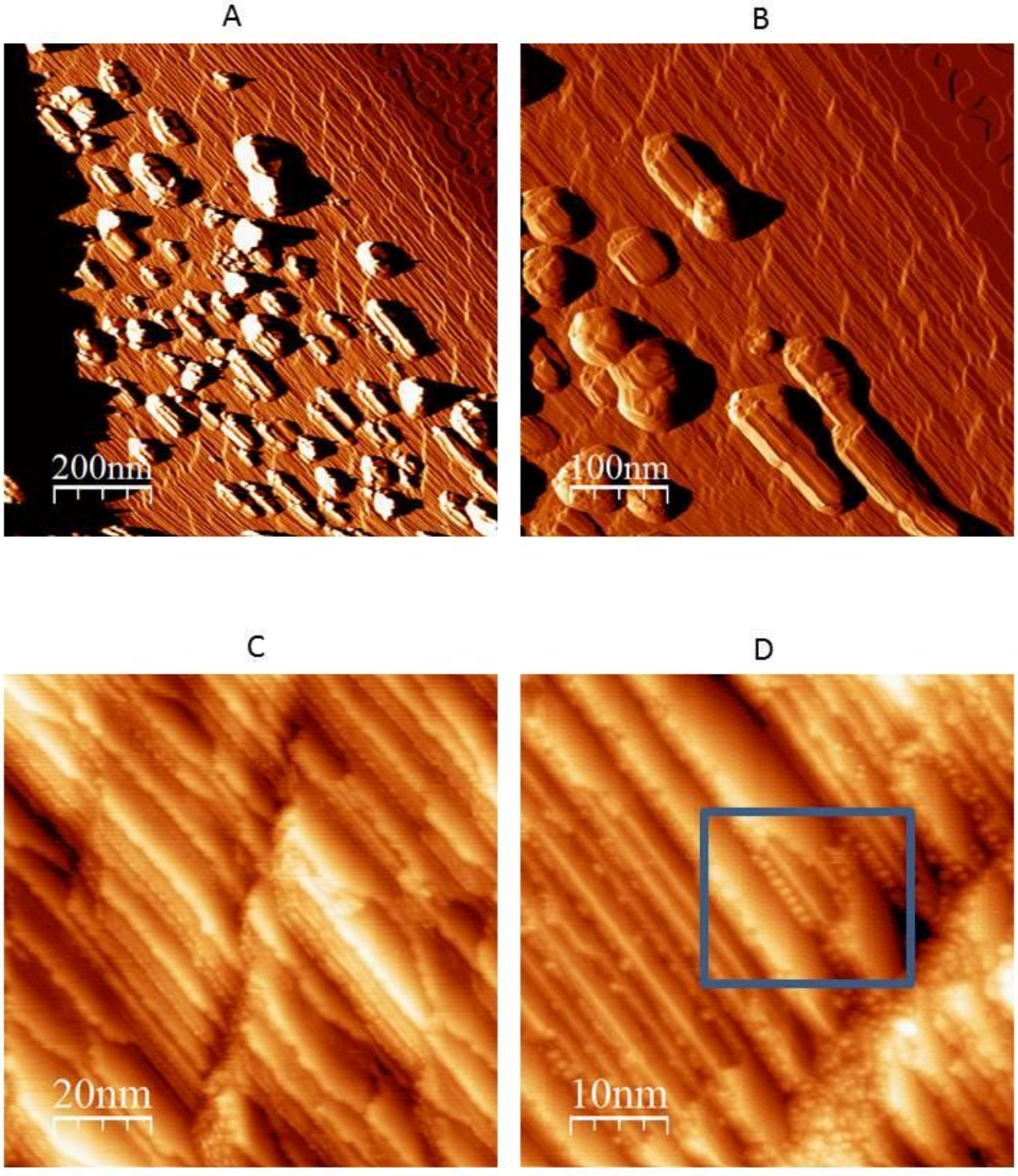

Figure 3

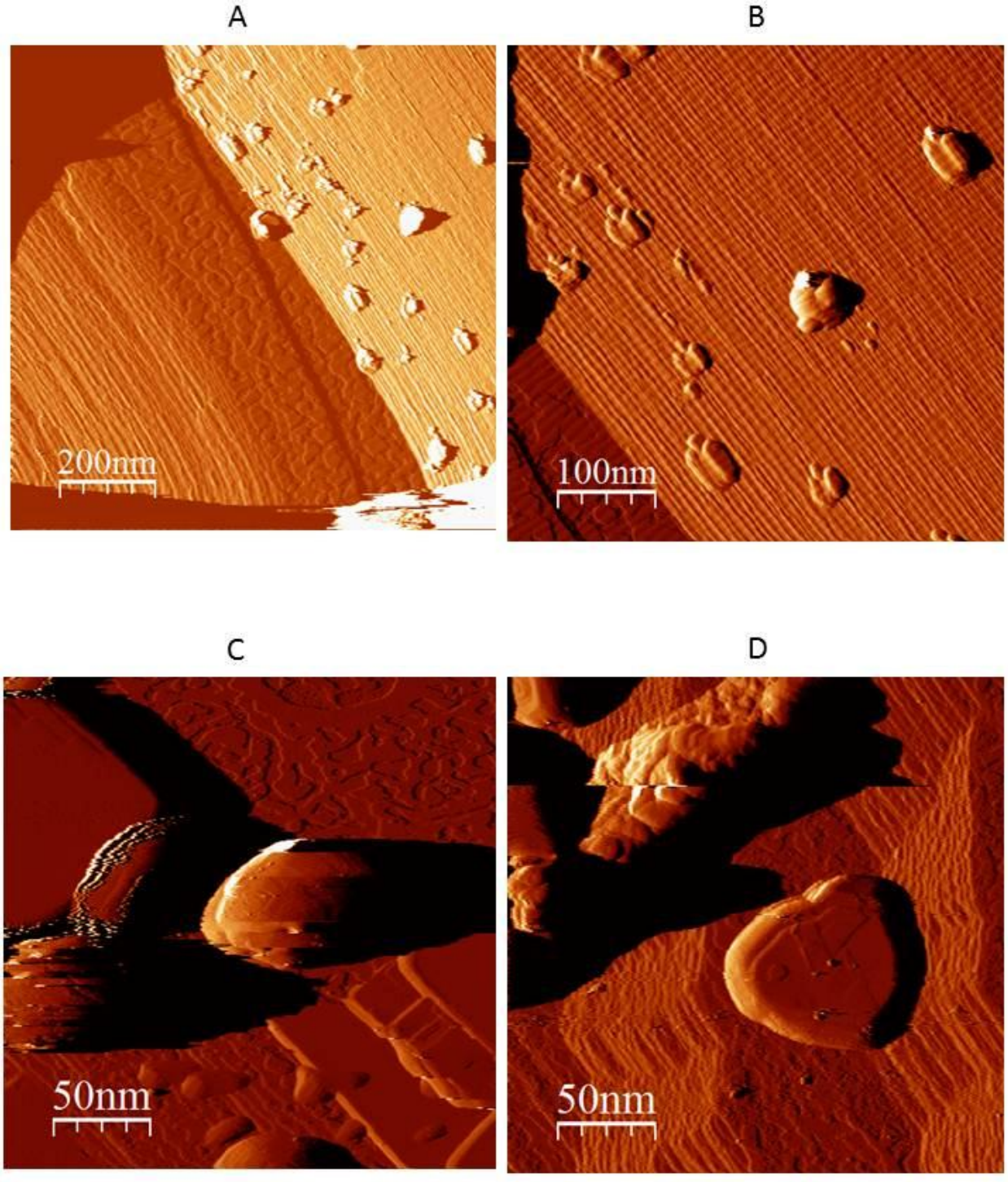

Figure 4

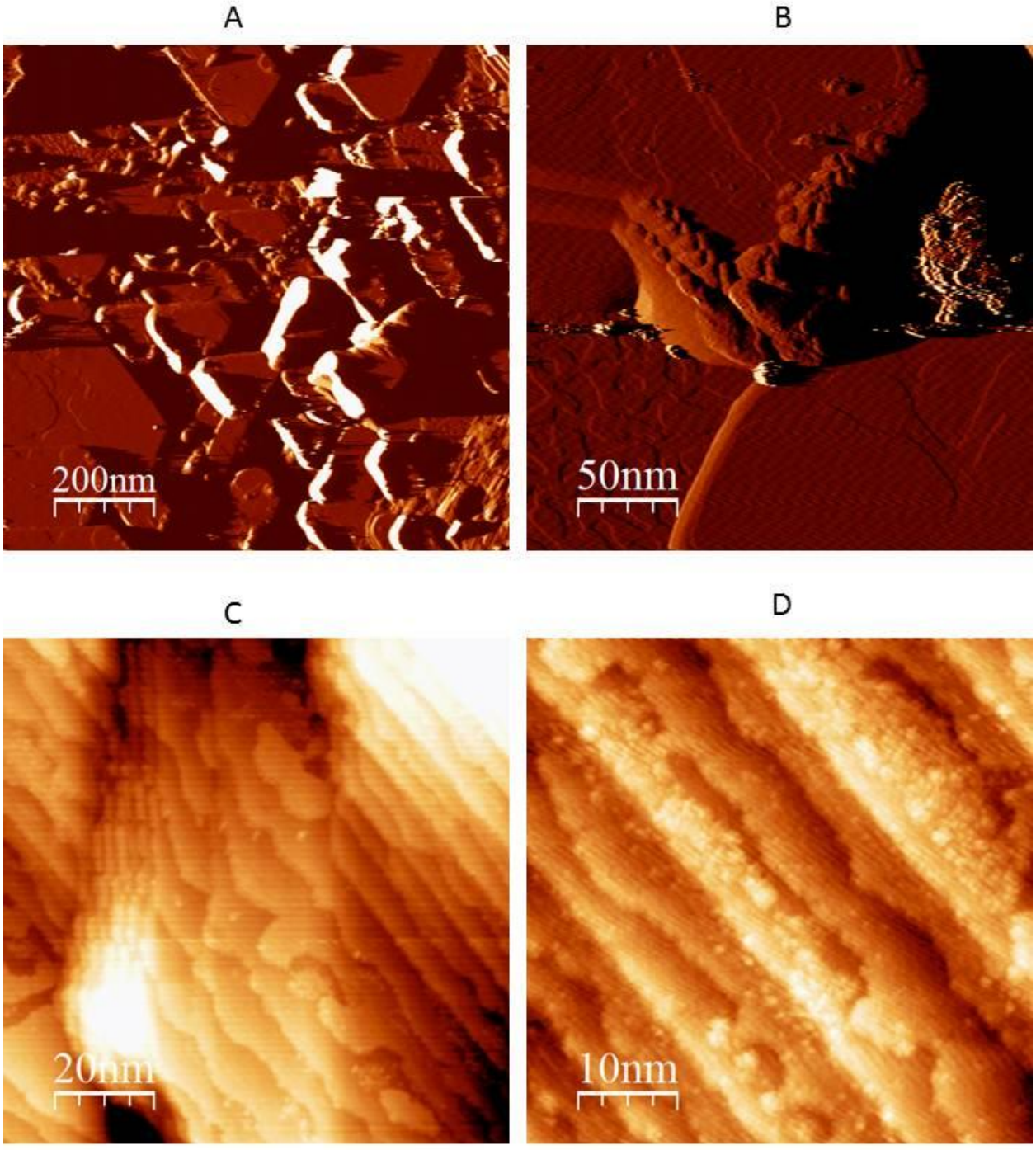

Figure 5

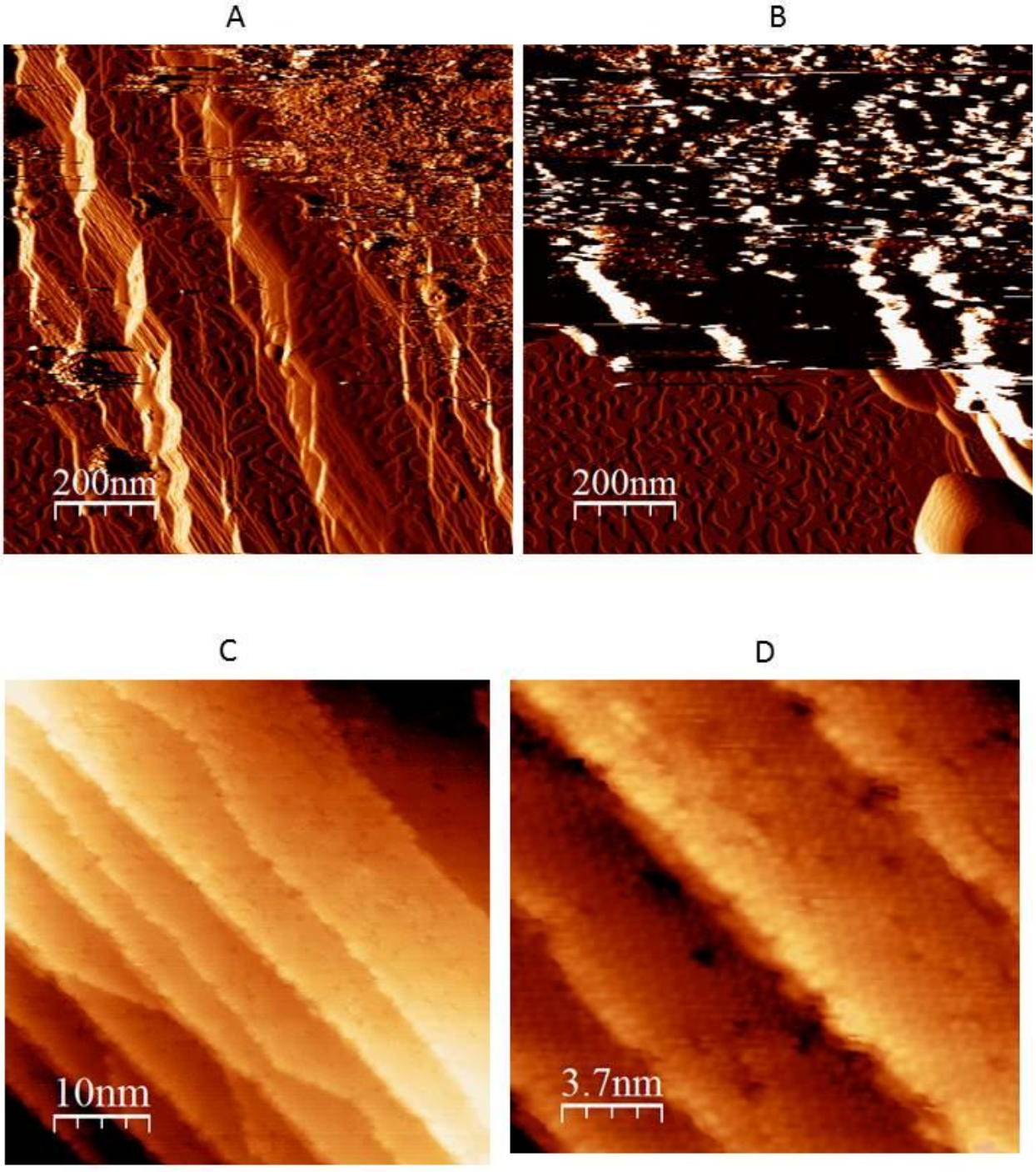

Figure 6

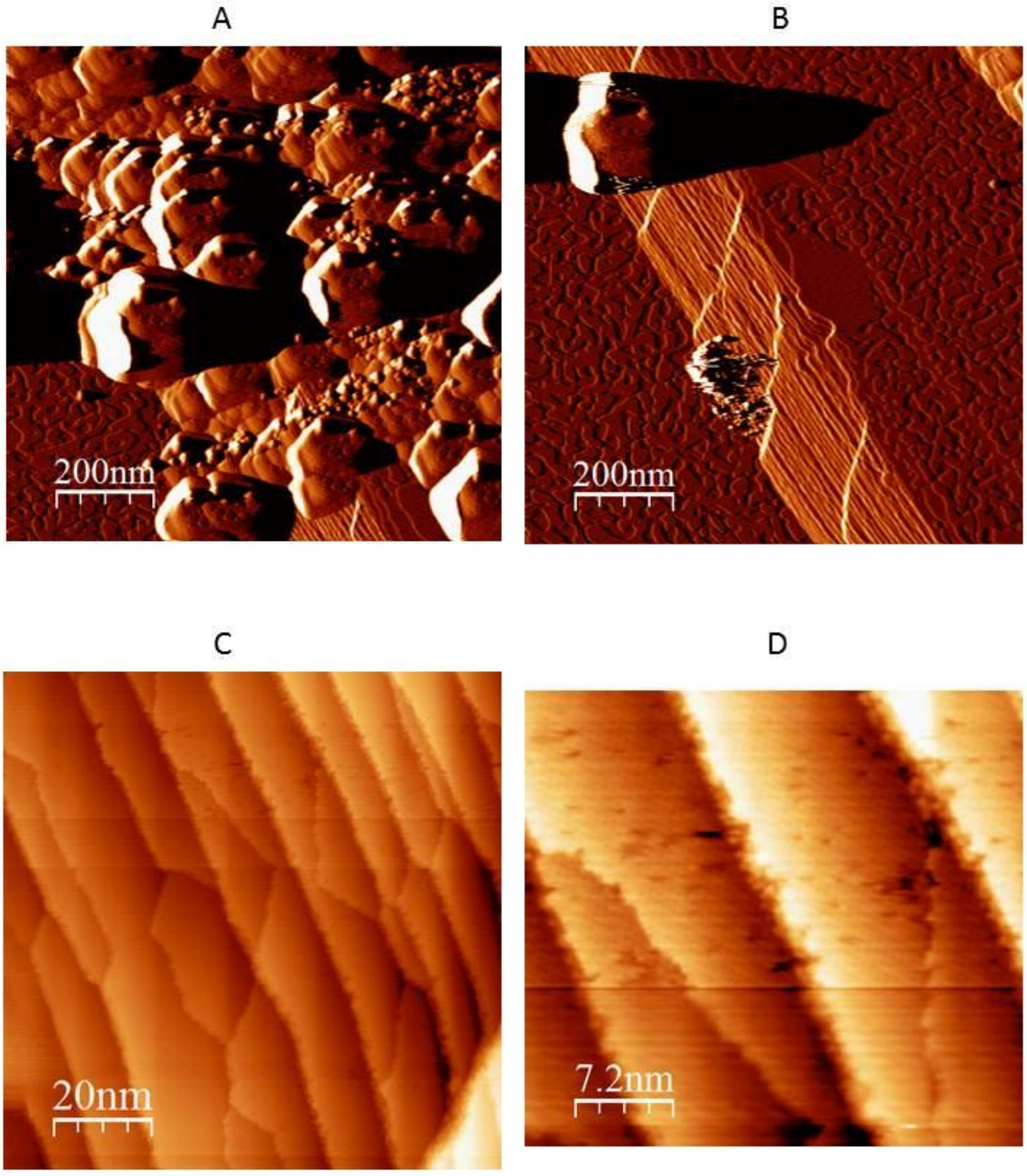

Figure 7

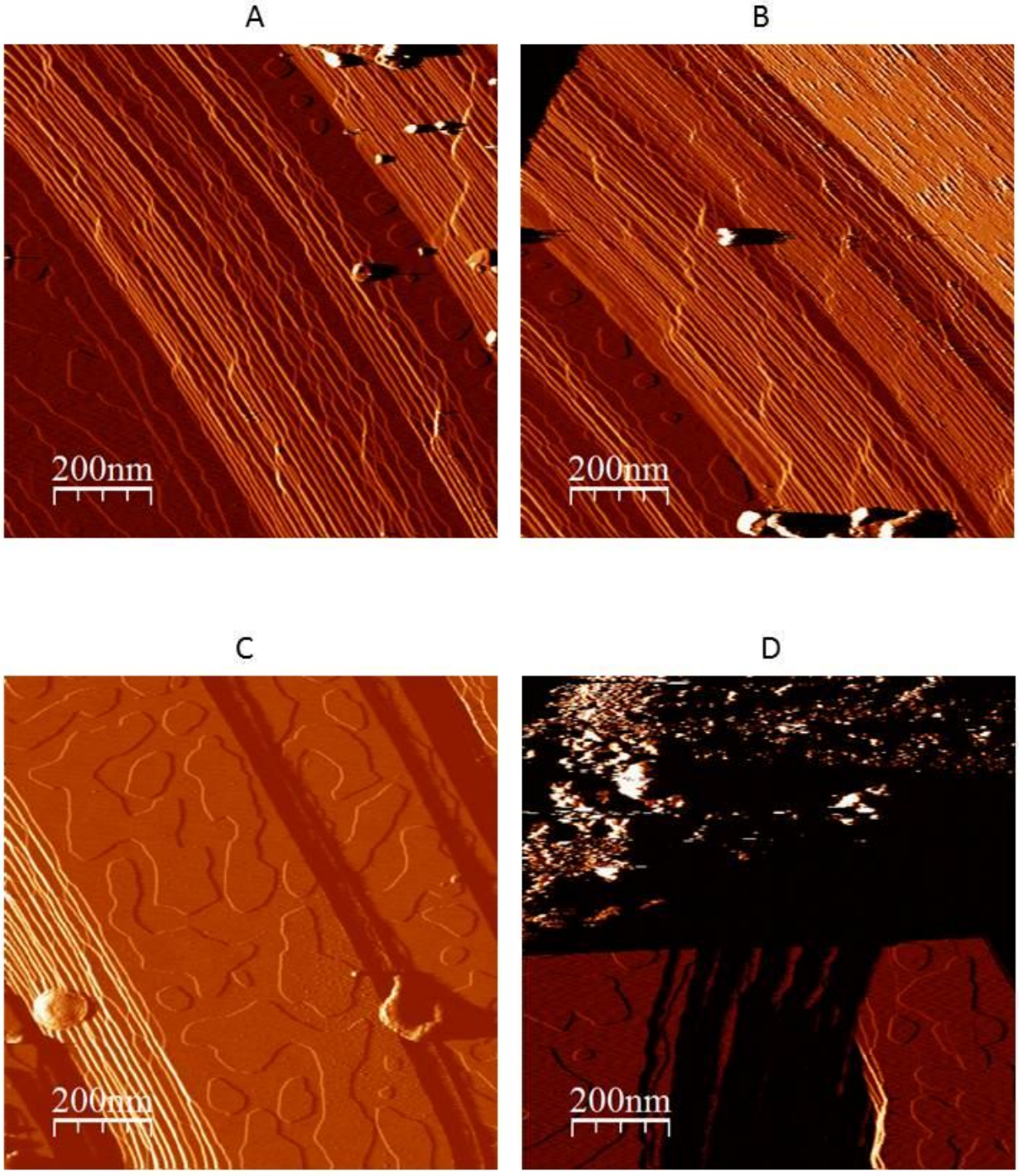

Figure 8

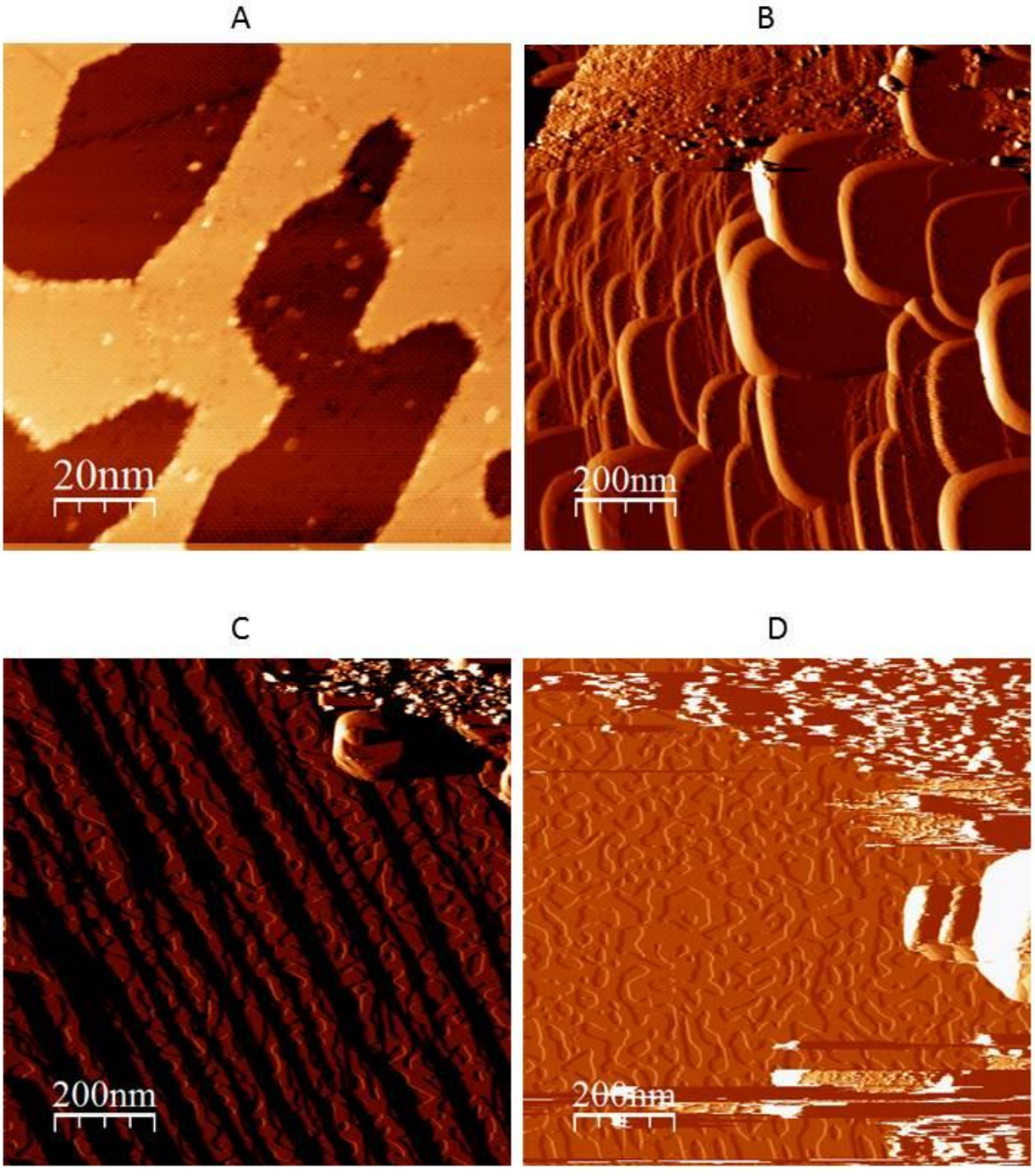

Figure 9

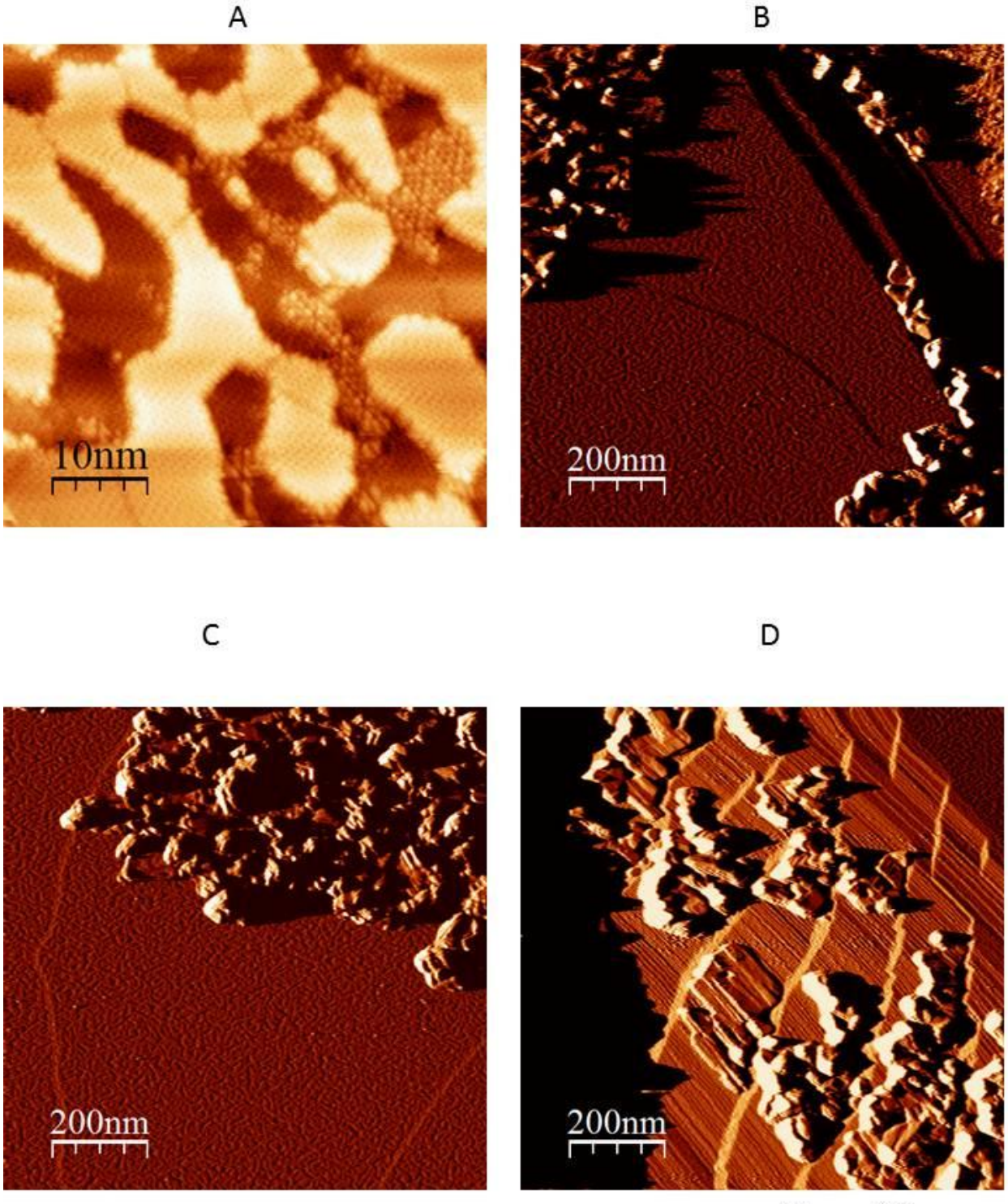

Figure 10

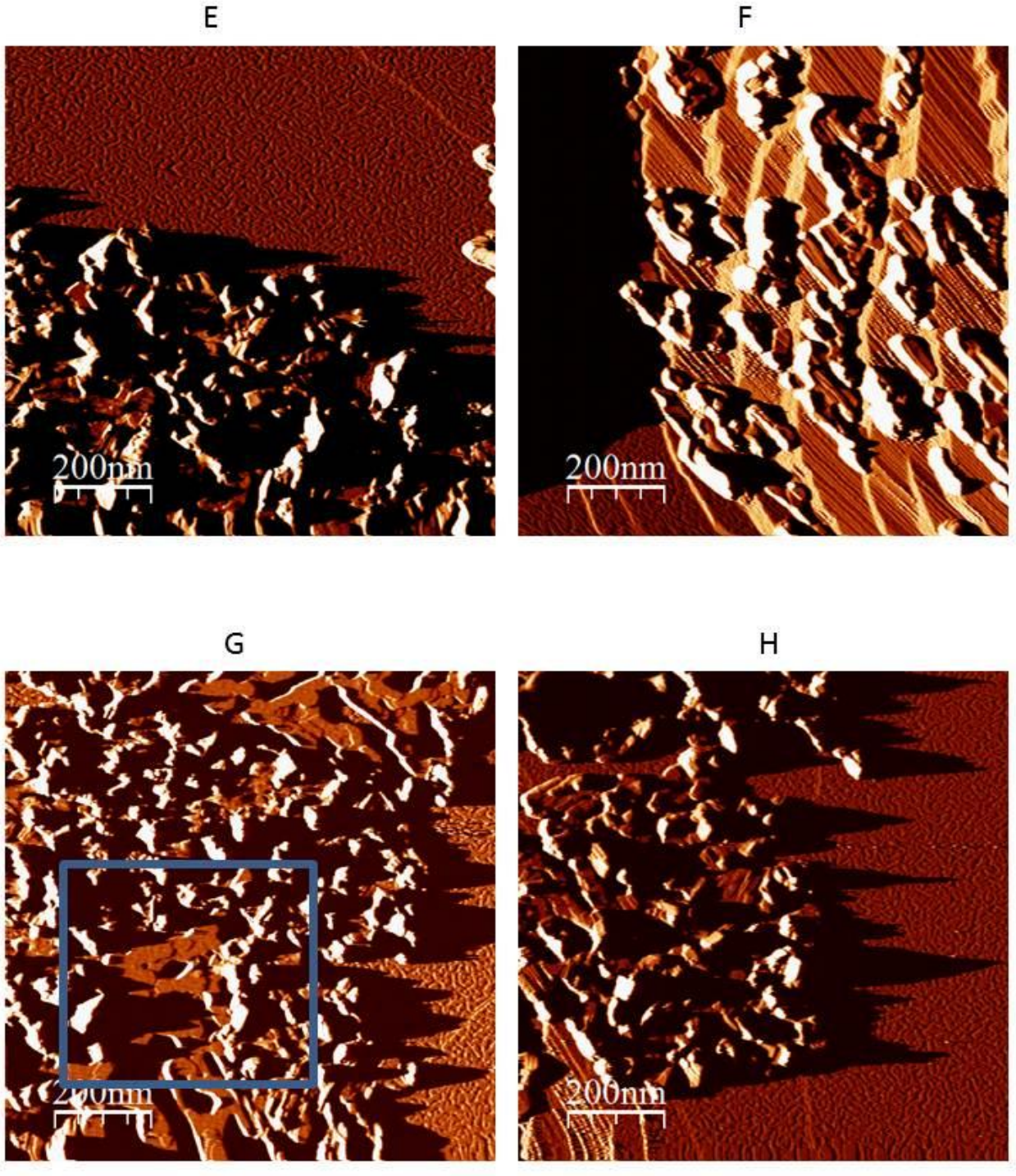

Figure 11

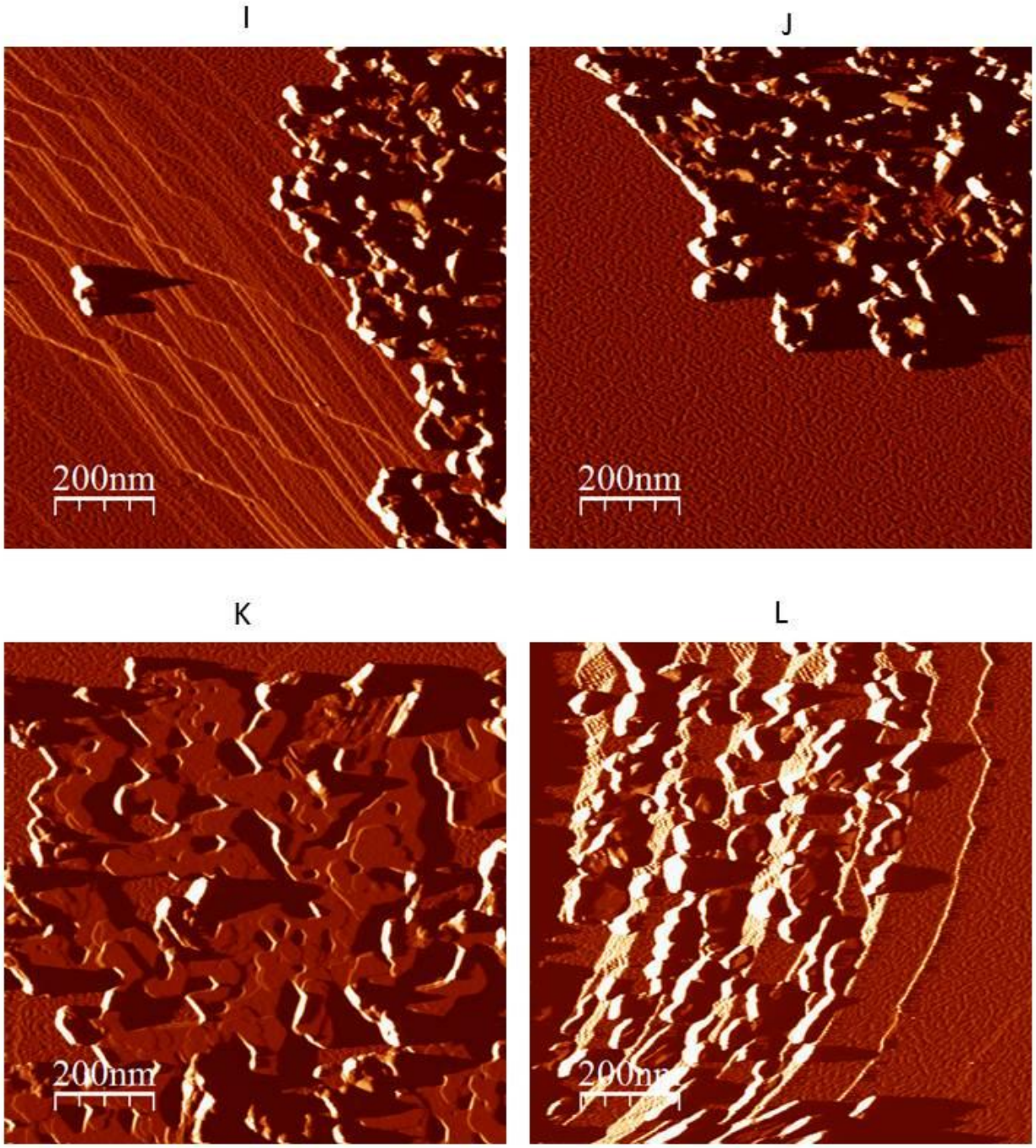

Figure 12

LIST OF TABLES

Ag/Si(111) Data List	Table 1. Experiments, Dates, Data Comments				
Date	**Images / Spectrum**	**Action**	**Bk #, Page #**	**File Name**	**Notes**
5/27/2009	m1-m4	Clean 7x7 Si(111)	Bk 2, pg 3	052709	250x250+ nm2 terraces, good tip resolution
	m5-m24	Deposited Ag ~0.5ML with sample at 600K	Bk 2, pg 4		Omicron evap, elongated images with some creep - due to sample temp.
	m24-m36	Annealed the sample at 600K for 3 mins	Bk 2, pg 4		Nice resolution, good island counting images.
	m36-60	Annealed the sample at 600K for 20 mins	Bk 2, pg 4		Mixture of island counting and hi-res, low voltages for imagin, rims
5/28/2009	m1-m3	Clean 7x7 Si(111)	Bk 2, pg 5	052809	Clean surface 500x500+ nm2 terraces
	m4-m9	Deposited ~0.5ML of Ag with sample at 600K	Bk 2, pg 5		Some temperature creep, a few counting islands images
	m10-m24	Anneal sample for 1 hour @600K	Bk 2, pg 5		Island counting
	m24-m48	Anneal sample for 1 hour @600K	Bk 2, pg 5		Island counting

Table 1. Continued

	m48-	Anneal sample for 2 hours @600K	Bk 2, pg 5		Island counting
5/30/2009	m1, m2	Clean 7x7 Si(111)	Bk 2, pg 6	053009	Overview
	m3-m6	Deposited 1-1.2ML of Ag	Bk 2, pg 6		100x100 highest mag
	m7-m62	Nanostructuring Bias dots, lines, pits. Close ups and angles	Bk 2, pg 7		Low/High Res and everything in between
	m63-m91	Ag deposition ~0.2ML	Bk 2, pg 7		Good res, lots of line/pit img
	m92-m118	Ag deposition ~0.2ML	Bk 2, pg 7		Some mech noise, good res
5/31/2009	m1,m2	Clean 7x7 Si(111)	Bk 2, pg 7	053109	Overview
	m3-m5	Ag deposition ~1-1.2ML	Bk 2, pg 8		Overview
	m6-m29	rt. 3 conversion, Nanostructuring Bias dots, lines, pits. Close ups and angles	Bk 2, pg 8		Good quality, different res
	m30-m40	Ag deposition ~0.5ML	Bk 2, pg 8		Large pool of nanostructuring with Ag, good quality
	m41-m52	Ag deposition ~0.5ML	Bk 2, pg 8		Low noise, lines, pits, dots
	m53-m66	Ag deposition ~0.5ML	Bk 2, pg 8		good quality, hi res
	m82-m98	Ag deposition ~1.25ML	Bk 2, pg 9		good quality, hi res
6/1/2009	m2-m5	Clean 7x7 Si(111)	Bk 2, pg 9	060109	Overview, hi res

Table 1. Continued

	m24-m36	Ag deposition ~2.5ML	Bk 2, pg 10		Good res, lots of material around structures
	m37-m48	Ag deposition ~2.5ML	Bk 2, pg 10		Good res, hi contrast, very high coverage
	m49-m60	Ag deposition ~2.5ML	Bk 2, pg 10		Tip a bit dirty
8/23/2009	m1-m11	Ag deposition for ~0.3ML at 500K	Bk 2, pg 22	082309	Hi quality, res 100x100 max
	m12-m19	500K anneal for 10min	Bk 2, pg 22		

8/25/2009	m1-m4	Clean 7x7 Si(111)	Bk 2, pg 23	082509	Overview
	m5-m29	Ag deposition for ~0.3ML at 500K	Bk 2, pg 23		Great res, a bit of creep, island str resolved
	m49-m65	500K anneal for 10mins	Bk 2, pg 23		some creep, great hi res
8/26/2009	m1-m6	Clean 7x7 Si(111)	Bk 2, pg 24	082609	Overview
	m7-m31	Ag deposition for ~0.3ML, 1min anneal at 500K AFTER dpsn.	Bk 2, pg 24		Very hi res, great overview
	m32-m45	Anneal at 500K for 2min	Bk 2, pg 24		excellent res, island structure
	m46-m70	Anneal at 500K for 3min	Bk 2, pg 24		great res, 0.5V step 'STS'
8/28/2009	m1, m2	Clean 7x7 Si(111)	Bk 2, pg 25	082809	Overview
	m3-m20	Ag deposition for ~0.3ML at 600K + 2min after dpsn.	Bk 2, pg		Great res, island

Table 1. Continued

			25		structure, good island/hole img, 'STS'
8/29/2009	m1-m3	Clean 7x7 Si(111)	Bk 2, pg 26	082909	Overview
	m4-m9	Ag depostion for 0.3ML at 550K + 2min after dpsn.	Bk 2, pg 26		good qlty, isl/hole measuring
	m10	Flash Si 2x, clean surface	Bk 2, pg 26		Overview
	m11-m16	Ag depostion for 0.3ML at 570K + 2min after dpsn.	Bk 2, pg 26		good qlty, isl/hole measuring
9/1/2009	m1,m2	Clean 7x7 Si(111)	Bk 2, pg 27	090109	Overview
	m3-m11	Ag deposition for ~1ML, rt.3 conversion at 800K, sample at 250K	Bk 2, pg 28		Good qlty, noise at hi res
	m12-m24	Ag deposition for ~0.15ML	Bk 2, pg 28		large scale, island close ups and island counting
	m25-m33	Ag deposition for ~0.15ML	Bk 2, pg 28		large scale, island close ups and island counting
1/13/2010	m1-m26	Clean 7x7, ~0.2ML Ag depsn. At 700K	Bk 2, pg 34	11310	Hi res, rt.3 isl/hl in the defects of 7x7, very nice
1/15/2010	m10-m27	Clean 7x7, ~1ML Ag depsn. At 700K	Bk 2, pg 35	11510	good qlty, hi res rt.3 and 7x7
2/1/2010	m7	Ag deposition for ~1.5ML, 800K anneal for 2min - rt.3 conversion	Bk 2, pg 44	2110	Overview
	m8-m15	Cooldown to 150K	Bk 2, pg 44		mech noise at 100x100nm2 or better

Table 1. Continued

	m41-m51	Ag deposition for ~0.1ML	Bk 2, pg 45		some islands, resolve shape and position, larger scale
	m52-m63	Ag deposition for ~0.3ML	Bk 2, pg 45		few islands, large scale, counting
	m64-m71	Ag deposition for ~0.5ML	Bk 2, pg 45		so so quality, large scale, counting only
2/2/2010	m1-m5	Ag deposition for 1ML, 800K anneal for 2min	Bk 2, pg 45	2210	Overview
	m6-m25	140K cooldown	Bk 2, pg 46		some noise and drift, no rt.3
	m26-m51	Ag deposition for ~0.25ML	Bk 2, pg 46		very hi res rt.3, Ag in rt.3 dislocations
2/25/2010	XPS	Ag deposition 1ML at 800K + 2min, x=16.2, y= 6, z=45, α=10	Bk 2, pg 53	02251001	0 to 1000eV, 0.5eV step
	XPS	x=16.2, y= 6, z=42.5, α=10	Bk 2, pg 53	0225002	0 to 1000eV, 0.5eV step
	XPS	x=16.2, y= 6, z=47, α=10	Bk 2, pg 53	0225003	0 to 1000eV, 0.5eV step
	XPS	Survey File	Bk 2, pg 53	0225004	0 to 1000eV, 0.5eV step
7/14/2010	m1-m7	Ag deposition 1ML, 800K anneal for 30sec, cooldown to 150K	Bk 2, pg 71	71410	Noisy overview
	m8-m25	Ag deposition for ~0.15ML	Bk 2, pg 71		noise, island counting
	m26-m36	Ag deposition for ~0.15ML	Bk 2, pg 73		low qlty, counitng only
7/29/2010	m1-m7	Ag deposition for 1ML, 800K anneal for 1min	Bk 2, pg 76	072610	Overview

Table 1. Continued

	m13, m14	Cooldown to 170K	Bk 2, pg 78		Clean Standard
	m15-m33	Ag deposition for ~0.15ML	Bk 2, pg 78		Creep, lo res, counting
	m34-m48	Ag deposition for ~0.15ML	Bk 2, pg 78		Decent quality, counting
	m49-m62	Ag deposition for ~0.15ML	Bk 2, pg 78		good qlty, island shapes
	m63-m78	Ag deposition for ~0.5ML	Bk 2, pg 78		ok qlty, island distributions
8/3/2010	m1-m3	Ag deposition for ~1ML, 2min 600K anneal, 45sec 800K anneal	Bk 2, pg 79	8310	Overview
	m4	Cooldown to 175K	Bk 2, pg 79		Overview
	m5-m26	Ag deposition for ~0.15ML	Bk 2, pg 80		Large area, good res, count
	m27-m45	Ag deposition for ~0.15ML	Bk 2, pg 80		Good res, diff sizes, isl details
	m46-m69	Ag deposition for ~0.15ML	Bk 2, pg 80		Good res, hi detail, counting
	m70-m90	Ag deposition for ~0.5ML	Bk 2, pg 80		Isl morph details, good res
9/13/2010	m1-m11	Ag deposition for 1ML, 800K anneal for 2min, Cool to 150K	Bk 2, pg 92	91310	Great rt.3 res, overview
	m12-m25	Ag deposition for ~0.15ML	Bk 2, pg 93		Good res, low coverage
	m26-m41	Ag deposition for ~0.15ML	Bk 2, pg 93		Good res, counting, hi detail
	m5-m29	Ag deposition for ~0.2ML	Bk 2, pg		Great rt.3 res, isl in

Table 1. Continued

			95		detail
	m30-m38	Ag deposition for ~0.2ML	Bk 2, pg 95		Larger images, good detail
9/21/2010	m1,m2	Ag deposition for 1ML, 800K anneal for 1.5min, Cool to 115K	Bk 2, pg 97	92110	Stepped overview
	m18-m30	Ag deposition for ~0.2ML	Bk 2, pg 97		Good res, nice detail, count
9/23/2010	m1-m6	Ag deposition for 1ML, 800K anneal for 1.5min, Cool to 212K	Bk 2, pg 98	92310	Cold rt.3 Overview
	m7-m19	Ag deposition for ~0.2ML	Bk 2, pg 98		Ok res, some noise, mul tip?
	m20-m38	Ag deposition for ~0.2ML	Bk 2, pg 98		Good res, isl details, count
10/7/2010	m1-m7	Ag deposition for 1ML, 800K anneal for 1.5min, Cool to 60K	Bk 2, pg 99	100710	Hi mech noise, tip issues
	m8-m25	Ag deposition for ~0.2ML	Bk 2, pg 99		Some 3x1, mech noise
	m26-m34	Ag deposition for ~0.2ML	Bk 2, pg 99		Mech noise, tip unstbl, count
	m7-m16	Ag deposition for ~0.1ML	Bk 2, pg 101		well resolved wetting layer
	m17-m21	Ag deposition for ~0.1ML	Bk 2, pg 102		steps, good res wetting layer
	m22-m25	Ag deposition for ~0.1ML, 800K anneal for 1.5min Cool to 123K	Bk 2, pg 102		Highly stepped surface
	m26-m36	Ag deposition for ~0.1ML	Bk 2, pg 102		Steps, mech noise, low cvrg
	m37-	Ag deposition for ~0.1ML	Bk 2, pg		Ok res, some noise,

Table 1. Continued

	m49		102		counting
3/10/2011	m1-m13	Ag deposition for 1ML, 800K anneal for 1.5min	Bk 2, pg 106	031011	Rt.3 ok res, overview
	m14-m21	Imaging during 200L of O2	Bk 2, pg 107		good res, rt.3 edges/terraces
	m22-m34	Post 200L exposure imaging	Bk 2, pg 107		good res, rt.3
3/17/2011	m1-m16	Clean Si(111) 7x7	Bk 2, pg 109	031711	Overview
	m21-m33	Ag deposition for ~0.25ML	Bk 2, pg 110		Good res, Ag in dislocations
	m34-m58	O2 Exposure for 200L	Bk 2, pg 110		good res, smll/lrg image areas
7/24/2011	m1-m12	Ag deposition for ~0.8ML, 800K anneal for 1.5min	Bk 2, pg 125	072411	rt.3 overview
	m13-m28	Ag deposition for ~20ML	Bk 2, pg 125		nice res, large scale
	m29-m51	Anneal the surface at 350K for 5sec	Bk 2, pg 125		great res, large scare
	m52-m72	Anneal surface at 400K for 5sec	Bk 2, pg 126		good res Ag morph, lrg scale
	m73-m90	Anneal surface at 500K for 5sec	Bk 2, pg 126		lrg scale, Ag morphology
	m91-m108	Anneal surface at 550K for 5sec	Bk 2, pg 126		lrg scale, steps/terrace, Ag isl
	m109-m125	Anneal surface at 600K for 5sec	Bk 2, pg 126		lrg scale Ag morphology
7/26/2011	m1-m7	Ag deposition for 1ML, 800K anneal for 1.5min	Bk 2, pg 127	072611	Overview

Table 1. Continued

	m8-m32	Ag deposition for 10ML	Bk 2, pg 127		great res, smal/large scare
	m59-m69	Anneal the surface at 650K for 5min	Bk 2, pg 127		ok res, large areas
7/30/2011	m1-m5	Ag deposition for 1ML, 800K anneal for 1.5min	Bk 2, pg 129	073011	rt.3 overview
	m17-m45	Anneal the surface at 550K for 5min	Bk 2, pg 129		good res, smll/lrg isl areas
	m46-m73	Anneal the surface at 650K for 5min	Bk 2, pg 129		lrg Ag isl, steps/terraces
8/1/2011	m1-m5	Ag deposition for 1ML, 800K anneal for 1.5min, Ag dpsn 10ML	Bk 2, pg 130	080111	Ag isl morphology
	m6-m51	Anneal the surface 700K	Bk 2, pg 130		steps, Ag morph, islands
8/3/2011	m1-m12	Ag deposition for 1ML, 800K anneal for 1.5min, Ag dpsn 10ML	Bk 2, pg 131	080311	Ag isl morphology
	m13-m55	Anneal the surface at 750K for 5min	Bk 2, pg 131		good res, smll/lrg isl trrc/step
8/4/2011	m1-m11	Ag deposition for 1ML, 800K anneal for 1.5min, Ag dpsn 10ML	Bk 2, pg 131	080411	Ag isl overview
	m12-m59	Anneal the surface at 800K for 5min	Bk 2, pg 131		good res, smll/lrg isl trrc/step
8/8/2011	m1-m5	Ag deposition for 1ML, 800K anneal for 1.5min, Ag dpsn 10ML	Bk 2, pg 132	080811	Nice Overview
	m6-m37	Anneal the surface at 850K for 5min	Bk 2, pg 132		Lrg terrace/step
8/11/2011	m1-m52	Ag deposition for 1ML, 800K anneal for 1.5min, Ag dpsn 10ML	Bk 2, pg 134	081111	Good res, lrg/small overview
		Sample maintained at 700K during deposition			

Table 1. Continued

9/5/2011	m1-m12	Au deposition ~0.25ML on Si(111)-7x7	Bk 2, pg 139	090511	Hi res, wettig layer
	m27-m39	Au deposition ~0.25ML	Bk 2, pg 139		Hi res, wett layer restructure
9/5/2011	m40-m75	Anneal the surface at 800K for 1.5min	Bk 2, pg 139	090511	Hi res, nice surface details
9/7/2011	m1-m4	Ag deposition for 1ML, 800K anneal for 1.5min	Bk 2, pg 140	090711	rt.3 overview
	m5-m44	Au deposition for 1ML	Bk 2, pg 140		Hi res, Si etch, isl morph
9/12/2011	m1-m14	Ag deposition for 1ML, 800K anneal for 1.5min	Bk 2, pg 141	091211	Ok res, overview
		Au deposition for 1ML	Bk 2, pg 141		Terrace/step Si etch detail
	m15-m45	Anneal the surface at 500K for 2min	Bk 2, pg 142		Hi res, isl morph, steps
9/17/2011	m1-m23	Ag deposition for 1ML, 800K anneal for 1.5min	Bk 2, pg 143	091711	Great res, step/terrace
	m24-m58	Anneal the surface at 500K for 2min	Bk 2, pg 143		Great res, diff sizes
	m59-m84	Anneal the surface at 600K for 2min	Bk 2, pg 143		Good res, large scale
9/19/2011	m1-m29	Ag deposition ~1.25ML on Si(111)-7x7	Bk 2, pg 144	091911	Good res, isl detail
		<0.1ML Pentacene deposition	Bk 2, pg 144		No Pn evidence on surface
9/24/2011	m1-m36	Ag deposition ~1.25ML on Si(111)-7x7	Bk 2, pg 146	092411	Good res, isl detail, step/terr
		<0.1ML Pentacene deposition	Bk 2, pg 146		Little Pn evidence

Table 1. Continued

9/25/2011	m1-m31	Ag deposition ~1.25ML on Si(111)-7x7	Bk 2, pg 146	092511	Ok res, no Pn hi res
9/26/2011	m1-45	Ag deposition ~1.25ML on Si(111)-7x7	Bk 2, pg 147	092611	Good res, isl on terr/step
		~2ML Pentacene deposition	Bk 2, pg 147		No Pn resolved
		~2ML Pentacene deposition	Bk 2, pg 148		Hi res Mul layer Pn overview
10/1/2011	m1-m56	Ag deposition ~1.5ML on Si(111)-7x7	Bk 2, pg 149	100111	Good res, some mech noise
		~2ML Pentacene deposition	Bk 2, pg 149		Some Pn resolved on isl
10/2/2011	m1-m48	Ag deposition for 1.2ML, 800K anneal for 1.5min	Bk 2, pg 149	100211	Good res, small/large scale
		~2ML Pentacene deposition	Bk 2, pg 149		Pn layers on the rt.3
10/6/2011	m1-m64	Ag deposition ~1.5ML on Si(111)-7x7	Bk 2, pg 150	100611	Good res, lrg/small overview
		~1ML Pentacene deposition	Bk 2, pg 150		Pn resolved on islands
10/8/2011	m1-m59	Ag deposition ~1.5ML on Si(111)-7x7	Bk 2, pg 151	100811	Good res, mul tip
		~1ML Pentacene deposition	Bk 2, pg 151		some noise,
		~1.5ML Pentacene deposition, Cooldown to 70K	Bk 2, pg 154		Some multiple tip
10/17/2011	m1-m60	Ag deposition ~1.5ML on Si(111)-7x7	Bk 2, pg 154	101711	Great Pn layer resolution
		~1.5ML Pentacene deposition, Cooldown to 70K			Small nucleation

Table 1. Continued

					centers
10/18/2011	m1-m32	Ag deposition ~1.5ML on Si(111)-7x7	Bk 2, pg 155	101811	Ag isl overview

TECHNICAL APPENDIX

Silicon 7x7 recipe

Make sure your sample holder is outgassed clean! If the majority of parts used in the holder are brand new, you're better off outgassing the holder with a dummy sample and then putting the real wafer in.

1. Prior to flashing, outgas the Si at 600° C until pressure is in 10^{-11} torr range.

2. Bring up to 870° C (10 – 15 min) and see if pressure recovers quickly. If so, continue.

3. After everything has been outgassed and chamber pressure is good you can try to make the 7x7. There are 3 annealing steps that yield optimal terrace width:

1.Hold the sample at 1250° C for 30 sec – be careful here because if you overshoot slightly your sample will melt

2.Drop temperature to 850° C. This is where the steps begin to flow.At this stage, cool slowly to 750° C. Good cooling rate is ~ 1° C/s

2. From 750° C to 400° C cooling rate can be doubled

3. After 400° C just turn the power off

4. Let the sample cool for at least 15 minutes between successive flashes

5. Don't flash TSP while flashing Si or heating/cooling sample

6. There are a number of caceats to always watch out for in order to achieve optimal terrace width. These are Carbon poisoning and Ni plated tools. Excessive deposition of organics

on the Si sample results in terrace pinning, as Carbon atoms cannot be entirely driven off by thermal cleaning. Nickel leaches into Silicon and causes a somewhat similar effect, so NO METAL tools are to be used in preparing and handling the Silicon wafers.

7. Below is a list of references that may help you in preparation of various Si surfaces for experiments. These references contain different recipes aimed at different results, but in reading through those you may be able to gain insight to devise something to fit your particular function.

Some helpful references:

1. R.J. Phaneuf, N.C. Bartelt, E.D. Williams, W. Swiech, and E. Bauer, *The Crossover from Metastable to Unstable Facet Growth on Si(111).* Physical Review Letters, **71**: p. 2284-2287. 1993

2. S. Song, M. Yoon, S.G.J. Mochrie, G.B. Stephenson, and S.T. Milner, *Faceting kinetics of stepped Si(113) surfaces: dynamic scaling and nano-scale grooves.* Surface Science, **372**: p. 37-63. 1997.

3. M. Yoon, S.G.J. Mochrie, M.W. Tate, S.M. Gruner, and E.F. Eikenberry, *Anisotropic Coarsening of Periodic Grooves: Time-Resolved X-Ray Scattering.* Physical Review Letters, **80**: p. 337-340. 1998.

4. A. Baski and L. Whitman, *High index Si surfaces on the (001) to (111) azimuth.* Surface Science, **392**: p. 69-85. 1997.

5. X.-S. Wang and E.D. Williams, *Step Structures on Br-Chemisorbed Vicinal Si(111).* Surface Science, **400**: p. 220-231. 1998.

6. V. Tsai, X.-S. Wang, E.D. Williams, J. Schneir, and R. Dixson, *Conformal Oxides on Si Surfaces.* Applied Physics Letters, **71**: p. 1495-1497. 1997.

7. B.Z. Olshanetsky, A.E. Solovyov, A.E. Dolbak, and A.A. Maslov, *Structures of clean and nickel-containing high Miller index surfaces of Si.* Surface Science, **306**: p. 327-341. 1994.

8. Y.-N. Yang and E.D. Williams, *The Role of Carbon in the Faceting of Silicon Surfaces on the (111) to (100) Azimuth.* Journal of Vacuum Science and Technology, **A8**: p. 2481-2488. 1990.

224 Spedding Chamber Tips and Tricks

1. STM

Pneumatic legs tend to oscillate. Try not to lean or place anything heavy on the table surface before running STM. Legs are particularly vulnerable to periodic oscillation as they're pumped up. Before STM, make sure the legs are fully extended without touching their outer shells.

There is a gas doser needle in the back of the STM bell chamber. It is aimed directly at the sample and is ~ 2" away. Bake that line each time before using a new reagent. Occasionally the needle may touch the floating stage introducing vibration. If you see lots of mechanical noise, raise and then lower the STM stage a few times. This also helps if you're getting lots of noise from the cooling block.

Gas rack pumps ARE NOT a major factor in vibration. That being said, thoroughly pad all the lines from the rack that lay on the table. This includes the LT line connected to the roughing pump.

Flow rate of cooling water has major impact on image quality. Omicron EFM 3 has temperature readout on the display panel. Adjust the flow rate to maintain temperature below 20°C. 3 L a minute is a fairly robust value. Also pay attention to building maintenance emails. Any time there is work done on water lines, water bubbles are introduced in the system – this will introduce lots of vibration.

When setting up the cooling block for LN_2 or LHe:

- Assemble everything shortly before you use it. Letting the π shaped line sit submerged in coolant induces icicle formation on the other end and prevents liquid flow.
- Always make sure you're sucking up LIQUID and NOT GAS. To ensure liquid, initially keep the needle valve closed on the Cryo-Vac gauge. Turn on the Temperature control unit. Pump out the line after it has been fully assembled with a roughing pump and open the coarse valve. Repeat the pumping and opening of the coarse valve until you see temperature dropping on the T control unit. A good place to stop is when you drop 0.1 K every few seconds. Close the coarse valve and adjust the micro valve. 5-7 mm has been optimal for me.
- Anything but the MAX setting for heating on the T control cannot keep up with even the lowest flow rates.

- Watch the cooling progress for about an hour; in that time span it is usually clear whether your coolant flow rate is too high.
- It takes about 2-3 hours for temperature to equilibrate. The STM tip is always at RT, so you'll get a fair amount of drift in the first hour of scanning.
- LOOSEN the cooling block and slide it off the sample backplate AS SOON AS you're done with your experiments, otherwise you may come back to a cracked sample/top plate the next day.

Vibration from the LN2 line can be substantial. Pad all the lines and make sure the sample is all the way in the stage and securely tightened. Raise and lower the stage a few times if conditions don't improve.

Stopping the scan at a small image area before backing out the tip will drastically improve your chances of finding the same area after re-approach.

Scanning at 120% speed over stepped areas at -3V is a great way to clean the tip.

Using the tip flasher keeps tips cleaner AND sharper.

The wobble stick doesn't have much rotational freedom. Be very gentle with it as it cannot stand much abuse.

Most tip crashes occur during tip transfers. If you plan on using the flasher frequently, make sure you have a backup tip. Keeping the tip in UHV will improve its quality with time.

The piezo is fully exposed under the stage. As the number of depositions climb, it will start sticking more and more. A very gentle tap with a wobble stick will usually free it; however, this is not a fix. Plan for addressing this issue in the future, either through cleaning or finding a replacement.

If you do heavy post image processing in SCALA as you collect data, the program may freeze and crash your tip. It's safer to process using WsXM on a separate computer.

SCALA is fairly customizable and has a number of "open source" features.

2. Evaporators

Typical E-beam setup

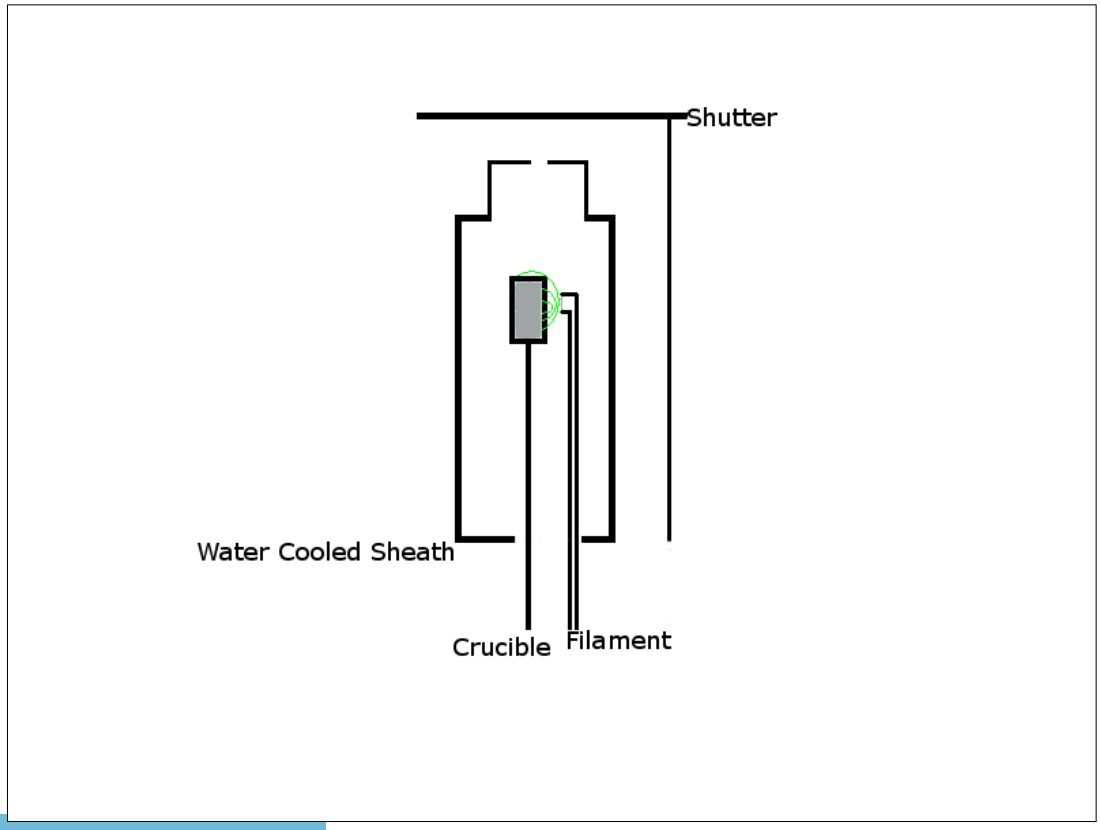

If your sample to evaporant distance is small, it is best to use a Knudsen Cell – a crucible with a pinhole. This will give a constant flux.

The Omicron EFM 3 Manual is a great source of information for crucible sizes. It also provides a technical drawing of the crucible that will fit into the EFM 3 as well as Mantis.

Outgas evaporators as soon as the bakeout box is disassembled. DO NOT run water during this outgas. Use filaments as heat source w/o high voltage.

If you have a new crucible, it needs to be outgassed by itself prior to putting any material in it.

Pentacene Evaporator

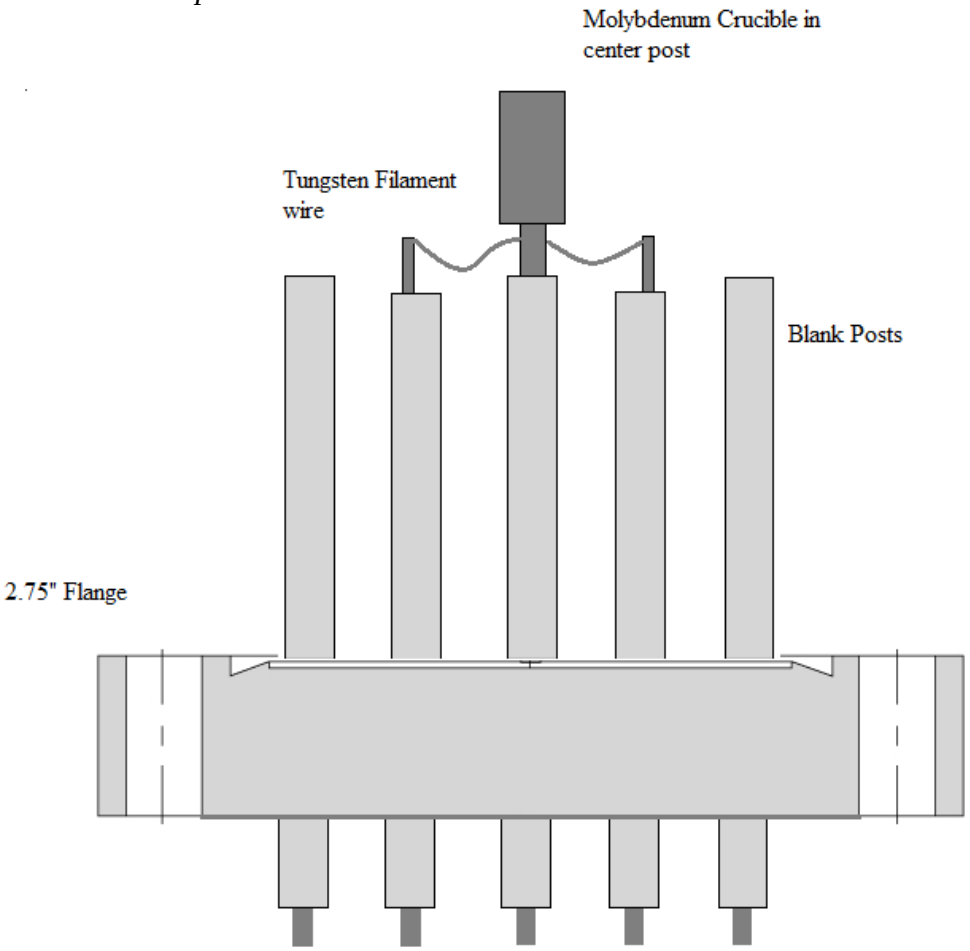

Pentacene evaporator should be heated by filament only. However, the setup is e-beam ready. You can reuse the crucible if there isn't any interest in continuing with pentacene in the group. Wash it with benzene in the sonicator followed by the standard acetone/methanol procedure. This crucible has a set-screw nut as a cap. To get it out simply use a size 0-80 screw as the hole has threading. Outgas at 2-3 A for 6 hrs. Deposition starts at 4.4 A, I was getting around 3 ML/min at that filament power.

You can get a good feel for the shutter position during warm up. At 2 A the filament is pretty bright, so rotating the shutter through will make it clear when it is opened and closed. The rod on which the shutter sits comes down the center of the flange. Try to rotate the shutter half way between two "closed" positions, this way there will be least flux interference.

The Omicron evaporator is highly robust. There is little power fluctuation and flux is highly stable. It is also much easier to take apart and service. Unfortunately, because of a 90̊degree joint in a cooling line, it does seem to induce more vibration.

The Mantis evaporator needs a 30 min warm-up before deposition. The power output is prone to fluctuation. If you're planning on doing simultaneous deposition with two sources, adjust the cooling rate to account for that. Every small part has to be specially ordered, including things like filaments.

Rods are easier and cleaner to evaporate than material in crucibles. However, rods are harder to set up initially. Also you'll generally get a higher flux out of a rod. Crucible liners are a bit of a scam. If your evaporant wets the material the crucible is made out of – you have to use one regardless. Otherwise liquefied material is likely to permanently seal the liner to the crucible. This makes crucibles single material use, but DRASTICALLY reduces the volume of material available for deposition. Liners are usually made out of alumina and will take a long time to outgas.

Use an e-beam setup whenever you can. It provides the finest control for power output. Unfortunately an e-beam is not an option for materials with melting points < 300°C – like all the organics.

Every time something in the evaporator is changed, the flux needs to be recalibrated. Calibrations on the 7x7 are probably your best bet. Practically every material has been studied on Si. Finding and reading relevant literature will give you an idea of growth modes and coverages before analyzing images in WsXM.

WsXM is a stand-alone MatLab package. Learn from the source and you will become a master of data processing.

3. XPS

Beam size at the sample is ~1 cm. No useful data can be gotten from double decker samples, because there is much interference and the final output peaks are from the sample + entire top plate + studs.

There is a small grounding wire inside the gun that attaches right next to cooling water inlets. Make sure that ground is secure; otherwise the gun will continuously trip.

For best results 18 MΩ water should be used for cooling the XPS.

Our hemispherical analyzer has a single channeltron multiplier. You need to do a lot of scan averaging to get good energy resolution.

4. Ion Pump

You will nearly always get a short after initial power on post bake.

With time Ti whiskers will grow inside the pump, shorting it out. Use a DC power supply to pass current between the pump's HV input and ground. Check with a HV ohmmeter afterwards. This will help burn away some of the whiskers, but the process may take a few days.

Tapping with a rubber mallet may be used as a final line of defense, but obviously, exercise caution.

5. Image Processing in WsXM.

Playing with 3D and Contour plot functions will really help you visualize your surface and separate real features from artifacts. A well prepared 3D image will tell a much better story than a 2D.

Be careful with the FFT filter! It's a great tool for checking inverse space periodicity and will give an insight to unit cell structure, although filtering function is finicky and takes a great deal of trial and error before producing a nice filtered image. Keep in mind, after filtering spatial measurements on the image are meaningless.

Derivative mode is bread and butter of images with high corrugation. If you have a surface with high roughness, this is the function to use. Once again, no height measurements should be taken after this filter.

2nd Fit plane is excellent for images that have interesting features sitting at different heights.

Flatten fits a polynomial to the background. Use itse carefully because it can and will severely disturb real heights on a corrugated image.

Matrix Convolution is an excellent filter. However, you will lose sharpness in the final image – this can be both a good and a bad thing.

Redimension can be an excellent tool for cleaning up some periodic artifacts

Remove Lines works similar to redimension and can be very helpful for touchup in the image. Getting rid of tip drops is one of many examples.

Reverse is another tool that should not be underestimated. Much insight about what you're looking at can be gathered from this function. I highly recommend it.

Gaussian Smooth is a great way to hide small amplitude electric noise.

Spot Cleaner requires finesse in use, I found it to be similar to FFT, great for an occasional situation. Play around with this function – but don't expect much from it.

Tip surface dilation is a fantastic way to compare two images of the same area that show different features. One can get much better insight into what is real and what is not.

Recalibrate is a powerful feature that can be instrumental in conjunction with Derivative and 3D modes.

Local and Global Plane should be your go to features in initial processing. The heights remain real and you're not mathematically altering your data in any way.

Line Profile is your friend! A copy/paste of the image from WsXM into Excel converts the image into data columns. Remember this when it's time to make publishable figures!

You should always take a look at your Roughness analysis, because it is a great way to check heights and get a feel for how sharp your tip actually is. It is not so useful if you have tons of different types of features on the surface.

Flooding - you will be doing a lot of it. Always View Centers and View Perimeters! This will prevent you from counting things that shouldn't be counted. Use Plane feature extensively on small cut-out regions of the image and use Global plane less often. Cut up image into smaller pieces if you have to. This function gives the most wealth of information per click. Learn to love it, because it puts a number to any feature instantly making qualitative guesstimates into quantitative measurements.

Z-Scale is a part of Redimension.

Palette settings is another function you need to learn to love. So much more can be shown with a simple brightness/contrast adjustment. Play a lot with color schemes! You are not altering the data with this setting, you are just showing off your raw data without fancy filters.

Display info. Anytime you have to show an image record size, bias, current, image name and date right there in your presentation, this saves a lot of searching back and forth. All the parameters are displayed when using this function.

Keep in mind, what you're looking at is mathematical data made to look like an image. Everything you can do with numbers can be done with images. This is where learning basic MatLab skills will set your data apart.

GREEN-BLACK THIEL SMILODON

PARTS LIST

(2) OKGEAR 6FT DVI DIGITAL DUAL LINK CABLE

(2) LITE ON 20X DVDR BURNER

(1) RAIDMAX SMILODON ATX MID TOWER WITH 500W PS

(1) BYTECC BLACK INTERNAL 1.44 MB FLOPPY

(2) SAMSUNG SPINPOINT HD103UJ 1TB SATA 3GB/S HDD

(2) HANNS-G 22" WIDESCREEN MONITOR

(1) PNY VCGGTX260XPB GEFORCE GTX 260

(1) LOGITECH STANDARD KEYBOARD

(1) LOGITECH G7 RF MOUSE

(2) PATRIOT 2X2GB DDR2 1200 PC 9600 RAM

(1) LOGITECH QUICKCAM ORBIT AF 2.0MP

(1) GENIUS MIC-01A 3.5MM MICROPHONE

(1) LOGITECH S-220 17WATT 2.1 SPEAKER SYSTEM

(1) ASUS P5Q LGA 775 INTEL P45 ATX MOTHERBOARD

(1) INTEL CORE 2 DUO E8400 WOLFDALE 3.0GHZ

NOTES

- Originally configure with Win XP SP3
- Upgraded to Win 7 64bit Pro
- HDD formatted separately, not in RAID array
- DUAL Boot to Ubuntu 8.1
- Backup on 2nd HDD